Winter 12-15-2016

Ongoing and Visually-Evoked Cortical Activity Measured Across Multiple Spatial Scales

Nathaniel Caleb Wright
Washington University in St. Louis

WASHINGTON UNIVERSITY IN ST. LOUIS

Department of Physics

Dissertation Examination Committee:
Ralf Wessel, Chair
Anders Carlsson
Jim Miller
Woodrow Shew
Larry Snyder

Ongoing and Visually-Evoked Cortical Activity Measured Across Multiple Spatial Scales

by
Nathaniel Wright

A dissertation presented to
The Graduate School
of Washington University in
partial fulfillment of the
requirements for the degree
of Doctor of Philosophy

December 2016
St. Louis, Missouri

Table of Contents

List of Figures

List of Tables

Acknowledgments

I'd like to thank my advisor Ralf Wessel. Ralf's principled approach to his work has encouraged me to be organized, to plan carefully, to remain calm and circumspect when things are not working as planned, and to not fudge the details. He has encouraged me to have a broader perspective, and by helping me over and over with my writing and presentations, he's made me a better communicator. Most importantly, he is clearly devoted to his family. I'm thankful that I've spent my first years as a researcher under Ralf's instruction.

I'd like to thank my fellow lab members and collaborators, past and present. David Morton, Jeff Pobst, Thomas Crockett, and Mahmood Hoseini have donated a lot of time to teaching me. James Johnson, Zhengyu Ma, Tina Xia, Tansel Baran Yasar, and Mahmood have offered an enormous amount of feedback and helpful insights. Mahmood has been my closest collaborator, and I will always value the time we spent at our whiteboards. I am also indebted to Dr. Woodrow Shew and Dr. Michael Ariel. I have enjoyed working with and learning from you.

Finally, I'd like to thank my family. My parents, sisters, and in-laws have supported and encouraged me in my graduate work. I especially want to thank my wife Alisa, who helps me to have the right perspective. I wouldn't have pursued this degree without her encouragement. My wife and children make me even more thankful for my work, because it provides for them. I'm glad we get to be together.

Nathaniel Wright

Washington University in St. Louis

December 2016

ABSTRACT

Ongoing and Visually-evoked Cortical Activity Measured Across Multiple Spatial Scales
by
Nathaniel C. Wright
Doctor of Philosophy in Physics
Washington University in St. Louis, 2016
Professor Ralf Wessel, Chair

The visual cortex is a densely-interconnected network of neurons, which receives sensory input from the early visual pathway, and represents information about the visual world in the resulting spatiotemporal activity patterns. These patterns are mediated by cortical interactions that span multiple spatial scales (i.e., neuron-neuron, neuron-population, and population-population). Such interactions are a fundamental property of cortical function, and capture the contribution of the cortex to sensory coding. Yet these interactions are only beginning to be understood, in part because of the challenge of recording ongoing and visually-evoked activity across multiple spatial scales in individual studies. In this thesis, we present the results of such a study. Using the *ex vivo* turtle eye-attached whole-brain preparation, we simultaneously recorded the membrane potentials from pairs of cortical pyramidal neurons, as well as the nearby local field potential (LFP). In a parallel set of experiments, we recorded the LFP from multiple locations using a microelectrode array. To identify relevant cortical properties, we supplemented our experimental approach with network simulations. Our results quantify cortical interactions using a variety of coordination measures, and suggest that ongoing cortical activity, synaptic clustering, synaptic adaptation, and emergent network phenomena fundamentally shape the distribution and dynamics of coordination levels. Together, these results contribute to a clearer picture of cortical visual processing, and the roles of specific anatomical and emergent cortical properties in network function.

Chapter 1

Introduction: the study of cortical activity across multiple spatial scales

1.1 Neurons and neuronal populations interact across multiple spatial scales

The visual cortex is an enormous population of densely interconnected neurons. Its role in the brain is often described in terms of information and language: it receives information about the visual world from the early visual pathway (i.e., the retina, optic nerve, and lateral

geniculate nucleus, or LGN) that is written in a relatively low-level language, and combines these basic ingredients to represent more complex properties of the visual world in a language that can in turn be understood by yet higher-order areas (**Fig. 1.1a**). There is actually much more to it than this (including complex feedback loops involving LGN, cortex, and these higher-order areas, **Fig. 1.1b**), but this one function alone is incredible and essential to overall brain function.

How does a population of neurons accomplish this? Essentially, through interactions. Each of the hundreds of thousands of cortical neurons receives inputs from and sends outputs to thousands of other cortical neurons (**Fig. 1.1**). The anatomical arrangements of these excitatory and inhibitory connections define countless "microcircuits"(Földy, Dyhrfjeld-Johnsen, & Soltesz, 2005; Shepherd, 2011). Through these connections, groups of neurons that receive information about disparate aspects of the visual world are able to interact, and complex attributes of an organism's surroundings are represented in complex spatiotemporal cortical spiking patterns(Harris & Mrsic-Flogel, 2013). Thus, the study of cortical function is fundamentally a study of neuronal interactions.

Which interactions, then, should the neuroscientist study? It would be reasonable to start with those between pairs of neurons. But which of the hundreds of thousands of cortical neurons should the experimenter target? Given the sheer magnitude of the cortex, perhaps it would make sense to create a more tractable problem by first grouping neurons into populations, and measuring the interactions between pairs of populations. This, however, requires defining an appropriate population size (hopefully in line with what the cortex actually uses), and again choosing an appropriate pair. Neuroscientists have addressed this confounding issue in a reasonable way: by choosing lots of different scales. Studies spanning several decades have investigated cortical activity (and pairwise interactions) at the level of the neuron, the local

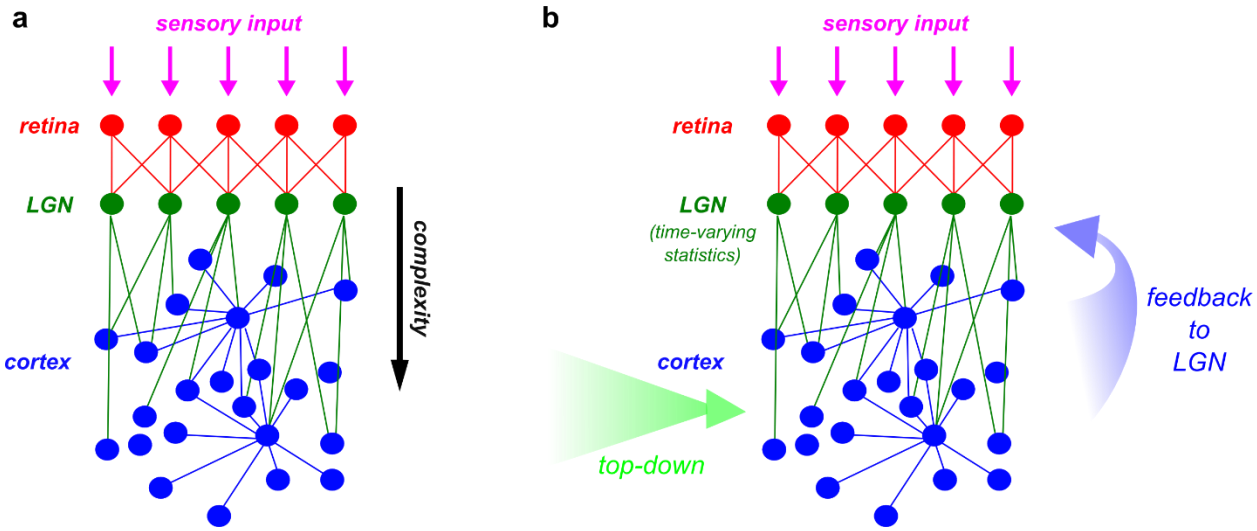

Figure 1.1 The cortex is dominated by interactions across multiple spatial scales. (a) An extremely simplified view of the early visual pathway (that is, from retina to cortex). Information about the visual world travels from retina to lateral geniculate nucleus (LGN) and finally to cortex. Along the way, the increasing complexity of within- and across-layer connectivity (not always depicted, for simplicity) results in an increasingly-complex representation of the sensory input. (b) A more realistic (but still relatively simplified) approximation of the early visual pathway recognizes that the time-varying statistics of LGN neurons, the strong feedback from cortex to LGN, and top-down modulation from higher-order areas are likely to influence cortical activity.

population, and much larger regions of cortex. The answer to the above question is a bit surprising: interactions take place at a variety of spatial scales (neuron-neuron, neuron-population, population-population)(Panzeri, Macke, Gross, & Kayser, 2015). Moreover, the interactions among groups, and even the very identities of groups in terms of component members, change dynamically during spontaneous and sensory-evoked activity(Averbeck & Lee, 2004; Harris, 2005). In addition, the interactions at one scale (e.g., population-population) are constrained by those at other scales (e.g., neuron-neuron). Indeed, even with relatively simple connectivity rules, model networks can exhibit a variety of complex, population-wide emergent phenomena(Beggs, 2008; Keane & Gong, 2015). Finally, large-scale fluctuations (that is, activity patterns spanning multiple populations) appear to affect the sensory responses of individual neurons(Okun et al., 2015; Petersen, Hahn, Mehta, Grinvald, & Sakmann, 2003; Scholvinck, Saleem, Benucci, Harris, & Carandini, 2015). Simply put, it would appear there is no "one scale" at which the brain operates, nor "one most important scale", nor even a single scale that is independent of the others.

It has thus become increasingly clear that the study of cortical function (i.e., interactions) must be very broad. To date, most studies have focused on a single spatial scale, and our knowledge has grown by comparing results across studies. With advances in recording techniques, it is now becoming possible to simultaneously measure cortical activity across multiple scales. This is a powerful approach; certain questions can only be addressed via such simultaneous measurements. For example, what is the impact of a spontaneous change in cortical state (defined by the activity of a large population) on the sensory response of a single neuron? What is the mechanistic (i.e., synaptic) basis for this influence? How do network-wide fluctuations impact subthreshold correlations between pairs of nearby neurons? What are the

small-scale interactions that give rise to large-scale measurables (e.g., ECoG signals)? This last question is extremely relevant to treating neurological disorders. In humans, recording techniques are typically non-invasive, and measure large-scale population activity. Many neurological disorders are associated with irregularities in these signals. Pharmacology, however, typically acts at the level of the synapse. Treating such disorders requires a detailed understanding of the neuron-neuron interactions that give rise to these large-scale phenomena.

1.2 Experimental approach

In this thesis, we present the results of a multi-scale study; we recorded ongoing and visually-evoked cortical activity in an intact visual system using single- and multi-whole-cell recordings, local field potential (LFP) recordings from single electrodes, and simultaneous LFP recordings using microelectrode arrays (MEAs) that spanned large regions of cortex (**Fig. 1.2**). MEA recordings of visual responses are by no means rare; indeed, they are commonly achieved in awake, behaving animals. It is extremely difficult, however, to achieve stable whole-cell recordings *in vivo*. Multi-scale studies thus tend to be constrained to the larger end of the spectrum of recording scales. Here, we gain access to extremely small-scale interactions via the *ex vivo* turtle eye-attached wholebrain preparation, which is ideally-suited to the full barrage of recording techniques listed above, and specifically stable whole-cell recordings.

These recording techniques have one distinct advantage in common: they all provide a measure of cortical activity that is at least approximately spike-rate independent. The LFP, for example, can be conservatively described as a measure of cortical activity in a small volume near the electrode tip(Katzner et al., 2009) (**Fig. 1.2a**), and there may be some contribution from local spikes(Destexhe, 1998). While a more specific description invites controversy, recent work has

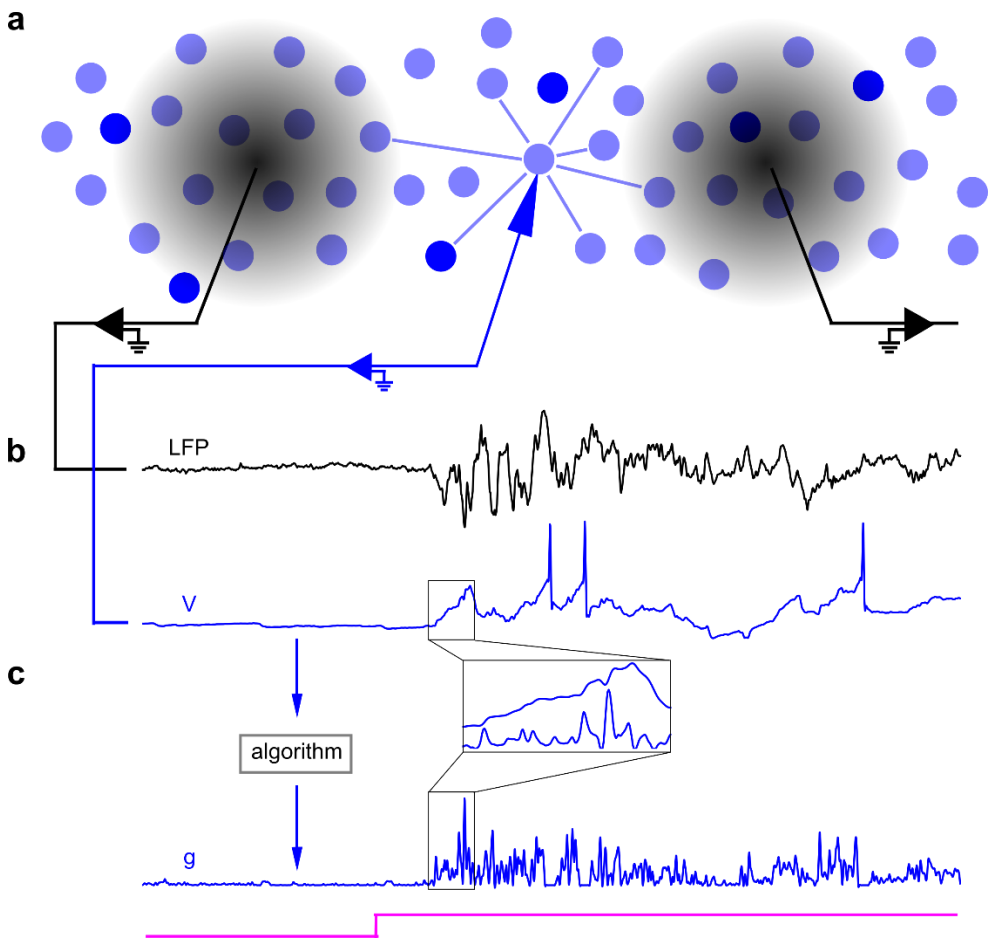

Figure 1.2 Individual recording modalities have specific strengths and weaknesses, and our experimental approach combines the strengths of each. (a) The majority of cortical neurons are sparse-spiking (low opacity dots), and a minority (high-opacity dots) respond to sensory stimulation with high spike rates. The local field potential (LFP, black circles) provides a measure of cortical activity in a nearby population, with a neuron's contribution to the LFP falling off with distance from the electrode. An individual neuron samples a very specific cortical subpopulation (connections indicated by light blue lines), and patch clamp recordings allow the experimenter to "tap into" this microcircuitry. (b) Both the LFP and membrane potential (V) provide a continuous measure of cortical activity. The utility of each signal for certain analyses is independent of spike rate. (c) We use an algorithm to infer the excitatory synaptic conductance (g) from V, which disentangles excitatory inputs from inhibitory, and provides a more temporally-precise view of synaptic activity (inset).

demonstrated that the LFP can be a reliable predictor of local, synchronous synaptic currents(Haider, Schulz, Häusser, & Carandini, 2016; Okun, Naim, Lampl, Nain, & Lampl, 2010). This is a useful measure of cortical activity, given that spiking in cortex is sparse, with the majority of neurons(Shoham, O'Connor, & Segev, 2006) firing too seldom to provide reliable statistics for certain analyses(Cohen & Kohn, 2011) (even in response to strong sensory stimulation). Further, the membrane potential can be thought of as a proxy for a probability to spike. These techniques thus give voice to "dark" neurons by being agnostic to output spike rate (**Fig. 1.2b**).

Each technique also has specific strengths and limitations. For instance, despite its utility as a spike-rate-independent measure, the LFP suffers from at least three shortcomings. First, the contribution of a given synaptic event to the LFP falls off with distance to the electrode (**Fig. 1.2a**), and the exact nature of this distance-dependence is unclear(Riera et al., 2012). Second, the events that take place within the LFP-defined sphere are averaged across time and space, thus limiting spatiotemporal resolution. Finally, the extracellular electrode is what defines the sampled population. There is no reason *a priori* to assume such a population represents a complete or relevant cortical microcircuit. Thus, while the MEA tracks cortical activity across large spatial scales, it's impossible to use this tool to track the interactions within and across cortical microcircuits. Fortunately, this is a specific benefit of membrane potential recordings. Each cortical neuron samples an extremely large and broadly-distributed presynaptic pool, and the patch clamp electrode therefore allows the experimenter to "tap into" the cortical microcircuitry (**Fig. 1.2**). The ability to infer presynaptic spiking is tempered, however, by the membrane time constant (which smooths synaptic events), and the fact that near-simultaneous excitatory and inhibitory synaptic inputs mask one another at the level of the membrane

potential. In chapter 5, we present and apply a work-around: we use an algorithm(Yaşar, Wright, & Wessel, 2016) to infer the excitatory synaptic conductance (g) from the membrane potential (**Fig. 1.2c**). This provides a more temporally-precise measure of excitatory presynaptic spiking, at the expense of information about inhibition.

1.3 Organization of this thesis

This thesis begins with a chapter detailing relevant background information, followed by several chapters describing cortical interactions during ongoing and visually-evoked activity. The order of these latter chapters essentially reflects increasing spatial scale. This work is thus a "chain" of studies, linked in the printed order by at least one common recording modality. The final chapter describes phenomena we observed but did not study in-depth, which motivates future work.

- **Chapter 2: Turtle dorsal cortex pyramidal neurons comprise two distinct cell types with indistinguishable visual responses**
    - An analysis of pyramidal neuron subtypes in turtle visual cortex, according to passive and active electrophyisiological properties, which describes the "machinery" of the preparation we study.
    - Thomas Crockett is the first author, and this chapter also appears in his thesis.
    - This chapter has been published in PLOS ONE(Crockett, Wright, Thornquist, Ariel, & Wessel, 2015).

- **Chapter 3: Network activity influences the subthreshold and spiking visual responses of pyramidal neurons in a three-layer cortex**
    - An investigation of ongoing and visually-evoked cortical activity, as revealed by intracellular recordings of the subthreshold membrane potential and action potentials of pyramidal neurons, with an emphasis on the relationship between ongoing and evoked activity.
    - This chapter is being prepared for submission to a peer-reviewed journal.
- **Chapter 4: Adaptation modulates correlated response variability in visual cortex**
    - This chapter investigates correlated variability (or "noise correlations") in the fast subthreshold fluctuations in pairs of nearby pyramidal neurons, and incorporates a model investigation that reveals a close link to network oscillations.
    - Mahmood S. Hoseini is co-author of this chapter, which also appears in his thesis.
    - This chapter is being prepared for submission to a peer-reviewed journal.
- **Chapter 5: The coupling of synaptic inputs to local cortical activity differs among pyramidal neurons and adapts following stimulus onset**
    - Here, we use an algorithm (developed by Tansel Baran Yasar) to estimate ongoing and visually-evoked excitatory synaptic inputs from single-trial membrane potential recordings, study the across-trial variability of these inputs and coupling with that of the nearby LFP, and use a model network to identify relevant network properties.
    - Tansel Baran Yasar and Mahmood S. Hoseini are co-authors of this chapter, and versions of this work also appear in their theses.
    - This chapter is being prepared for submission to a peer-reviewed journal.

- **Chapter 6: Adaptation to sensory input tunes visual cortex to criticality**
    - This chapter deals with properties that emerge in networks of neurons subject to particular interaction rules, and the results suggest that during vision, the cortical network self-organizes to a state that is optimal for sensory encoding, primarily by mediating pairwise interactions via synaptic adaptation.
    - Woodrow Shew is first author of this chapter. Jeff Pobst, Wesley P. Clawson, and Yahya Karimipanah are co-authors of this chapter, which also appears in their theses.
    - This chapter has been published in Nature Physics(Shew et al., 2015).
- **Chapter 7: Future work in the *ex vivo* turtle eye-attached whole-brain preparation**
    - This chapter describes (i) various experimental observations that we did not investigate in-depth, and (ii) ideas for future projects that should expand on the work presented here.

Averbeck, B. B., & Lee, D. (2004). Coding and transmission of information by neural ensembles. *Trends in Neurosciences*, *27*(4), 225–30. http://doi.org/10.1016/j.tins.2004.02.006

Beggs, J. M. (2008). The criticality hypothesis: how local cortical networks might optimize information processing. *Philosophical Transactions of the Royal Society A: Mathematical, Physical and Engineering Sciences*, *366*(1864), 329–343. http://doi.org/10.1098/rsta.2007.2092

Cohen, M. R., & Kohn, A. (2011). Measuring and interpreting neuronal correlations. *Nature*

Neuroscience, *14*(7), 811–819. http://doi.org/10.1038/nn.2842

Crockett, T., Wright, N., Thornquist, S., Ariel, M., & Wessel, R. (2015). Turtle dorsal cortex pyramidal neurons comprise two distinct cell types with indistinguishable visual responses. *PLoS ONE*, *10*(12), 1–22. http://doi.org/10.1371/journal.pone.0144012

Destexhe, a. (1998). Spike-and-wave oscillations based on the properties of GABAB receptors. *The Journal of Neuroscience : The Official Journal of the Society for Neuroscience*, *18*(21), 9099–9111.

Földy, C., Dyhrfjeld-Johnsen, J., & Soltesz, I. (2005). Structure of cortical microcircuit theory. *The Journal of Physiology*, *562*(Pt 1), 47–54. http://doi.org/10.1113/jphysiol.2004.076448

Haider, B., Schulz, D. P. A., Häusser, M., & Carandini, M. (2016). Millisecond Coupling of Local Field Potentials to Synaptic Currents in the Awake Visual Cortex. *Neuron*, *90*(1), 35–42. http://doi.org/10.1016/j.neuron.2016.02.034

Harris, K. D. (2005). Neural signatures of cell assembly organization, *6*(May), 399–407.

Harris, K. D., & Mrsic-Flogel, T. D. (2013). Cortical connectivity and sensory coding. *Nature*, *503*(7474), 51–8. http://doi.org/10.1038/nature12654

Katzner, S., Nauhaus, I., Benucci, A., Bonin, V., Ringach, D. L., & Carandini, M. (2009). Local Origin of Field Potentials in Visual Cortex. *Neuron*, *61*(1), 35–41. http://doi.org/10.1016/j.neuron.2008.11.016

Keane, A., & Gong, P. (2015). Propagating waves can explain irregular neural dynamics. *J Neurosci*, *35*(4), 1591–1605. http://doi.org/10.1523/jneurosci.1669-14.2015

Okun, M., Naim, A., Lampl, I., Nain, A., & Lampl, I. (2010). The Subthreshold Relation

between Cortical Local Field Potential and Neuronal Firing Unveiled by Intracellular Recordings in Awake Rats. *Journal of Neuroscience*, *30*(12), 4440–4448. http://doi.org/10.1523/JNEUROSCI.5062-09.2010

Okun, M., Steinmetz, N. a., Cossell, L., Iacaruso, M. F., Ko, H., Barthó, P., … Harris, K. D. (2015). Diverse coupling of neurons to populations in sensory cortex. *Nature*, *521*(7553), 511–515. http://doi.org/10.1038/nature14273

Panzeri, S., Macke, J. H., Gross, J., & Kayser, C. (2015). Neural population coding: combining insights from microscopic and mass signals. *Trends in Cognitive Sciences*, *19*(3), 162–172. http://doi.org/10.1016/j.tics.2015.01.002

Petersen, C. C. H., Hahn, T. T. G., Mehta, M., Grinvald, A., & Sakmann, B. (2003). Interaction of sensory responses with spontaneous depolarization in layer 2/3 barrel cortex. *Proceedings of the National Academy of Sciences of the United States of America*, *100*(23), 13638–43. http://doi.org/10.1073/pnas.2235811100

Riera, J. J., Ogawa, T., Goto, T., Sumiyoshi, A., Nonaka, H., Evans, A., … Kawashima, R. (2012). Pitfalls in the dipolar model for the neocortical EEG sources. *Journal of Neurophysiology*, *108*(4), 956–75. http://doi.org/10.1152/jn.00098.2011

Scholvinck, M. L., Saleem, A. B., Benucci, a., Harris, K. D., & Carandini, M. (2015). Cortical State Determines Global Variability and Correlations in Visual Cortex. *Journal of Neuroscience*, *35*(1), 170–178. http://doi.org/10.1523/JNEUROSCI.4994-13.2015

Shepherd, G. M. (2011). The microcircuit concept applied to cortical evolution: from three-layer to six-layer cortex. *Frontiers in Neuroanatomy*, *5*(May), 30. http://doi.org/10.3389/fnana.2011.00030

Shew, W. L. W. L., Clawson, W. P. W. P., Pobst, J., Karimipanah, Y., Wright, N. C. N. C., & Wessel, R. (2015). Adaptation to sensory input tunes visual cortex to criticality. *Nature Physics*, *11*(8), 659–663. http://doi.org/10.1038/nphys3370

Shoham, S., O'Connor, D. H., & Segev, R. (2006). How silent is the brain: Is there a "dark matter" problem in neuroscience? *Journal of Comparative Physiology A: Neuroethology, Sensory, Neural, and Behavioral Physiology*, *192*(8), 777–784. http://doi.org/10.1007/s00359-006-0117-6

Yaşar, T. B., Wright, N. C., & Wessel, R. (2016). Inferring presynaptic population spiking from single-trial membrane potential recordings. *Journal of Neuroscience Methods*, *259*, 13–21. http://doi.org/10.1016/j.jneumeth.2015.11.019

Chapter 2

Turtle Dorsal Cortex Pyramidal Neurons Comprise Two Distinct Cell Types with Indistinguishable Visual Responses

A detailed inventory of the constituent pieces in cerebral cortex is considered essential to understand the principles underlying cortical signal processing. Specifically, the search for pyramidal neuron subtypes is partly motivated by the hypothesis that a subtype-specific division of labor could create a rich substrate for computation. On the other hand, the extreme integration of individual neurons into the collective cortical circuit promotes the hypothesis that cellular individuality represents a smaller computational role within the context of the larger network. These competing hypotheses raise the important question to what extent the computational function of a neuron is determined by its individual type or by its circuit connections. We created electrophysiological profiles from pyramidal neurons within the sole cellular layer of turtle visual cortex by measuring responses to current injection using whole-cell recordings. A blind clustering algorithm applied to these data revealed the presence of two principle types of pyramidal neurons. Brief diffuse light flashes triggered membrane potential fluctuations in those same cortical neurons. The apparently network driven variability of the visual responses concealed the existence of subtypes. In conclusion, our results support the notion that the importance of diverse intrinsic physiological properties is minimized when neurons are embedded in a synaptic recurrent network.

2.1 Introduction

Cortical pyramidal neuron subtype classification has become an area of intense research in neuroscience (Molyneaux et al., 2007). Cortical pyramidal neurons display a vast diversity of properties in numerous dimensions, including morphology, electrophysiology, gene expression, connectivity, and axonal projections (Schubert et al., 2001; Staiger et al., 2004; Arlotta et al., 2005; Molyneaux et al., 2009). Many of these properties covary, indicating that the heterogeneity found in pyramidal neurons is not due to random events but instead due to their separation into specific cellular subtypes (Soltesz, 2006) that is choreographed by transcriptional regulation during neuronal development (Molyneaux et al., 2015). Generating a census of pyramidal neuron subtypes is thought fundamental to the accurate observation and manipulation of brain activity (Lee et al., 2014) and to the development of cell-type and circuit-specific therapies to treat brain disorders (Brumback and Sohal, 2014). As a case in point, the laminar organization of pyramidal neurons in neocortex (Fig 2.1A) plays a key role in the processing of visual inputs, as indicated by layer and cell-type specificity of sensory responses (Gilbert and Wiesel, 1979; Armstrong-James et al., 1992; Brecht and Sakmann, 2002; Martinez et al., 2005; de Kock et al., 2007).

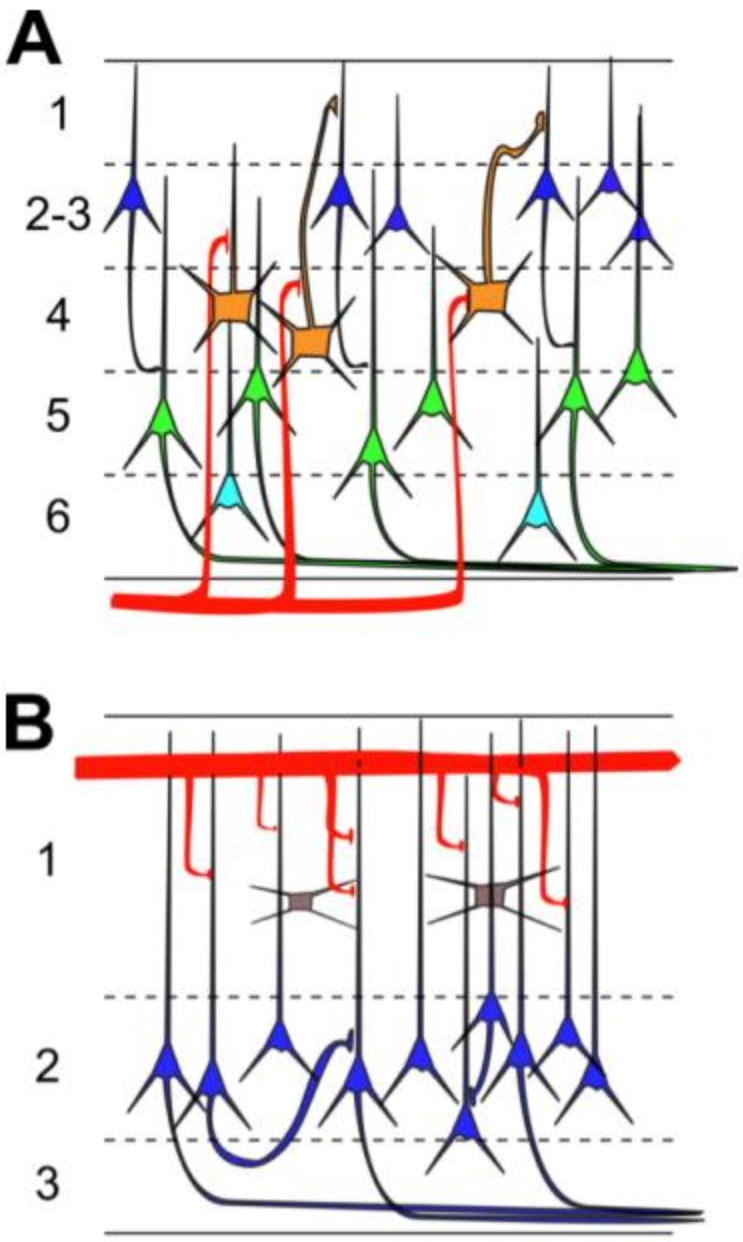

Figure 2.1 Basic microcircuit of neocortex and turtle dorsal cortex. ***A***, The neocortex consists of 6 layers with multiple types of pyramidal neurons (color) and thalamic inputs (red) terminating in spatially restricted regions. For clarity, interneurons are omitted in this schematic diagram. ***B***, The turtle dorsal cortex consists of one cellular layer (#2) of densely packed pyramidal neurons (blue), sandwiched between two neuropil layers (#1 and 3) that are densely packed with dendrites and axons, and also contain interneurons (grey). Sensory afferents (red) from the lateral geniculate

nucleus (LGN) make en-passant synapses in superficial layer 1 on distal segments of pyramidal neuron dendrites and on superficial inhibitory interneurons.

The search for pyramidal neuron subtypes is particularly significant in the trilaminar allocortex (Swanson, 2003), which contains a single layer of densely packed somata of pyramidal neurons sandwiched between layers filled with dendrites, axons, and a few scattered interneurons (Fig 2.1B). In part because of its ancestral position in evolutionary history (Striedter, 2005), information about the allocortex is believed to facilitate the investigation of the neocortex (Shepherd, 2011; Fournier et al., 2014). Three prominent examples of allocortex are the mammalian piriform cortex (Neville and Haberly, 2004) and hippocampus (Johnston and Amaral, 2004), and the reptilian dorsal cortex (Ulinski, 2007). Based on morphological and intrinsic electrophysiological properties, two classes of pyramidal neurons were classified in mouse piriform cortex (Suzuki and Bekkers, 2006, 2011) and the CA1 and subiculum regions of rat hippocampus (Graves et al., 2012). Less is known about the reptilian dorsal cortex, which holds a strategic position among the examples of allocortex. It receives input from lateral geniculate nucleus (LGN) (Heller and Ulinski, 1987; Mulligan and Ulinski, 1990) and thus exemplifies a trilaminar visual cortex (Reiner, 2000; Ulinski, 2007) that processes information from a well-defined spatio-temporal-chromatic visual input space. Information about pyramidal neuron subtypes in the trilaminar dorsal cortex is limited. Variations of properties among pyramidal neurons in the dorsal cortex of turtle (Connors and Kriegstein, 1986) include firing patterns (Mancilla et al., 1998), axonal projection targets (Ulinski, 1986), and molecular markers (Dugas-Ford et al., 2012). It is not known however, whether the variation of properties reflects the existence of pyramidal neuron subtypes or the broad distribution of properties in one neuron type.

Here, we investigate pyramidal neurons within the single layer of densely packed somata of turtle dorsal cortex (Fig 2.2) and uncover the presence of two main electrophysiological types, however with highly fluctuating and indistinguishable responses to visual stimulation of the retina.

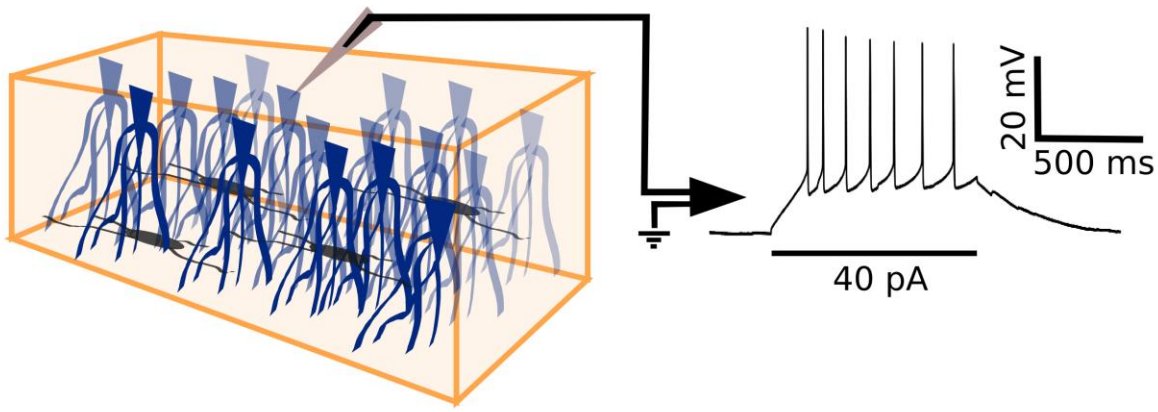

Figure 2.2 Whole-cell recordings from pyramidal neurons in turtle visual cortex. Schematic diagram of an isolated piece of turtle dorsal cortex (left panel) with the ventricular side up and containing pyramidal neurons (blue) and interneurons (grey). A whole-cell recording of the pyramidal neuron membrane potential in response to current injection (right panel) is obtained with a patch electrode (grey triangle) that is positioned at the pyramidal neuron soma under visual guidance with DIC optics.

2.2 Materials and Methods

2.2.1 Ex vivo cortex preparation, visual stimulation, and intracellular recording.

Procedures used in this study were approved by Washington University's Institutional Animal Care and Use Committee and conform to the guidelines of the National Institutes of Health on the Care and Use of Laboratory Animals. Red-eared slider turtles (*Trachemys scripta elegans*, 150 - 200 g weight, 12-15 cm carapace length, of either sex. Niles Biological Inc, Sacramento, CA,

USA) were used in this study. Following anesthesia (intravenous propofol 10 mg/kg) and rapid decapitation by a guillotine, we surgically removed the brain, optic nerves, and eyes from the cranium as described earlier (Kriegstein, 1987; Mancilla et al., 1998; Senseman, 1996; Saha et al., 2011). In brief, during surgery we cut the conjunctiva and extraocular muscles to free the eyes from their orbits. After removing the brain from the skull, we cut rostro-caudally along the medial cortex, starting at the ventricle of the olfactory bulb. This cut preserves the normal afferent input of the visual cortical area, because the geniculocortical pathway traverses the lateral cortical wall within the lateral forebrain bundle (Mulligan and Ulinski, 1990). Subsequently, two medio-lateral cuts to the telencephalon at its anterior and posterior ends prepared for unfolding of the hemisphere and exposing the ventricular surface. For the isolated-cortex preparation, a slab of the cortex was separated from the rest of the brain by cutting along the dorsal ventricular ridge. For the eye-attached whole-brain preparation, the anterior half of the contralateral eye was removed and the vitreous was drained to expose the retina in an eye-cup; the ipsilateral eye was removed. The preparation (cortex slab or eye-attached whole-brain) was transferred to the recording chamber (RC-27LD, Warner Instruments) positioned on an air table and under a fixed-stage upright fluorescent microscope (BX-51WI, Olympus) equipped with differential interference contrast (DIC) optics. The unfolded cortex with the ventricular side up was pinned with short pieces of tungsten wires (25 µm diameter) to a Sylgard (Dow Corning) anchor at the periphery of the recording chamber. The eye-cup, brain, and/or cortex were continuously perfused (2 mL/min) with artificial cerebrospinal fluid (in mM; 85 NaCl, 2 KCl, 2 MgCl2, 45 Na HCO3, 20 D glucose, and 3 CaCl2 bubbled with 95% O2 and 5% CO2), adjusted to pH 7.4 at room temperature. For diffuse whole-field visual stimulation of the retina, a red light emitting diode (LED) was positioned 2 cm above the eye cup. Timed brief flashes of 10 ms duration were presented with at least thirty seconds

between flashes. Approximately 2-3 hrs passed between induction of anesthesia and the start of the experimental recordings. Whole-cell recordings from neurons within the cellular layer of visual cortex were obtained with visually guided (DIC optics) patching using pipettes (4-8 MΩ) pulled from borosilicate glass and filled with a standard electrode solution (in mM, 124 $KMeSO_4$, 2.3 $CaCl_2$-$2H_20$, 1.2 $MgCl_2$, 10 HEPES, 5 EGTA) with 0.04% biocytin for intracellular labeling. Current clamp recordings were made at room temperature (21-24 °C) using an AxoClamp 2B (Axon Instruments) amplifier, digitized with an acquisition board (National Instruments PCI-MIO-16E-4) and controlled using custom LabVIEW software. In turtle visual cortex, spike train differences between pyramidal neurons and interneurons have been reported (Connors and Kriegstein, 1986; Colombe, et al. 2004). In addition, we are confident that the vast majority of our neurons are indeed pyramidal, for the following three reasons. First, neurons were selected from within the densely packed cellular layer, which is clearly distinguishable using DIC optics due to the striking increase in the density of neurons versus the less populous layers 1 and 3. Second, pyramidal neurons account for approximately 80-90% of neurons in the dorsal cortex and are by far the most numerous neurons in layer 2 (Ulinski, 2007). Third, histological spot checks of a third of the neurons in our data set revealed no morphological evidence for interneurons. Therefore, we assume that any contribution of interneurons to the dataset is negligible and we refer to the dataset of recorded neurons as pyramidal neurons. A recorded neuron was accepted in the database when the membrane potential was more negative than -40 mV and the action potential amplitude was larger than 25 mV.

2.2.2 Electrophysiological analysis.

Following five minutes of recording spontaneous membrane potential fluctuations, 14 electrophysiological parameters were obtained for subsequent pyramidal neuron type analysis: (1)

Resting membrane potential (V_{rest}) was measured and current was injected through the recording electrode for 1 second duration with at least 2 seconds of wait time between trials, starting at -70 pA and increasing by 10 pA each trial until a spike was elicited (Shen and Kriegstein, 1986; Christophe et al., 2005; Sosulina et al., 2006). Although the pyramidal neurons were studied within their endogenous cortical circuits, there was no evidence from these recordings that synaptic activity was being modulated by the injected current pulses. We presume, therefore, that the 14 electrophysiological parameters only reflect the intrinsic nature of the recorded neuron. (2) Rheobase current (I_r) was defined as the lowest current for which an action potential was elicited in three consecutive trials (Calvin and Sypert, 1976; Baranyi et al., 1993). Single-spike parameters (3-8) were determined by averaging at least three trials of rheobase current injection. (3) Action potential voltage threshold (V_{th}) was determined as the point of maximum inflection where the third derivative of the voltage is maximized (Baranyi et al., 1993; Sekerli et al., 2004; Christophe et al., 2005). (4) Action potential amplitude (AP Height) was measured from voltage threshold to the peak of the action potential (Takahashi, 1964; Cauli et al., 2000; Gallopin et al., 2005; Andjelic et al., 2009). Action potential duration was measured both (5) halfway between threshold and peak (W_{AP}) (Nowak et al., 2003; Sosulina et al., 2006; Andjelic et al., 2009) and (6) at threshold ($W_{AP,thresh}$) (Calvin and Sypert, 1976; McCormick et al., 1985; Christophe et al., 2005). It should be noted that this definition of "action potential width at threshold ($W_{AP,thresh}$)" can lead to spurious results when applied to neurons with complex and long-lasting depolarization above threshold following the first action potential (Larkum et al., 2008). (7) The action potential fall rate (Min(dV/dt)) was measured as the maximum downslope in the falling phase of the spike (McCormick et al., 1985; Baranyi et al., 1993; Nowak et al., 2003). (8) The time to peak of the afterhyperpolarization (L_{AHP}) was measured as the time elapsed between crossing the threshold

voltage in the falling phase of the action potential to the peak of the afterhyperpolarization (Takahashi, 1965; Calvin and Sypert, 1976). This peak was defined as the post-spike voltage trough. (9) Input resistance (IR) was determined by examining the membrane voltage drop in response to 1-s hyperpolarizing current pulses (Cauli et al., 2000; Gallopin et al., 2005; Sosulina et al., 2006; Andjelic et al., 2009). (10) The membrane time constant (t_m) was determined by fitting an exponential function (Kaleidagraph, Synergy Software, Reading, PA) to voltage traces in response to hyperpolarizing current injection (McCormick et al., 1985; Shen and Kriegstein, 1986; Baranyi et al., 1993). Spike train parameters (11-14) were measured and averaged for several trials where multiple spikes were elicited in response to depolarizing 1-s current pulses. (11) Action potential duration increase ($W_{AP\ Inc.}$) is $(D_2 - D_1)/D_2$ where D_1 and D_2 are the durations at half-max (5) of the first and second spikes, respectively, after beginning depolarizing current injection (Cauli et al., 1997, 2000; Andjelic et al., 2009). (12) Action potential amplitude decrement ($V_{peak\ Dec.}$) is $(A_1 - A_2)/A_1$ where A_1 and A_2 are the amplitudes (4) of those spikes (Cauli et al., 2000; Andjelic et al., 2009). (13) Action potential frequency adaptation ratio (AP FAR) is the ratio of the first interspike interval (ISI) to the average of the last three interspike intervals (Porter et al., 2001; Christophe et al., 2005; Wang et al., 2006). (14) Interspike interval variability (ISI Var) during rhythmic firing is the variance of the interspike intervals over the current injection interval (Calvin and Sypert, 1976). Neurons that never elicited more than one spike were assigned an AP duration increase of 200, an AP amplitude reduction of 100, an adaptation ratio of 0, and an ISI variability of 0.

2.2.3 Unsupervised clustering

To classify neurons, unsupervised clustering using Ward's linkage method was utilized (Ward, 1963). In this algorithm, neurons begin as individual points in a 14-dimensional parameter

space and are grouped in a bottom-up fashion. To ensure that equal weight be given to each of them, parameters were standardized with a mean of 0 and a standard deviation of 1 (Sosulina et al., 2006) prior to analysis. At each step, the neurons or clusters of neurons with minimum between-cluster distance (least Euclidean distance) are merged into a larger cluster. Operationally this is equivalent to finding the pair of clusters that leads to minimum increase in total within-cluster variance after merging. The result of this recursive algorithm is visualized on a dendrogram (tree diagram) as a horizontal bar joining the neurons drawn at a height corresponding to the linkage distance – the Euclidean distance between the two merged neurons/clusters in parameter space. In the next step, two more neurons/clusters are merged. Eventually, neurons are closer to neuron pairs or higher clusters than to other individuals and merge with those pairs into even greater population subclusters, or clusters merge with one another. These collections continue merging step by step until all neurons are contained within one supercluster.

Ward's linkage method generates a dendrogram, but does not provide a rationale at what height to cut the dendrogram into groups and thus cannot inform about an absolute number of clusters. We determined the number of putative pyramidal neuron subtypes among the dataset by dividing the clustering tree into higher-order clusters as suggested by the Thorndike procedure (Thorndike, 1953; Cauli et al., 2000; Andjelic et al., 2009) and validated by silhouette analysis (Rousseeuw, 1987; Karagiannis et al., 2009).

Silhouette analysis quantifies the likelihood that a neuron should be a member of the cluster it was placed in by comparing the mean distance in parameter space between the neuron and its intracluster companions, a_i and the mean distance between it and those neurons in the next closest cluster b_i (Rousseeuw, 1987; Karagiannis et al., 2009) This comparison is normalized by the

maximum of the two averages, giving a neuron silhouette value of $S_i = \frac{(b_i - a_i)}{\max(a_i;b_i)}$, where S_i is strictly bound by $-1 < S_i < 1$. A negative value suggests a potential misclassification, since the neuron in question is then closer in parameter space to the members of a different cluster of neurons than to those of the cluster to which it is assigned. The average silhouette value for the clustering is then given by averaging over all of the neurons $S_{average} = \langle S_i \rangle$ and thus $S_{average}$ is also strictly bound, $-1 < S_{average} < 1$.

Complementary to Ward's clustering, k-means clustering generates clusters in a top-down manner using a predetermined number of k clusters (Hartigan and Wong, 1979). Starting from a random cluster centroid position, positions are iteratively optimized. Thus suboptimal assignment of neurons to specific clusters is dynamically corrected across iterations. The process is repeated different random initial positions of the k-cluster centroids. In k-means clustering, the number of k clusters must be predetermined and, in this study, was chosen to equal the number of clusters inferred from the Ward's method. Additional analysis (not shown) was done with higher numbers of clusters.

2.2.4 Model simulation.

The model network consisted of three clusters of neurons separated by type, including two distinct excitatory groups (A and B, 1000 neurons each) and one inhibitory (200 neurons), with reciprocal connectivity. Intracluster (P_{in}) and intercluster (P_{out}) connection probabilities controlled the likelihood of synaptic connections between neurons. Model neurons were implemented as described earlier (Izhikevich, 2003). Inhibitory neurons and the excitatory neurons of type A and B differed by their defining parameter values (inhibitory: a = 0.1, b = 2, c = -50, d = 2, C_m = 20 µF, R = 100 MΩ; excitatory type A: a = 0.02, b = 0.25, c = -65, d = 0.05, C_m = 20 µF, R = 400

MΩ; excitatory type B: a = 0.02, b = 0.2, c = -65, d = 8, C_m = 30 μF, R = 250 MΩ). Synaptic currents were simulated as described earlier (Brunel and Wang, 2003). Parameters for excitatory currents were V_{syn} = 0 mV, τ_l = 0.5 ms, τ_r = 0.2 ms, τ_d = 1 ms and for inhibitory current were V_{syn} = -70 mV, τ_l = 0.5 ms, τ_r = 0.5 ms, τ_d = 5 ms. Synaptic strength between the possible combinations of external inputs (E), pyramidal neurons (P) and interneurons (I) was parameterized by g_{syn} as follows (in nS): P-to-P, 0.29; P-to-I, 0.3; I-to-P, 3.8; I-to-I, 4.0; E-to-P, 3; E-to-I, 5.2. All neurons received excitatory input in the form uncorrelated Poisson pulse trains at low rate thus generating a baseline level of network activity. The brief external stimulus (mimicking the LGN input caused by a diffuse whole-field flash) to the model network consisted of a 4.5 times increase in the Poisson pulse rate for the duration of 100 ms and exclusively to type A neurons.

2.3 Results

We obtained whole-cell recordings from 225 pyramidal neurons selected under visual guidance with DIC optics from the cellular layer of the turtle visual (dorsal) cortex (Fig 2.2). The densely packed pyramidal neuron somata within the cellular layer appear indistinguishable by visual inspection. Neurons were selected from a region located central between rostral and caudal dorsal cortex. From the recorded membrane potential responses to somatic current injections (1 s duration; 2 s wait time between trials), we obtained the neurons' electrophysiological properties, which we quantified with a selected set of 14 parameters (Fig 2.3A). The parameter set was chosen on the basis of (i) providing distinct, as opposed to redundant, features (Nowak et al., 2003) and (ii) showing variability over the collection of neurons (Cauli et al., 1997, 2000). The resulting distributions of the 14 parameters from the 225 recorded pyramidal neurons were neither multimodal nor Gaussian (Fig 2.3B), thus indicating the possibility for multiple types of pyramidal neurons within the cellular layer of turtle visual cortex.

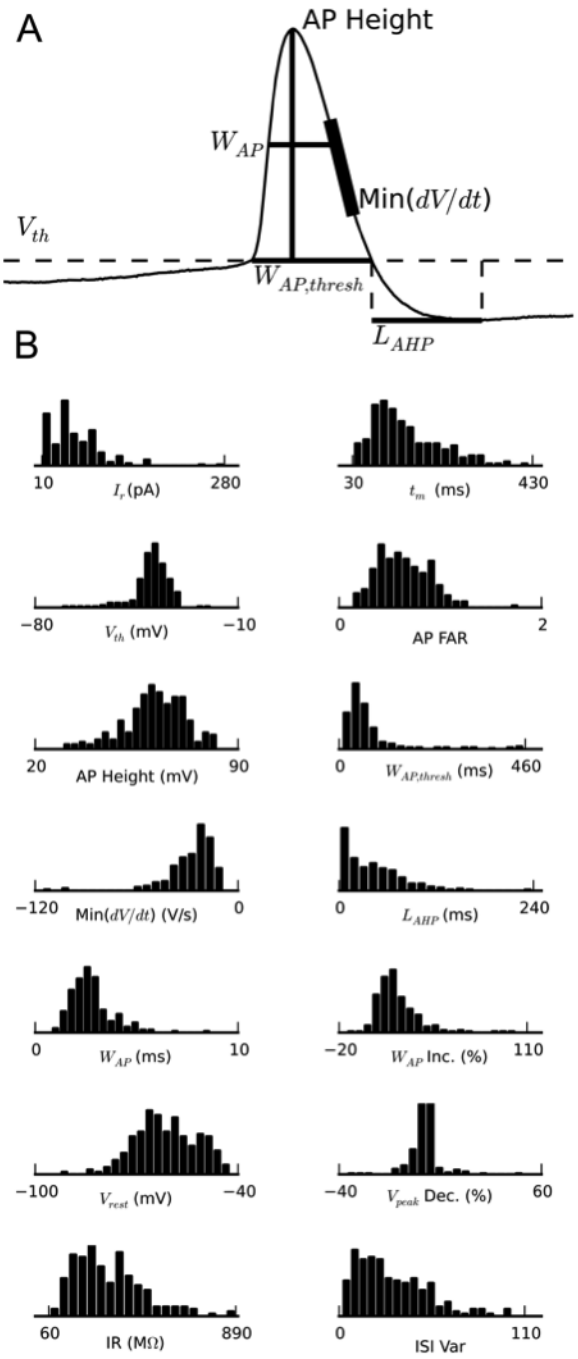

Figure 2.3. Distribution of electrophysiological properties. ***A***, Illustration of how a subset of the parameters were measured from the action potential shape of the first action potential in response to somatic current injection: threshold voltage (V_{th}), width at threshold ($W_{AP,thresh}$), width at half-

max (W_{AP}), height, maximum fall rate (Min(dV/dt)), and afterhyperpolarization latency (L_{AHP}). ***B***, Distribution of the measured values for the 14 electrophysiological parameters from membrane potential recordings in response to somatic current injection from 225 pyramidal neurons: rheobase current (I_r), membrane time constant (t_m), action potential voltage threshold (V_{th}), action potential frequency adaptation ratio (AP FAR), action potential amplitude (AP Height), action potential duration at threshold ($W_{AP,thresh}$), action potential fall rate (Min(dV/dt)), time to peak of the afterhyperpolarization (L_{AHP}), action potential duration halfway between threshold and peak (W_{AP}), action potential duration increase ($W_{AP\ Inc.}$), resting membrane potential (V_{rest}), action potential amplitude decrement ($V_{peak\ Dec.}$), input resistance (IR), interspike interval variability (ISI Var). The apparent deviations from normal distributions suggest that there are discrete groups of pyramidal neurons within this population.

2.3.1 Two main types of pyramidal neurons

To evaluate the number of pyramidal neuron types within the cellular layer (Fig 2.1B, layer 2), we analyzed the data set consisting of 225 neurons in a 14-dimensional parameter space using Ward's linkage method (Ward, 1963). This bottom-up hierarchical clustering algorithm (Method) generates a linkage plot (a tree diagram called a dendrogram) (Fig 2.4). The choice of a threshold in this linkage plot then determines the number of distinct clusters (pyramidal neuron types). No rigorous algorithm exists to choose the threshold. One widely used criterion (Cauli et al., 1997, 2000; Andjelic et al., 2009) is the Thorndike procedure (Thorndike, 1953), which holds that the threshold should be drawn at the merge that provides the largest increase in mean intracluster variance. According to this rationale, the unsupervised clustering algorithm identifies two main classes of pyramidal neurons in layer 2 of turtle visual cortex (Fig 2.4).

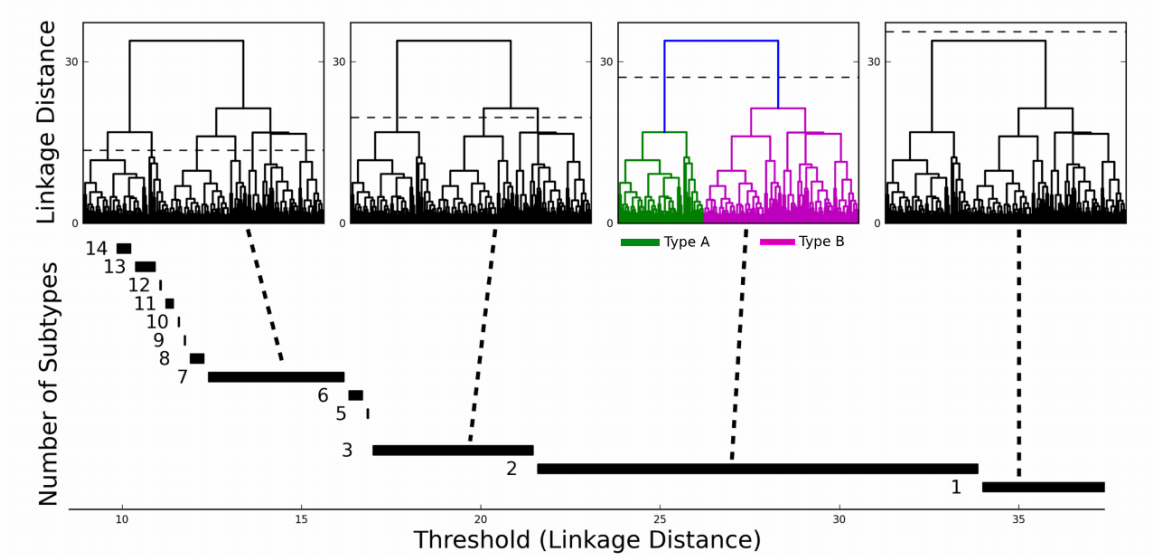

Figure 2.4 Two main types of pyramidal neurons in turtle dorsal cortex. (**TOP**) Ward's unsupervised clustering applied to a sample of 225 pyramidal neurons from turtle dorsal cortex, with each neuron characterized by 14 electrophysiological parameters. The x-axis in each plot represents the individual neurons. The y-axis represents the Euclidean distance between the two merged neurons/clusters in parameter space. Dashed lines in the four identical dendrograms indicate possible threshold choices. The dashed line in the colored dendrogram marks the threshold as suggested by the Thorndike procedure, which indicates two types of pyramidal neurons. (**BOTTOM**) The number of types increases with decreasing threshold in units of the linkage distance. The most robust choice of the threshold value is suggested by the widest range of threshold values in normalized parameter space for which the number of pyramidal neuron types is constant. This choice also indicates two main types of pyramidal neurons in turtle dorsal cortex.

To evaluate the quality of Ward's clustering, we computed the silhouette values for all neurons (Rousseeuw, 1987; Karagiannis et al., 2009). A positive silhouette value indicates that a data point resides closest to its cluster's centroid, whereas a negative silhouette value indicates that the data point lies closer to the centroid of a different cluster (see Methods), suggesting a possible

misclassification. We found that Ward's clustering of the data set into two clusters results in mostly positive silhouette values (average silhouette $\langle S_{ward} \rangle = 0.184$), suggesting two cell types within the data (Fig 2.5A). In contrast, assuming a larger number of clusters (lower threshold) for Ward's clustering resulted in lower average silhouettes (n = 3: $\langle S \rangle = 0.109$) and a greater number of negative individual neuron silhouettes (data not shown).

To evaluate the robustness of the classification into two types, we compared the silhouette values of the bottom-up based Ward's clustering with those from k-means clustering (Hartigan and Wong, 1979). The k-means algorithm differs from the Ward's linkage method in three important ways; it is top-down, contains operational randomness, and predetermines the number of clusters. Applying k-means clustering with k = 2 resulted in mostly positive silhouette values (average silhouette $\langle S \rangle = 0.180$) (Fig 2.5B), thus validating the number of types determined from Ward's clustering. In contrast, silhouette analysis for k-means clustering when assuming a larger number of types resulted in lower average silhouettes (n = 3: $\langle S \rangle = 0.145$) and a greater number of negative individual neuron silhouettes (data not shown).

To evaluate the statistical significance of the k-means clustering of control data, we compared its silhouette values with those from clustering of randomized databases (new database randomization for each k-mean run). Parameter values were shuffled across neurons, destroying the correlations between parameter values while maintaining the same mean, median, and standard deviation of each parameter. We found that the silhouette values for the control data set were consistently higher than the silhouette values for the scrambled dataset (Fig 2.5C). The analysis, seen in Figure 5, was averaged over 1000 K-means and scrambled K-means classifications and their silhouette values. For quantitative comparison, the average silhouette width was used as a global measure of quality of clustering. We found that both Ward's clustering (2 types) and k-

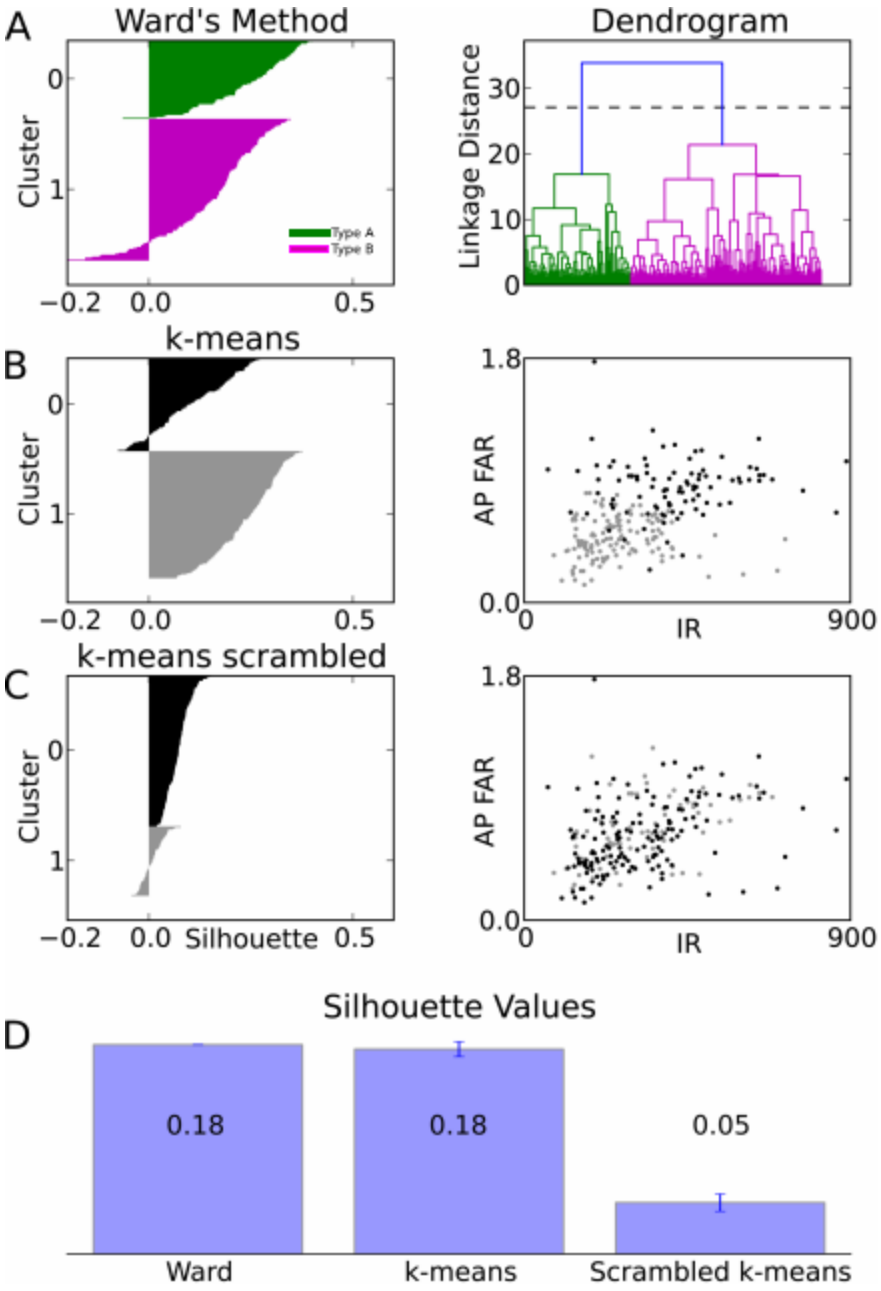

Figure 2.5 Comparison of clustering algorithms. ***A***, Silhouette plot of Ward's clustering. Within each cluster (green/A and magenta/B), cells are ranked (vertical axis) in decreasing order of their silhouette values (horizontal axis). Large positive silhouette values indicate that the data point is close to its cluster's centroid, whereas negative silhouette values indicate that the data point is closer to the centroid of the other cluster. Right panel: The dendrogram from Ward's clustering is shown for comparison. ***B***, Silhouette plot for one rendition of k-means clustering (k = 2). Right panel: The plot of clustered data points (black and gray) within the plane spanned by the input resistance (IR) and the action potential frequency adaptation ratio (AP FAR) illustrates the partial separation of data points from different clusters in this plane alone. ***C***, Silhouette plot for one

rendition of k-means clustering (k = 2) on the scrambled data set. Right panel: The plot of clustered data points (scrambled data set) within the same plane of parameters as in C, reveals the lack of separation caused by scrambling. ***D***, Comparison between the average silhouette for the Ward's and k-means (k = 2) clustering of the original dataset and the average silhouette of randomized databases. Scrambling of the data set causes a consistent loss of quality in the clustering. Error bar of the average silhouette for k-means clustering is evaluated by the SD over 1000 renditions of the original data set and by independent randomization for each rendition of the scrambled data sets.

means clustering (k = 2) of the original data generated significantly larger average silhouette width than k-means clustering (k = 2) on randomized data sets (Fig 2.5D). This reduction in clustering quality by randomization suggests that the clustering quality of the original database is not generated by accidental random correlations between measurements. Rather, the covariation of properties in the original database indicates the existence of two main types of pyramidal neurons, to which we refer to as type A (green) and B (magenta) in the text and figures.

Plotting the occurrence of parameter values for their respective type assignments generated distributions that resemble Gaussian distributions (Fig 2.6). This further supports the notion of two types.

Of the 14 parameters considered, the two resulting types of pyramidal neurons differed most in three parameters (and their physically related counterpart): resting membrane potential (rheobase current), input resistance (membrane time constant), and action potential frequency adaptation ratio (ISI variability) (Table 1 and Fig 2.6, 7). For these three parameters, neither mean was within three standard deviations of the other.

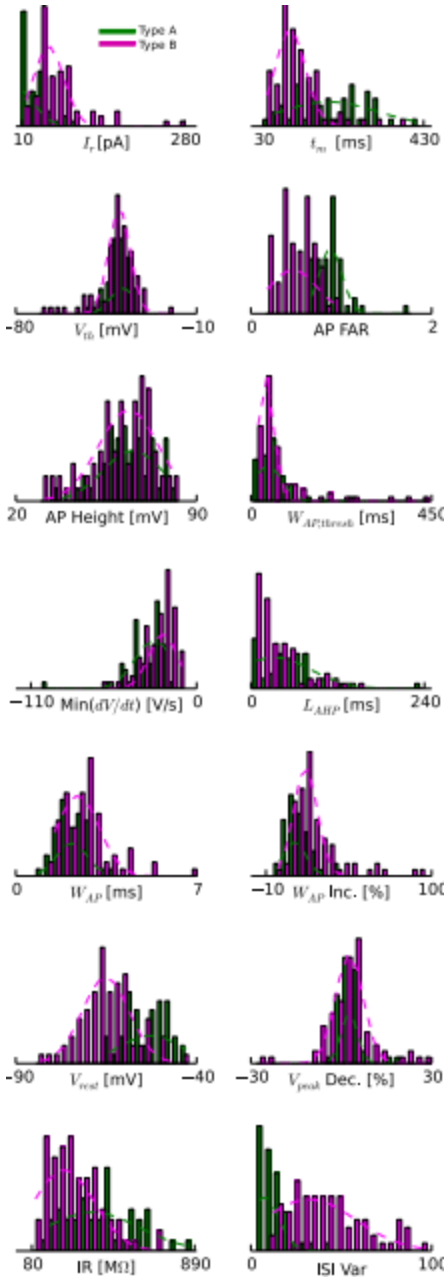

Figure 2.6. Physiological differences between the two main types of pyramidal neurons based on Ward's clustering. Histograms of the distribution of the 14 electrophysiological properties shown in Fig. 3B and corresponding Gaussian fits for the two main types (green/A and magenta/B). Abbreviations as in Fig. 3B.

Parameter	Type A (n = 80)	Type B (n = 145)
Rheobase Current (pA):	33.9 ± 13.0	72.6 ± 19.3
AP Voltage Threshold (mV):	-38.9 ± 2.3	-40.2 ± 3.7
AP Height (mV):	64.7 ± 4.8	59.4 ± 5.2
Maximum AP Downslope (mV/ms):	-34.4 ± 8.6	-23.2 ± 5.0
AP half-width (ms):	2.2 ± 0.3	3.1 ± 0.6
Resting Membrane Potential (mV):	-53.2 ± 2.8	-65.8 ± 3.7
Input Resistance (MΩ):	423 ± 80	271 ± 56
AP Frequency Adaptation Ratio:	0.874 ± 0.104	0.499 ± 0.084
AP Duration at Threshold (ms):	59.9 ± 18.0	82.9 ± 47.5
AHP Time to Peak (ms):	56.2 ± 20.5	32.9 ± 15.5
AP Duration Increase (%):	14.6 ± 6.7	23.1 ± 7.7
AP Amplitude Decrement (%):	4.3 ± 3.4	1.0 ± 3.9
ISI Variability:	15.1 ± 5.4	39.8 ± 10.0
Membrane Time Constant (ms):	198 ± 42	121 ± 27

Table 2.1. Properties of the two main types of pyramidal neurons in turtle visual cortex. Mean and standard deviation for all values.

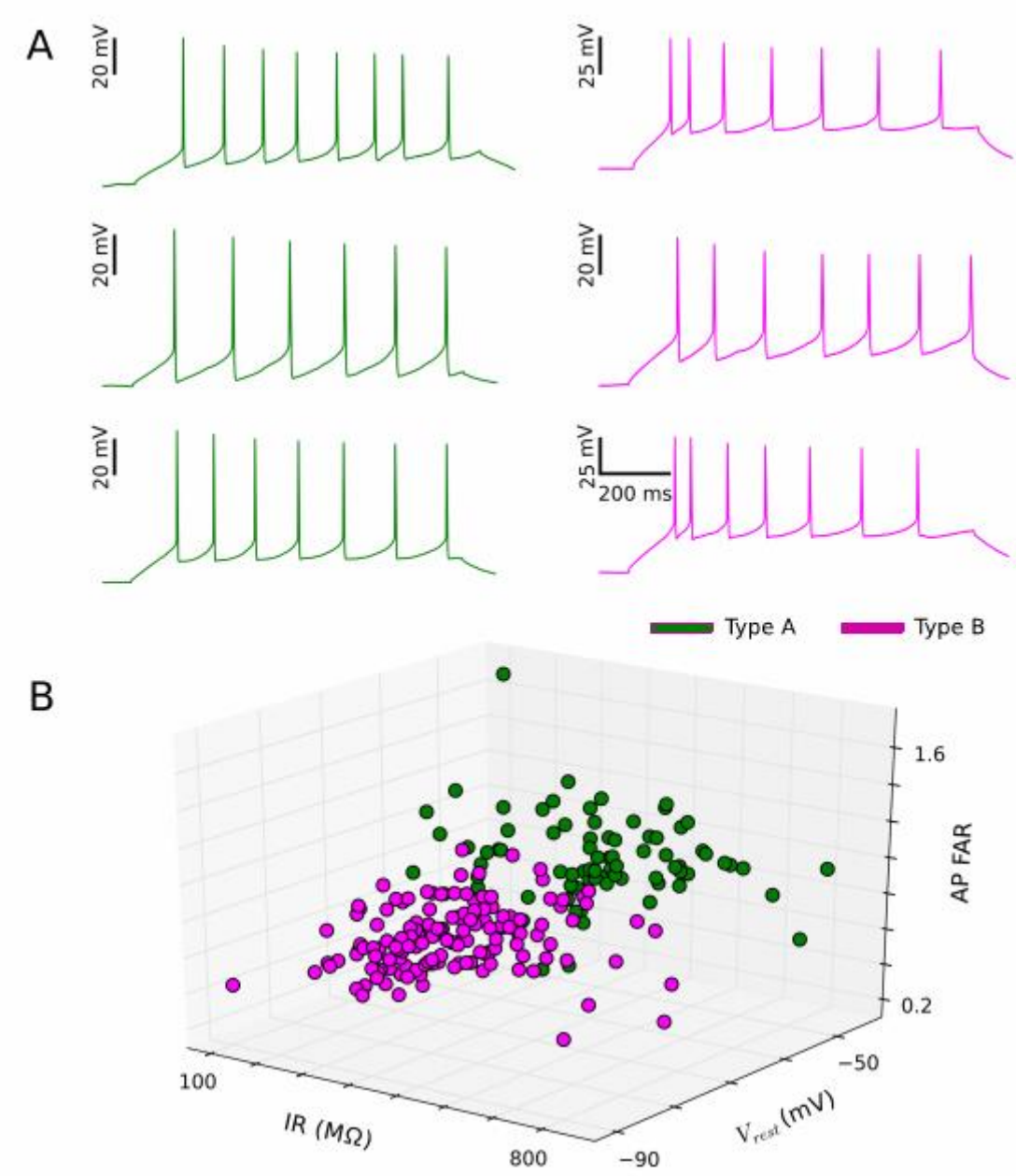

Figure 2.7 Three physiological parameters produce good separation of the two main pyramidal neuron subtypes. ***A***, Representative membrane potential responses to somatic current injections for three pyramidal neurons from each subtype (green/A and magenta/B). Input currents ranged from 50 to 70 pA. ***B***, Partial separation between the two main pyramidal neuron subtypes is observed in a plot of clustered data points (green/A and magenta/B) within the space spanned by the resting membrane potential (V_{rest}), the input resistance (IR), and the action potential frequency adaptation ratio (AP FAR).

2.3.2 The impact of network incorporation on cellular individuality

Turtle dorsal cortex consists of approximately 80,000 pyramidal neurons and 20,000 interneurons (Ulinski, 2007). A single pyramidal neuron receives some 300 thalamic fiber synapses on the distal portion of its spiny apical dendrites (Smith et al., 1980), whereas other cortical pyramidal neurons and interneurons contact the thousands of spines along the spatial extent of the apical and basal dendrites (Desan, 1984). This extensive incorporation of a pyramidal neuron into the cortical circuitry raises the question to what extent the cellular individuality (probed with somatic current injection during ongoing network activity) endures when sensory input pushes the network into a state of high activity (Shew et al., 2015).

To address this question experimentally, we obtained visually guided whole-cell recordings from pyramidal neurons within the cellular layer of visual cortex using the turtle ex vivo eye-attached whole-brain preparation (Method, Fig 2.8A). Subsequent to somatic current injection for offline neuron type classification (as described above), we flashed light (640 nm wavelength, LED, 10 ms duration, 30 s wait between trials) onto the spatial extent of the intact retina within the eye cup and recorded the membrane potential visual responses of the cortical pyramidal neuron (Fig 2.8B). For all pyramidal neurons recorded, visual responses started approximately 100 ms after the brief flash of light and typically lasted for more than 1000 ms. Trial-to-trial variability was extensive, comparable in amplitude to the mean response. The persistent activity and the trial-to-trial variability indicate a significant contribution of the network activity to the cellular visual response of both pyramidal neuron types. Specifically, visual responses consisted of broad depolarization, mediated by a superposition of numerous excitatory

and inhibitory postsynaptic potentials. Responses for the two neuron types appeared largely indistinguishable (Fig 2.8C).

The observed similarity of the visual responses for type A and B neurons raises the question to what extent the integration of a cell within a network overrides the contribution of cellular properties to its response. To address this question, we investigated the impact of connectivity on the time course of the response to a brief external input in a model network (Fig 2.9A). The model network consisted of excitatory model neurons type A and B and of inhibitory model neurons. The three groups of neurons differed in the cellular properties (**Table 2**). A given neuron from a group projects to neurons within its group and to neurons in the other two groups. The level of connectivity was parameterized by the intracluster (P_{in}) and intercluster (P_{out}) connection probabilities. To increase the model challenge of reproducing similar responses with different neuron types, we connected external inputs exclusively to model neurons type A. This differential external input was further motivated by experimental evidence for afferent inputs to one type only from (i) earlier molecularbiological investigations in turtle (Dugas-Ford et al., 2012), and (ii) studies of piriform cortex (Suzuki and Bekkers, 2011).

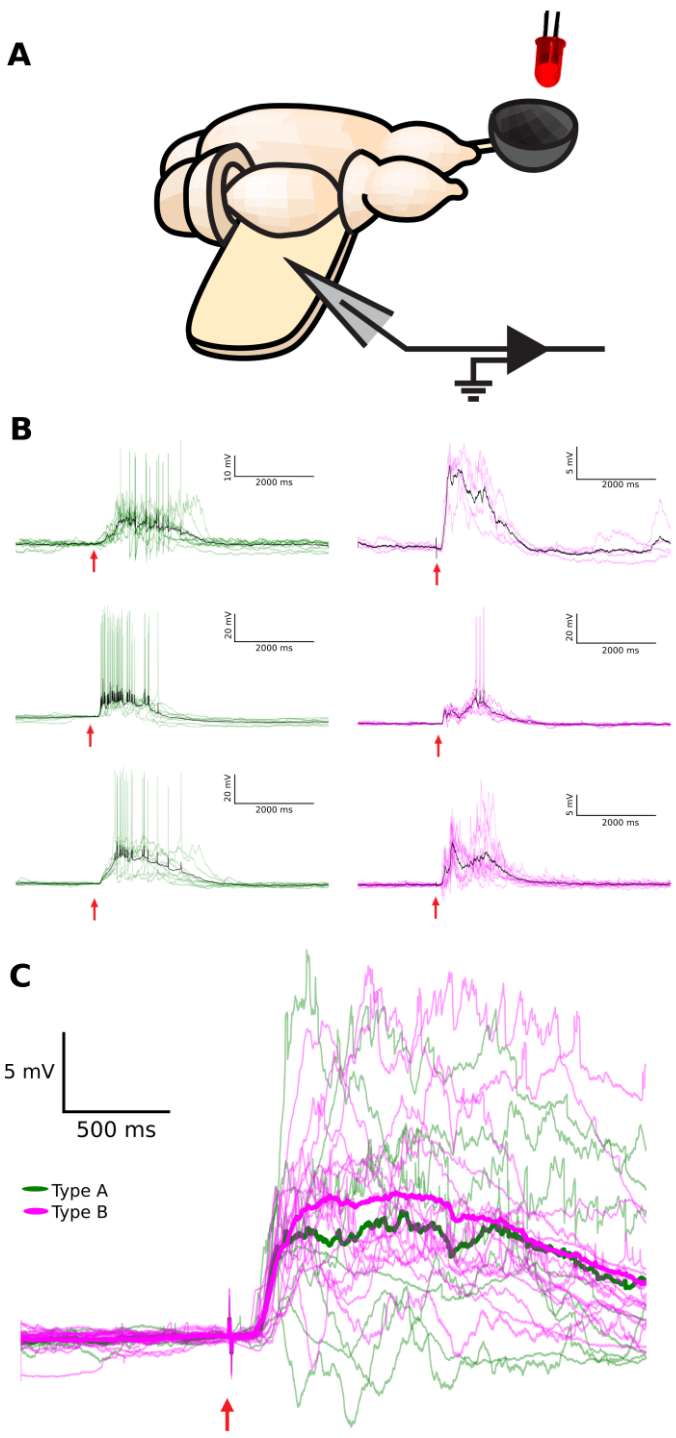

Figure 2.8 Visual response properties of the two physiologically defined pyramidal neuron types. ***A***, Schematic of the turtle ex vivo eye-attached whole-brain preparation. A diffuse flash of light from the LED (red) is projected onto the intact retina within the eye-cup (gray bowl), while the membrane potential from a pyramidal neuron is recorded with a patch electrode (gray triangle)

inserted into the unfolded visual cortex. ***B***, Pyramidal neuron membrane potential responses to brief flashes of light (10 ms, 640 nm; red arrow) persist long beyond the duration of the flash, are variable from trial-to-trial, and display sparse spiking. Trial averages are shown in black. Representative membrane potential visual responses to flashes are shown for three pyramidal neurons from each physiologically defined type (green/A and magenta/B). The responses are fluctuating and similar for both types. ***C***, The time courses of trial-averaged membrane potential (after spike clipping) of all pyramidal neurons recorded in response to flashes (8 type A (green), 16 type B (magenta)). Averages across pyramidal neuron visual responses of the same physiological type are plotted in bold (green/A and magenta/B).

(Table 2)

Parameter	Excitatory A (visual input)	Excitatory B (no visual input)	Inhibitory
a	0.02	0.02	0.1
b	0.25	0.2	2
c	-65	-65	-50
d	0.05	8	2
C_m (μF)	20	30	20
R (MΩ)	400	250	100
N	500	500	150

Table 1.2. Parameters used to define the model neurons.

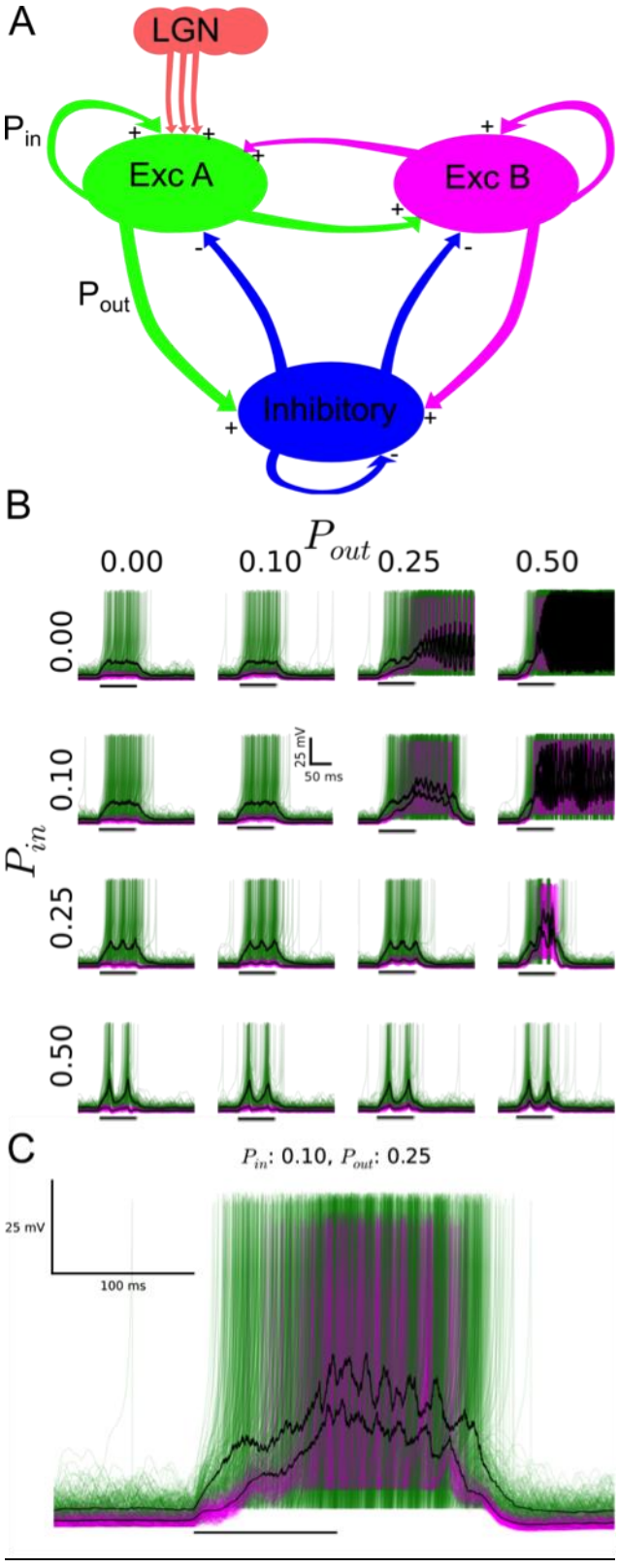

Figure 2.9 A model network with pulsed external inputs reproduces the similarity of the responses for two types of excitatory neurons. ***A***, Conceptual cartoon illustrating key model features,

including inhibitory neurons (blue) and two types of excitatory neurons (green/A and magenta/B), with excitatory external inputs ("LGN", orange) limited to one excitatory type (green/A). Intracluster and intercluster connection probabilities are parameterized by P_{in} and P_{out}, respectively. ***B***, Simulated membrane potential responses for the two types of excitatory model neurons (green/A and magenta/B) in response to a brief (100 ms, black horizontal bar) increase in the external input (increased rate of the Poisson pulse trains) for multiple combinations of intracluster and intercluster connection probabilities, each ranging between 0.0 and 0.5. For clarity, simulation results for 200 of the 1000 neurons of each excitatory type are plotted. ***C***, The connection probability combination of $P_{in} = 0.1$ and $P_{out} = 0.25$ best reproduces the experimentally observed persistent activity and the similarity of the type A (green) and the type B (magenta) response to brief external inputs.

We investigated the membrane potential of excitatory model neurons type A and B in response to a brief increase in the spike rate of the external inputs for varying levels of connectivity. For vanishing intercluster connectivity, the response was limited to type A, as expected (Fig 2.9B). With increasing intercluster connectivity, the response in type A started to activate the type B and inhibitory neurons, resulting in complex network activity. Importantly, at an intermediate level of connectivity ($P_{in} = 0.1;\ P_{out} = 0.25$), the simulated model responses (Fig 2.9C) resembled qualitatively the time course and similarity of the recorded visual responses of the two types of pyramidal neurons in turtle visual cortex (Fig 2.8B).

2.4 Discussion

The dichotomy between cellular individuality and network integration raises a profound question in neuroscience. To what extent does subtype identity of a pyramidal neuron impact the neuron's dynamic and signal processing when it is incorporated in an extensively interconnected network, such as microcircuits of cerebral cortex? To address this question, we examined the classification of turtle visual cortex pyramidal neurons based on intrinsic electrophysiological properties (Fig 2.6). We then probed the neuron's responses to visual stimulation (Fig 2.8), which concurrently pushed the network into a state of intense emergent activity. We discovered two main electrophysiological types of pyramidal neurons (Fig 2.4) and found that their visual responses were indistinguishable and apparently dominated by emergent network activity (Fig 2.8B, C). Given the limitation in our study of visual stimulation to diffuse flashes, we cannot exclude the possibility that exploration of more complex stimuli would reveal cell-type specific visual responses. A model network, when tuned to a suitable level of connectivity, reproduced the similarity of the responses of the two cell types (Fig 2.9). In future model investigations it will be fruitful to investigate in an extensive parameter search under what conditions of intrinsic physiology and connectivity cell-type specific differences in the responses to external inputs can arise.

2.4.1 Parameter selection

In this investigation of pyramidal neuron types, parameter selection was guided by minimizing redundant information and by evidence from previous studies that parameter values varied significantly among subpopulations of pyramidal neurons. For instance, the following parameters have previously been shown to vary between subgroups of pyramidal neurons in

neocortex: input resistance (Takahashi, 1965; Baranyi et al., 1993; Christophe et al., 2005; Sosulina et al., 2006); resting membrane potential (Sosulina et al., 2006); membrane time constant (Calvin and Sypert, 1976); action potential amplitude (Christophe et al., 2005, McCormick et al., 1985), voltage threshold (Chistophe et al., 2005), duration at half-maximum amplitude (Sosulina et al., 2006, Baranyi et al., 1993), duration at threshold (Calvin and Sypert, 1976, Takahashi, 1965), maximum rate of decay (Baranyi et al., 1993), rheobase current (Baranyi et al., 1993), the time to the peak of the afterhyperpolarization (Calvin and Sypert, 1976, Takahashi, 1965); action potential frequency adaptation ratio (Porter et al., 2001; Christophe et al., 2005); action potential duration increase and action potential amplitude reduction (Cauli et al., 1997, 2000). In addition, resting membrane potential, input resistance, action potential frequency adaptation ratio, and rheobase current have all also been shown to vary with genetically defined subtypes among pyramidal neurons in mouse visual cortex and somatosensory cortex (Groh et al., 2010).

2.4.2 Classification algorithms

After feeding measured parameters into the Ward's linkage method clustering algorithm, the choice of the threshold intergroup linkage distance determines the number of inferred clusters (Fig 2.4). The subjectivity of this choice has been addressed using different strategies. One strategy is to reduce the subjectivity inherent to the choice of threshold by adding cells of different types (e.g. pyramidal neurons in an interneuronal classification study) to the data base (Cauli et al., 1997, 2000; Karagiannis et al., 2009; Helmstaedter et al., 2009) or by overlaying morphology on purely electrophysiological clusters (Nowak et al., 2003; Krimer et al., 2005; Andjelic et al., 2009). Another strategy is to elevate the confidence levels behind clustering by analyzing the clustering results for different threshold levels and comparing relative "accuracy" measurements across those schemes. Strategies to this end include silhouette analysis (Rousseeuw, 1987; Karagiannis et al.,

2009) and the Mann-Whitney Test (Mann and Whitney, 1947; Sosulina et al., 2006). A third family of strategies uses inherent properties of the clustering itself to determine the threshold. With each intercluster merge the number of clusters decreases but the mean intracluster variance increases. The Thorndike procedure (Thorndike, 1953) suggests that the threshold should be drawn at the merge that provides the largest increase in mean intracluster variance and has been used in several neuronal classification studies (Cauli et al., 1997, 2000; Andjelic et al., 2009). The application of fuzzy clustering algorithms to the classification of fusiform neocortical neurons suggested a final test (Battaglia et al., 2013). For each number of subtypes from N = 1 (all cells are indistinct and members of one superpopulation) to N = the number of cells recorded (all cells are unique and no meaningful crossover exists among them) there is some finite range of threshold linkage distances for which N subtypes appear from the data. The correct N, and from that the correct threshold, should be chosen from the largest range of thresholds which gives the same number of subtypes (Fig 2.4). For the study presented here, the number of subtypes was determined by applying the Thorndike and Battaglia criteria and was corroborated through k-means (Hartigan and Wong, 1979) and silhouette (Rousseeuw, 1987) analysis.

2.4.3 Two pyramidal neuron types in allocortex

The allocortex is a phylogenetically ancient trilaminar cortical structure (Swanson, 2003). Well-studied contemporary model systems of allocortex are the mammalian piriform cortex (Neville and Haberly, 2004; Suzuki and Bekkers, 2013) and hippocampus (Johnston and Amaral, 2004) and the reptilian dorsal cortex (Ulinski, 2007). All three model systems are largely congruent in their microcircuit structure (Shepherd, 2011; Fournier et al., 2014). Layer 2 contains densely packed somata of pyramidal neurons. Pyramidal neuron dendrites and axons project into the adjacent layers 1 and 3. Afferents make en-passant synapses in superficial layer 1 on interneurons

and on distal segments of dendrites from layer 2 pyramidal neurons. Scattered interneurons in layer 1 and 3 mediate feed-forward and feed-back inhibition (Fig 2.1B).

The laminar specificity of pyramidal neuron types in the six-layered neocortex raises the question whether the sole layer of pyramidal neuron somata in allocortex consists of discrete types of pyramidal neurons. Based on morphological and intrinsic electrophysiological properties, two types of pyramidal neurons have been identified in mouse piriform cortex (Suzuki and Bekkers, 2006, 2011) and rat hippocampus (Graves et al., 2012).

In this study, we have extended the question to a third model system of allocortex, namely the dorsal cortex of turtle. Earlier investigations of pyramidal neurons in this system revealed a variation of input resistance (Larkum et al., 2008), firing patterns (Mancilla et al., 1998), axonal projection targets (Ulinski, 1986), and molecular markers (Dugas-Ford et al., 2012). However, these valuable studies did not quantify to what extent the variation of those properties reflects the existence of pyramidal neuron subtypes or the broad distribution of properties in one neuron type. Here, based on the parameterization of intrinsic electrophysiological properties and unsupervised clustering, we have identified two types of pyramidal neurons in turtle dorsal cortex. Broadly speaking, type A neurons tend to be more excitable and tend to show less spike adaptation than type B neurons (Fig 2.6, 7).

2.4.4 Type-specific connectivity

The apparent congruence of microcircuit structure and the coincidence of two types of pyramidal neurons in the three model systems of allocortex raises the question to what extent neuronal type correlates with connectivity in the three systems. In mouse hippocampus, the two distinct principal neuron types in layer 2 are inversely modulated by glutamate and acetylcholine

acting on metabotropic receptors, which advances the notion that the two types support two parallel signal pathways (Graves et al., 2012). In mouse piriform cortex, the semilunar principal neurons in layer 2 receive stronger afferent inputs, whereas the superficial pyramidal neurons of the same layer receive stronger associational (intracortical) inputs (Suzuki and Bekkers, 2011). Our visual response data from the two types of pyramidal neurons in turtle dorsal cortex, combined with the model investigation, suggest that strong associational (intracortical) inputs are common to both types.

2.4.5 Comparative analysis of allocortex and neocortex

Given the ancestral position of allocortex in evolutionary history (Striedter, 2005), it is instructive to highlight our results from turtle dorsal cortex within the context of related studies of pyramidal neuron subtypes in neocortex. First, of the 14 parameters considered for the cluster analysis, the two resulting types of pyramidal neurons differed most in their excitability (resting membrane potential, rheobase current) and spike adaptation (spike frequency adaptation ratio, ISI variability). Interestingly, those parameters have previously been shown to vary across genetically defined subtypes of layer 5 pyramidal neurons in mammalian somatosensory and visual cortex (Groh et al., 2010). Second, the separation of early and late sensory responses, visible in some neurons, is not unique to turtle visual cortex, rather they have previously been observed in mouse barrel cortex (Sachidhanandam et al., 2013). Third, the similarity of the fluctuating responses for the two types of pyramidal neurons in turtle visual cortex resembles the previously observed similarity of receptive field properties for morphological and electrophysiological pyramidal neuron subtypes within the same layer of cat visual cortex (Nowak et al., 2003). Fourth, the inference of two pyramidal neuron subtypes in turtle visual cortex is consistent with the molecular evidence for cortical L4/input and L5/output cell-type homologies across amniotes (Dugas-Ford

et al., 2012). It is thus tempting to speculate that the classified type A and B pyramidal neurons of turtle visual cortex express two selective mRNA profiles that match the mammalian cortical L4/input and L5/output neurons, respectively. However, tests of this tantalizing speculation must await future studies.

2.4.6 The dichotomy of cellular individuality and associational circuits

A subtype-specific division of labor is believed to create a rich substrate for computation (Klausberger and Somogyi, 2008; Moore et al. 2010). On the other hand, profuse associational connections are thought to implement complex sensory processing (Johnson et al., 2000). Here we showed that pyramidal neuron membrane potential responses to a diffuse brief flash of light were characterized by persistent activity of high trial-to-trial variability. The response was not type-specific (Fig 2.8). This observation, combined with the model investigation (Fig 2.9), suggests that the answer to the signal-processing role of neurons vs network appears to depend on the question/perspective at hand. This neuron-network duality of circuit dynamics and computation addresses the inability of the classical concepts "neuron" or "network" to describe the dynamics and computation of microcircuit-scale cortical tissue during the visual processing of spatiotemporal complex scenes.

Acknowledgements: The authors thank Mahmood Hosseini for his help in developing the computational model. This research was supported by a Whitehall Foundation grant #20121221 and a NSF CRCNS grant #1308159 to R. Wessel.

Andjelic S, Gallopin T, Cauli B, Hill EL, Roux L, Badr S, Hu E, Tamás G, Lambolez B. Glutamatergic nonpyramidal neurons from neocortical layer VI and their comparison with pyramidal and spiny stellate neurons. J Neurophysiol. 2009;101:641-654.

Arlotta P, Molyneaux BJ, Chen J, Inoue J, Kominami R, Macklis JD. Neuronal subtype-specific genes that control corticospinal motor neuron development in vivo. Neuron. 2005;45:207-221.

Armstrong-James M, Fox K, Das-Gupta A. Flow of excitation within rat barrel cortex on striking a single vibrissa. J Neurophysiol. 1992;68:1345–1358.

Baranyi A, Szente MB, Woody CD. Electrophysiological characterization of different types of neurons recorded in vivo in the motor cortex of the cat. II. Membrane parameters, action potentials, current-induced voltage responses and electronic structures. J Neurophysiol. 1993;69:1865-1879.

Battaglia D, Karagiannis A, Gallopin T, Gutch HW, Cauli B. Beyond the frontiers of neuronal types. Frontiers in Neural Circuits. 2013;7:13.

Bekkers JM, Suzuki N. Neurons and circuits for odor processing in the piriform cortex. TINS. 2013;36:429-438.

Brecht M, Sakmann B. Dynamic representation of whisker deflection by synaptic potentials in spiny stellate and pyramidal cells in the barrels and septa of layer 4 rat somatosensory cortex. J Physiol. 2002;543:49-70.

Brumback A, Sohal V. Intrinsic excitability defects in specific subtypes of medial prefrontal cortex pyramidal neurons in a mouse model of autism. Neurology. 2014;82(10 Suppl 7):S329.

Brunel N, Wang X. What determines the frequency of fast network oscillations with irregular neural discharges? I. Synaptic dynamics and excitation-inhibition balance. J Neurophysiol. 2003;90:415-430.

Calvin W, Sypert G (1976) Fast and slow pyramidal tract neurons: an intracellular analysis of their contrasting repetitive firing properties in the cat. J Neurophysiol. 39:420-434.

Cauli B, Audinat E, Lambolez B, Angulo MC, Ropert N, Tsuzuki K, Hestrin S, Rossier J. Molecular and Physiological Diversity of Cortical Nonpyramidal Cells. J Neurosci. 1997;17:3894–3906.

Cauli B, Porter JT, Tsuzuki K, Lambolez B, Rossier J, Quenet B, Audinat E. Classification of fusiform neocortical interneurons based on unsupervised clustering. Proc Natl Acad Sci USA. 2000;97:6144-6149.

Christophe E, Doerflinger N, Lavery DJ, Molnár Z, Charpak S, Audinat E. Two populations of layer V pyramidal cells of the mouse neocortex: development and sensitivity to anesthetics. J Neurophysiol. 2005;94:3357-3367.

Colombe JB, Sylvester J, Block J, Ulinski PS. Subpial and stellate cells: two populations of interneurons in turtle visual cortex. J Comp Neurol. 2004;471:333–351.

Connors BW, Kriegstein AR. Cellular physiology of the turtle visual cortex: distinctive properties of pyramidal and stellate neurons. J Neurosci. 1986;6:164-177.

de Kock CPJ, Bruno RM, Spors H, Sakmann B. Layer- and cell-type-specific suprathreshold stimulus representation in rat primary somatosensory cortex. J Physiol. 2007;581:139–154.

Desan PH. The Organization of the Cerebral Cortex of the Pond Turtle, Pseudemys scripta elegans [dissertation]. Cambridge (MA): Harvard University; 1984.

Dugas-Ford J, Rowell JJ, Ragsdale CW. Cell-type homologies and the origins of the neocortex. Proc Natl Acad Sci USA. 2012;109:16974-16979.

Fournier J, Müller CM, Laurent G. Looking for the roots of cortical sensory computation in three-layered cortices. Curr Opin Neurobiol. 2014;31:119-126.

Gallopin T, Geoffroy H, Rossier J, Lambolez B. Cortical sources of CRF, NKB, and CCK and their effects on pyramidal cells in the neocortex. Cereb Cortex. 2005;16:1440-1452.

Gilbert C, Wiesel T. Morphology and intracortical projections of functionally characterised neurones in the cat visual cortex. Nature. 1979;280:120-125.

Graves AR, Moore SJ, Bloss EB, Mensh BD, Kath WL, Spruston N. Hippocampal pyramidal neurons comprise two distinct cell types that are countermodulated by metabotropic receptors. Neuron. 2012;76:776–789.

Groh A, Meyer HS, Schmidt EF, Heintz N, Sakmann B, Krieger P. Cell-type-specific properties of pyramidal neurons in neocortex underlying a layout that is modifiable depending on the cortical area. Cereb Cortex. 2010;20:826–836.

Hartigan JA, Wong MA. A k-means clustering algorithm. Journal of the Royal Statistical Society. Series C (Applied Statistics). 1979;28:100–108.

Heller SB, Ulinski PS. Morphology of geniculocortical axons in turtles of the genera Pseudemys and Chrysemys. Anat Embryol. 1987;175:505-515.

Helmstaedter M, Sakmann B, Feldmeyer D. The relation between dendritic geometry, electrical excitability, and axonal projections of L2/3 interneurons in rat barrel cortex. Cereb Cortex. 2009;19:938-950.

Izhikevich EM. Simple model of spiking neurons. IEEE Transactions on Neural Networks. 2003;14:1569-1572.

Johnston D, Amaral DG. Hippocampus. In: Shepherd G, editor. The synaptic organization of the brain. New York: Oxford University Press; 2004. p. 455-498.

Johnson DMG, Illig KR, Behan M, Haberly, LB. New features of connectivity in piriform cortex visualized by intracellular injection of pyramidal cells suggest that 'primary' olfactory cortex functions like 'association' cortex in other sensory systems. J Neurosci. 2000;20:6974-6982.

Karagiannis A, Gallopin T, Dávid C, Battaglia D, Geoffroy H, Rossier J, Hillman EMC, Staiger JF, Cauli B. Classification of NPY-expressing neocortical interneurons. J Neurosci. 2009;29:3642–3659.

Klausberger T, Somogyi P. Neuronal diversity and temporal dynamics: the unity of hippocampal circuit operations. Science. 2008;321:53-57.

Kriegstein AR. Synaptic responses of cortical pyramidal neurons to light stimulation in the isolated turtle visual system. J Neurosci. 1987;7:2488-2492.

Krimer LS, Zaitsev AV, Czanner G, Kröner S, González-Burgos G, Povysheva NV, Iyengar S, Barrionuevo G, Lewis DA. Cluster analysis-based physiological classification and morphological properties of inhibitory neurons in layers 2-3 of monkey dorsolateral prefrontal cortex. J Neurophysiol. 2005;94:3009–3022.

Larkum ME, Watanabe S, Lasser-Ross N, Rhodes P, Ross WN. Dendritic properties of turtle pyramidal neurons. J Neurophysiol. 2008;99:683–694.

Lee AT, Gee SM, Vogt D, Patel T, Rubenstein JL, Sohal VS. Pyramidal neurons in prefrontal cortex receive subtype-specific forms of excitation and inhibition. Neuron. 2014;81:61-68.

Mancilla JG, Fowler M, Ulinski PS. Responses of regular spiking and fast spiking cells in turtle visual cortex to light flashes. Vis Neurosci. 1998;15:979-993.

Mann HB, Whitney DR. On a test of whether one of two random variables is stochastically larger than the other. The Annals of Mathematical Statistics. 1947;18:50-60.

Martinez LM, Wang Q, Reid RC, Pillai C, Alonso JM, Sommer FT, Hirsch JA. Receptive field structure varies with layer in the primary visual cortex. Nat Neurosci. 2005;8:372–379.

McCormick DA, Connors BW, Lighthall JW, Prince DA. Comparative electrophysiology of pyramidal and sparsely spiny stellate neurons of the neocortex. J Neurophysiol. 1985;54:782–806.

Molyneaux BJ, Arlotta P, Menezes JR, Macklis JD. Neuronal subtype specification in the cerebral cortex. Nat Rev Neurosci. 2007;8:427-437.

Molyneaux BJ, Arlotta P, Fame RM, MacDonald JL, MacQuarrie KL, Macklis JD. Novel subtype-specific genes identify distinct subpopulations of callosal projection neurons. J Neurosci. 2009;29:12343-12354.

Molyneaux BJ, Goff LA, Brettler AC, Chen HH, Brown JR, Hrvatin SS, Rinn JL, Arlotta P. DeCoN: Genome-wide analysis of in vivo transcriptional dynamics during pyramidal neuron fate selection in neocortex. Neuron. 2015;85:1-14.

Moore CI, Carlen M, Knoblich U, Cardin JA. Neocortical interneurons: From diversity, strength. Cell. 2010;142:184-188.

Mulligan KA, Ulinski PS. Organization of geniculocortical projections in turtles: Isoazimuth lamellae in the visual cortex. J Comp Neurol. 1990;296: 531-547.

Neville KR, Haberly LB. Olfactory cortex. In: Shepherd GM, editor. The synaptic organization of the brain. New York: Oxford UK; 2004. p. 415-454.

Nowak LG, Azouz R, Sanchez-Vives MV, Gray CM, McCormick DA. Electrophysiological classes of cat primary visual cortical neurons in vivo as revealed by quantitative analyses. J Neurophysiol. 2003;89:1541-1566.

Porter JT, Johnson CK, Agmon A. Diverse types of interneurons generate thalamus-evoked feedforward inhibition in the mouse barrel cortex. J Neurosci. 2001;21:2699–2710.

Reiner A. A hypothesis as to the organization of cerebral cortex in the common amniote ancestor of modern reptiles and mammals. In: Bock GA, Cardew G, editors. Evolutionary developmental biology of the cerebral cortex. London: Novartis; 2000. p. 83-108.

Rousseeuw PJ. Silhouettes: A graphical aid to the interpretation and validation of cluster analysis. Journal of Computational and Applied Mathematics. 1987;20:53–65.

Sachidhanandam S, Sreenivasan V, Kyriakatos A, Kremer Y, Petersen CCH. Membrane potential correlates of sensory perception in mouse barrel cortex. Nat Neurosci. 2013;16:1671-1677.

Saha D, Morton D, Ariel M, Wessel R. Response properties of visual neurons in the turtle nucleus isthmi. J Comp Physiol A. 2011;197:153-165.

Schubert D, Staiger JF, Cho N, Kötter R, Zilles K, Luhmann HJ. Layer-Specific intracolumnar and transcolumnar functional connectivity of layer V pyramidal cells in rat barrel cortex. J Neurosci. 2011;21:3580-3592.

Sekerli M, Del Negro CA, Lee RH, Butera RJ. Estimating action potential thresholds from neuronal time-series: new metrics and evaluation of methodologies. IEEE Trans Biomed Eng. 2004;51:1665-1672.

Senseman DM. Correspondence between visually evoked voltage-sensitive dye signals and synaptic activity recorded in cortical pyramidal cells with intracellular microelectrodes. Visual Neurosci. 1996;13:963-977.

Shen JM, Kriegstein AR. Turtle hippocampal cortex contains distinct cell types, burst-firing neurons, and an epileptogenic subfield. J Neurophysiol. 1986;56:1626-1649.

Shepherd GM. The microcircuit concept applied to cortical evolution: from three-layer to six-layer cortex. Frontiers in Neuroanatomy. 2011;5:30.

Shew WL, Clawson WP, Pobst J, Karimipanah Y, Wright NC, Wessel R. Adaptation to sensory input tunes visual cortex to criticality. Nature Physics. 2015; doi:10.1038/nphys3370.

Smith LM, Ebner FF, Colonnier M. The thalamocortical projection in *pseudemys* turtles: a quantitative electron microscopic study. J Comp Neurol. 1980;190:445-461.

Soltesz I. Diversity in the neuronal machine. New York: Oxford University Press; 2006.

Sosulina L, Meis S, Seifert G, Steinhäuser C, Pape H. Classification of projection neurons and interneurons in the rat lateral amygdala based upon cluster analysis. Mol Cell Neurosci. 2006;33:57-67.

Staiger JF, Flagmeyer I, Schubert D, Zilles K, Kötter R, Luhmann HJ. Functional diversity of layer IV spiny neurons in rat somatosensory cortex: quantitative morphology of electrophysiologically characterized and biocytin labeled cells. Cereb Cortex. 2004;14:690-701.

Striedter GF. Principles of brain evolution. Sunderland (MA): Sinauer Associates; 2005.

Suzuki N, Bekkers JM. Neural coding by two classes of principal cells in the mouse piriform cortex. J Neurosci. 2006;26:11938-11947.

Suzuki N, Bekkers JM. Two layers of synaptic processing by principal neurons in piriform cortex. J Neurosci. 2011;31:2156-2166.

Swanson LW. Brain architecture: Understanding the basic plan. New York: Oxford University Press; 2003.

Takahashi K. Slow and fast groups of pyramidal tract cells and their respective membrane properties. J Neurophysiol. 1965;28:908-924.

Thorndike R. Who belongs in the family? Psychometrika. 1953;18:267-276.

Ulinski PS. Organization of corticogeniculate projections in the turtle, Pseudemys scripta. J Comp Neurol. 1986;254:529-542.

Ulinski PS (2007) Visual cortex of turtles. In: Kaas JA, editor. Evolution of nervous systems; a comprehensive reference. London: Elsevier; 2007. p. 195-203.

Wang Y, Markram H, Goodman PH, Berger TK, Ma J, Goldman-Rakic PS. Heterogeneity in the pyramidal network of the medial prefrontal cortex. Nat Neurosci. 2006;9:534-542.

Ward JH. Hierarchical grouping to optimize an objective function. Journal of the American Statistical Association. 1963;58:236-244.

Chapter 3

Network activity influences the subthreshold and spiking visual responses of pyramidal neurons in a three-layer cortex

A primary goal of systems neuroscience is to understand cortical function, which typically involves studying spontaneous and sensory-evoked cortical activity. Most such studies focus on spiking in populations of neurons. While advantageous in many respects, this approach is limited in scope; it records the activities of a minority of neurons, and gives no direct indication of the underlying subthreshold dynamics. Membrane potential recordings can fill these gaps in our understanding, but are difficult to obtain *in vivo*. Here, we record subthreshold cortical visual responses in the *ex vivo* turtle eye-attached whole-brain preparation, which is ideally-suited to such a study. In the absence of visual stimulation, the network is "synchronous"; neurons display network-mediated transitions between low- and high-conductance membrane potential states. The prevalence of these slow-wave transitions varies across turtles and recording sessions. Visual stimulation evokes similar high-conductance states, which are on average larger and less reliable when the ongoing state is more synchronous. Responses are muted when immediately preceded by large, spontaneous high-conductance events. Evoked spiking is sparse, highly variable across trials, and mediated by concerted synaptic inputs that are in general only very weakly correlated with inputs to nearby neurons. Together, these results highlight the multiplexed influence of the cortical network on the spontaneous and sensory-evoked activity of individual cortical neurons.

3.1 Introduction

Spikes are fundamental to cortical function; they are the means by which individual neurons receive and transmit information, and are the unit of language for cortical ensembles that encode sensory information. Understandably, then, most studies of cortical sensory responses have focused on the spiking activities of (increasingly large) populations of neurons. Yet this approach yields an incomplete picture of sensory cortex, for three reasons. First, it reveals the activity of a minority of neurons; most cells spike very rarely, if at all(Shoham, O'Connor, & Segev, 2006), and of those that do, few have spike rates sufficient for certain analyses(Cohen & Kohn, 2011) (**Figure 3.1a**). Second, neuronal populations defined by the recording device's field of view are unlikely to represent complete cortical microcircuits (**Figure 3.1b**). (While the local field potential (LFP) is both easily obtained and less susceptible to the first issue, this signal too is ultimately defined by the device (**Figure 3.1b**).) Third, the purely suprathreshold view of cortex leaves certain important questions unanswered. For example, some competing hypotheses of cortical function are not easily distinguishable by the spiking statistics of small populations, but predict very different subthreshold dynamics for individual neurons(DeWeese & Zador, 2006; M. Rudolph & Destexhe, 2003; Stevens & Zador, 1998; Tan, Chen, Scholl, Seidemann, & Priebe, 2014). This third point motivates recording the membrane potential, which in fact neatly addresses the first two issues as well. First, each neuron samples an enormous and biologically-relevant presynaptic pool (**Figure 3.1b**), and thus the subthreshold membrane potential communicates

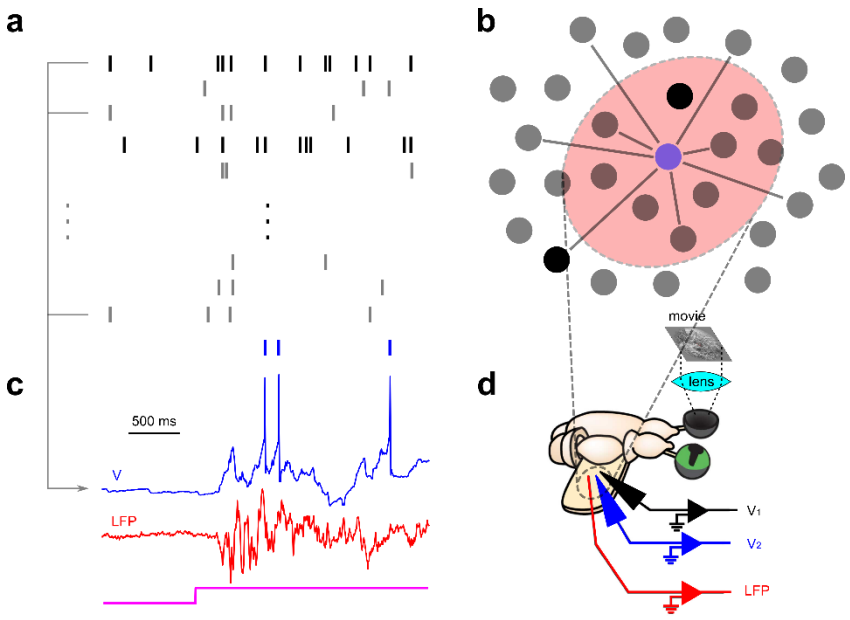

Figure 3.1 Whole-cell recordings supplement our understanding of cortical activity. (a) Ongoing and sensory evoked cortical spiking is sparse; a minority of neurons (high opacity rasters) spike often enough to give sufficient spike counts for some analyses. (b) Devices used to record population spiking activity define sets of neurons which are primarily sparse-spiking (low-opacity dots). These populations do not in general represent cortical microcircuits. The local field potential (LFP, red region) is useful for estimating synaptic activity, but only in a small electrode-defined region. A given neuron (e.g., blue dot) is a useful network sub-sampler; it receives inputs from a biologically relevant presynaptic pool spanning large regions of cortex. (c) The membrane potential of a cortical neuron (blue trace) provides (i) a spike-rate independent measure of neuronal activity, and (ii) estimates the spiking activity of the presynaptic pool. The simultaneously-recorded nearby LFP (red trace) is useful for interpreting this subthreshold activity in the context of local synaptic activity. (d) We simultaneously record the membrane potentials from groups of cortical neurons (as well as the nearby LFP) in the turtle eye-attached whole-brain *ex vivo* preparation, during ongoing and visually-evoked activity.

information about spiking in that pool (**Figure 3.1c**). Second, the membrane potential is a spike-rate independent measure of activity in the recorded neuron, and therefore gives voice to sparse-spiking neurons (**Figure 3.1c**). For these reasons, it is vital to supplement the vast literature on cortical spiking with studies of subthreshold sensory responses.

This is easier said than done; while stable patch clamp recordings are readily achievable in slice and cell culture, they are extremely difficult to obtain *in vivo*. Consequently, studies of subthreshold visual responses are relatively rare. Accordingly, we have recorded ongoing and visually-evoked subthreshold and spiking activity from cortical pyramidal neurons in the *ex vivo* turtle eye-attached wholebrain preparation (**Figure 3.1d**), which is ideally-suited to such an investigation(Crockett, Wright, Thornquist, Ariel, & Wessel, 2015; Saha, Morton, Ariel, & Wessel, 2011). Specifically, it allows for stable patch clamp recordings (lasting up to two hours) from neurons in a three-layer visual cortex (analogous to mammalian piriform cortex and hippocampus(Fournier, Müller, & Laurent, 2015; Naumann et al., 2015; Shepherd, 2011)) subject to inputs from an intact visual pathway. In some cases, we simultaneously record the nearby LFP to interpret the subthreshold events in the context of local synaptic activity (**Figure 3.1d**).

Here, we present four key observations. First, we find that the ongoing network state is "synchronous"; subthreshold activity reveals a relatively quiescent "low-conductance" state that is frequently interrupted by "high-conductance" events. The increase in synaptic conductance results in slow-wave activity (or broad membrane potential depolarizations) with fast nested subthreshold fluctuations. High-conductance event onsets are correlated across pairs of nearby neurons, and coincide with oscillations in the nearby local field potential (suggesting they are network-generated). Second, brief and extended visual stimulation evoke persistent high-conductance states that are qualitatively similar to larger spontaneous synaptic events, and less

synchronous than pre-stimulus activity. Spiking in this state is sparse and highly-variable across trials (in terms of both precise timing and spike counts). Third, visual stimulation that interrupts or follows soon after large, spontaneous events evokes responses that are muted relative to the average. Finally, while the evoked state is asynchronous at long time scales, spikes are preceded by concerted excitatory synaptic inputs that are not in general coordinated across neighboring neurons. These brief, pre-spike depolarizations are more pronounced for neurons exhibiting stronger slow-wave fluctuations during ongoing activity.

Taken together, these results provide a rare view into the subthreshold dynamics of cortical visual responses. They highlight the effects of network-mediated synaptic activity on the spiking of individual neurons, and demonstrate the utility of the membrane potential as a tool for sampling the state of a presynaptic population. Ultimately, this diagnostic tool suggests strong network influences on single-neuron activity across multiple spatiotemporal scales.

3.2 Results

In order to investigate the nature of spontaneous and evoked subthreshold cortical activity, we obtained whole-cell recordings from neurons in the *ex vivo* turtle eye-attached whole-brain preparation (**Figure 3.1**), both in the absence of visual stimulation (**Figure 3.2a**), and in response to brief and extended visual stimulation (**Figure 3.3a**, see Methods).

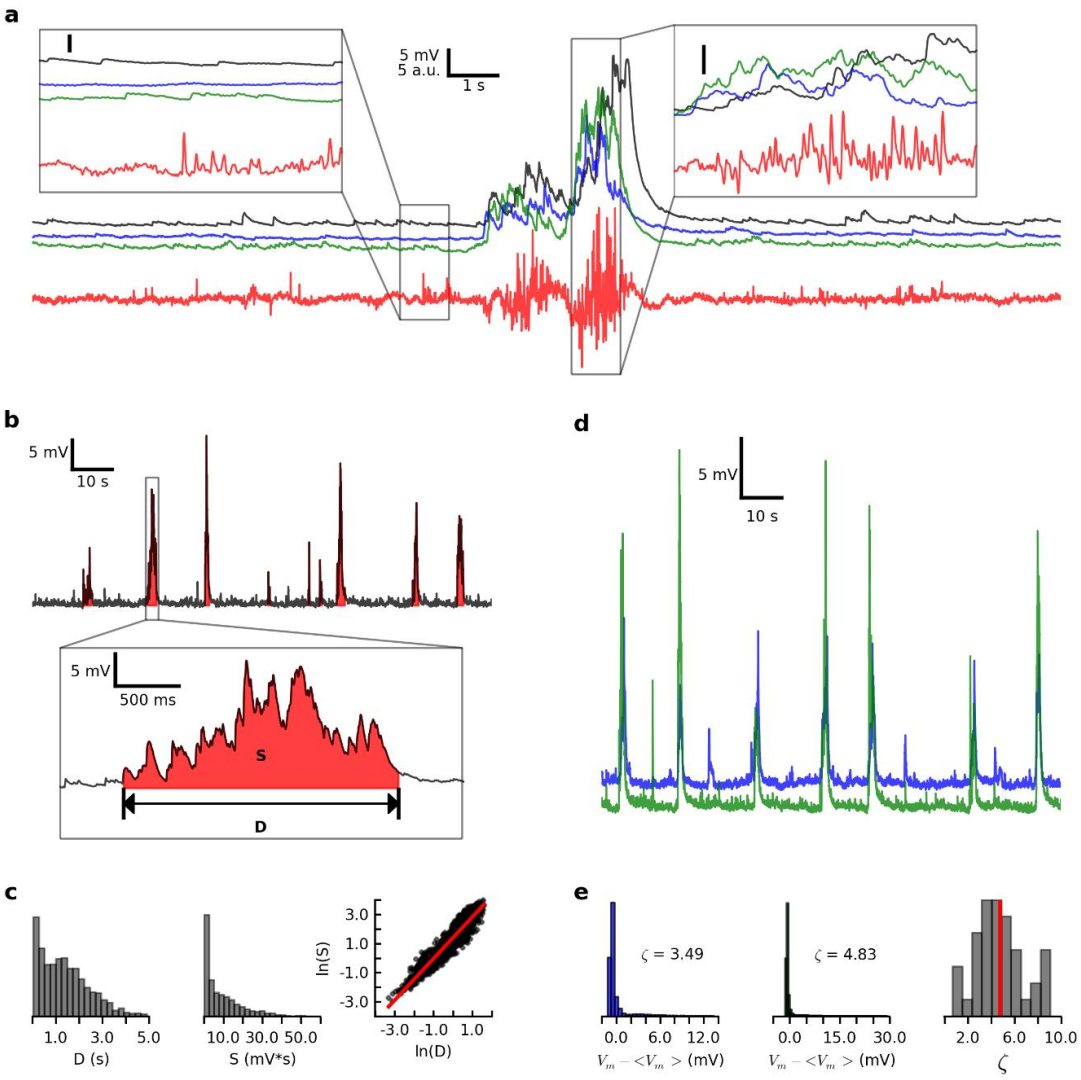

Figure 3.2 During spontaneous activity, the low-conductance membrane potential state is interrupted by broadly-correlated high-conductance events. (a) Subthreshold membrane potentials from three simultaneously-recorded neurons (black, blue, and green traces) and the nearby LFP (red trace) in the absence of visual stimulation. Left (right) inset: 1 s of "low-conductance" ("high-conductance") activity. (b) Top: spontaneous membrane potential recording, with high conductance events filled in red. Bottom: enlarged view of an individual spontaneous high-conductance event. D is event duration, and S (area under curve) is event size. (c) Distributions of high-conductance event durations (left) and sizes (middle), for 1389 events from 40 cells in 16 turtles. Right: natural log of size vs. natural log of duration, for all events. Red line indicates significant linear regression fit ($r = 0.95$, slope = 1.43, $P < 1 \times 10^{-300}$). (d) Spontaneous subthreshold membrane potentials from two simultaneously-recorded neurons. (e) Left and center: distributions of mean-subtracted membrane potentials for the two neurons in (e), with distribution

skew (ζ). Right: distribution of skews for spontaneous activity for 40 neurons from 16 turtles. Red line indicates across-cell mean skew.

3.2.1 Spontaneous activity is characterized by transitions between low- and high-conductance states

To help identify the effects of visual stimulation on subthreshold activity, we first sought to characterize spontaneous activity. To this end, we recorded from 40 neurons while maintaining the preparation in complete darkness. For 25 of these cells, we simultaneously recorded the nearby

LFP. In the absence of visual stimulation, membrane potentials were typically far from action potential threshold, displaying small, but frequent postsynaptic potentials (PSPs, **Figure 3.2a, left inset**). Occasionally, coordinated barrages of PSPs interrupted these periods of relative quiescence (**Figure 3.2a**). For most cells, the longer-duration barrages resulted in broad membrane potential depolarizations, with nested higher-frequency fluctuations (**Figure 3.2a, right inset**). The onset of large "high-conductance events" was correlated across pairs of nearby neurons, and coincided with the onset of oscillations in the nearby LFP (**Figure 3.2a**).

We used an algorithm to detect these spontaneous events (see Methods) and quantified the duration (D) and size (S) of each (considering only those between 100 ms and 5 s in duration, **Figure 3.2b**). Both S and D varied considerably across events (**Figure 3.2c**), and had a strong log-log relationship ($r = 0.94$, slope = 1.43, $P < 1 \times 10^{-300}$, linear regression fit, for 1362 high-conductance events from 40 cells in 16 turtles, **Figure 3.2c, right**).

We next sought to understand these subthreshold dynamics in the context of network activity. To do this, we made use of the fact that membrane potential distributions carry statistical signatures of the presynaptic network state. In the so-called "asynchronous" state, for example, random synaptic inputs result in subthreshold membrane potentials that evolve according to a "random walk", and membrane potential distributions are thus approximately Gaussian (with small or negative skew(DeWeese & Zador, 2006; Tan et al., 2014)). In contrast to this scenario, we found that the largest of the spontaneous high-conductance events observed here had greater amplitudes and durations than those predicted for an asynchronous network with the same mean activity level, as captured by the long, depolarized tails of membrane potential distributions (**Figure 3.2e, left and center**). These tails yielded positive distribution skews (ζ) for all cells (population-average skew $< \zeta > = 4.74 +/- 2.08$, mean +/- s.e.m., **Figure 3.2e, right**). As such, ongoing activity in this preparation was consistent with the well-characterized "synchronous network state" observed across a variety of mammalian cortical areas(Bennett, Arroyo, & Hestrin, 2013; Crochet & Petersen, 2006; DeWeese & Zador, 2006; Gentet, Avermann, Matyas, Staiger, & Petersen, 2010; Petersen, Hahn, Mehta, Grinvald, & Sakmann, 2003; J. F. a Poulet & Petersen, 2008; Tan et al., 2014). In this state, the subthreshold activities of individual neurons, which provide a measure of presynaptic network activity, indicate brief periods of elevated activity that are broadly coordinated across time and cortical space.

3.2.2 Visual stimulation evokes high-conductance states with large across-trial variability and sparse spiking

Next, we characterized cortical responses to visual stimulation. For 23 cells from nine turtles, we recorded ongoing activity and responses to either whole-field or sub-field flashes (and obtained at least 12 valid trials, see Methods). In response to flashes, neurons received persistent

barrages of synaptic inputs that were coincident with nearby LFP oscillations (**Figure 3.3a**). This activity was qualitatively similar to longer-duration spontaneous high-conductance events (compare to **Figure 3.2a**). For individual neurons, the response time course was highly variable across trials (**Figure 3.3a**). Across all neurons and trials, this was also true for response latency (**Figure 3.3b**), size (**Figure 3.3c**), and duration (**Figure 3.3d**). For this type of stimulus, evoked activity in retinal ganglion cells was unlikely to continue beyond a few hundred milliseconds after stimulus onset(Marchiafava, 1983). Thus, the late response phase was likely due to persistent intracortical and/or thalamocortical activity.

We next investigated the effects of persistent sensory input by recording from 48 cells from 15 turtles while presenting extended visual stimulation (with at least 12 valid trials, see Methods). These stimuli evoked subthreshold responses that were qualitatively similar to flash responses in the early response phase, but displayed clear temporal structure hundreds of milliseconds later (**Figure 3.3e**). Thus, although intracortical inputs were likely extremely strong in the late response phase (as suggested by the persistent responses to brief flashes), the modulatory effects of sensory input were also evident.

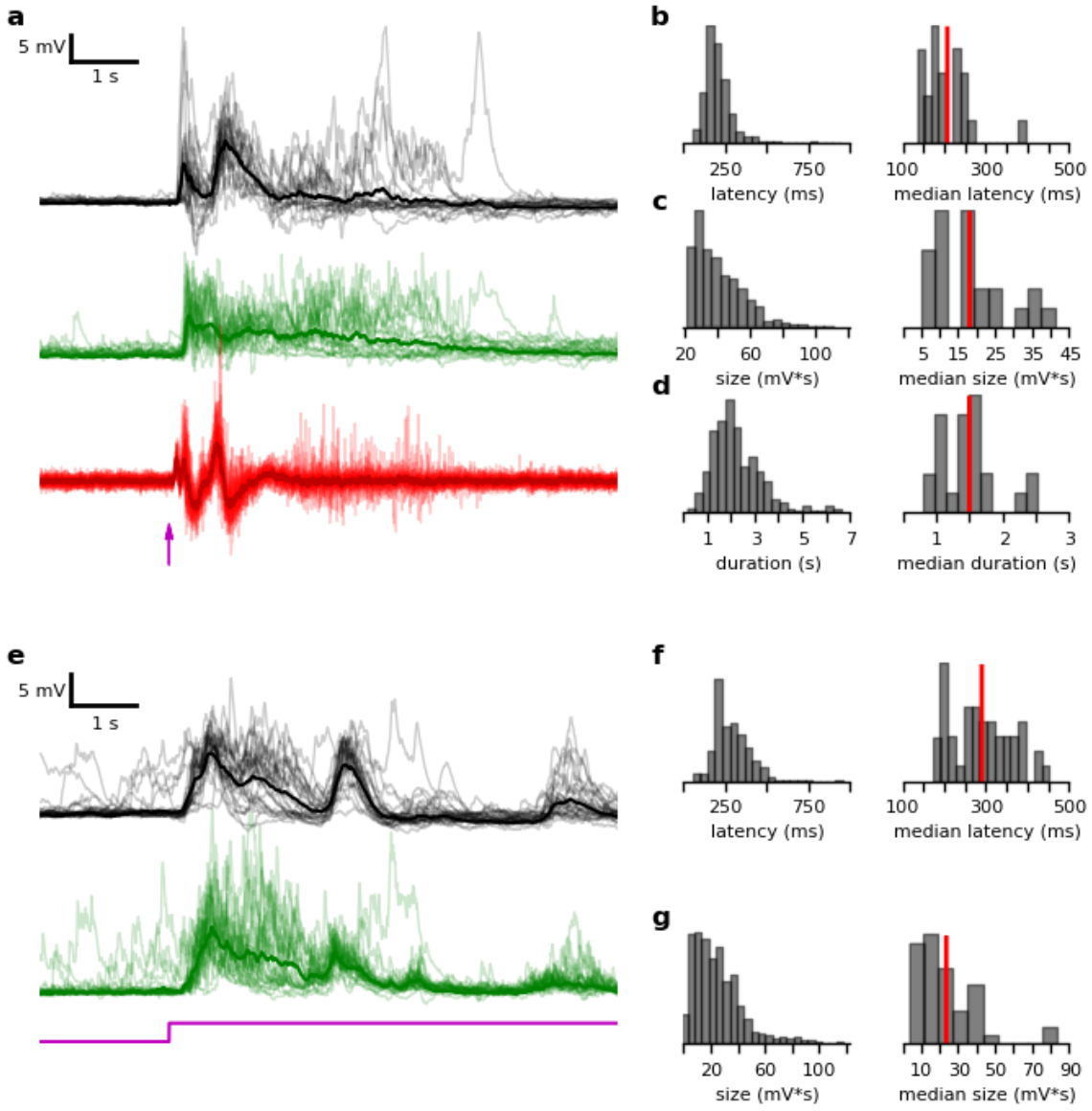

Figure 3.3 Subthreshold visually-evoked activity is highly variable across cells and trials. (a) Membrane potentials from two simultaneously-recorded neurons (black and green traces) and the nearby LFP (red traces), with individual trials in low opacity, and across-trial averages in high opacity. Stimulus is whole-field red flash (flash onset at arrow, see Methods). (b) Left: distribution of subthreshold response latencies (see Methods) for 559 trials from 23 cells in 9 turtles. Stimulus is either red whole-field or sub-field flash (see Methods) Right: distribution of across-trial median response latencies for these cells. Red line indicates across-cell average. (c) Same as in (a), but for response size (see Methods). (d) Same as in (a), but for response duration (see Methods). (e) Same as in (a), but stimulus is naturalistic movie (see Methods), for a different pair of simultaneously-recorded neurons. (f, g) Same as in (b, c), but for extended visual stimuli (1087 trials from 48 cells in 15 turtles, see Methods).

Finally, we characterized evoked spiking activity. Spikes were sparse in general, and highly variable across trials in terms of precise spike timing and total spike counts (**Figure 3.4a**). The population-average rate was 0.37 +/- 0.74 Hz (mean +/- s.e.m.) in the two seconds after stimulus onset (for all stimuli, N = 79 cells, **Figure 3.4a, inset**). Of the 79 recorded cells (with at least 12 valid trials, see Methods), 24 (or 30%) did not spike at all in this window. Of those that did, the average rate was 0.53 +/- 0.83 Hz.

We inspected the time course of evoked spiking by constructing peri-stimulus time histograms (PSTHs) for all cells with at least one evoked spike in the 7 s after stimulus onset, across all trials. In response to brief flashes, most spikes occurred in the 2 s after stimulus onset (**Figure 3.4b**). Between 4 s and 7 s after stimulus onset, spike rates fell below pre-stimulus levels. That is, the strong bouts of evoked activity in the 4 s after the onset of brief flashes appeared to suppress spontaneous spiking. The early (0 to 2 s) spiking responses to movies were similar to those for flashes, but rates were elevated above those for brief flashes in the later response (**Figure 3.4c**).

3.2.3 Evoked high-conductance states are broadly asynchronous

We next sought to more carefully characterize the effects of visual stimulation on the network state, as communicated by single-neuron subthreshold membrane potentials. As shown above, at broad time scales (on the order of seconds), the network was in a synchronous state during spontaneous activity; rather than hovering near action potential threshold, neurons were driven near threshold by barrages of synaptic inputs (**Figure 3.2a**). On shorter times scales (hundreds of milliseconds), evoked activity appeared closer to the description of asynchrony

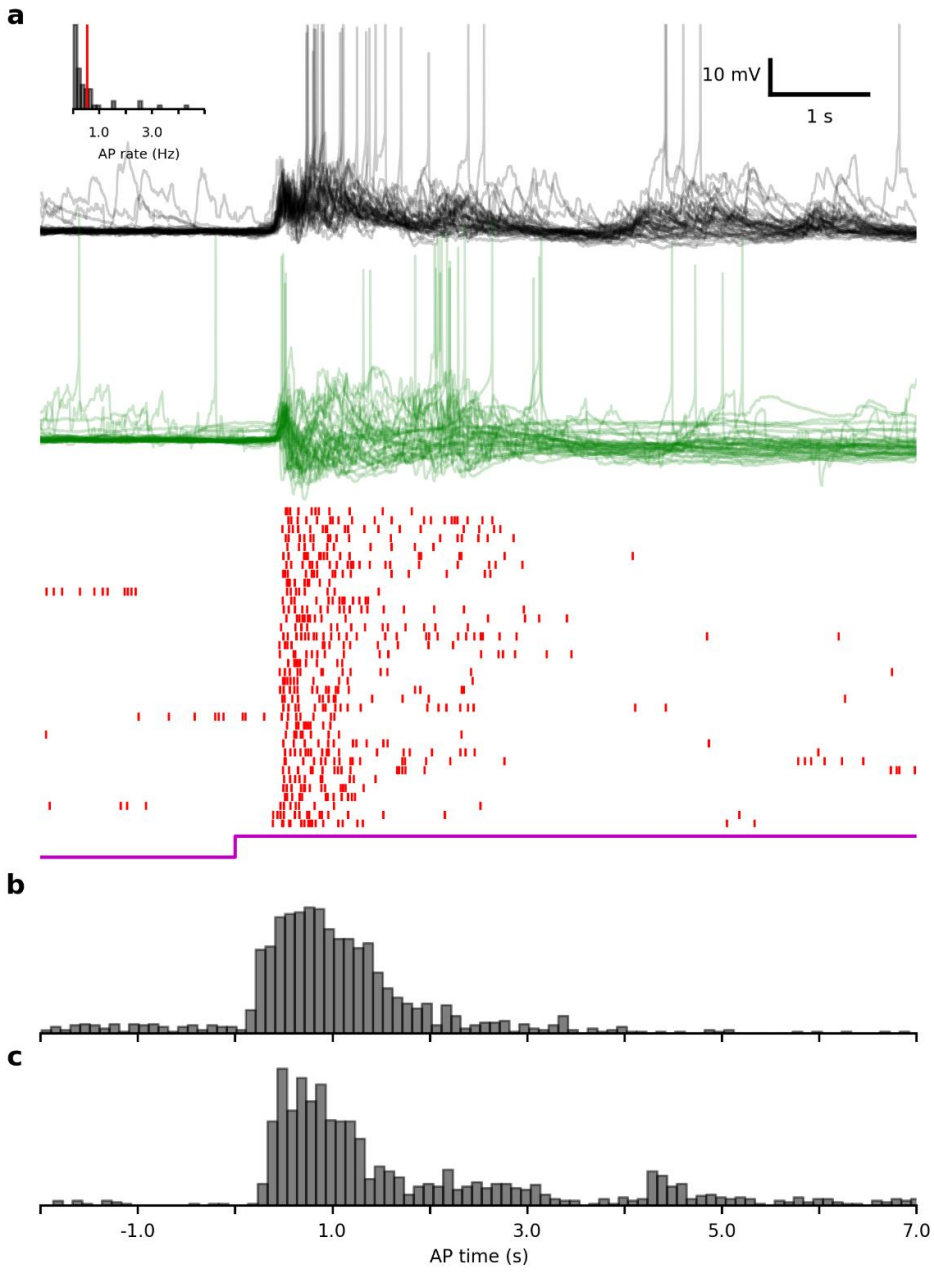

Figure 3.4 Visually-evoked spiking is sparse, and highly variable across cells and trials. (a) Membrane potentials of two simultaneously-recorded neurons (black and green traces) and nearby multi-unit activity (red rasters) during ongoing and visually-evoked activity, across multiple stimulus presentations. Rasters are stacked in ascending trial order. Inset: distribution of across-trial average evoked spike rates for 27 cells in 8 turtles, for all stimuli (see methods). (b) Peristimulus time histogram of intracellularly-recorded spikes for responses to flashes (1196 spikes from 27 cells in 8 turtles, see Methods). (c) Same as in (b), but for responses to extended stimuli (1185 spikes from 33 cells in 14 turtles, see Methods).

(**Figure 3.3a, e**). Was this, in fact, the case? That is, did visual stimulation cause a shift from synchrony to asynchrony in the network?

We addressed this question by calculating skews for residual membrane potentials (membrane potential time series with across-trial average time series subtracted) during ongoing and visually-evoked activity, for responses to all stimuli (see Methods). For each cell, we considered an "ongoing" window of pre-stimulus activity (2 s to 0 s before stimulus onset), and an "evoked" window of activity (starting at response onset, and lasting 2 s, **Figure 3.5a**, see Methods). Consistent with our observations of long spontaneous recordings (**Figure 3.2e**), ongoing skew values (**Figure 3.5b, top**) were typically large and positive (population-average ongoing skew $\langle\zeta\rangle$ = 1.82 +/- 1.43, **Figure 3.5c**). For most cells, skew decreased from the ongoing to evoked window (**Figure 3.5b, bottom**), an effect that was significant for the population as a whole (evoked $\langle\zeta\rangle$ = 1.14 +/- 0.67, $P = 3.2 \times 10^{-4}$ for ongoing-evoked comparison, Wilcoxon signed-rank test, **Figure 3.5c**). Thus, evoked activity was less synchronous than ongoing, on time scales of hundreds of milliseconds to seconds.

3.2.4 In the broadly-asynchronous evoked state, action potentials are preceded by concerted synaptic inputs

Having established the relatively asynchronous nature of the evoked state (at long time scales), we next asked whether the same was true at short time scales. Specifically, we asked whether synaptic inputs preceding visually-evoked spikes were consistent with an asynchronous network, in which neurons hovering just below threshold "randomly walk" the remaining distance to threshold. For each cell, we considered all spikes in a 4 s window of activity beginning 75 ms after stimulus onset (see Methods). We isolated a 50 ms ("pre-spike") window of activity (ending

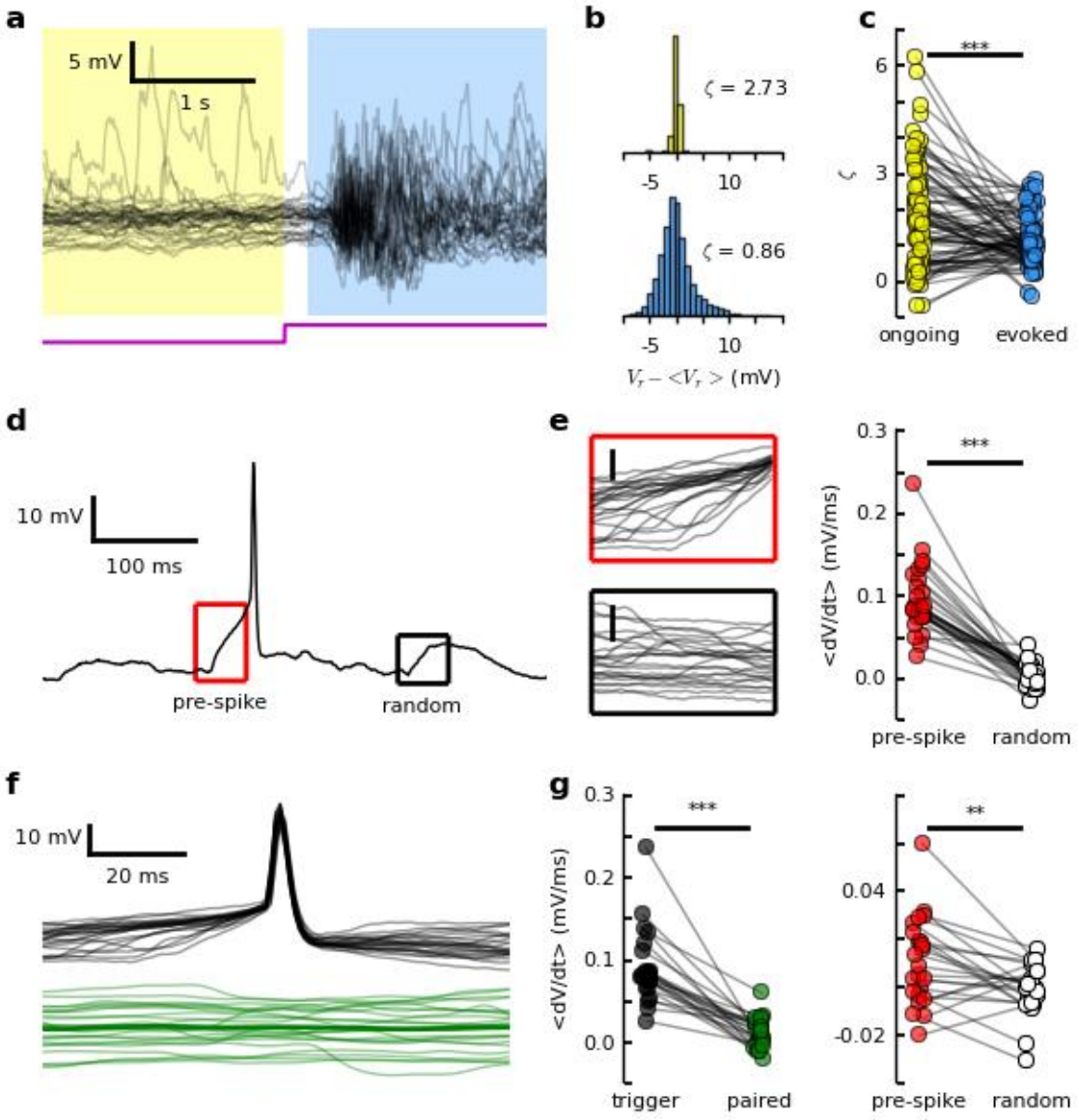

Figure 3.5 Visual stimulation affects coordination at multiple spatiotemporal scales. (a) Residual membrane potentials (see Methods) for ongoing (yellow) and evoked (blue) activity, for repeated presentations of motion-enhanced movie (see Methods). (b) Distributions of residual membrane potentials and distribution skews (ζ) for ongoing (top) and evoked (bottom) epochs, for traces in (a). (c) Ongoing and evoked skews for all 81 cells from 25 turtles. Each pair of connected dots indicates ongoing and evoked skews for one cell. Line above plot indicates significant change in skew from ongoing to evoked windows ($P = 3.2 \times 10^{-4}$, Wilcoxon signed-rank test). (d) Example visually-evoked high-conductance event. Red box indicates 50 ms ("pre-spike") window ending 5 ms before spike threshold crossing (see Methods). Black box indicates 50 ms ("random")

window randomly-selected from the same high-conductance event (see Methods). (e) Pre-spike (left, top) and corresponding random (left, bottom) traces for all visually-evoked spikes for example neuron in (d). Scale bars indicate 5 mV. Each trace is fitted with a straight line via linear regression, and the slope is defined to be dV/dt. The slopes are averaged across traces for each window type, yielding <dV/dt> for pre-spike and random windows for each neuron. Right: <dV/dt> for pre-spike (red dots) and random (white dots) windows for 30 cells from 15 turtles. Asterisks above plot indicate significant difference in the populations of values ($P = 1.73 \times 10^{-6}$, Wilcoxon signed-rank test). (f) Visually-evoked spike-triggered membrane potentials for "trigger" cell (black traces) and simultaneously-recorded "paired" cell (green traces, with across-trial average in high opacity, see Methods). Short spikes are due to downsampling (see Methods). (g) Left: <dV/dt> for trigger cells (black dots) and paired cells (green dots), for 23 triggered-paired cell pairs (from 19 pairs of simultaneously-recorded cells) in 11 turtles. Note that under certain conditions, a single pair of simultaneously recorded cells can yield two trigger-paired cell pairs. Asterisks above plot indicate significant difference in the two populations of values ($P = 2.70 \times 10^{-5}$, Wilcoxon signed-rank test). Right: same as in (e, right), but for 23 paired cells from 11 turtles ($P = 0.007$, Wilcoxon signed-rank test).

5 ms before each threshold crossing), as well as a corresponding 50 ms window of activity randomly-selected from the same 4 s window (**Figure 3.5d**). For this analysis, we required that the "random" window contain no spikes (see Methods), and that a neuron have at least six evoked spikes across all trials. In the brief pre-spike window, neurons tended to be depolarized by several millivolts (**Figure 3.5e, top**), in contrast to the relatively flat traces in randomly-selected windows (**Figure 3.5e, bottom**). Across the population, the average pre-spike depolarization far exceeded that during random windows (population grand average rate of change $\overline{< dV/dt >}$ = 0.093 +/- 0.039 mV/ms pre-spike window, 0.002 +/- 0.014 mV/ms random window, $P = 1.73 \times 10^{-6}$ for pre-spike – random comparison, Wilcoxon signed-rank test, **Figure 3.5e, right**, see Methods). In other words, at short time scales (on the order of tens of milliseconds), neurons in the evoked high-conductance state were subject to coordinated excitatory synaptic inputs. This result is inconsistent with the picture of a purely asynchronous network.

3.2.5 Pre-spike synaptic inputs are not strongly-correlated across nearby neurons

These pre-spike trajectories suggested coordinated spiking in presynaptic pools of neurons at short time scales. How widespread was this coordinated activity? To answer this question, we considered 19 pairs of simultaneously-recorded neurons, and inspected the subthreshold trajectories of the non-spiking ("paired") neuron in windows preceding spikes in the "trigger" neuron (**Figure 3.5f**). In general, when one cell was driven to spike, the nearby paired neuron was subject to significantly smaller depolarization ($\overline{< dV/dt >}$ = 0.09 +/- 0.043 mV/ms for trigger cells, 0.01 +/- 0.02 mV/ms for paired cells, P = 2.7 x 10^{-5} for comparison, Wilcoxon signed-rank test, **Figure 3.5f, 3.5g, left**). While small, this drive to paired cells was slightly (and significantly) stronger than that during randomly-selected windows of evoked activity ($\overline{< dV/dt >}$ = 6.3 x 10^{-4} +/- 0.01 mV/ms for random windows, P = 0.007 for pre-spike – random comparison, Wilcoxon signed-rank test, **Figure 3.5g, right**). Thus, the synchronous, pre-spike drive to a given neuron was very nearly private to that neuron.

Taken together, these results suggest that in the evoked high-conductance state, neurons are raised toward threshold by a baseline level of synaptic input that is relatively asynchronous and non-specific across neurons at long time scales. Within this evoked state, neurons receive a final "push" to threshold by coordinated spiking in the presynaptic population. These brief windows of strong, coordinated activity are not in general common across neurons, but are instead isolated to specific microcircuits.

3.2.6 Spontaneous and evoked subthreshold activity are related

We have so far considered ongoing and evoked activity separately. While all neurons were subject to large spontaneous events, the prevalence of slow-wave activity was remarkably variable

across neurons (representing variability across turtles, as well as across recording sessions in a given turtle, **Figure 3.2e; 3.6a, b**). As this likely reflected a variability in the network state, we asked whether this attribute of spontaneous activity had any apparent impact on the visual response.

First, we quantified the prevalence of the slow-wave fluctuations in ongoing activity by calculating the fast Fourier transform (FFT) of the 9.5 s of pre-stimulus activity, and integrating over low frequencies (1 – 5 Hz), resulting in the quantity FFT_δ (see Methods)(Sachidhanandam, Sreenivasan, Kyriakatos, Kremer, & Petersen, 2013). In agreement with qualitative inspection of voltage traces (**Figure 3.6a, left; 3.6b, left**), this metric was highly variable across trials (**Figure 3.6a, right; b, right**) and the across-trial average value ($<FFT_\delta>$) varied across cells (**Figure 3.6c**).

We next inspected for a relationship between the prevalence of slow-wave fluctuations (i.e., $<FFT_\delta>$) and various response properties. First, we asked whether $<FFT_\delta>$ was related to the average subthreshold response size (<S>, as in **Figure 3.3c, g**). These quantities were, in fact, positively correlated (**Figure 3.6d**). Further, these larger responses were also less reliable than smaller responses (as quantified by $<R^2>$, the average variance of single-trial responses explained by the across-trial average response, **Figure 3.6e**, and see Methods). Finally, we asked whether $<FFT_\delta>$ (indicating ongoing coordination strength at one temporal scale) could predict evoked coordination strength at shorter temporal scales (that is, the average evoked pre-spike depolarization <dV/dt>, as in **Figure 3.6d, e**). These two quantities were anti-correlated (though the coefficient was only significant when two extreme data points were removed, **Figure 3.6f**). That is, when the ongoing state was more synchronous, neurons were also closer to threshold in the evoked state, and thus required less additional depolarization to reach threshold.

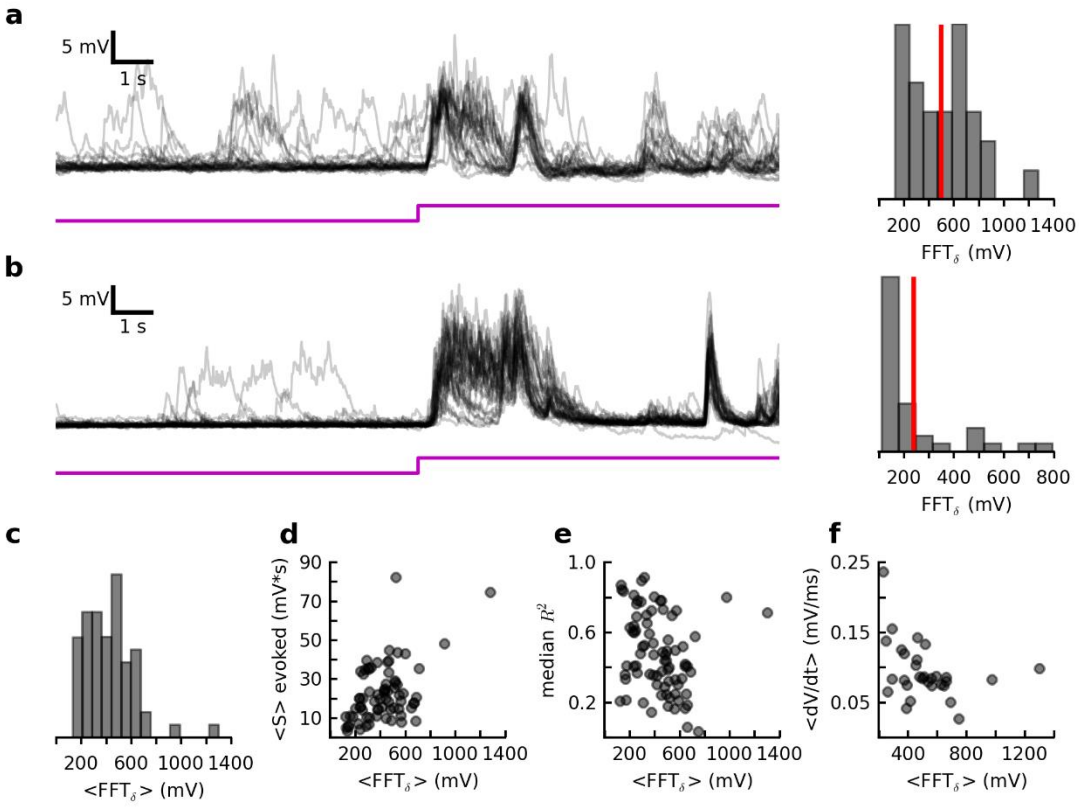

Figure 3.6 Ongoing and evoked cortical activity are related. (a – c) The prevalence of spontaneous slow-wave fluctuations varied across recording sessions and turtles. (a) Left: ongoing and evoked activity recorded from a single neuron in response to multiple presentations of a naturalistic movie (see Methods). Right: distribution of FFT_δ (the integrated low-frequency (1 – 5 Hz) FFT for ongoing activity) for all trials (see Methods), for cell in (a). Red vertical line indicates $<FFT_\delta>$, the across-trial mean. (b) Same as in (a), but for a different neuron (from the same turtle, but an earlier recording session). (c) Distribution of $<FFT_\delta>$ values for 66 cells from 22 turtles. (d – f) The prevalence of slow-wave fluctuations in ongoing activity was related to properties of evoked activity. (d) Across-trial average subthreshold response size (<S>) vs. $<FFT_\delta>$ for 72 cells from 23 turtles (i.e., all data points from Fig 3c, g). Ranks are significantly related ($r = 0.39$, $P = 6.7 \times 10^{-4}$, Spearman rank correlation). (e) Across-trial median evoked R^2 (a proxy for response reliability, see Methods) vs. $<FFT_\delta>$ for 79 cells from 25 turtles. Ranks are significantly related ($r = -0.34$, $P = 1.9 \times 10^{-3}$, Spearman rank correlation). (f) Mean evoked pre-spike depolarization (<dV/dt>) vs. $<FFT_\delta>$ for 30 cells from 15 turtles (i.e., data points in Figure 3.5e, right). Ranks are not significantly related ($r = -0.36$, $P = 0.049$, Spearman rank correlation). Note: quantities are significantly linearly related when the data points corresponding to the two largest $<FFT_\delta>$ values (i.e., the outliers in (c)) are excluded ($r = -0.54$, $P = 0.003$, linear regression). Cells used in (d – f) vary across subFigure 3.s, due to differences in requirements for calculating values on y-axis. Threshold p-value for significance has been Bonferroni-adjusted for three comparisons.

Together, these results demonstrate a strong relationship between properties of the ongoing network state and those of evoked activity. Specifically, a greater prevalence of spontaneous transitions between low- and high-conductance states predicted larger and less reliable subthreshold visual responses, and smaller depolarizations immediately preceding evoked spikes.

3.2.7 Visual response size depends on spontaneous activity immediately preceding the stimulus

One possible explanation for the above observations is that ongoing depolarizations add to evoked, and the random appearance of these events contributes to response variability. Alternatively, strong slow-wave activity may be consistent with a network that is more "activated" for large visual responses, yet a given spontaneous event preceding the stimulus inhibits the response.

To distinguish between these competing hypotheses, we first segregated visual stimulation trials for each cell into two categories: "low" trials, in which the stimulus was preceded by at least 2 s of quiescent ongoing activity (**Figure 3.7a, top**), and "high" trials, in which the stimulus either interrupted or followed soon after a large spontaneous high-conductance event (**Figure 3.7b, bottom**, see Methods). To be included in this analysis, we required a cell to have at least three "high" trials. This effectively restricted the set of included cells to those displaying relatively prominent slow-wave ongoing activity. We then calculated the subthreshold response size scaled by the maximum across-trial response size (S'/S'_{max}) in a 2 s post-stimulus window, and averaged across trials (see Methods). We found that "high" responses were significantly smaller than "low" responses (population grand average response amplitude $\overline{< S'/S'_{max} >}$ = 0.78 +/-

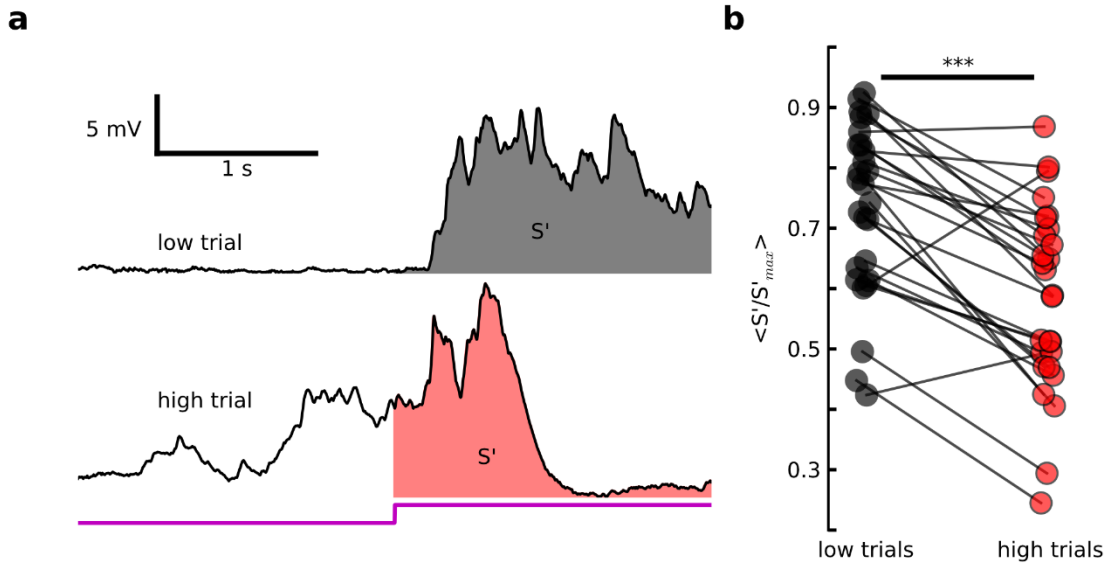

Figure 3.7 Large, spontaneous pre-stimulus events correspond to smaller visual responses. (a) Two example responses from one cell to presentation of naturalistic movie (see Methods). Top: "low trial", in which stimulus presentation is preceded by low-conductance state. Bottom: "high trial", in which stimulus is preceded by or interrupts a large, spontaneous high-conductance event. S' is the area under the curve for the 2 s after stimulus onset. (b) Average scaled S' (see Methods) for low (black dots) and high (red dots) trials for 27 cells from 15 turtles. Asterisks above plot indicate significant difference between the two populations of values ($<S'/S'_{max}>$ = 0.73 +/- 0.14 for low trials, 0.58 +/- 0.15 for high trials, P = 6.01 x 10^{-5} for low-high comparison, Wilcoxon signed-rank test.

0.10 for "low" responses, 0.68 +/- 0.14 for "high" responses, P = 4.52 x 10^{-4} for comparison, Wilcoxon signed-rank test, **Figure 3.7b**). Evidently, while a cortex with more frequent spontaneous high-conductance events yielded larger average responses (**Figure 3.6d**), a given visual response was, in fact, inhibited by excessive activity in the window immediately preceding the stimulus.

3.3 Discussion

In order to investigate ongoing and visually-evoked subthreshold and spiking cortical activity, we obtained whole-cell recordings from neurons in the three-layer visual cortex of the *ex vivo* turtle eye-attached whole-brain preparation. To infer properties of the corresponding network activity, we investigated the statistics of subthreshold activity at two distinct time scales for individual neurons, and for pairs of simultaneously-recorded neurons, and compared to results predicted by theory. Finally, we investigated the relationship between ongoing and evoked network activity by comparing properties of the two network states (as communicated by subthreshold activity).

In the absence of visual stimulation, neurons were usually in a relatively quiescent "low-conductance" state, with random transitions into depolarized "high-conductance" states (**Figure 3.2a**). These are often referred to as "Down" and "Up" states, respectively, but the conductance-based labels underscore the synaptic origin of these events, which signal changes in the activity level of a neuron's presynaptic pool. While drastic Up-Down transitions can be brought on by anesthesia(Destexhe, Rudolph, & Paré, 2003), many studies have demonstrated similar non-Gaussian spontaneous fluctuations in a variety of areas in awake preparations, including mouse(Bennett et al., 2013) and primate(Tan et al., 2014) visual cortex, rat auditory cortex(DeWeese & Zador, 2006), rodent somatosensory cortex(Crochet & Petersen, 2006; Gentet et al., 2010; Petersen et al., 2003; J. F. a Poulet & Petersen, 2008), and even in reduced preparations, including thalamocortical slice(Cossart, Aronov, & Yuste, 2003; Graupner & Reyes, 2013; MacLean, Watson, Aaron, & Yuste, 2005; Sanchez-Vives & McCormick, 2000). Previous work has shown that the transient increases in presynaptic firing are due to waves of activity

propagating across the cortex(Petersen et al., 2003). These waves (also observed in turtle cortex(Senseman & Robbins, 1999)) are thought to be generated intracortically(Sanchez-Vives & McCormick, 2000; Steriade, Contreras, Curró Dossi, & Nuñez, 1993), though they can be triggered and shaped by external inputs(Hirata & Castro-Alamancos, 2011; MacLean et al., 2005; J. F. A. Poulet, Fernandez, Crochet, & Petersen, 2012; Rigas & Castro-Alamancos, 2007). Recent computational work suggests that the cortical excitation/inhibition balance is crucial to this phenomenon(Keane & Gong, 2015). Thus, the spontaneous membrane potential dynamics we observe here likely reflect the complex spatiotemporal population activity patterns that emerge in balanced cortical networks.

Visual stimulation evoked high-conductance states (**Figure 3.3a, e**) that were qualitatively similar to longer-duration spontaneous high-conductance events (**Figure 3.2a, b, d**). It is possible there is more than a passing resemblance between these two types of activity. Previous work has uncovered striking similarities between ongoing and evoked activity in cortex(Kenet, Bibitchkov, Tsodyks, Grinvald, & Arieli, 2003; Luczak, Barthó, & Harris, 2009; Sakata & Harris, 2009), and specifically in the subthreshold activity of individual cortical neurons(MacLean et al., 2005). Because a neuron's subthreshold time series communicates a spatiotemporal sequence of cortical firing, this indicates similar spontaneous and evoked firing patterns. Such observations are consistent with the view that spontaneous cortical events broadly sample the set of all possible spatiotemporal patterns in the cortical "response manifold"(Ringach, 2009). While we did not perform an in-depth investigation of this topic, this preparation has great potential for such a study. First, it represents an important advance beyond the slice preparation; intracortical connectivity is preserved, and cortical activity is evoked by visual (rather than electrical) stimulation. Second, multi-whole-cell recordings allow for a "higher-dimensional" view of cortical firing than that

afforded by individual whole-cell recordings. Future work can therefore enhance our understanding of the relationship between ongoing and evoked cortical activity.

Previous studies have described a stimulus-induced transition from cortical synchrony to asynchrony(Tan et al., 2014). In other words, pre-stimulus subthreshold activity includes frequent periods of broadly-correlated depolarization, and evoked activity more closely follows the "random walk" dynamics consistent with Poisson process inputs. Yet in other studies, sensory-evoked spikes are preceded by strong depolarizations, indicating concerted presynaptic firing(Gentet et al., 2010; J. F. a Poulet & Petersen, 2008). We observed both of these seemingly-contradictory phenomena (**Figure 3.5a-e**). This paradox is actually predicted for neurons in the high-conductance state; while the inputs to a neuron may be relatively random, the reduced membrane time constant make the neuron a better coincidence detector(Destexhe et al., 2003; Michael Rudolph & Destexhe, 2003). Thus, evoked spikes in a given neuron are more likely to result from nearly-coincident synaptic inputs, and to be more tightly phase-locked to those of the presynaptic population. This mechanism for spike synchronization is most effective when a neuron's reduced time constant (promoting coincidence detection) outweighs its reduced distance from spike threshold (which makes the depolarized cell more likely to spike in response to even small additional inputs). We found that the balance between these two biophysical influences depended on cortical state; pre-spike depolarization was smaller when the ongoing cortical state was consistent with larger depolarizations (**Figure 3.6d, f**), suggesting the coincidence-detection mechanism was more easily "saturated". Our observations thus provide a rare, intracellular view of the relationship between long-time-scale coordination during ongoing activity and short-time-scale coordination (leading to spikes) during visual processing.

Pairwise recordings revealed a spatial dimension to coordination as well; at a fixed temporal scale (tens of milliseconds), activity could become strongly coordinated in a given microcircuit (**Figure 3.5d**), but was not, in general, coordinated across cortical space (**Figure 3.5f, g**). This is likely due at least in part to the nature of cortical connectivity; dense interconnectivity supports broadly-distributed states of enhanced excitability (that is, broadly-coordinated transitions to high-conductance states), while the "constellation-like" specificity of this connectivity (with a minority of extremely strong connections, and a majority of weak ones(Cossell et al., 2015)) diversifies the coupling strengths among neurons in a local population(Hofer et al., 2011; Okun et al., 2015). This may create preferred pathways for the propagation of spikes within the high-conductance state. Combined with the observed temporal dependence, this result demonstrates just two of the possibly many spatiotemporal scales at work in the likely "multiplexed" cortical code(Panzeri, Brunel, Logothetis, & Kayser, 2010).

While anatomical connectivity is extremely influential to evoked activity, the ongoing network state is also thought to play an important role. For instance, some set of conditions hidden from the experimenter modulates the degree of ongoing cortical slow-wave activity (or synchrony). How do the variables controlling these properties of ongoing activity affect sensory responses? Previous studies have reported a rich dependence of cortical response properties on the spontaneous cortical state(Ecker et al., 2014; Haider, Schulz, Häusser, & Carandini, 2016; Sachidhanandam et al., 2013; Scholvinck, Saleem, Benucci, Harris, & Carandini, 2015). Accordingly, we found that stronger slow-wave fluctuations predicted visual responses that were on average larger (**Figure 3.6d**) and less reliable (**Figure 3.6e**) than those corresponding to more quiescent ongoing states. While we did not directly investigate the deeper implications, two results suggest a nonlinear relationship between the ongoing state and cortical function; the enhanced

variability at the high end of the synchrony "spectrum" seems disadvantageous for sensory encoding, while the smaller responses at the other end may be as well. The optimal state may be an intermediate level of synchrony, balancing these two phenomena. In support of this idea, recent work has suggested that maximum dynamic range occurs in a cortex tuned to the critical state(W. L. Shew, Yang, Petermann, Roy, & Plenz, 2009), which also coincides with intermediate levels of network synchrony(Gautam, Hoang, McClanahan, Grady, & Shew, 2015; Yang, Shew, Roy, & Plenz, 2012). Where the cortex sits on this spectrum is likely governed by top-down control, most generally tracked by level of arousal. Indeed, intermediate levels of arousal correspond to intermediate spontaneous membrane potential levels and enhanced perception(Mcginley, David, & McCormick, 2015). It will be important for future work to identify such general principles of cortical function (e.g., criticality) that govern phenomena commonly observed in experiment (e.g., synchrony, as observed in the statistics of population spiking or subthreshold membrane potential fluctuations), as well as the synaptic basis of top-down interactions.

Finally, there is the question of how the condition of the cortex at or immediately preceding stimulus onset influences the response. This question becomes increasingly relevant as the ongoing network state becomes more synchronous, as large, spontaneous events become more common. Many studies have observed that the probabilistic nature of ongoing activity contributes to across-trial response variability(Arieli, Sterkin, Grinvald, & Aertsen, 1996; Destexhe et al., 2003; Hirata & Castro-Alamancos, 2011; Scholvinck et al., 2015). The exact nature of the interaction is an item of debate(M. A. Castro-Alamancos, 2009). On the one hand, spontaneous depolarization brings neurons closer to threshold prior to the arrival of excitatory sensory input. Accordingly, some studies show that enhanced levels of pre-stimulus activity correspond to larger responses(Arieli et al., 1996; Azouz & Gray, 1999; Gutnisky, Beaman, Lew, & Dragoi, 2016;

Haider, Duque, Hasenstaub, Yu, & McCormick, 2007). On the other hand, spontaneous synaptic barrages reduce input resistance(Cowan & Wilson, 1994; Destexhe et al., 2003; Paré, Shink, Gaudreau, Destexhe, & Lang, 1998) and depress synapses(M A Castro-Alamancos & Connors, 1997; M. A. Castro-Alamancos, 2009; Markram, Wang, & Tsodyks, 1998). In addition, spontaneous depolarization increases the driving force for inhibition(M. A. Castro-Alamancos, 2009), and thus the IPSP amplitudes associated with short-latency, disynaptic feedforward inhibiton(Mancilla & Ulinski, 2001). Consistent with this view, some studies have reported that large spontaneous events suppress evoked activity(Petersen et al., 2003; Sachdev, Ebner, & Wilson, 2004). Our results are in agreement with these latter studies; when the visual stimulus interrupted or followed soon after a large spontaneous event, the subthreshold response was muted (**Figure 3.7**). Evidently, suppressing mechanisms (likely including those described above) more than counterbalanced the reduced distance to threshold in the presynaptic population.

What are the implications of this dependency on the pre-stimulus condition? Previous work provides conflicting answers. In some cases, a high-conductance pre-stimulus state corresponds to muted responses that are less reliable across trials(Crochet & Petersen, 2006), thus compromising response fidelity. Still, in barrel cortex, this muted responses (resulting from either spontaneous pre-stimulus events(Civillico & Contreras, 2012; Petersen et al., 2003), or the presentation of a background stimulus(Ollerenshaw, Zheng, Millard, Wang, & Stanley, 2014; Zheng, Wang, & Stanley, 2015)) are more confined to the column corresponding to the stimulated whisker, which promotes stimulus-response mutual information. Elsewhere, a more active pre-stimulus condition yields larger responses, that are less effective at transmitting information(Gutnisky et al., 2016). Finally, at least one study shows no measurable relationship between the pre-stimulus state and the size or reliability of the early cortical

response(Sachidhanandam et al., 2013). Of course, another possibility is that the "adapted" state resulting from prominent pre-stimulus activity is optimized for some functions (e.g., discrimination) at the expense of others (e.g., detection)(Ollerenshaw et al., 2014; Zheng et al., 2015). Evidently, it will be important for future studies to address the impact of the pre-stimulus state on sensory responses using carefully-designed stimuli and information-theoretic measures of both detection and discrimination. As in the discussion of long-time-scale ongoing "state", it will be important to incorporate behavior; a recent study has shown that diminished "late" responses (corresponding to stimuli delivered in the Up state) causally impair perception(Sachidhanandam et al., 2013). This combined approach can be extremely challenging to implement (especially when involving patch clamp recording), but is becoming increasingly feasible. While such techniques are being developed, it will be important to continue to document the effects of the pre-stimulus cortical state on sensory responses to the extent possible; this will reveal which aspects of the interaction generalize across areas and species.

In conclusion, these results contribute to a clearer picture of the subthreshold dynamics of cortical visual responses. They highlight the importance of the relationship between the ongoing network state and subthreshold evoked activity. Further, they show that evoked spiking is shaped by presynaptic activity that is coordinated at multiple spatiotemporal scales. As such, this study is in agreement with previous work suggesting that anatomical and emergent cortical network properties play vital roles in cortical sensory processing, and provides a rare view of this influence at the level of the membrane potential.

3.4 Methods

3.4.1 Surgery

All procedures were approved by Washington University's Institutional Animal Care and Use Committees and conform to the guidelines of the National Institutes of Health on the Care and Use of Laboratory Animals. Fourteen adult red-eared sliders (*Trachemys scripta elegans*, 150-1000 g) were used for this study. Turtles were anesthetized with Propofol (2mg Propofol/kg), then decapitated. Dissection proceeded as described previously(Crockett et al., 2015; Saha et al., 2011; W. L. W. L. Shew et al., 2015). In brief, immediately after decapitation, the brain was excised from the skull, with right eye intact, and bathed in cold extracellular saline (in mM, 85 NaCl, 2 KCl, 2 $MgCl_2$*$6H_2O$, 20 Dextrose, 3 $CaCl_2$-$2H_2O$, 45 $NaHCO_3$). The dura was removed from the left cortex and right optic nerve, and the right eye hemisected to expose the retina. The rostral tip of the olfactory bulb was removed, exposing the ventricle that spans the olfactory bulb and cortex. A cut was made along the midline from the rostral end of the remaining olfactory bulb to the caudal end of the cortex. The preparation was then transferred to a perfusing chamber (Warner RC-27LD recording chamber mounted to PM-7D platform), and placed directly on a glass coverslip surrounded by Sylgard. A final cut was made to the cortex (orthogonal to the previous and stopping short of the border between medial and lateral cortex) allowing the cortex to be pinned flat, with ventricular surface exposed. Multiple perfusion lines delivered extracellular saline, adjusted to pH 7.4 at room temperature, to the brain and retina in the recording chamber.

3.4.2 Intracellular Recordings

We performed whole-cell current clamp recordings from 39 cells in 14 preparations. Patch pipettes (4-8 MΩ) were pulled from borosilicate glass and filled with a standard electrode solution (in mM; 124 $KMeSO_4$, 2.3 $CaCl_2$-$2H_2O$, 1.2 $MgCl_2$, 10 HEPES, 5 EGTA) adjusted to pH 7.4 at

room temperature. Cells were targeted for patching using a dual interference contrast microscope (Olympus). All cells were located within 300 microns of an extracellular recording electrode. Intracellular activity was collected using an Axoclamp 900A amplifier, digitized by a data acquisition panel (National Instruments PCIe-6321), and recorded using a custom Labview program (National Instruments), sampling at 10 kHz. The visual cortex was targeted as described previously(W. L. W. L. Shew et al., 2015).

3.4.3 Extracellular Recordings

We performed extracellular recordings at 12 recording sites in seven preparations. We used tungsten microelectrodes (MicroProbes heat treated tapered tip), with approximately 0.5 MΩ impedance. Electrodes were slowly advanced through tissue under visual guidance using a manipulator (Narishige), while monitoring for spiking activity using custom acquisition software (National Instruments). Extracellular activity was collected using an A-M Systems Model 1800 amplifier, band-pass filtered between 1 Hz and 20,000 Hz, digitized (NI PCIe-6231), and recorded using custom software (National Instruments), sampling at 10 kHz.

3.4.4 Visual Stimulation

Whole-field flashes were presented using either a red LED (Kingbright, 640nm), mounted to a manipulator and positioned 1 – 5 cm above the retina, or a projector-lens system (described below). The mean LED light intensity (irradiance) at the retina was 60 W/m^2. For one turtle, we used these same LEDs in conjunction with 200 micron optical fibers (Edmund Optics) to project sub-field flashes (1 ms – 200 ms) onto the visual streak. Other stimuli were presented using using a projector (Aaxa Technologies, P4X Pico Projector), combined with a system of lenses (Edmund Optics) to project images generated by a custom software package directly onto the retina. The

mean irradiance at the retina was 1 W/m^2. This system was used to present brief (100 ms – 250 ms) whole-field and sub-field flashes (red or white), sustained (10 s) gray screen, a naturalistic movie ("catcam") a motion-enhanced movie (courtesy Jack Gallant), and a phase-shuffled version of the same movie (courtesy Jack Gallant and Woodrow Shew). In all cases, the stimulus was triggered using a custom Labview program (National Instruments).

For each cell and extracellular recording site, we selected one of the five stimuli listed above to present across all trials. The preparation was in complete darkness before and after each stimulus presentation. Extended stimuli lasted either 10 s or 20 s, and flashes lasted between 1 ms and 250 ms, with at least 30 s between the end of one presentation and the beginning of the next. In all cases, visual stimulation trials were repeated at least 12 times.

3.4.5 Data included in analysis

For each extracellular recording site, we used visual inspection to determine the quality of the recordings. In general, we excluded recording sites from consideration if voltage traces displayed excessive 60 Hz line noise, low-frequency noise (likely reflecting a damaged electrode), or on average small response amplitudes relative to baseline.

For the analysis of intracellular recordings, we required at least twelve visual stimulation trials (unless stated otherwise, see below).

3.4.6 Processing of intracellular and extracellular voltage recordings

Raw data traces were down-sampled to 1000 Hz. We used an algorithm to detect spikes in the membrane potential, and the values in a 20 ms window centered on the maximum of each spike were replaced via interpolation. Finally, we applied a 100 Hz lowpass Butterworth filter. We did

not perform these last two steps for "trigger cells" used to calculate spike-triggered averages (**Figure 3.5d-g**, and see below)

In addition, we detrended spontaneous recordings. To do this, for each time step, we subtracted a value obtained from a 10 s window beginning at that time step. The value we used depended on the median membrane potential (MMP) of the cell in each full recording; if the MMP was above -60 mV, we used the median value of the 10 s window for detrending. If MMP was below -60 mV, we used the fifth percentile of the window. The reasoning for this was as follows: in the detrending process, we seek to subtract from the membrane potential at a given point in time a good estimate of the "true" resting membrane potential (RMP) near that point in time. When MMP is low, high-conductance events usually result in large depolarizations. Even when using large sliding windows in the detrending process, these depolarizations can lead to spurious changes in the detrended membrane potential before and after each event. We therefore use the fifth percentile of the window for low-MMP cells, as it is less susceptible than the median to outlier membrane potential values above MMP, and is therefore a better estimate of RMP in the neighborhood of the event. For neurons with high MMP, on the other hand, IPSPs can be quite large during high-conductance events (due to the increased distance from the inhibitory reversal potential). In fact, the membrane potential often drops below MMP during these events, meaning the fifth percentile does as well. In this case, the median of the window is a better estimate of RMP in the neighborhood of the event.

3.4.7 Detecting and quantifying spontaneous high-conductance events

We used an algorithm to detect spontaneous high-conductance events in each detrended spontaneous voltage trace (**Figure 3.5b, top**). First, we detected all "bumps" (i.e., windows of

activity in which the membrane potential exceeded the standard deviation of the full trace by at least a factor of 1.5). Then, we detected "high bumps" (using instead a threshold factor of 4). Finally, given these "bumps" and "high bumps", we identified "high-conductance events". First, we combined "bumps" separated by less than 500 ms of silence. Any "bump" in this refined set that also included a "high bump" was defined to be a "high-conductance event". For each event (of duration D in ms), we defined the size (S in mV*s) to be the area under the curve (**Figure 3.5b, bottom**).

3.4.8 Subthreshold response latencies

For each presentation of a stimulus (flashes and extended stimuli), we calculated response latency (**Figure 3.3b, f**) by first considering the membrane potential in a window of activity beginning 9 s before and ending 9 s after stimulus onset. We then calculated the slope (dV/dt) as a function of time for this sub-trace. We excluded the trial from consideration if 1) visual stimulation clearly interrupted a large spontaneous Up state, or 2) large PSPs were present immediately before stimulus onset (indicating the possible onset of a spontaneous high-conductance event). We considered condition 1 (2) to be satisfied if any value of the slope trace in the 500 ms (200 ms) preceding stimulus onset exceeded six (four) times the standard deviation of the entire slope trace. If neither of these conditions were met, we defined the response latency to be the time after stimulus onset at which the slope trace exceeded three times the standard deviation of the entire slope trace. Finally, "latencies" smaller than 50 ms were excluded.

3.4.9 Subthreshold response duration

To calculate the duration (D) of a subthreshold flash response (**Figure 3.3c**), we first applied the high-conductance event detection algorithm (described above for spontaneous events)

to a window (18 s centered on the stimulus onset) extracted from the full voltage trace. With the resulting set of event times (i.e., event onset, offset pairs), we considered the response onset to be the first event onset time in the window between 50 ms and 1 s after stimulus onset. The response offset was the last event offset time in a window between response onset and 7 s after stimulus onset. Only trials with valid onset and offset times were included.

3.4.10 Subthreshold response size

To calculate subthreshold response size (S) for flashes (**Figure 3.3d**) and extended stimuli (**Figure 3.3g**), we first detected the response duration (as described above). Then, for each response window, we subtracted the fifth percentile of the membrane potential (calculated from the full trial). We defined the response size to be the area under the curve for the response window. Note that for extended stimuli, activity typically persisted beyond the window used to calculate response size. For this type of stimulus, then, S is a measure of evoked activity in at most the first 7 s of the response (and is still a useful measure for comparisons across events (**Figure 3.3g, left**) and cells (**Figure 3.3g, right**) for extended stimuli only).

3.4.11 Evoked action potential rates

To identify spike times in intracellular recordings of visual responses (**Figure 3.4a**), we first estimated the first derivative of the voltage trace (V') by calculating the change in membrane potential for each (1 ms) time step. We then defined spike times to be those at which the value of V' was at least 20 times the standard deviation of V'. Finally, we calculated the average spike rate for each cell in a two-second window after stimulus onset (**Figure 3.4a, inset**), which was a window that contained most of the evoked spikes in a typical trial (**Figure 3.4b, c**).

3.4.12 Multi-unit activity

We determined multi-unit spiking activity for one recording session, to provide an example of spiking patterns in a population nearby two intracellularly-recorded neurons (**Figure 3.4a, bottom**). Multi-unit spike times for each trial were defined to be those at which the value of the high-pass-filtered (250 Hz Butterworth) extracellular trace was at least six times the standard deviation of the full trace.

3.4.13 Peristimulus time histograms

We constructed peristimulus time histrograms (PSTHs) for responses to brief (**Figure 3.4b**) and extended (**Figure 3.4c**) stimuli. For each stimulus, we pooled the responses from all intracellular recordings. For each trial, spike times were detected as described above. We included all trials that contained at least one spike in the 7 s after stimulus onset.

3.4.14 Residual membrane potentials and residual skew

For each recorded cell, we calculated the residual time series (single-trial time series with across-trial average time series subtracted, **Figure 3.5a**). We then considered two windows of activity: the ongoing (2 s to 0 s before stimulus onset), and evoked (0 s to 2s after response onset) windows. Response onset was determined as described above (for response latency calculations). For each trial and epoch, we subtracted the average value for that epoch, and concatenated the resulting trace to a single time series. We then calculated the skew of the concatenated time series (**Figure 3.5b**). We compared the results for all cells (**Figure 3.5c**) using the Wilcoxon signed-rank test.

3.4.15 Spike-triggered membrane potentials

For each cell and visual stimulation trial, we determined evoked action potential times, as described above. An action potential was included in this analysis if it occurred between 75 ms and 4 s after stimulus onset. We included a cell in this analysis if it spiked at least six times in this response window across all trials. For each spike, the threshold crossing time was defined to be the first zero-crossing of the second time derivative of V in the 5 ms preceding the spike time. This represents the maximum change in membrane potential slope immediately before the spike. We estimated the second derivative (V'') at each time step *k* using Taylor series expansion(Sekerli, Del Negro, Lee, & Butera, 2004):

$$V'' \approx \frac{-V_{k-2} + 16V_{k-1} - 30V_k + 16V_{k+1} - V_{k+2}}{12(\Delta t)^2}$$

where Δt is the size of the time step (1 ms).

We then considered a 50 ms "pre-spike" window of activity ending 5 ms before threshold crossing. For each spike, we also considered a 50 ms "random" window of activity that (i) was taken from the same 4 s response window; and (ii) did not contain an action potential (**Figure 3.5d**). We found the slope of the trace in each window via linear regression, and then averaged across trials (yielding <dV/dt> for pre-spike and random windows, **Figure 3.5e**). We compared <dV/dt> for the two window types using the Wilcoxon signed-rank test.

We performed a similar analysis for pairs of simultaneously-recorded neurons. For each pair, if either of the cells had at least six evoked spikes across all trials, it was treated as the "trigger" cell, and the other as the "paired" cell (**Figure 3.6f**). Average "pre-spike" and "random" depolarizations (<dV/dt>) were calculated as described above, using the spike times from the trigger cell. We compared <dV/dt> values for trigger and paired cells (**Figure 3.6g, left**), and for

pre-spike and random windows for paired cells (**Figure 3.6g, right**) using the Wilcoxon signed-rank test.

3.4.16 Low-frequency FFT of ongoing activity

For each cell, we considered the ongoing activity in the 9.5 s before stimulus onset (**Figure 3.6a, b**), and calculated the fast Fourier transform (implemented using the numpy.fft routine, with documentation available at https://docs.scipy.org/doc/numpy/reference/generated/numpy.fft.fft.html). We averaged the sum of the 1 – 5 Hz Fourier coefficients across all trials, yielding $\langle FFT_\delta \rangle$, **Figure 3.6c**), which, for a given cell, was a reliable proxy for the prevalence of large, spontaneous high-conductance events in the pre-stimulus window (**Figure 3.6a, b**).

3.4.17 Response reliability

For each cell, we considered a 2 s window of evoked activity beginning at stimulus onset. For this window, we regressed each single-trial response onto the average response, yielding R^2 (the explained variability). For each cell, we took the across-trial median R^2 value (**Figure 3.6e**) to be the "response reliability".

3.4.18 "Low" and "high" visual response trials and scaled response size

We segregated the visual responses for each cell into two categories defined by ongoing activity: "low" and "high" trials. For each recording, we used an algorithm to identify all high-conductance events (as described above). The trial was designated a "high" trial if a spontaneous high-conductance event (i) ended within 2 s of stimulus onset; or (ii) was interrupted by stimulus onset (**Figure 3.7a**). A cell was required to have at least three high and three low trials to be

included in this analysis. We forced the two trial sets to contain the same number of trials by randomly excluding trials from the longer of the two sets. Of these remaining trials, we considered a 2s window of activity beginning at stimulus onset. From this evoked window, we subtracted a baseline value (the fifth percentile, calculated from the full, original voltage trace). We defined the response size (S') to be the area under the resulting curve (**Figure 3.7a**). We scaled each response size by the maximum response size (S'_{max}) in the retained trials, and averaged across trials (yielding $<S'/S'_{max}>$. We then compared the populations of average scaled responses using the Wilcoxon signed-rank test (**Figure 3.7b**). Because the process of excluding trials was random, we ensured the significant difference indicated in **Figure 3.7b** was robust to iterations of the calculation (data not shown).

3.4.19 Statistical analysis

All statistical tests were performed using Python 2.7.

Before applying any significance test that assumed normality, we performed an omnibus test for normality on the associated dataset(s). This test compares the skew and kurtosis of the population from which the dataset was drawn to that of a normal distribution, returning a p-value for a two-sided chi-squared test of the null hypothesis that the data is drawn from a normal distribution. This test is valid for sample sizes of 20 or larger, and was implemented using scipy.stats.mstats.normaltest (documentation and references available at http://docs.scipy.org/doc/scipy-0.14.0/reference/generated/scipy.stats.mstats.normaltest.html). We report these p-values as the result of a "two-sided omnibus chi-shared test for normality".

When asking whether a parameter of interest changed significantly across two sets of conditions for a population, we applied the Wilcoxon signed-rank test, which returns a p-value for

the two-sided test that the two related paired samples are drawn from the same distribution. This test assumes normality, and was implemented using scipy.stats.wilcoxon (documentation and references available at http://docs.scipy.org/doc/scipy/reference/generated/scipy.stats.wilcoxon.html).

Acknowledgments: We thank Woodrow Shew for assistance with the design of the visual stimulus. We thank Thomas Crockett for contributing data. This research was supported by a Whitehall Foundation grant #20121221 (R.W.) and a NSF CRCNS grant #1308159 (R.W.).

Author Contributions: N.W. and R.W. conceived the study and designed the experiments. N.W. performed the experiments and analyzed the data. N.W. and R.W. wrote the paper.

Competing Financial Interests: The authors declare no competing financial interests.

Arieli, A., Sterkin, A., Grinvald, A., & Aertsen, A. (1996). Dynamics of ongoing activity: explanation of the large variability in evoked cortical responses. *Science (New York, N.Y.)*, *273*(5283), 1868–1871. http://doi.org/10.1126/science.273.5283.1868

Azouz, R., & Gray, C. M. (1999). Cellular mechanisms contributing to response variability of cortical neurons in vivo. *The Journal of Neuroscience : The Official Journal of the Society for Neuroscience*, *19*(6), 2209–2223.

Bennett, C., Arroyo, S., & Hestrin, S. (2013). Subthreshold mechanisms underlying state-dependent modulation of visual responses. *Neuron*, *80*(2), 350–7.

http://doi.org/10.1016/j.neuron.2013.08.007

Castro-Alamancos, M. A. (2009). Cortical Up and Activated States: Implications for Sensory Information Processing. *The Neuroscientist*, *15*(6), 625–634. http://doi.org/10.1177/1073858409333074

Castro-Alamancos, M. A., & Connors, B. W. (1997). Distinct forms of short-term plasticity at excitatory synapses of hippocampus and neocortex. *Proceedings of the National Academy of Sciences of the United States of America*, *94*(8), 4161–6. http://doi.org/10.1073/pnas.94.8.4161

Civillico, E. F., & Contreras, D. (2012). Spatiotemporal properties of sensory responses in vivo are strongly dependent on network context, *6*(April), 1–20. http://doi.org/10.3389/fnsys.2012.00025

Cohen, M. R., & Kohn, A. (2011). Measuring and interpreting neuronal correlations. *Nature Neuroscience*, *14*(7), 811–819. http://doi.org/10.1038/nn.2842

Cossart, R., Aronov, D., & Yuste, R. (2003). Attractor dynamics of network UP states in the neocortex, *423*(May), 13–16. http://doi.org/10.1038/nature01610.1.

Cossell, L., Iacaruso, M. F., Muir, D. R., Houlton, R., Sader, E. N., Ko, H., … Mrsic-flogel, T. D. (2015). Functional organization of excitatory synaptic strength in primary visual cortex. *Nature*, *000*(00), 1–5. http://doi.org/10.1038/nature14182

Cowan, R. L., & Wilson, C. J. (1994). Spontaneous firing patterns and axonal projections of single corticostriatal neurons in the rat medial agranular cortex. *Journal of Neurophysiology*, *71*(1), 17–32. Retrieved from

http://www.ncbi.nlm.nih.gov/pubmed/8158226

Crochet, S., & Petersen, C. C. H. (2006). Correlating whisker behavior with membrane potential in barrel cortex of awake mice. *Nature Neuroscience*, *9*(5), 608–610. http://doi.org/10.1038/nn1690

Crockett, T., Wright, N., Thornquist, S., Ariel, M., & Wessel, R. (2015). Turtle dorsal cortex pyramidal neurons comprise two distinct cell types with indistinguishable visual responses. *PLoS ONE*, *10*(12), 1–22. http://doi.org/10.1371/journal.pone.0144012

Destexhe, A., Rudolph, M., & Paré, D. (2003). The high-conductance state of neocortical neurons in vivo. *Nature Reviews. Neuroscience*, *4*(9), 739–751. http://doi.org/10.1038/nrn1198

DeWeese, M. R., & Zador, A. M. (2006). Non-Gaussian Membrane Potential Dynamics Imply Sparse, Synchronous Activity in Auditory Cortex. *Journal of Neuroscience*, *26*(47), 12206–12218. http://doi.org/10.1523/JNEUROSCI.2813-06.2006

Ecker, A. S., Berens, P., Cotton, R. J., Subramaniyan, M., Denfield, G. H., Cadwell, C. R., … Tolias, A. S. (2014). State dependence of noise correlations in macaque primary visual cortex. *Neuron*, *82*(1), 235–48. http://doi.org/10.1016/j.neuron.2014.02.006

Fournier, J., Müller, C. M., & Laurent, G. (2015). Looking for the roots of cortical sensory computation in three-layered cortices. *Current Opinion in Neurobiology*, *31*, 119–126. http://doi.org/10.1016/j.conb.2014.09.006

Gautam, S. H., Hoang, T. T., McClanahan, K., Grady, S. K., & Shew, W. L. (2015). Maximizing Sensory Dynamic Range by Tuning the Cortical State to Criticality. *PLoS Computational*

Biology, *11*(12), 1–15. http://doi.org/10.1371/journal.pcbi.1004576

Gentet, L. J., Avermann, M., Matyas, F., Staiger, J. F., & Petersen, C. C. H. (2010). Membrane potential dynamics of GABAergic neurons in the barrel cortex of behaving mice. *Neuron*, *65*(3), 422–35. http://doi.org/10.1016/j.neuron.2010.01.006

Graupner, M., & Reyes, A. D. (2013). Synaptic Input Correlations Leading to Membrane Potential Decorrelation of Spontaneous Activity in Cortex. *Journal of Neuroscience*, *33*(38), 15075–15085. http://doi.org/10.1523/JNEUROSCI.0347-13.2013

Gutnisky, D. A., Beaman, C. B., Lew, S. E., & Dragoi, V. (2016). Spontaneous Fluctuations in Visual Cortical Responses Influence Population Coding Accuracy. *Cerebral Cortex*, bhv312. http://doi.org/10.1093/cercor/bhv312

Haider, B., Duque, A., Hasenstaub, A. R., Yu, Y., & McCormick, D. A. (2007). Enhancement of visual responsiveness by spontaneous local network activity in vivo. *Journal of Neurophysiology*, *97*(6), 4186–202. http://doi.org/10.1152/jn.01114.2006

Haider, B., Schulz, D. P. A., Häusser, M., & Carandini, M. (2016). Millisecond Coupling of Local Field Potentials to Synaptic Currents in the Awake Visual Cortex. *Neuron*, *90*(1), 35–42. http://doi.org/10.1016/j.neuron.2016.02.034

Hirata, A., & Castro-Alamancos, M. A. (2011). Effects of cortical activation on sensory responses in barrel cortex. *Journal of Neurophysiology*, *105*(4), 1495–1505. http://doi.org/10.1152/jn.01085.2010

Hofer, S. B., Ko, H., Pichler, B., Vogelstein, J., Ros, H., Zeng, H., … Mrsic-Flogel, T. D. (2011). Differential connectivity and response dynamics of excitatory and inhibitory neurons in

visual cortex. *Nature Neuroscience*, *14*(8), 1045–52. http://doi.org/10.1038/nn.2876

Keane, A., & Gong, P. (2015). Propagating waves can explain irregular neural dynamics. *J Neurosci*, *35*(4), 1591–1605. http://doi.org/10.1523/jneurosci.1669-14.2015

Kenet, T., Bibitchkov, D., Tsodyks, M., Grinvald, A., & Arieli, A. (2003). Spontaneously emerging cortical representations of visual attributes. *Nature*, *425*(6961), 954–956. http://doi.org/10.1038/nature02078

Luczak, A., Barthó, P., & Harris, K. D. (2009). Spontaneous Events Outline the Realm of Possible Sensory Responses in Neocortical Populations. *Neuron*, *62*(3), 413–425. http://doi.org/10.1016/j.neuron.2009.03.014

MacLean, J. N., Watson, B. O., Aaron, G. B., & Yuste, R. (2005). Internal dynamics determine the cortical response to thalamic stimulation. *Neuron*, *48*(5), 811–823. http://doi.org/10.1016/j.neuron.2005.09.035

Mancilla, J. G., & Ulinski, P. S. (2001). Role of GABA(A)-mediated inhibition in controlling the responses of regular spiking cells in turtle visual cortex. *Visual Neuroscience*, *18*(1), 9–24. Retrieved from http://www.ncbi.nlm.nih.gov/pubmed/11347819

Marchiafava, P. L. (1983). An ``antagonistic'' surround facilitates central responses by retinal ganglion cells. *Vision Research*, *23*(10), 1097–1099. Retrieved from http://www.ncbi.nlm.nih.gov/pubmed/6649427

Markram, H., Wang, Y., & Tsodyks, M. (1998). Differential signaling via the same axon of neocortical pyramidal neurons. *Proc Natl Acad Sci U S A*, *95*(9), 5323–8. http://doi.org/10.1073/pnas.95.9.5323

Mcginley, M. J., David, S. V., & McCormick, D. A. (2015). Cortical Membrane Potential Signature of Optimal States for Sensory Signal Detection. *Neuron*, *87*(1), 179–192. http://doi.org/10.1016/j.neuron.2015.05.038

Naumann, R. K., Ondracek, J. M., Reiter, S., Shein-Idelson, M., Tosches, M. A., Yamawaki, T. M., & Laurent, G. (2015). The reptilian brain. *Current Biology*, *25*(8), R317–R321. http://doi.org/10.1016/j.cub.2015.02.049

Okun, M., Steinmetz, N. a., Cossell, L., Iacaruso, M. F., Ko, H., Barthó, P., … Harris, K. D. (2015). Diverse coupling of neurons to populations in sensory cortex. *Nature*, *521*(7553), 511–515. http://doi.org/10.1038/nature14273

Ollerenshaw, D. R. R., Zheng, H. J. V. J. V, Millard, D. C. C., Wang, Q., & Stanley, G. B. B. (2014). The adaptive trade-off between detection and discrimination in cortical representations and behavior. *Neuron*, *81*(5), 1152–1164. http://doi.org/10.1016/j.neuron.2014.01.025

Panzeri, S., Brunel, N., Logothetis, N. K., & Kayser, C. (2010). Sensory neural codes using multiplexed temporal scales. *Trends in Neurosciences*, *33*(3), 111–120. http://doi.org/10.1016/j.tins.2009.12.001

Paré, D., Shink, E., Gaudreau, H., Destexhe, A., & Lang, E. J. (1998). Impact of spontaneous synaptic activity on the resting properties of cat neocortical pyramidal neurons In vivo. *Journal of Neurophysiology*, *79*(3), 1450–1460.

Petersen, C. C. H., Hahn, T. T. G., Mehta, M., Grinvald, A., & Sakmann, B. (2003). Interaction of sensory responses with spontaneous depolarization in layer 2/3 barrel cortex. *Proceedings of the National Academy of Sciences of the United States of America*, *100*(23),

13638–43. http://doi.org/10.1073/pnas.2235811100

Poulet, J. F. a, & Petersen, C. C. H. (2008). Internal brain state regulates membrane potential synchrony in barrel cortex of behaving mice. *Nature*, *454*(7206), 881–5. http://doi.org/10.1038/nature07150

Poulet, J. F. A., Fernandez, L. M. J., Crochet, S., & Petersen, C. C. H. (2012). Thalamic control of cortical states. *Nature Neuroscience*, *15*(3), 370–372. http://doi.org/10.1038/nn.3035

Rigas, P., & Castro-Alamancos, M. A. (2007). Thalamocortical Up states: differential effects of intrinsic and extrinsic cortical inputs on persistent activity. *The Journal of Neuroscience : The Official Journal of the Society for Neuroscience*, *27*(16), 4261–72. http://doi.org/10.1523/JNEUROSCI.0003-07.2007

Ringach, D. L. (2009). Spontaneous and driven cortical activity: implications for computation. *Current Opinion in Neurobiology*, *19*(4), 439–44. http://doi.org/10.1016/j.conb.2009.07.005

Rudolph, M., & Destexhe, A. (2003). A Fast-Conducting , Stochastic Integrative Mode for Neocortical Neurons In Vivo, *23*(6), 2466–2476.

Rudolph, M., & Destexhe, A. (2003). Characterization of subthreshold voltage fluctuations in neuronal membranes. *Neural Computation*, *15*(11), 2577–618. http://doi.org/10.1162/089976603322385081

Sachdev, R. N. S., Ebner, F. F., & Wilson, C. J. (2004). Effect of subthreshold up and down states on the whisker-evoked response in somatosensory cortex. *Journal of Neurophysiology*, *92*(6), 3511–3521. http://doi.org/10.1152/jn.00347.2004

Sachidhanandam, S., Sreenivasan, V., Kyriakatos, A., Kremer, Y., & Petersen, C. C. H. (2013).

Membrane potential correlates of sensory perception in mouse barrel cortex. *Nature Neuroscience*, *16*(11), 1671–7. http://doi.org/10.1038/nn.3532

Saha, D., Morton, D., Ariel, M., & Wessel, R. (2011). Response properties of visual neurons in the turtle nucleus isthmi. *Journal of Comparative Physiology A*, *197*(2), 153–165. http://doi.org/10.1007/s00359-010-0596-3

Sakata, S., & Harris, K. D. (2009). Laminar Structure of Spontaneous and Sensory-Evoked Population Activity in Auditory Cortex. *Neuron*, *64*(3), 404–418. http://doi.org/10.1016/j.neuron.2009.09.020

Sanchez-Vives, M. V, & McCormick, D. A. (2000). Cellular and network mechanisms of rhythmic recurrent activity in neocortex. *Nature Neuroscience*, *3*(10), 1027–1034. http://doi.org/10.1038/79848

Scholvinck, M. L., Saleem, A. B., Benucci, a., Harris, K. D., & Carandini, M. (2015). Cortical State Determines Global Variability and Correlations in Visual Cortex. *Journal of Neuroscience*, *35*(1), 170–178. http://doi.org/10.1523/JNEUROSCI.4994-13.2015

Sekerli, M., Del Negro, C. A., Lee, R. H., & Butera, R. J. (2004). Estimating action potential thresholds from neuronal time-series: New metrics and evaluation of methodologies. *IEEE Transactions on Biomedical Engineering*, *51*(9), 1665–1672. http://doi.org/10.1109/TBME.2004.827531

Senseman, D. M., & Robbins, K. a. (1999). Modal behavior of cortical neural networks during visual processing. *The Journal of Neuroscience : The Official Journal of the Society for Neuroscience*, *19*(10), RC3. Retrieved from http://www.ncbi.nlm.nih.gov/pubmed/10234049

Shepherd, G. M. (2011). The microcircuit concept applied to cortical evolution: from three-layer to six-layer cortex. *Frontiers in Neuroanatomy*, *5*(May), 30. http://doi.org/10.3389/fnana.2011.00030

Shew, W. L. W. L., Clawson, W. P. W. P., Pobst, J., Karimipanah, Y., Wright, N. C. N. C., & Wessel, R. (2015). Adaptation to sensory input tunes visual cortex to criticality. *Nature Physics*, *11*(8), 659–663. http://doi.org/10.1038/nphys3370

Shew, W. L., Yang, H., Petermann, T., Roy, R., & Plenz, D. (2009). Neuronal Avalanches Imply Maximum Dynamic Range in Cortical Networks at Criticality. *The Journal of Neuroscience : The Official Journal of the Society for Neuroscience*, *29*(49), 15595–15600. http://doi.org/10.1523/JNEUROSCI.3864-09.2009

Shoham, S., O'Connor, D. H., & Segev, R. (2006). How silent is the brain: Is there a "dark matter" problem in neuroscience? *Journal of Comparative Physiology A: Neuroethology, Sensory, Neural, and Behavioral Physiology*, *192*(8), 777–784. http://doi.org/10.1007/s00359-006-0117-6

Steriade, M., Contreras, D., Curró Dossi, R., & Nuñez, A. (1993). The slow (< 1 Hz) oscillation in reticular thalamic and thalamocortical neurons: scenario of sleep rhythm generation in interacting thalamic and neocortical networks. *The Journal of Neuroscience : The Official Journal of the Society for Neuroscience*, *13*(8), 3284–99. Retrieved from http://www.ncbi.nlm.nih.gov/pubmed/8340808

Stevens, C. F., & Zador, a M. (1998). Input synchrony and the irregular firing of cortical neurons. *Nature Neuroscience*, *1*(3), 210–7. http://doi.org/10.1038/659

Tan, A. Y. Y., Chen, Y., Scholl, B., Seidemann, E., & Priebe, N. J. (2014). Sensory stimulation

shifts visual cortex from synchronous to asynchronous states. *Nature*, *509*(7499), 226–229. http://doi.org/10.1038/nature13159

Yang, H., Shew, W. L., Roy, R., & Plenz, D. (2012). Maximal Variability of Phase Synchrony in Cortical Networks with Neuronal Avalanches. *Journal of Neuroscience*, *32*(3), 1061–1072. http://doi.org/10.1523/JNEUROSCI.2771-11.2012

Zheng, H. J. V., Wang, Q., & Stanley, G. B. (2015). Adaptive shaping of cortical response selectivity in the vibrissa pathway. *Journal of Neurophysiology*, *113*(10), 3850–3865. http://doi.org/10.1152/jn.00978.2014

Chapter 4

Adaptation modulates correlated response variability in visual cortex

Cortical sensory responses are highly variable across stimulus presentations. This variability can be correlated across neurons (due to some combination of dense intracortical connectivity, cortical activity level, and cortical state), with fundamental implications for population coding. Yet the interpretation of correlated response variability (or "noise correlation") has remained fraught with difficulty, in part because of the restriction to extracellular neuronal spike recordings. Here, we measured response variability and its correlation at the most microscopic level of electrical neural activity, the membrane potential, by obtaining dual whole-cell recordings from pairs of cortical pyramidal neurons during visual processing. We found that during visual stimulation, correlated variability adapts towards an intermediate level and that this correlation dynamic is mediated by intracortical mechanisms. A model network with external inputs, synaptic depression, and structure reproduced the observed dynamics of correlated variability. These results establish that intracortical adaptation self-organizes cortical circuits towards a balanced regime at which network coordination maintains an intermediate level.

4.1 Introduction

Sensory cortex is not simply one layer in a feedforward network (**Fig. 4.1a**); it receives strong inputs from thalamus, but intracortical feedback dominates cortical circuitry (**Fig. 4.1b**). This tangle of cortical connections causes neural activity to be coordinated across multiple spatial and temporal scales(Ohiorhenuan et al., 2010; Panzeri, Brunel, Logothetis, & Kayser, 2010). Moreover, in a given cortical network, the strength of this coordination can vary with activity level and network state(Doiron, Litwin-Kumar, Rosenbaum, Ocker, & Josić, 2016; Haider, Schulz, & Carandini, 2016; Okun et al., 2015; Poulet & Petersen, 2008; Renart et al., 2010; Scholvinck, Saleem, Benucci, Harris, & Carandini, 2015), which is considered to have implications for cortical function(Averbeck, Latham, & Pouget, 2006; Averbeck & Lee, 2004; Moreno-Bote et al., 2014; Zohary, 1994). For example, weak coordination corresponds to a larger "library" of words available to the spatiotemporal code, while stronger coordination supports signal propagation (**Fig. 4.1c**). The realized level of coordination in active cortical circuits is expected to represent a balance between such competing system needs. Two unanswered questions concerning coordination continue to block our path to understanding sensory processing in cerebral cortex. First, what are the levels of cortical coordination during sensory processing, and to what extent do these levels change with varying stimulus conditions (**Fig. 4.1c**)? Second, what mechanisms are responsible for the realized level of cortical coordination and its changes?

Recording the spike trains from pairs of neurons for repeated presentations of an identical stimulus and evaluating the level of correlated response variability (or "noise correlation") has remained the work horse of investigating cortical coordination (see Cohen, Kohn 2011, and Doiron, Kumar 2016 for reviews). This spike-based approach is popular in part because of the

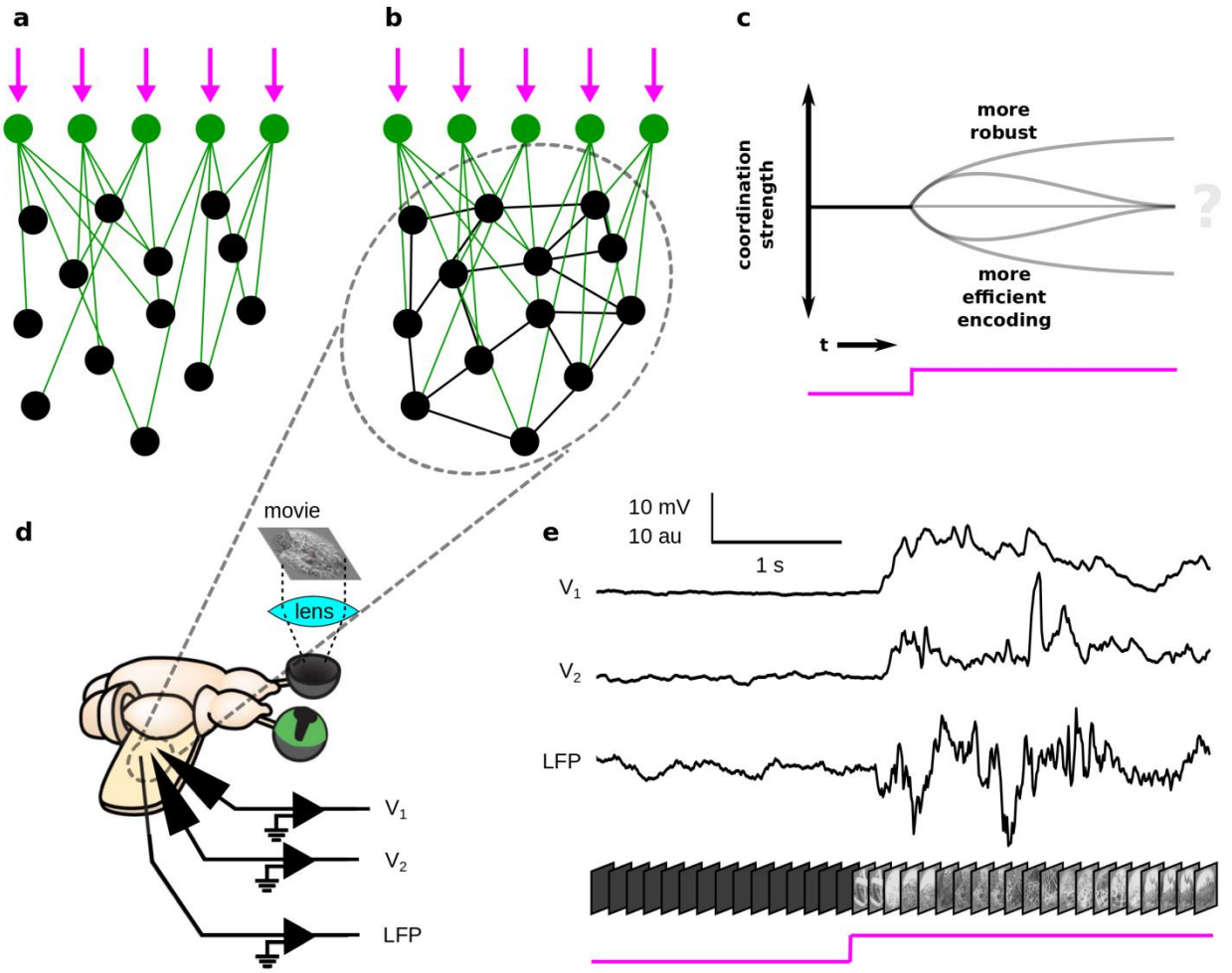

Figure 4.1 Investigating the dynamics of correlated variability in recurrent circuits of visual cortex. (a) Feedforward thalamocortical network subject to sensory inputs (magenta). Coordination between pairs of cortical neurons (black) is determined by convergence patterns in thalamic inputs (green). (b) A more realistic, interaction-dominated thalamocortical network, in which the inputs to any one cortical neuron arise primarily from other cortical neurons. Coordination is thus a function of both feedforward and recurrent inputs. (c) The level of cortical coordination affects cortical function, and it is unknown if and how this changes with sensory stimulation. (d) We simultaneously recorded the membrane potentials from pairs of cells, as well as the nearby LFP, during ongoing and visually-evoked activity in a densely-interconnected thalamocortical network. (e) Pairwise membrane potential recordings provided a measure of cortical coordination across stimulus conditions that avoids the pitfalls of spike data.

relative ease of obtaining spiking responses from pairs of neurons in intact brains. Reported values of spike-based noise correlation tend to be significantly nonzero, but results have varied across studies(Cohen & Kohn, 2011; Doiron et al., 2016; Hansen, Chelaru, & Dragoi, 2012; Scholvinck et al., 2015; Tan, Chen, Scholl, Seidemann, & Priebe, 2014). Furthermore, the interpretation of cortical coordination from spike data is littered with complications, including a spike-rate dependence of noise correlation values(Cohen & Kohn, 2011; de la Rocha, Doiron, Shea-Brown, Josić, & Reyes, 2007), the underrepresentation of sparse-spiking neurons, and possible biases introduced by the spike-sorting process(Cohen & Kohn, 2011; Schulz, Sahani, & Carandini, 2015). In conclusion, the important study of cortical coordination, including its relation to mechanisms and function, has been restricted by its focus on spike recordings, and continues to represent an unmet challenge in systems neuroscience.

In response to this need, we investigated the dynamics of correlated response variability at the level of the membrane potential by obtaining dual whole-cell recordings from pairs of cortical pyramidal neurons during visual processing (**Fig. 4.1d, e**). We found a high level of trial-to-trial membrane potential response variability. Further, correlated variability in the gamma band range of membrane potential fluctuations increased at stimulus onset, but returned to pre-stimulus values during continued visual stimulation. A brief visual stimulus, triggering persistent cortical activity, elicited a similar dynamic of correlated variability, thus implicating an intracortical mechanism. A model network with small-world connectivity, external inputs, and synaptic depression reproduced the observed dynamics of correlated variability, and further indicated that network oscillations play a crucial role. Taken together, these results establish adaptation towards an intermediate level of coordination as a fundamental principle of cortical organization during visual processing.

4.2 Results

To quantify response variability and its correlation across neurons, we recorded the membrane potential (V) from 35 pairs of pyramidal neurons in visual cortex of the turtle *ex vivo* eye-attached whole-brain preparation during visual stimulation of the retina (**Fig. 4.1d**). Ongoing activity in turtle visual cortex was largely quiet. In contrast, visual stimuli evoked barrages of postsynaptic potentials in cortical pyramidal neurons that were accompanied by extensive fluctuations in the nearby local field potential recording (**Fig.1e**), indicating strong concurrent network activity.

4.2.1 Pyramidal neuron membrane potential visual responses are highly variable

We recorded from 19 pairs of pyramidal neurons while presenting continuous visual stimulation, and from 16 pairs while presenting brief flashes (see Methods). Single-neuron membrane potential responses to repeated presentations of extended stimuli varied from trial to trial, with a response variability magnitude that exceeded the trial-averaged mean response (**Fig. 4.2a**). Importantly, the magnitude of the response variability was qualitatively unchanged when the visual stimulus consisted of brief flashes, which evoked long-lasting responses in visual cortex (**Fig. 4.2b**). This stimulus invariance of the trial-to-trial response variability indicates an intra-thalamocortical origin of the network activity and the resulting membrane potential fluctuations.

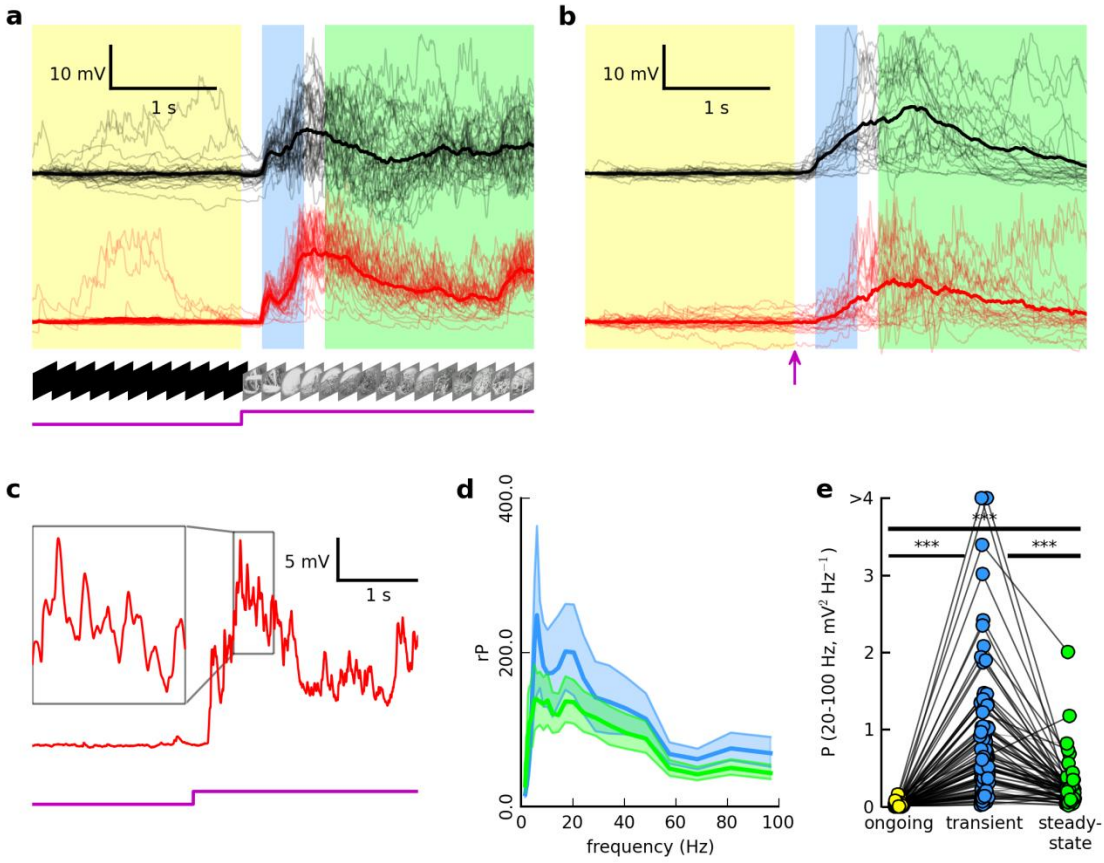

Figure 4.2 Dynamics and complexity of trial-to-trial response variability. (a) Single-trial responses (low opacity) and across-trial average responses (high opacity) for two simultaneously-recorded neurons. Stimulus is naturalistic movie (see Methods). Single trials artificially aligned for clarity. (b) Same as in (a), but for a different pair of cells, and stimulus is 150 ms red (640 nm) whole-field flash, with onset at magenta arrow, (see Methods). (c) Single-trial response from cell in (a). Inset: high-frequency activity nested within the broader depolarization. (d) Average relative power spectrum (evoked power divided by ongoing) of residuals for red traces in (a) for the transient (blue) and steady-state (green) epochs. Shaded regions indicate +/- 95% confidence intervals by bootstrapping method. (e) Trial-averaged gamma (20 – 100 Hz) power for 79 cells, for brief and extended visual stimulation. Each dot represents the across-trial average gamma power for one cell for that epoch. Dark (light) lines connecting dots represent (in)significant changes in gamma power for that cell across epochs. Across-epoch significance for each cell determined by comparing bootstrap intervals. Asterisks above line connecting two epochs indicates results of Wilcoxon signed-rank significance test for difference in populations of values for those epochs (**: $0.001 < P < 0.01$; ***: $P < 0.001$; no asterisk and gray line: $P > 0.05$). Two outliers truncated for clarity.

For any given trial of visual stimulation, the evoked membrane potential fluctuations were large and consisted of high-frequency fluctuations nested within broader deflections (**Fig. 4.2c**). To quantify the frequency content of the single-trial fluctuations from the mean response, we first calculated the membrane potential residual (V_r), which is the single-trial membrane potential recording from which the trial-averaged membrane potential time series has been subtracted. We then divided the evoked residuals into two analysis windows: the transient (200 to 600 ms after stimulus onset) and steady-state (800 to 2800 ms after stimulus onset) windows (**Supplementary Information 1**). Finally, we calculated the relative power spectral density (rP), which is the power spectral density of the membrane potential residual for the transient or

steady-state window divided by its trial-averaged counterpart from the ongoing window (2 s prior to stimulus onset).

This analysis revealed four important features concerning the spectral content of the residual membrane potential fluctuations and of the trial-to-trial response variability. First, evoked power of residual membrane potential fluctuations in the 0.1 to 100 Hz range typically increased by two orders of magnitude compared to ongoing activity (**Fig. 4.2d, Supplementary Fig. 4.2**). Second, the frequency content of the membrane potential residual varied across trials (as indicated by the broad confidence bands in **Fig. 4.2d**). Third, the relative power spectral density typically consisted of a prominent peak located approximately in the 4 to 10 Hz theta range and a broader, but distinct, distribution in the 20 to 100 Hz gamma range. Fourth, for both movies and flashes, gamma power increased from the ongoing to the transient window, and significantly decreased from transient to steady-state (**Fig. 4.2e**). Gamma power of the transient activity varied drastically across cells.

Together, these data establish that cortical pyramidal neuron membrane potential visual responses (i) have complex temporal dynamics, (ii) are highly variable from trial to trial, and (iii) differ from neuron to neuron (**Fig. 4.2**).

4.2.2 Correlated variability adapts during visual stimulation

The complex and extensive variability of membrane potential visual responses (**Fig. 4.2**) and the interconnected nature of cortical circuits (**Fig. 4.1b**) raised the question to what extent the response variability is correlated across pyramidal neurons. To address this question, we calculated the Pearson correlation coefficient between residual membrane potential fluctuations for each trial and window of interest, i.e., the ongoing, transient, and steady-state windows. We focused on gamma-band (20 – 100 Hz) activity, which captures the fast, nested membrane potential fluctuations (**Fig. 4.2c, inset, Fig. 4.3a**, and see **Supplementary Information 2**). This band of activity is thought to be associated with narrow "windows of opportunity" for spiking, determining the precise timing of spikes within a broader depolarization (see Haider, McCormick, 2009 for a review). Trial-averaged correlation coefficients (CC) for ongoing activity were broadly distributed across pairs of pyramidal neurons (**Fig. 4.3b**), and the population average (<CC>) was significantly nonzero (<CC> = 0.03, P = 0.006, one-sided t-test). In response to continuous visual stimulation, trial-averaged correlation coefficients increased significantly compared to ongoing values (**Fig. 4.3b**), to an elevated population average of <CC> = 0.11 ($P = 2.9 \times 10^{-4}$ for ongoing – transient comparison, Wilcoxon signed-rank test). In the steady-state period, i.e., during continued stimulus presentation, trial-averaged correlation coefficients returned to near-ongoing values (<CC> = 0.041, $P = 1.6 \times 10^{-4}$ for transient – steady-state comparison, P > 0.05 for ongoing – steady-state comparison).

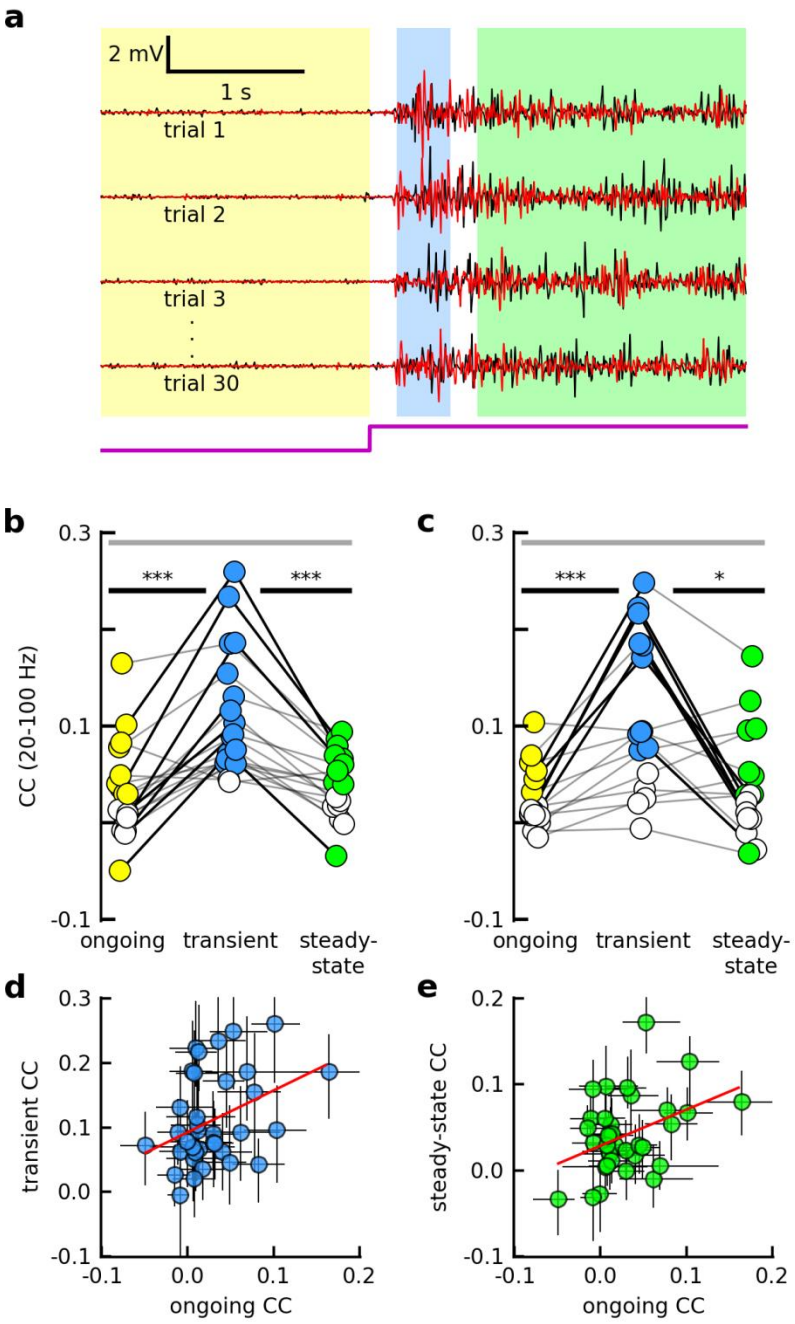

state epoch (r^2 = 0.15, P = 0.02).

Figure 4.3 Evoked gamma band correlated variability appeared to be modulated by internal mechanisms. (a) Examples of gamma band (20 – 100 Hz) residual membrane potential pairs for several trials (same pair as in 2a). (b) Trial-averaged CC values for each of 19 pairs, 20 – 100 Hz, continuous visual stimulation (see Methods). Each dot represents the across-trial average CC value for one pair for that epoch. Colored (white) dots represent values (not) significantly different from zero (one-sided t-test). Otherwise, same as in 2e. (c) Same as in (b), but for 16 pairs, and brief visual stimulation (see Methods). (d) Across-trial average transient CC vs. average ongoing CC for each pair, for all stimuli. Error bars indicate 95% confidence intervals by bootstrapping method. Red line indicates significant linear regression fit (r^2 = 0.14, P = 0.026). (e) Same as (d), but for steady-

These results were largely robust with respect to choices of window sizes and gaps between windows (see **Supplementary Information 1** and **Supplementary Fig. 4.1**). These changes in correlated variability primarily reflected changes in phase synchrony in the gamma band residual activity of simultaneously-recorded neurons (see **Supplementary Information 3** and **Supplementary Fig. 4.4**). In contrast, low-frequency (0.1 – 20 Hz) CC values followed a different dynamic (**Supplementary Fig. 4.3a, b**) and were not significantly related to gamma-band CC (see **Supplementary Information 2** and **Supplementary Fig. 4.3c - e**).

The observed dynamics of gamma band correlated variability in response to continuous visual stimulation could be imposed by the spatiotemporal structure of the stimulus, or alternatively, could be intrinsic to the thalamocortical system. To distinguish between these two hypotheses, we recorded from 16 pyramidal neuron pairs while presenting brief flashes (1 ms – 200 ms) of light, which evoked responses lasting several seconds in the visual cortex (**Fig. 4.2b**). We found that across the population of all pairs, CC values for responses to brief stimuli were not significantly different from those for continuous stimuli ($p > 0.05$, Wilcoxon rank-sum test, for all epochs, see **Supplementary Information 4**, and **Supplementary Fig. 4.5**). Importantly, the same dynamics of correlated variability were observed for brief stimuli ($\langle CC \rangle = 0.03$, $P = 0.003$ ongoing, $\langle CC \rangle = 0.11$, $P = 3.0 \times 10^{-5}$ transient, $\langle CC \rangle = 0.041$, $P = 0.006$ steady-state, one-sided t-test; $P = 6.4 \times 10^{-4}$ for ongoing – transient comparison, $P = 0.020$ transient – steady-state comparison, $P > 0.05$ ongoing – steady-state comparison, Wilcoxon signed-rank test, **Fig. 4.3c**). The similarity of the dynamics of correlated variability for brief and continuous stimuli implicates a mechanism that is stimulus-invariant and likely to be intracortical in origin.

The evidence of an intracortical origin of correlated variability suggested to us that the correlated variability of ongoing activity for a given pair should be predictive of its correlated variability in response to visual stimulation. Indeed, we found that CC values during the ongoing epoch were significantly related to CC values for both evoked epochs (r = 0.38, P = 0.03, transient vs. ongoing, **Fig. 4.3d**; r = 0.39, P = 0.02, steady-state vs. ongoing, **Fig. 4.3e**, Pearson correlation). This observation suggests a close link between the underlying mechanisms that determine ongoing and evoked correlated variability, with connectivity being one candidate mechanism(Luczak, Barthó, & Harris, 2009; MacLean, Watson, Aaron, & Yuste, 2005).

4.2.3 Correlated variability is related to the network state

Recent experimental and computational work suggests that the level of coordination between pairs of neurons might be shaped not only by anatomical connectivity, but also by network activity level and network state(Doiron et al., 2016; Haider et al., 2016; Okun et al., 2015; Poulet & Petersen, 2008; Renart et al., 2010; Scholvinck et al., 2015). We therefore asked how well network activity level and/or network state could explain the observed dynamics of correlated variability.

As a proxy for network activity level, we inferred the level of presynaptic spiking activity using the average gamma power in residual membrane potentials. As a population, the gamma power dynamic (**Fig. 4.2e**) was qualitatively similar to that of CC (**Fig. 4.3b, c**). In contrast, for a given pair of cells, the geometric mean of the absolute change in power ($\sqrt{|\Delta P_1 \Delta P_2|}$) was not related to the magnitude of the change in CC amplitude for the ongoing – to – transient transition (r = 0.28, P = 0.10, Pearson correlation). The two quantities were however related for the transient – to – steady-state transition (r = 0.40, P = 0.017, Pearson correlation) (**Fig. 4.4b**). In conclusion,

changes in network activity levels alone did not fully explain the changes in gamma band correlated variability.

Next, we sought a measure of the network state. Specifically, we focused on the degree of action potential synchrony as an indicator of network state. Computational work has shown that synchronous network spiking can generate prominent subthreshold membrane potential fluctuations in a narrow frequency band (Brunel & Wang, 2003). Here, we used a measure of power spectrum "peakiness" in the 20 to 100 Hz range as a proxy for synchronous network spiking. The residual relative power spectra (rP) of some cells tended to contain peaks in the gamma band during the transient epoch, which were often smaller or absent in the steady-state (**Fig. 4.2d**, **Supplementary Fig. 4.2**). To quantify this aspect of the power spectrum for each cell and epoch, we defined the quantity M as the ratio of the maximum relative power in the gamma range (rP_{max}) to the average relative gamma power (rP_{avg}) (**Fig. 4.4b, top**). Across the population of cells, M varied continuously, and the population average (<M>) decreased significantly from transient to steady-state (<M> = 1.65 transient, <M> = 1.54 steady-state, $P = 2.2 \times 10^{-4}$ for transient – steady-state comparison) (**Fig. 4.4b, bottom**). For the population of pairs, we found that the geometric mean of the absolute change in M ($\sqrt{|\Delta M_1 \Delta M_2|}$) was significantly related to the amplitude of the change in CC (r = 0.40, P = 0.02 ongoing – to – transient; r = 0.41, P = 0.01 transient – to – steady-state, Pearson correlation, where $\Delta M = M_{trans} - 1$ for the ongoing – transient transition) (**Fig. 4.4c**). In conclusion, for a given pair of cells, the change in network state, measured as a change in gamma spectrum "peakiness", was an indicator of the change in correlated variability.

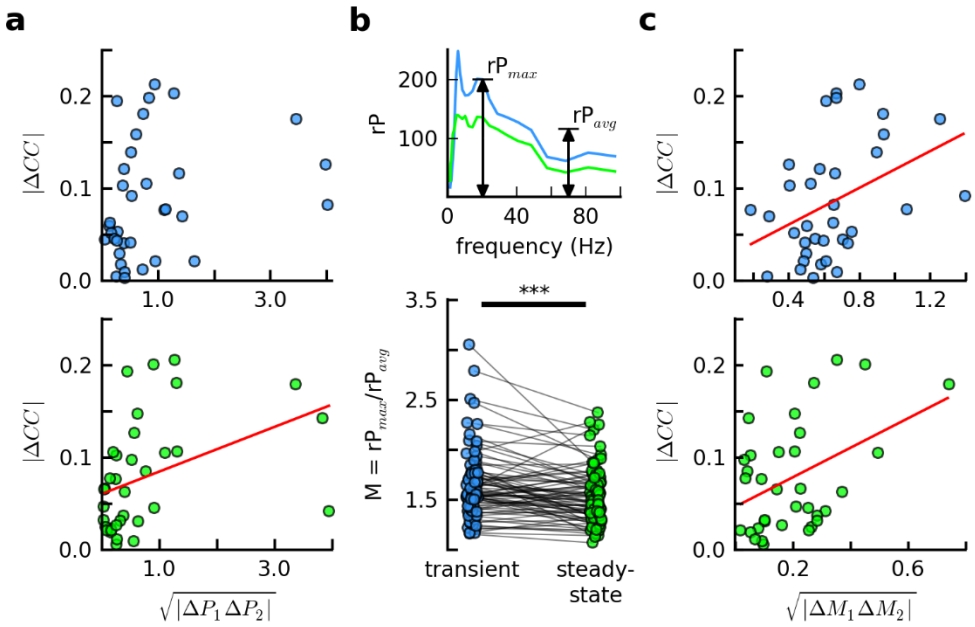

Figure 4.4 Changes in CC are related to changes in the shape of relative power spectra. (a) Absolute value of change in CC (evoked minus ongoing) vs. absolute value of geometric mean of change in gamma power, for each pair, for transient (top), and steady-state (bottom) epochs. (b) Top: same as in 2(d), but confidence bands omitted for clarity. For each cell, the peak power index (M), is defined as the maximum relative power value in the gamma range (rP_{max}), divided by the average over the gamma range (rP_{avg}). Bottom: M for all recorded cells (brief and continuous stimulation), for transient (blue) and steady-state (green) epochs. (c) Same as in (a), but for absolute value of geometric mean of change in M, for all cells. If present, red lines indicate significant linear regression fit ($P < 0.05$).

4.2.4 Synaptic time constants, synaptic depression, and synaptic clustering together mediate the dynamics of correlated variability

What biophysical mechanisms could mediate the experimentally-observed response properties (i.e., across-trial variability (**Fig. 4.2a, b**), subthreshold gamma oscillations (**Fig. 4.2c, 3a**), the dynamics of correlated variability (**Fig. 4.3**) and its network state dependence (**Fig. 4.4**))? To address this question, we investigated a model network (Methods) of 800 excitatory and 200 inhibitory leaky integrate-and-fire neurons, with Poisson process external inputs to all excitatory neurons (**Fig. 4.5a**). Excitatory-to-excitatory and excitatory-to-inhibitory connections had small-world connectivity, with 5% connection probability. Inhibitory-to-inhibitory and inhibitory-to-excitatory synapses were random, with 20% connection probability. An increase in the external input rate mimicked the stimulus. We selected a set of synaptic rise and decay times(Brunel & Wang, 2003; X.-J. J. Wang, 2010) that were consistent with gamma oscillations in the instantaneous network firing rate when the network was subject to strong external drive. Motivated by previous experiments(Chung, Li, & Nelson, 2002) and models(Levina, Herrmann, & Geisel, 2007), we implemented adaptation via short-term synaptic depression with recovery (Methods). Armed with this battery of mechanisms and structural complexity, we simulated the network spiking in response to repeated stimulus presentations (20 trials).

The model network reproduced the experimentally-observed response variability and gamma oscillations. The simulated membrane potentials from randomly-selected excitatory model neurons revealed fluctuations and across-trial response variability (**Fig. 4.5b**) that were qualitatively similar to what we observed from recorded membrane potentials of pyramidal neurons (**Fig. 4.2a, b**). Furthermore, the gamma band residuals of simulated membrane potentials

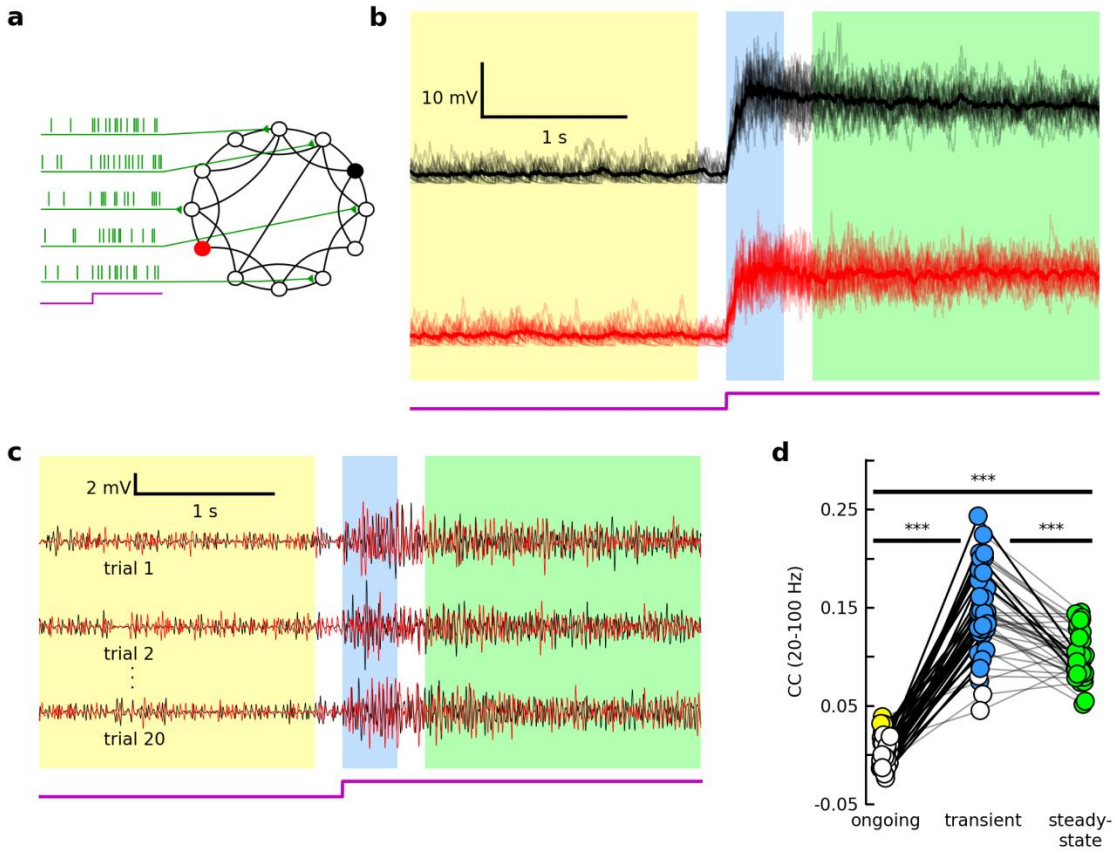

Figure 4.5 A model network strengthens the "internal mechanism" hypothesis, suggesting crucial roles for network oscillations. (a) The model network was composed of 800 excitatory LIF neurons with small-world connectivity, and 200 randomly-connected inhibitory LIF neurons (not depicted). All excitatory neurons received Poisson external inputs, and the stimulus was modeled as a gradual increase in the external input rate (see Methods). (b – c) Same as in **Fig. 4.3b**, **c**, but two excitatory model neurons randomly-selected from the network (see Methods). (d) Same as in **Fig. 4.3d**, but for forty pairs of excitatory neurons, generated from twenty neurons randomly-selected from the network.

(**Fig. 4.5c**) largely resembled the experimentally-observed residual subthreshold gamma oscillations (**Fig. 4.3a**). Residual power spectra were peaked in the gamma range (**Supplementary Fig. 4.6a, top**), at frequencies that coincided with peaks in the spectra of the instantaneous network firing rate (**Supplementary Fig. 4.6a, bottom**). Due to synaptic depression with slow recovery, the model also reproduced the eventual decrease in the total gamma power in membrane potential residuals (**Supplementary Fig. 4.6b**), and in the amplitudes of gamma-band peaks in the residual membrane potential and population spike rate spectra (**Supplementary Fig. 4.6a**).

In addition, the model network reproduced the experimentally-observed dynamics of correlated variability. The simulated correlated variability increased significantly from ongoing to transient (<CC> = 0.003 ongoing, 0.146 transient, $P = 3.6 \times 10^{-8}$ for ongoing – transient comparison) (**Fig. 4.5d**), a trend that was consistent with our experimental results (**Fig. 4.3b, c**). Mediated by synaptic depression, correlated variability decreased significantly from transient to steady state (<CC> = 0.10 steady-state, $P = 1.49 \times 10^{-6}$ for transient – steady-state comparison, $P = 3.6 \times 10^{-8}$ for ongoing – steady-state comparison) (**Fig. 4.5d**). In contrast, when synaptic depression was absent, correlated variability increased from transient to steady state (**Supplementary Fig. 4.7a**).

As observed in experiment, this dynamic of correlated variability depended crucially on network activity oscillations. When synaptic time constants for excitation and inhibition were chosen to be identical (see **Methods** and **Supplementary Information 5**), the stimulus instead pushed the network into a regime of asynchronous activity, as evidenced by the population spike-rate and residual membrane potential power spectra (**Supplementary Fig. 4.6c**). This had little effect on the overall network activity level and gamma power dynamics (**Supplementary Fig. 4.6d**). Correlated variability, however, was very weakly modulated by the stimulus

(**Supplementary Fig. 4.7b**), in contrast with our experimental results (**Fig. 4.3b, c**). This dependence on network oscillations had a synaptic basis: in the synchronous model network, not only were correlations between synaptic conductances stronger than those in the asynchronous network, the lag between excitation and inhibition was larger, allowing for a longer temporal window in which synaptic input correlations could be manifested in pairs of membrane potentials(Doiron et al., 2016; Renart et al., 2010) (**Supplementary Fig. 4.8**). In conclusion, changes in network oscillations, rather than network activity levels alone, determine the changes in correlated variability.

The network oscillation dynamic described here is not the only one capable of reproducing the experimentally-observed dynamic of correlated variability. For example, a similar randomly-connected network generates oscillations that either invade the entire network or are absent, and the CC dynamic can be reproduced by abolishing the oscillation early in the transient window via strong synaptic depression (data not shown). This oscillation dynamic is inconsistent with the experimental results, in which gamma oscillations were strongest during the transient epoch, but persisted in the steady-state (**Fig. 4.3a, 4a, Supplementary Fig. 4.4a**). In contrast, the small-world network reproduces the correct network oscillation temporal dynamics (**Fig. 4.5c**, **Supplementary Fig. 4.6a, bottom, 9a**). Furthermore, the spatial arrangement of connections introduced by the small-world architecture adds a spatial dimension to the dynamics of network activity (see **Supplementary Information 5**, **Supplementary Fig. 4.9a**). Soon after stimulus onset, when synaptic connections are near their default strength, oscillatory spiking is largely coherent across the network of excitatory neurons. However, because of synaptic depression and the distance-dependence of connections, the network dynamically subdivides, and coherent oscillations proceed among spatially separate groups of neurons in the steady-state. This

spatiotemporal dynamic predicts a dependence of CC temporal dynamics on distance between neurons (**Supplementary Fig. 4.9b, c**).

Taken together, these results strengthen the hypothesis that the experimentally-observed dynamics of correlated variability are primarily driven by the dynamics of thalamocortical network oscillations. As such, synaptic time constants and synaptic depression are two intrinsic parameters relevant to correlated variability. Constraining the model to also produce a realistic network oscillation temporal dynamic reveals an additional role for synaptic clustering.

4.3 Discussion

To study how cortical coordination evolves during visual processing, we measured correlated variability between the membrane potentials of pyramidal neuron pairs in turtle visual cortex during ongoing and visually-evoked activity. This approach provides an exceedingly rare and much-needed view into the subthreshold events underlying coordinated spiking activity(Doiron et al., 2016), and importantly, is uncorrupted by issues associated with spike-based investigations. For example, the process for targeting cells for recording is agnostic to the cells' spike rates, and this study thus gives voice to the "dark" neurons that overwhelmingly populate the cortex(Shoham, O'Connor, & Segev, 2006), but are rarely represented in the vast literature on correlated variability. By supplementing our experimental approach with a model network investigation, we further addressed the relative contribution of the thalamocortical network to the dynamics of correlated variability, and identified relevant network variables.

We found that both continuous and brief visual stimulation evoked large, low-frequency membrane potential fluctuations (**Fig. 4.1e**), with nested gamma-band (20 – 100 Hz) oscillations

(**Fig. 4.2c, 3a**), both of which varied significantly from trial to trial (**Fig. 4.2a, b, 3a**). This gamma-band variability was significantly correlated across the population of pairs in a given window of activity (**Fig. 4.2b, c**). It is reasonable to ask whether this is at all relevant to sensory processing, given that cortical neurons transmit spikes, and not subthreshold fluctuations. Previous work suggests it is. First, the fluctuations themselves are important for interpreting spiking activity in networks of sparse-spiking neurons; subthreshold gamma oscillations define narrow windows in which a given neuron is most likely to fire, and thus determine precise spike timing(Haider & McCormick, 2009; Yu & Ferster, 2010). Second, the across-trial variability of these fluctuations constrains that of the spiking activity(Carandini, 2004); spiking responses can be no more reliable than the corresponding subthreshold activity. Finally, if and when neurons do spike in this visually-evoked "high conductance" state, the spike correlations will be shaped by state-induced changes in response gain, distance from threshold, and subthreshold correlations(Doiron et al., 2016). In fact, this last relationship may be supralinear(Lyamzin et al., 2015), meaning that small changes in subthreshold correlated variability can have major repercussions for supra-threshold coordination.

What determines the strength of correlations in these single-trial deviations for a given pair of neurons? Anatomical connectivity is one obvious candidate, but what are the relative contributions from feedforward and recurrent connections (**Fig. 4.1b**)? Recent work has shown that the coupling of the spiking activity of a neuron with that of the population is stimulus-invariant(Okun et al., 2015; Scholvinck et al., 2015), suggesting a crucial role for intracortical connectivity. In agreement with this, we found that gamma band correlated variability for ongoing and evoked activity was significantly related, for both the non-adapted (transient, **Fig. 4.2e**) and adapted (steady-state, **Fig. 4.2f**) conditions. In addition, although all pairs of neurons were

separated by less than 300 microns, and therefore likely received similar sensory inputs(Mulligan & Ulinski, 1990), correlated variability was broadly-distributed across the population during a given window of activity (**Fig. 4.3b, c**). This variability suggests that the sparse connectivity of the cortex dramatically affects the distribution of pairwise correlations(Renart et al., 2010). Indeed, alternate network models with higher connectivity were unable to reproduce this variability (data not shown).

Connectivity was not the only relevant parameter; for most pairs of neurons, and for the population as a whole, gamma band correlated variability increased with visual stimulation, but then relaxed to near ongoing values, despite persistent activity (**Fig. 4.2**). That is, for a given network (i.e., an anatomical arrangement of feedforward and recurrent connections), the level of coordination was not static. This was true for responses to both continuous and brief stimulation (**Fig. 4.3b, c**) suggesting the dynamic did not simply reflect a change in the statistics of the sensory inputs. Previous experimental work implicates the cortical state: coordination in spiking activity(Okun et al., 2015; Scholvinck et al., 2015), synaptic inputs(Atallah & Scanziani, 2009; Haider et al., 2016), and membrane potentials(Yu & Ferster, 2010) appear to be related to network synchrony. Accordingly, we found ample experimental and computational evidence implicating an evolving network state. Specifically, changes in correlated variability across epochs were related to changes in properties of membrane potential power spectra (**Fig. 4.4b, c**), and reflected a phase synchrony dynamic (**Supplementary Fig. 4.4**) consistent with a network adapting from a "disinhibited" to a "balanced" state(Yang, Shew, Roy, & Plenz, 2012). In addition, the model revealed a strong relationship between network spike-rate oscillations and gamma-band correlated variability (**Supplementary Information 5**), and also demonstrated the synaptic basis: synaptic current correlations and the lag between excitation and inhibition are larger for pairs of neurons in

a synchronous network than for those in an asynchronous network (**Supplementary Information 5**, **Supplementary Fig. 4.8**). As such, our experimental results relating correlated variability to network state are in simultaneous agreement with multiple experimental studies of cortical activity across a variety of preparations and spatial scales, and importantly, demonstrate this principle in action at the level of the membrane potential during sensory processing. Moreover, our model results confirm computational predictions relating synaptic current dynamics to membrane potential correlations(Doiron et al., 2016; Renart et al., 2010), and extend previous work by demonstrating the effects of synaptic clustering and adaptation.

Gamma band correlated variability decreased from transient to steady-state, yet remained significantly nonzero (**Fig. 4.2d, 3c**). While vanishingly-small values would theoretically support greater response fidelity(Zohary, 1994), this realized steady-state value may reflect the level of neuronal interaction necessary for cortical function (e.g., feature binding(Finger & König, 2014), effective signal propagation(Litwin-Kumar, Oswald, Urban, & Doiron, 2011), and general cognitive function(Womelsdorf et al., 2007)). In other words, cortical coordination during sensory processing is maintained at an intermediate level (i.e., less than that during the initial response phase, but larger than zero) that represents the ideal balance between competing cortical needs (**Fig. 4.1c**). This balanced state can be maintained across stimulus conditions by intrinsic adaptation mechanisms.

Previous studies have described a stimulus-induced abolition of low-frequency correlated variability in membrane potential(Yu & Ferster, 2010) and membrane potential – LFP(Tan et al., 2014) pairs in visual cortex. We observed no such decrease (**Supplementary Fig. 4.3a, b**). This discrepancy may be partially explained by the nature of ongoing activity. In these previous studies, visual stimulation interrupted large-amplitude, low-frequency events that were coherent across

electrodes and had random phase relative to stimulus onset. These fluctuations largely remained in residual traces, likely influencing pre-stimulus correlated variability. In contrast, these spontaneous "bursts" of activity occurred relatively infrequently in our experiments (**Fig. 4.1e, 2a, b**). To reproduce this quiescent – to – active sensory-evoked dynamic, we limited the inputs to our model neurons to those from external stimulation, and stimulus-triggered, yet internally-generated events. Our model could likely be modified to reproduce the results of these other works by adding a shared background fluctuation(Doiron et al., 2016). This brute-force implementation would not be very illuminating, however; spontaneous events can be strikingly similar to evoked(Luczak et al., 2009; MacLean et al., 2005; Ringach, 2009), and may therefore represent activity in the same microcircuits, triggered by events usually hidden from the experimenter. Reproducing spontaneous events in a manner that is consistent with their possible sources is beyond the scope of this study.

Here, we have focused on fundamental properties of the cortex (anatomical and emergent) that are likely to strongly influence correlated variability. Future work can more definitively assess the relative contributions to cortical coordination from various intracortical and extracortical sources not addressed here, such as strong inhibitory feedback(Bernacchia & Wang, 2013; Tetzlaff, Helias, Einevoll, & Diesmann, 2012), thalamic adaptation(Ollerenshaw, Zheng, Millard, Wang, & Stanley, 2014; Q. Wang, Webber, & Stanley, 2010), unequal adaptation of excitatory and inhibitory cortical synapses(Heiss, Katz, Ganmor, & Lampl, 2008), and the (time-varying) statistics of neuronal activity in the early visual pathway (e.g., correlations across thalamic inputs(Bujan, Aertsen, & Kumar, 2015; Whitmire, Waiblinger, Schwarz, & Stanley, 2016)), to name a few. Of particular interest are top-down influences (e.g., attention), which have been shown to impact spike-count correlations in awake, behaving preparations(Cohen & Maunsell,

2009; Ruff & Cohen, 2014). Our results predict that such higher-order inputs may impact correlated variability by influencing the network state. It will be interesting to test this hypothesis, and to determine the synaptic basis of the interaction if confirmed. Further, it is crucial to test for a relationship between subthreshold correlated variability and psychophysical performance, which will require a behavioral assay. As dual whole-cell recordings in awake, behaving preparations (possibly combined with other recording modalities across multiple areas) become increasingly common, future experiments can be designed to address these exciting questions.

4.4 Methods

4.4.1 Surgery

All procedures were approved by Washington University's Institutional Animal Care and Use Committees and conform to the guidelines of the National Institutes of Health on the Care and Use of Laboratory Animals. Sixteen adult red-eared sliders (*Trachemys scripta elegans*, 150-1000 g) were used for this study. Turtles were anesthetized with Propofol (2mg Propofol/kg), then decapitated. Dissection proceeded as described before(Crockett, Wright, Thornquist, Ariel, & Wessel, 2015; Saha, Morton, Ariel, & Wessel, 2011). In brief, immediately after decapitation, the brain was excised from the skull, with right eye intact, and bathed in cold extracellular saline (in mM, 85 NaCl, 2 KCl, 2 $MgCl_2$*$6H_2O$, 20 Dextrose, 3 $CaCl_2$-$2H_2O$, 45 $NaHCO_3$). The dura was removed from the left cortex and right optic nerve, and the right eye hemisected to expose the retina. The rostral tip of the olfactory bulb was removed, exposing the ventricle that spans the olfactory bulb and cortex. A cut was made along the midline from the rostral end of the remaining olfactory bulb to the caudal end of the cortex. The preparation was then transferred to a perfusing chamber (Warner RC-27LD recording chamber mounted to PM-7D platform), and placed directly

on a glass coverslip surrounded by Sylgard. A final cut was made to the cortex (orthogonal to the previous and stopping short of the border between medial and lateral cortex) allowing the cortex to be pinned flat, with ventricular surface exposed. Multiple perfusion lines delivered extracellular saline, adjusted to pH 7.4 at room temperature, to the brain and retina in the recording chamber.

4.4.2 Intracellular Recordings

For whole-cell current clamp recordings, patch pipettes (4-8 MΩ) were pulled from borosilicate glass and filled with a standard electrode solution (in mM; 124 $KMeSO_4$, 2.3 $CaCl_2$-$2H_2O$, 1.2 $MgCl_2$, 10 HEPES, 5 EGTA) adjusted to pH 7.4 at room temperature. Cells were targeted for patching using a dual interference contrast microscope (Olympus). Simultaneously recorded cells were located less than 300 microns apart, and all cells were located within 300 microns of an extracellular recording electrode. Intracellular activity was collected using an Axoclamp 900A amplifier, digitized by a data acquisition panel (National Instruments PCIe-6321), and recorded using a custom Labview program (National Instruments), sampling at 10 kHz. We excluded cells that did not display stable resting membrane potentials. The visual cortex was targeted as described below.

4.4.3 Extracellular Recordings

Extracellular recordings were achieved with tungsten microelectrodes (MicroProbes heat treated tapered tip), with approximately 0.5 MΩ impedance. Electrodes were slowly advanced through tissue under visual guidance using a manipulator (Narishige), while monitoring for activity using custom acquisition software (National Instruments). Extracellular activity was collected using an A-M Systems Model 1800 amplifier, band-pass filtered between 1 Hz and 20,000 Hz,

digitized (NI PCIe-6231), and recorded using custom software (National Instruments), sampling at 10 kHz.

4.4.4 Identification of Visual Cortex

We used a phenomenological approach to identify the visual cortex, described previously(Shew et al., 2015). In general, this region was centered on the anterior lateral cortex, in agreement with voltage-sensitive dye studies(D M Senseman & Robbins, 1999; David M Senseman & Robbins, 2002). Anatomical studies identify this as a region of cortex receiving projections from lateral geniculate nucleus(Mulligan & Ulinski, 1990).

4.4.5 Visual Stimulation

Whole-field flashes were presented using either a red LED (Kingbright, 640nm), mounted to a manipulator and positioned 1 – 5 cm above the retina, or a projector-lens system (described below). The mean LED light intensity (irradiance) at the retina was 60 W/m^2. For one turtle, we used these same LEDs in conjunction with 200 micron optical fibers (Edmund Optics) to project sub-field flashes (1 ms – 200 ms) onto the visual streak. Other stimuli were presented using a projector (Aaxa Technologies, P4X Pico Projector), combined with a system of lenses (Edmund Optics) to project images generated by a custom software package directly onto the retina. The mean irradiance at the retina was 1 W/m^2. This system was used to present brief (100 ms – 250 ms) whole-field and sub-field flashes (red or white), sustained (10 s) gray screen, a naturalistic movie ("catcam"), a motion-enhanced movie (courtesy Jack Gallant), and a phase-shuffled version of the same movie (courtesy Jack Gallant and Woodrow Shew). In all cases, the stimulus was triggered using a custom Labview program (National Instruments).

The preparation was in complete darkness before and after each stimulus presentation. Flashes lasted between 1 ms and 150 ms, with at least 20 s between flashes. Movies lasted either 10 s or 20 s, and were shown at least 12 times, with at least 30 s between the end of one presentation and the beginning of the next.

We presented continuous visual stimuli (movies) while recording from 19 pairs, and brief stimuli (diffuse flashes) while recording from 16 pairs.

4.4.6 Signal Processing

In all analyses, only cells with 12 or more visual stimulation trials were included. Raw data traces were down-sampled to 1000 Hz. Because action potentials in turtle cortical pyramidal neurons are relatively wide, spike waveforms still contributed to the band-pass filtered intracellular recordings. To remove these, an algorithm was used to detect spikes, and the membrane potential values in a 20 ms window centered on the maximum of each spike were replaced via interpolation. Finally, the traces were filtered (20 Hz lowpass or 20 – 100 Hz bandpass Butterworth filter).

4.4.7 Cross-correlation Analysis

For each single-trial voltage trace, the residual (V_r or deviation from the average activity) was found by subtracting the across-trial average time series from the single-trial time series:

$$V_r = V - \langle V \rangle_{trials}$$

Residuals were then separated into three epochs: the ongoing epoch (defined to be the two seconds prior to the onset of visual stimulation), the transient epoch (200 to 600 ms after stimulus onset),

and the steady-state epoch (800 to 2800 ms after stimulus onset; **Fig. 4.2a**). For each pair of simultaneously-recorded cells, the Pearson correlation between residual pairs was then calculated for each epoch and trial. The results were averaged across all trials, resulting in the trial-averaged correlated variability (CC) for each pair and epoch:

$$CC^{epoch} = \langle cov(V_{r,1}^{epoch}, V_{r,2}^{epoch}) / [var(V_{r,1}^{epoch}) var(V_{r,2}^{epoch})]^{1/2} \rangle_{trials}$$

Because the correlated variability of spike counts been shown to depend on the size of the window used for calculations(Schulz et al., 2015), we repeated the above process for three other sets of choices for epoch window sizes and gaps between epochs (see **Supplementary Information 1**).

The significance of CC for a given pair and epoch was determined by bootstrapping; CC was considered to be significantly nonzero if the average value +/- the 95% confidence level from bootstrapping did not include zero. Similarly, CC for two epochs were considered to be significantly different from one another if the bootstrapping intervals did not overlap.

For the population of pairs, we determined the significance of the population-average CC for a given epoch using the one-sample t-test (that is, by comparing to a zero-mean normal distribution with the same standard deviation). We tested for a significant change in population CC values across two epochs by applying the Wilcoxon signed-rank test to the two sets of CC values.

We also compared CC for responses to brief and continuous visual stimulation. First, pairs were segregated according to the stimulus presented, resulting in 16 brief and 19 extended-stimulus pairs. The two resulting sets of trial-averaged CC values were then compared using the Wilcoxon rank-sum test.

4.4.8 Power Analysis

For each trial and cell, we extracted a 5.8 s window of activity (with epoch windows and gaps between epochs as described above, plus 500 ms windows on each end to avoid filtering artifacts in the ongoing and steady-state epochs), and calculated the residual time series as described above. For each residual trace, we performed wavelet analysis in Matlab using software provided by C. Torrence and G. Compo (available at URL: http://paos.colorado.edu/research/wavelets/, ref). This resulted in a power time series for each cell, for multiple frequencies. For each frequency below 100 Hz, we averaged the time series across each epoch to obtain the average power at each frequency for each epoch. We then averaged across trials. For each pair, we also averaged across all frequencies in the gamma range (20 – 100 Hz), and plotted the resulting trial-averaged gamma power (P) in each epoch to inspect for trends across the population (**Fig. 4.2e**). We tested for significant changes in a given pair and across the population using the same methods as those described for CC values.

We next inspected for a relationship between changes in CC and changes in gamma power for a given pair. For the ongoing – to – transient and transient – to – steady-state transitions, we calculated the change in trial-averaged gamma power for each neuron

$$\Delta P_{neuron}^{epoch1 \rightarrow epoch2} = P_{neuron}^{epoch2} - P_{neuron}^{epoch1},$$

and took the geometric mean of the absolute values:

$$\sqrt{|\Delta P_1 \Delta P_2|}^{epoch1 \rightarrow epoch2} = \left[|\Delta P_1^{epoch1 \rightarrow epoch2} \Delta P_2^{epoch1 \rightarrow epoch2}|\right]^{1/2}$$

For each pair, we plotted the absolute value of the average change in CC vs. the result, and performed linear regression analysis (**Fig. 4.4a**).

For each cell, we also obtained the relative power spectrum (rP) for the transient and steady-state epochs, defined to be the trial-averaged evoked spectrum divided by the trial-averaged ongoing spectrum (**Fig. 4.2d, Supplementary Fig. 4.6a, c**):

$$rP_{neuron}^{epoch} = P_{neuron}^{epoch} / P_{neuron}^{ongoing}$$

Second, to obtain the "peakiness" of the relative power spectrum within the gamma range for each cell, we divided the maximum value of rP in the gamma range by the average value in the gamma range to obtain the "peak ratio" (M_{neuron}^{epoch}) (**Fig. 4.4b**, similar to Yu, Ferster 2010):

$$M_{neuron}^{epoch} = \frac{\left[\max(rP_{neuron}^{epoch})\right]_{gamma}}{\left[\text{avg}(rP_{neuron}^{epoch})\right]_{gamma}}$$

(where $M_{neuron}^{ongoing} = 1$). We then calculated the change in peak ratios across epochs:

$$\Delta M_{neuron}^{epoch1 \rightarrow epoch2} = M_{neuron}^{epoch2} - M_{neuron}^{epoch1}$$

and then the geometric mean of the absolute values for each simultaneously-recorded pair ($\sqrt{|\Delta M_1 \Delta M_2|}$). Finally, we inspected for a relationship between $\sqrt{|\Delta M_1 \Delta M_2|}$ and changes in CC for a given pair (**Fig. 4.4c**) as described above for changes in power.

4.4.9 Phase Concentration Analysis

For each residual trace in a given trial, we used wavelet analysis (described above) to calculate the phase of each signal as a function of time and frequency. We then averaged over all frequencies in the gamma range (20 – 100 Hz) to obtain the gamma phase time series for each trace ($\varphi_i(t)$). For each pair of residuals, we calculated the cosine of the phase difference, and averaged over each epoch to obtain the "phase concentration" (R) for each epoch and trial:

$$R_{epoch}^{trial} = \langle cos[\varphi_1(t) - \varphi_2(t)] \rangle_{epoch}^{trial}$$

We then averaged over all trials and analyzed the results for pairwise and population trends using the same methods as those described for CC values (**Supplementary Fig. 4.4b**). We also inspected for a relationship between changes in CC and changes in R for a given pair (**Supplementary Fig. 4.4c**) as described above for changes in power.

4.4.10 Network Models

To investigate the roles of network properties in our experimental results, we implemented a model network of 800 excitatory and 200 inhibitory leaky-integrate-and-fire neurons. Excitatory-excitatory connections had small-world connectivity(Bujan et al., 2015; Watts & Strogatz, 1998) (with 5% connection probability), and all other connections were random (with 5% excitatory-inhibitory, and 10% inhibitory-excitatory and inhibitory-inhibitory connection probability). Each nonzero entry in the connection weight matrix (W_{ij}^0) was drawn from a uniform distribution over the interval [0.0, 1.0).

The dynamics of the membrane potential (V) of each neuron evolved according to

$$\tau_m \frac{dV}{dt} = -g_L[V(t) - E_L] + I_{syn}(t)$$

where the membrane time constant τ_M = 50 ms (excitatory neurons), 25 ms (inhibitory), and the leak conductance g_L = 10 nS (excitatory), 5 (inhibitory). The leak reversal potential E_L for each neuron was a random value between -70 and -60 mV, drawn from a Gaussian distribution (to model the variability in resting membrane potentials observed across neurons in the experimental

data). The reversal potentials for the synaptic current $I_{syn}(t)$ were E_{GABA} = -68 mV, and E_{AMPA} = 50 mV.

The synaptic current for each synapse type (between presynaptic neurons of type X and postsynaptic neurons of type Y) had three relevant time course parameters: delay (τ_{LX}, that is, the lag between presynaptic spike time and beginning of conductance waveform), rise time (τ_{RYX}), and decay time (τ_{DYX}). Synaptic conductances were modeled as products of time-varying gating variables (S_{YX}) and maximum conductances (g_{YX}). Following a presynaptic spike at time 0, the gating variable dynamics were described by

$$S_{YX}(t) = \frac{\tau_m}{\tau_{DYX} - \tau_{RYX}} \left[exp\left(-\frac{t - \tau_{LX}}{\tau_{DYX}}\right) - exp\left(-\frac{t - \tau_{LX}}{\tau_{RYX}}\right) \right]$$

with time constants (in ms) τ_{LE} = 1.5, τ_{REE} = 0.2, τ_{DEE} = 1.0, τ_{RIE} = 0.2, τ_{DIE} = 1.0, τ_{LI} = 1.5, τ_{RII} = 1.5, τ_{DII} = 6.0, τ_{REI} = 1.5, τ_{DEI} = 6.0. Maximum conductance values (in nS) were g_{EE} = 1.0, g_{IE} = 6.0, g_{EI} = 30, g_{II} = 30. In response to a presynaptic spike in neuron *j* at time t_j^{spk}, the weight (W_{ij}) of a synapse connecting neurons *j* and *i* depressed and recovered according to

$$\frac{dW_{ij}}{dt} = -\frac{W_{ij}(t)}{\tau_{depress}} \delta(t - t_j^{spk}) + \frac{W_{ij}^0 - W_{ij}(t)}{\tau_{recover}}$$

with depression time constant $\tau_{depress}$ = 30 ms and recovery time constant $\tau_{recover}$ = 1500 ms. Depression and recovery time constants were chosen to give reasonable activity time courses for low-frequency (0 - 20 Hz) membrane potentials.

The spike threshold for each neuron was -40 mV. A neuron reset to -59 mV after spiking, and was refractory for 2 ms (excitatory) and 1 ms (inhibitory).

All excitatory neurons received Poisson external inputs. During "ongoing" activity, the external input rate to each neuron was 25 Hz. The stimulus was modeled as a gradual increase to 500 Hz; the input rate was increased by 95 Hz at stimulus onset, and by an additional 95 Hz every 50 ms for 200 ms. This gradual increase provided more realistic low-frequency membrane potentials than did a single step function stimulus, but did not qualitatively impact the results. The gating variables for external inputs had the same parameters as for excitatory-excitatory connections, and maximum conductances were g_E = 4 nS.

Each trial was 5.8 s in duration, with stimulus onset at 2.7 s, and the time step was 0.05 ms. The ongoing epoch was defined to be 2200 ms to 200 ms before stimulus onset, the transient epoch 0 ms to 400 ms after stimulus onset, and the steady-state epoch 600 ms to 2600 ms after stimulus onset. The additional 500 ms at the beginning and end of each trial ensured there were no wavelet filtering artifacts in the ongoing and steady-state epochs.

We then randomly selected 20 excitatory neurons from the entire population of 800 excitatory neurons, and generated 40 V-V pairs from these twenty nodes. Because action potential rates were higher in this model network than in experiment, and because action potentials can affect V-V correlated variability, we substituted "test" neurons for these network neurons before doing the calculation (see **Supplementary Information 6**). Test neurons were identical to network neurons, but all synaptic conductances were multiplied by a factor of 0.5, and spike threshold was raised to -30 mV, which was sufficient to eliminate all action potentials. Thus, a test neuron membrane potential acted as a network sub-sampler, representing the response to re-

scaled versions of inputs to the corresponding network neuron. For each pair of test neurons, we then calculated the same parameters as for experimental neuron pairs (CC, R, etc.). We also calculated cross correlations as a function of lag for residual synaptic conductance traces (**Supplementary Figure 8**). This process was identical to that described for the (zero lag) Pearson correlation coefficient described above, but was performed for all lags in +/- 50 ms.

For each trial, we calculated the instantaneous spike rate of all excitatory neurons in the network. We then calculated the power spectra of the transient and steady state spike rates using wavelet filtering, and averaged over all trials (**Supplementary Figure 6**), as described above.

To investigate the dependence on distance between neurons, we repeated the above analysis for this model using two alternate sets of randomly-selected neurons. First, we randomly selected 20 neurons from a group of 100 neighboring neurons. Second, we used a smaller group of 20 neighboring neurons (see **Supplementary Information 5**, and **Supplementary Figure 9**).

In addition, we implemented two alternate model versions (see **Supplementary Information 5**, and **Supplementary Figures 6, 7, 8**). In one, we eliminated synaptic adaptation. In the other, we maintained synaptic adaptation, but tuned synaptic time courses to give an asynchronous transient epoch (τ_{LX} = 1.5 ms, τ_{RYX} = 0.2 ms, τ_{DYX} = 1.0 ms for all X and Y). (In the absence of adaptation, this version was also asynchronous in the steady-state.)

Atallah, B. V., & Scanziani, M. (2009). Instantaneous Modulation of Gamma Oscillation Frequency by Balancing Excitation with Inhibition. *Neuron*, *62*(4), 566–577. http://doi.org/10.1016/j.neuron.2009.04.027

Averbeck, B. B., Latham, P. E., & Pouget, A. (2006). Neural correlations, population coding and computation. *Nature Reviews. Neuroscience*, *7*(5), 358–66. http://doi.org/10.1038/nrn1888

Averbeck, B. B., & Lee, D. (2004). Coding and transmission of information by neural ensembles. *Trends in Neurosciences*, *27*(4), 225–30. http://doi.org/10.1016/j.tins.2004.02.006

Bernacchia, A., & Wang, X.-J. (2013). Decorrelation by recurrent inhibition in heterogeneous neural circuits. *Neural Computation*, *25*(7), 1732–67. http://doi.org/10.1162/NECO_a_00451

Brunel, N., & Wang, X.-J. (2003). What determines the frequency of fast network oscillations with irregular neural discharges? I. Synaptic dynamics and excitation-inhibition balance. *Journal of Neurophysiology*, *90*(1), 415–430. http://doi.org/10.1152/jn.01095.2002

Bujan, A. F., Aertsen, A., & Kumar, A. (2015). Role of Input Correlations in Shaping the Variability and Noise Correlations of Evoked Activity in the Neocortex. *Journal of Neuroscience*, *35*(22), 8611–8625. http://doi.org/10.1523/JNEUROSCI.4536-14.2015

Carandini, M. (2004). Amplification of trial-to-trial response variability by neurons in visual cortex. *PLoS Biology*, *2*(9), E264. http://doi.org/10.1371/journal.pbio.0020264

Chung, S., Li, X., & Nelson, S. B. (2002). Short-term depression at thalamocortical synapses

contributes to rapid adaptation of cortical sensory responses in vivo. *Neuron*, *34*(3), 437–446. http://doi.org/10.1016/S0896-6273(02)00659-1

Cohen, M. R., & Kohn, A. (2011). Measuring and interpreting neuronal correlations. *Nature Neuroscience*, *14*(7), 811–819. http://doi.org/10.1038/nn.2842

Cohen, M. R., & Maunsell, J. H. R. (2009). Attention improves performance primarily by reducing interneuronal correlations. *Nature Neuroscience*, *12*(12), 1594–600. http://doi.org/10.1038/nn.2439

Crockett, T., Wright, N., Thornquist, S., Ariel, M., & Wessel, R. (2015). Turtle dorsal cortex pyramidal neurons comprise two distinct cell types with indistinguishable visual responses. *PLoS ONE*, *10*(12), 1–22. http://doi.org/10.1371/journal.pone.0144012

de la Rocha, J., Doiron, B., Shea-Brown, E., Josić, K., & Reyes, A. (2007). Correlation between neural spike trains increases with firing rate. *Nature*, *448*(7155), 802–6. http://doi.org/10.1038/nature06028

Doiron, B., Litwin-Kumar, A., Rosenbaum, R., Ocker, G. K., & Josić, K. (2016). The mechanics of state-dependent neural correlations. *Nature Neuroscience*, *19*(3), 383–393. http://doi.org/10.1038/nn.4242

Finger, H., & König, P. (2014). Phase synchrony facilitates binding and segmentation of natural images in a coupled neural oscillator network. *Frontiers in Computational Neuroscience*, *7*(January), 1–21. http://doi.org/10.3389/fncom.2013.00195

Haider, B., & McCormick, D. A. (2009). Rapid Neocortical Dynamics: Cellular and Network Mechanisms. *Neuron*, *62*(2), 171–189. http://doi.org/10.1016/j.neuron.2009.04.008

Haider, B., Schulz, D. P. A., & Carandini, M. (2016). Millisecond Coupling of Local Field Potentials to Synaptic Currents in the Awake Visual Cortex Report Millisecond Coupling of Local Field Potentials to Synaptic Currents in the Awake Visual Cortex, *90*, 35–42. http://doi.org/10.1016/j.neuron.2016.02.034

Hansen, B. J., Chelaru, M. I., & Dragoi, V. (2012). Correlated Variability in Laminar Cortical Circuits. *Neuron*, *76*(3), 590–602. http://doi.org/10.1016/j.neuron.2012.08.029

Heiss, J. E., Katz, Y., Ganmor, E., & Lampl, I. (2008). Shift in the Balance between Excitation and Inhibition during Sensory Adaptation of S1 Neurons. *The Journal of Neuroscience : The Official Journal of the Society for Neuroscience*, *28*(49), 13320–30. http://doi.org/10.1523/JNEUROSCI.2646-08.2008

Levina, A., Herrmann, J. M., & Geisel, T. (2007). Dynamical synapses causing self-organized criticality in neural networks. *Nature Physics*, *3*(12), 857–860. http://doi.org/10.1038/nphys758

Litwin-Kumar, A., Oswald, A.-M. M., Urban, N. N., & Doiron, B. (2011). Balanced synaptic input shapes the correlation between neural spike trains. *PLoS Computational Biology*, *7*(12), e1002305. http://doi.org/10.1371/journal.pcbi.1002305

Luczak, A., Barthó, P., & Harris, K. D. (2009). Spontaneous Events Outline the Realm of Possible Sensory Responses in Neocortical Populations. *Neuron*, *62*(3), 413–425. http://doi.org/10.1016/j.neuron.2009.03.014

Lyamzin, D. R., Barnes, S. J., Donato, R., Garcia-Lazaro, J. A., Keck, T., & Lesica, N. A. (2015). Nonlinear Transfer of Signal and Noise Correlations in Cortical Networks. *Journal of Neuroscience*, *35*(21), 8065–8080. http://doi.org/10.1523/JNEUROSCI.4738-14.2015

MacLean, J. N., Watson, B. O., Aaron, G. B., & Yuste, R. (2005). Internal dynamics determine the cortical response to thalamic stimulation. *Neuron*, *48*(5), 811–823. http://doi.org/10.1016/j.neuron.2005.09.035

Moreno-Bote, R., Beck, J., Kanitscheider, I., Pitkow, X., Latham, P., & Pouget, A. (2014). Information-limiting correlations. *Nature Neuroscience*, *17*(10), 1410–1417. http://doi.org/10.1038/nn.3807

Mulligan, K. a, & Ulinski, P. S. (1990). Organization of geniculocortical projections in turtles: isoazimuth lamellae in the visual cortex. *The Journal of Comparative Neurology*, *296*(4), 531–47. http://doi.org/10.1002/cne.902960403

Ohiorhenuan, I. E., Mechler, F., Purpura, K. P., Schmid, A. M., Hu, Q., & Victor, J. D. (2010). Sparse coding and high-order correlations in fine-scale cortical networks. *Nature*, *466*(7306), 617–21. http://doi.org/10.1038/nature09178

Okun, M., Steinmetz, N. a., Cossell, L., Iacaruso, M. F., Ko, H., Barthó, P., … Harris, K. D. (2015). Diverse coupling of neurons to populations in sensory cortex. *Nature*, *521*(7553), 511–515. http://doi.org/10.1038/nature14273

Ollerenshaw, D. R. R., Zheng, H. J. V. J. V, Millard, D. C. C., Wang, Q., & Stanley, G. B. B. (2014). The adaptive trade-off between detection and discrimination in cortical representations and behavior. *Neuron*, *81*(5), 1152–1164. http://doi.org/10.1016/j.neuron.2014.01.025

Panzeri, S., Brunel, N., Logothetis, N. K., & Kayser, C. (2010). Sensory neural codes using multiplexed temporal scales. *Trends in Neurosciences*, *33*(3), 111–120. http://doi.org/10.1016/j.tins.2009.12.001

Poulet, J. F. a, & Petersen, C. C. H. (2008). Internal brain state regulates membrane potential synchrony in barrel cortex of behaving mice. *Nature*, *454*(7206), 881–5. http://doi.org/10.1038/nature07150

Renart, A., de la Rocha, J., Bartho, P., Hollender, L., Parga, N., Reyes, A., & Harris, K. D. (2010). The asynchronous state in cortical circuits. *Science (New York, N.Y.)*, *327*(5965), 587–90. http://doi.org/10.1126/science.1179850

Ringach, D. L. (2009). Spontaneous and driven cortical activity: implications for computation. *Current Opinion in Neurobiology*, *19*(4), 439–44. http://doi.org/10.1016/j.conb.2009.07.005

Ruff, D. a, & Cohen, M. R. (2014). Attention can either increase or decrease spike count correlations in visual cortex. *Nature Neuroscience*, *17*(11), 1591–1597. http://doi.org/10.1038/nn.3835

Saha, D., Morton, D., Ariel, M., & Wessel, R. (2011). Response properties of visual neurons in the turtle nucleus isthmi. *Journal of Comparative Physiology A*, *197*(2), 153–165. http://doi.org/10.1007/s00359-010-0596-3

Scholvinck, M. L., Saleem, A. B., Benucci, a., Harris, K. D., & Carandini, M. (2015). Cortical State Determines Global Variability and Correlations in Visual Cortex. *Journal of Neuroscience*, *35*(1), 170–178. http://doi.org/10.1523/JNEUROSCI.4994-13.2015

Schulz, D. P. A., Sahani, M., & Carandini, M. (2015). Five key factors determining pairwise correlations in visual cortex. *Journal of Neurophysiology*, *114*(2), 1022–1033. http://doi.org/10.1152/jn.00094.2015

Senseman, D. M., & Robbins, K. a. (1999). Modal behavior of cortical neural networks during

visual processing. *The Journal of Neuroscience : The Official Journal of the Society for Neuroscience*, *19*(10), RC3. Retrieved from http://www.ncbi.nlm.nih.gov/pubmed/10234049

Senseman, D. M., & Robbins, K. a. (2002). High-speed VSD imaging of visually evoked cortical waves: decomposition into intra- and intercortical wave motions. *Journal of Neurophysiology*, *87*(3), 1499–514. Retrieved from http://www.ncbi.nlm.nih.gov/pubmed/11877522

Shew, W. L. W. L., Clawson, W. P. W. P., Pobst, J., Karimipanah, Y., Wright, N. C. N. C., & Wessel, R. (2015). Adaptation to sensory input tunes visual cortex to criticality. *Nature Physics*, *11*(8), 659–663. http://doi.org/10.1038/nphys3370

Shoham, S., O'Connor, D. H., & Segev, R. (2006). How silent is the brain: Is there a "dark matter" problem in neuroscience? *Journal of Comparative Physiology A: Neuroethology, Sensory, Neural, and Behavioral Physiology*, *192*(8), 777–784. http://doi.org/10.1007/s00359-006-0117-6

Tan, A. Y. Y., Chen, Y., Scholl, B., Seidemann, E., & Priebe, N. J. (2014). Sensory stimulation shifts visual cortex from synchronous to asynchronous states. *Nature*, *509*(7499), 226–229. http://doi.org/10.1038/nature13159

Tetzlaff, T., Helias, M., Einevoll, G. T., & Diesmann, M. (2012). Decorrelation of neural-network activity by inhibitory feedback. *PLoS Computational Biology*, *8*(8), e1002596. http://doi.org/10.1371/journal.pcbi.1002596

Wang, Q., Webber, R. M., & Stanley, G. B. (2010). Thalamic synchrony and the adaptive gating of information flow to cortex. *Nature Neuroscience*, *13*(12), 1534–1541.

http://doi.org/10.1038/nn.2670

Wang, X.-J. J. (2010). Neurophysiological and computational principles of cortical rhythms in cognition. *Physiological Reviews*, *90*(3), 1195–1268. http://doi.org/10.1152/physrev.00035.2008

Watts, D. J., & Strogatz, S. H. (1998). Collective dynamics of "small-world" networks. *Nature*, *393*(6684), 440–2. http://doi.org/10.1038/30918

Whitmire, C. J., Waiblinger, C., Schwarz, C., & Stanley, G. B. (2016). Information Coding through Adaptive Gating of Article Information Coding through Adaptive Gating of Synchronized Thalamic Bursting. *CellReports*, 1–13. http://doi.org/10.1016/j.celrep.2015.12.068

Womelsdorf, T., Schoffelen, J.-M., Oostenveld, R., Singer, W., Desimone, R., Engel, A. K., & Fries, P. (2007). Modulation of neuronal interactions through neuronal synchronization. *Science (New York, N.Y.)*, *316*(5831), 1609–12. http://doi.org/10.1126/science.1139597

Yang, H., Shew, W. L., Roy, R., & Plenz, D. (2012). Maximal Variability of Phase Synchrony in Cortical Networks with Neuronal Avalanches. *Journal of Neuroscience*, *32*(3), 1061–1072. http://doi.org/10.1523/JNEUROSCI.2771-11.2012

Yu, J., & Ferster, D. (2010). Membrane Potential Synchrony in Primary Visual Cortex during Sensory Stimulation. *Neuron*, *68*(6), 1187–1201. http://doi.org/10.1016/j.neuron.2010.11.027

Zohary, E. (1994). correlated neuronal discharge rate and its implications for psychophysical performance.

4.5 Supplementary Information

4.5.1 Supplementary Information 1: windows of activity chosen for analysis

When relating two measures of cortical coordination (e.g., correlated variability and network state), the ideal approach would be to determine both measures for the same dataset. Unfortunately, some experimental methods for recording large-scale population activity (e.g., microelectrode array, or MEA, recordings) and those for recording pairs of membrane potentials (pairwise whole-cell recordings) are not easily implemented in the same region of cortex simultaneously. Furthermore, inferring the network state (as in Shew, et al. 2015) requires a large number of neuronal avalanches, and therefore recording times that often surpass the amount of time a typical whole-cell patch remains stable. As such, we motivated our choice of windows for this study based on the results of a previous study of population activity in the same preparation(Shew et al., 2015).

In this previous work, the "transient" epoch for a given preparation was defined by the total network activity over all trials. Briefly, the activity at each electrode was band-pass filtered to give the local field potential (LFP), the absolute value of the resulting trace was divided by its standard deviation, and all such traces from responsive electrodes were summed to give the network activity for a single trial. All trials were overlaid, the 90^{th} percentile envelope was calculated, and the transient epoch was defined to be the full-width at half-max of this envelope. The "visually-driven steady-state" began at the end of the transient epoch, and ended with the stimulus. The transient epoch was calculated on a prep-by-prep basis, and across all preparations, lasted 423 ± 202 ms (mean ± SD). For nine preparations and four different stimuli, the transient

epoch was shown to be supercritical, and the visually-driven steady-state critical. There were not enough ongoing avalanches to determine the pre-stimulus state.

Translating this result into window choices for this study involved two additional considerations. First, the resting membrane potential of a neuron affects the amplitude of depolarization for a given level of synaptic input. As such, taking the absolute value and overlaying trials to calculate the 90^{th} percentile envelope, as above, for a pair of neurons may not be a viable approach. Second, correlated variability distributions (for spike data) can depend on window size, and so the three epochs should be of comparable duration. That is, a transient epoch of around 400 ms, and a steady-state epoch of nearly 10 s would not be appropriate. With this in mind, we chose the same epochs for all recorded pairs: the ongoing and steady-state epochs were chosen to be 2 s in duration, and the transient epoch 400 ms. Due to the observed variability in the previous study, epochs were separated by 200 ms (with the end of the ongoing epoch coinciding with stimulus onset, **Fig. 4.2a**).

These choices have implications for our assumptions about the network state during each epoch. Specifically, the transient epoch as defined in this study is presumed to be in general supercritical, but this has not been shown explicitly for this window choice. Furthermore, the label of "critical" is only valid for the full visually-driven steady-state from the previous study (see above), and the steady-state epoch as defined in this study is a subset of that activity. As such, we work under the somewhat weaker assumption that the cortex is supercritical during the transient epoch, and is adapting toward criticality during the steady-state (although it may not yet be critical).

To test the robustness of our results, we repeated the analysis for three other sets of epoch windows and gaps: the windows described above, but with a 300 ms gap between stimulus onset and beginning of transient epoch (**Supplementary Fig. 4.1a, b**), 1 s windows for all epochs with no gaps (**Supplementary Fig. 4.1c, d**), and 400 ms windows for all epochs, with 1 s gaps (**Supplementary Fig. 4.1e, f**). For all choices, the population trends were approximately the same, suggesting that the observed correlated variability values generally reflect those of "pre-stimulus" activity, the "early" response, and the "late" response. For a given epoch, however, across-population variability did decrease somewhat with increasing window size (e.g., compare **Supplementary Fig. 4.1d** and **f**), and so the increase in variability from ongoing to transient epochs in the original set of choices may be partially due to this effect.

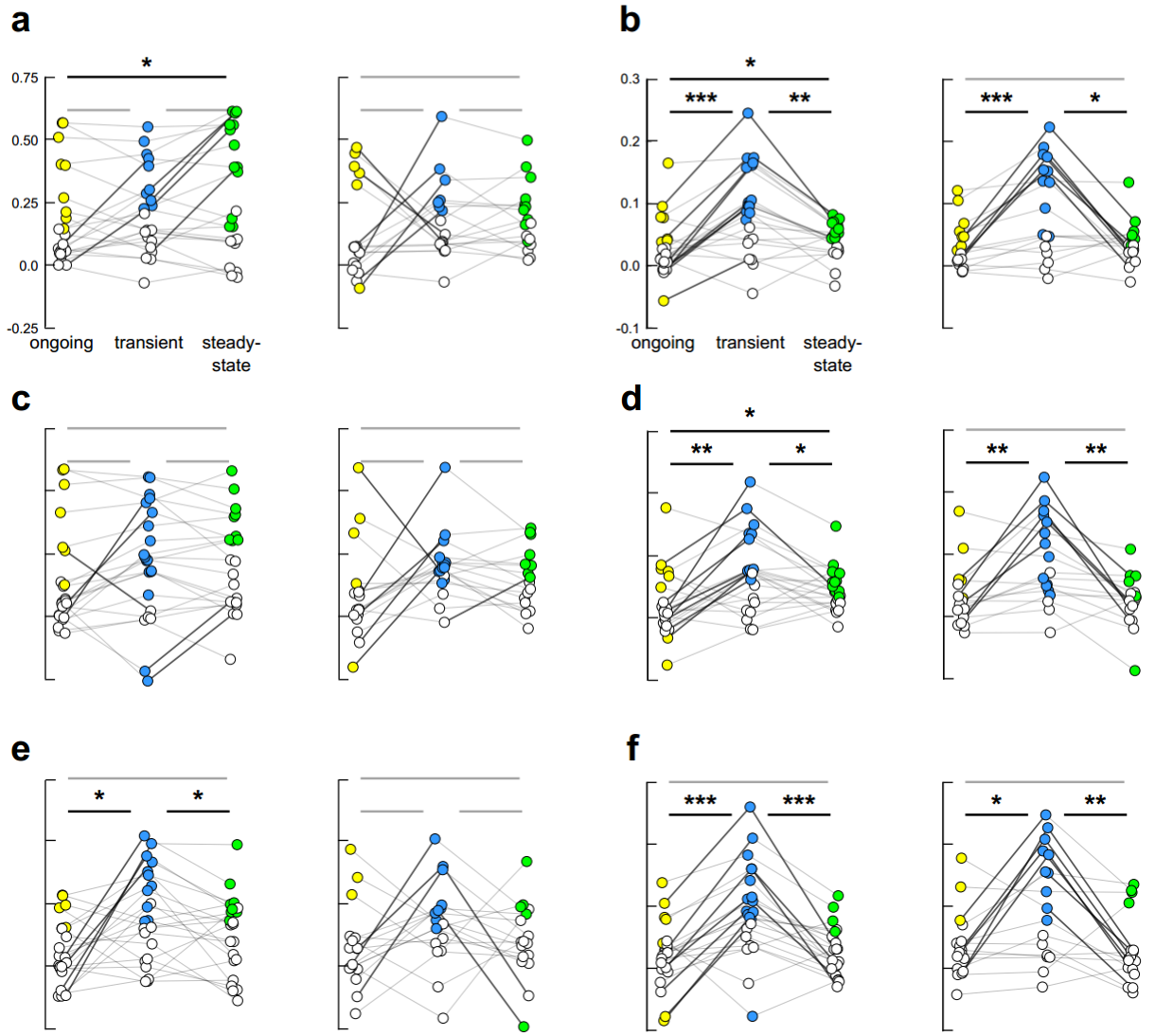

Supplementary Figure 4.1 Results for various choices of epoch windows and gaps between epochs. Vertical scales are the same for a, c, e, and for b, d, f. Bars and asterisks linking epochs indicate results of tests for significance of changes in values across epochs (Wilcoxon signed-rank test): light bars correspond to insignificant changes ($P > 0.05$), * to $0.01 < P < 0.05$, ** to $0.001 < P < 0.01$, *** to $P < 0.001$. (a) Correlated variability (as in **Fig. 4.2d**) for epoch windows (in ms) ongoing = 2000, transient = 400, steady-state = 2000, with 0 ms between then end of the ongoing epoch and stimulus onset, 300 ms between stimulus onset and the start of the transient epoch, and 200 ms between the end of the transient epoch and the start of the steady-state epoch, for extended (left) and brief (right) stimuli, 0.1 – 20 Hz. Hereafter, these choices are indicated by, e.g. epochs = (2000, 400, 2000), gaps = (0, 300, 200). (b) Same as in (a), but for 20 – 100 Hz. (c, d) Same as in (a, b), but for epochs = (1000, 1000, 1000), gaps = (0, 0, 0). (e, f) Same as in (a, b), but for epochs = (400, 400, 400), gaps = (800, 200, 1000).

4.5.2 Supplementary Information 2: spectral content of residual traces, frequency bands chosen for analysis, and low-frequency results

For each cell, we calculated the across-trial average power for the ongoing, transient, and steady-state epochs using the wavelet transform (see Methods). Across cells, visual stimulation (either brief or continuous) evoked a broad-band increase in residual power in the transient epoch (**Supplementary Fig. 4.2a**). Residual power generally decreased in the steady-state, but was still elevated above ongoing levels (**Supplementary Fig. 4.2b**). The height and location of peaks in residual relative power (rP) spectra varied across cells; for most cells (and for both response epochs), the peak frequency was in the 0.1 – 20 Hz range (**Supplementary Fig. 4.2c**). The size of the peaks (quantified by $M_{100} = rP_{max}/rP_{avg}$, calculated by considering all frequencies below 100 Hz) were generally large in the transient epoch, and varied continuously across cells (**Supplementary Fig. 4.2d**). Note that this definition for M_{100} is slightly different from that for M (used in Results and **Fig. 4.4b, c**), which is calculated using only frequencies in the 20 – 100 Hz range.

For the remainder of our analysis, we treated high- and low-frequency activity separately. There were three primary motivations for doing so. First, a recent study of V-LFP correlated variability (CC) in primate V1 found that low-frequency CC was stimulus-modulated, and high-frequency CC was not(Tan, Chen, Scholl, Seidemann, & Priebe, 2014). Second, it is a long-standing hypothesis that different frequency bands in cortical activity represent distinct functionalities(Buzsáki, 2006; Mazzoni, Brunel, & Panzeri, 2008; Wang, 2010), suggesting it is more reasonable to separate low and high frequencies than to analyze broad-band activity. Finally,

after separately calculating CC for low (0.1 – 20 Hz) and high (20 – 100 Hz) frequencies, we observed that the two sets of CC values were not significantly correlated (**Supplementary Fig. 4.3c**), suggesting correlated variability of the two bands was independently modulated by visual stimulation. We refer to the high-frequency component as "gamma activity", although the bounds of gamma activity vary across studies.

Population-averaged correlated variability (<CC>) for low frequencies gradually increased from ongoing to transient to steady-state for continous (<CC> = 0.176 ongoing, 0.212 transient, 0.303 steady-state, $P > 0.05$ for ongoing – to – transient, $P = 0.01$ for transient – to – steady-state, $P = 0.014$ for ongoing – to – steady-state transition, Wilcoxon signed-rank test, **Supplementary Fig. 4.3a**) and brief (<CC> = 0.120 ongoing, 0.19 transient, 0.18 steady-state, $P > 0.05$ for all across-epoch comparisons, Wilcoxon signed-rank test, **Supplementary Fig. 4.3b**) stimulation, although the modulation was stronger for extended.

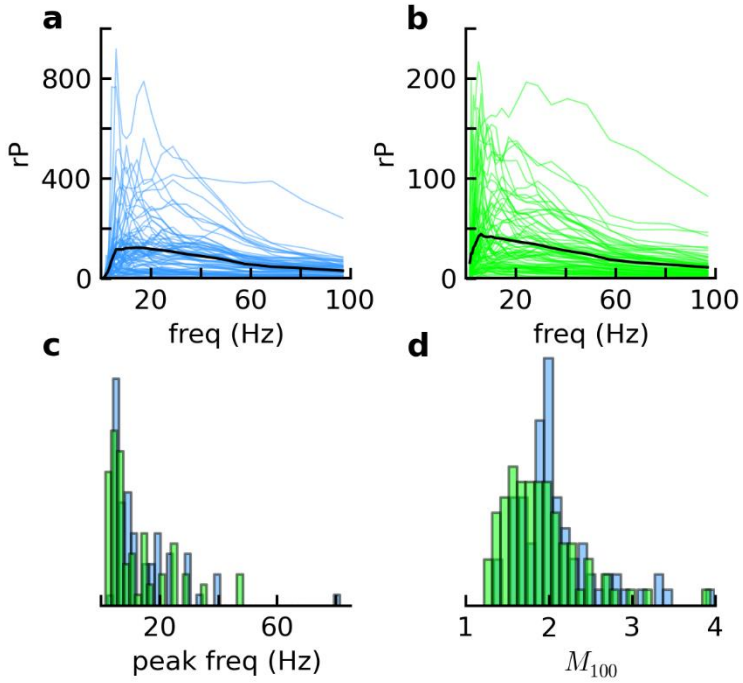

Supplementary Figure 4.2 Spectral properties of residual evoked activity vary across cells. (a) Across-trial average relative power (rP, evoked divided by ongoing) for individual cells (blue lines), and across-cell average (black) for the transient epoch. (b) Same as in (a), but for steady-state epoch. (c) Distribution of peak frequencies in the 0.1 – 100 Hz range for all cells for the transient (blue) and steady-state (green) epochs. (d) Same as in (c), but for M_{100}, the ratio of of rP_{max} to rP_{avg} for each cell.

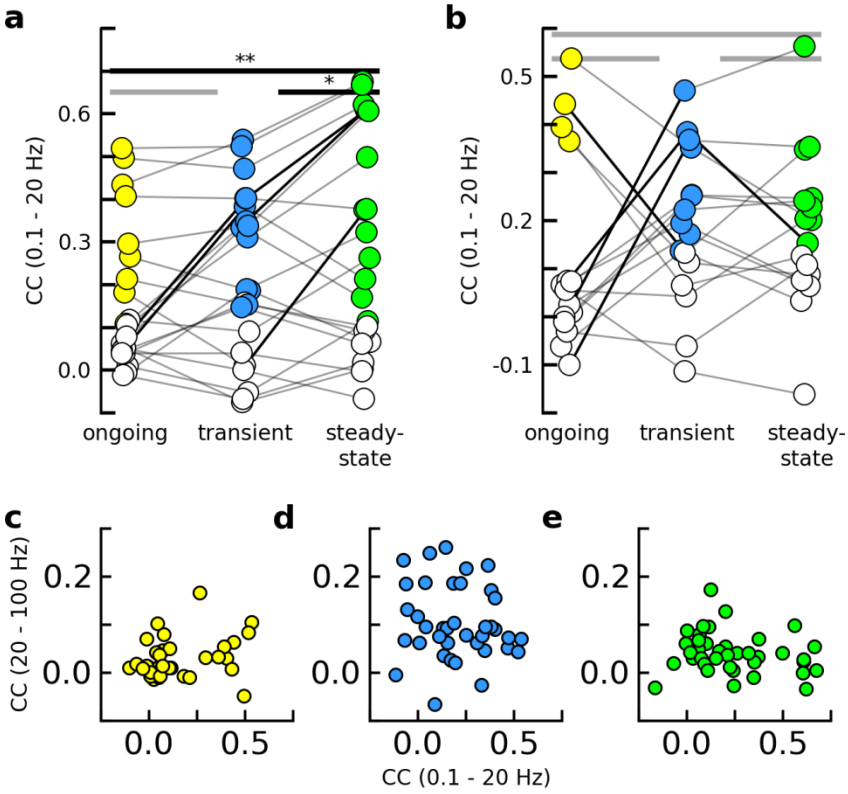

Supplementary Figure 4.3 Low - (0.1 – 20 Hz) and high - (20 – 100 Hz) frequency correlated variability were independent, and were modulated differently by visual stimulation. (a) Correlated variability (CC) trajectories for 0.1 – 20 Hz bandpass-filtered data, for continuous visual stimulation (compare with **Fig. 4.3b**). (b) Same as in (a), but for brief flashes (compare with **Fig. 4.3c**). (c - e) Across-trial average gamma band (20 – 100 Hz) CC vs. low-frequency (0.1 – 20 Hz) CC for each recorded pair (for both brief and continuous stimulation), for the ongoing (c), transient (d), and steady-state (e) epochs. All linear regression fits insignificant ($p > 0.05$).

4.5.3 Supplementary Information 3: Modulation of phase relationship by visual stimulation

In this study, we use the correlated variability of gamma band residual traces as a measure of coordination between neurons. For pairs of analog signals, another popular measure is the phase difference(Yang, Shew, Roy, & Plenz, 2012). This alternative measure is (non-trivially) related to correlation, and indeed, we did observe that some residual pairs tended to be more phase-locked during the transient than during the steady-state epoch (**Supplementary Fig. 4.4a**). To relate the results of our study to previous work, then, we also calculated the phase concentration of residual gamma band pairs (R), defined to be the cosine of the difference in phase angles for two residual traces, averaged over a window of interest, and then averaged over all trials (see Methods). The phase concentration takes a value of +1 for a pair of perfectly in-phase signals, -1 for perfectly out-of-phase signals, and 0 for two signals with random phase. Phase concentration does not take into account the amplitudes of the signals.

We found that across the population of all pairs (including both brief and continuous stimuli), the average phase concentration (<R>) followed the same dynamics as <CC> (<R> = 0.027 ongoing, 0.057 transient, 0.028 steady-state; $P = 4.22 \times 10^{-5}$ for ongoing – transient comparison, $P = 4.51 \times 10^{-6}$ for transient – steady-state comparison, P = 0.90 for ongoing – transient comparison, Wilcoxon signed-rank test, **Supplementary Fig. 4.4b**). Moreover, changes in CC were significantly related to changes in R (r = 0.643, $P = 3.05 \times 10^{-5}$ for ongoing – to – transient transition, r = 0.624, $P = 6.23 \times 10^{-5}$ for transient – to – steady-state transition, Pearson correlation, **Supplementary Fig. 4.4c**).

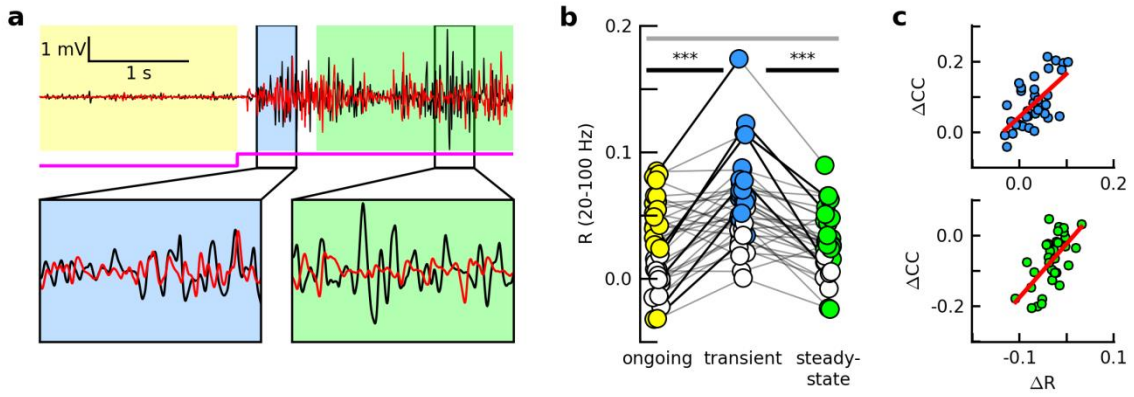

Supplementary Figure 4.4 Changes in correlated variability reflect changes in phase relationship between residual traces. (a) Top: single-trial residual trace pair (same cell pair as in **Fig. 4.3a**). Bottom: close-up of transient and steady-state activity. (b) Same as in **Fig. 4.3b**, but for phase concentration (R) of gamma band residual pairs, for all recorded pairs. (c) Change in CC vs. change in R across epochs for gamma band residual pairs for ongoing – to – transient transition (top) and transient – to – steady-state transition (bottom). Red lines indicate significant linear regression fit (r^2 = 0.413, P = 3.05 x 10^{-5} for ongoing – to – transient transition, r^2 = 0.388, P = 6.23 x 10^{-5} for transient – to – steady-state transition).

4.5.4 Supplementary Information 4: comparison of responses to brief and continuous visual stimulation

To investigate the dependence of correlated variability on the nature of the stimulus, we utilized both brief and continuous visual stimulation (see Methods and Results). Briefly, we recorded from 19 pairs while presenting continuous stimuli (lasting 10 s or longer), and 16 pairs while presenting brief (lasting 10 ms – 150 ms) subfield or whole-field flashes.

We compared the results in two ways. First, for each response epoch, we compared the sets of CC values for the extended and brief stimuli using the Wilcoxon rank-sum test (the distributions are visualized using histograms in **Supplementary Fig. 4.5**). For both epochs and frequency bands, the two sets of values were not significantly different ($P > 0.05$, Wilcoxon rank-sum test), suggesting feedforward sensory input plays at best a small role in determining noise correlation strength across the population. Low-frequency values were larger for continuous stimuli (see Supplementary Information 2), but not significantly so. Second, we qualitatively compared the across-epoch CC dynamics for the two stimulus types (see Results). In general, stimulus modulation of low-frequency CCs was weaker for brief stimuli (see Supplementary Information 2, **Supplementary Fig. 4.3a, b**), but for gamma band CCs, the dynamics were essentially the same (**Fig. 4.3b, c**).

It is important to note that in response to brief flashes, input to the cortex from the lateral geniculate nucleus (LGN) can continue beyond the duration of the stimulus. Specifically, previous work in turtle retina indicates that brief (220 ms) sub-field flashes of 646 nm light can evoked depolarization and spiking in retinal ganglion cells up to 200 ms after stimulus offset(Marchiafava,

1983). Thus, for a typical brief flash used in this study (e.g., 150 ms) it is possible that some sensory inputs to cortex persist during the steady-state epoch. There is no evidence, however, that persistent retinal responses to brief flashes last on the order of seconds. Furthermore, previous work has concluded that the AMPA- and NMDA-mediated EPSPs and GABA-mediated IPSPs that dominate persistent responses (to electrical stimulation of either cortex or LGN fibers) in turtle cortex are intracortical in origin, and distinct from excitatory LGN inputs(Larson-Prior, Ulinski, & Slater, 1991). As such, we assume that the vast majority of steady-state activity in response to brief visual stimulation can be attributed to intracortical feedback.

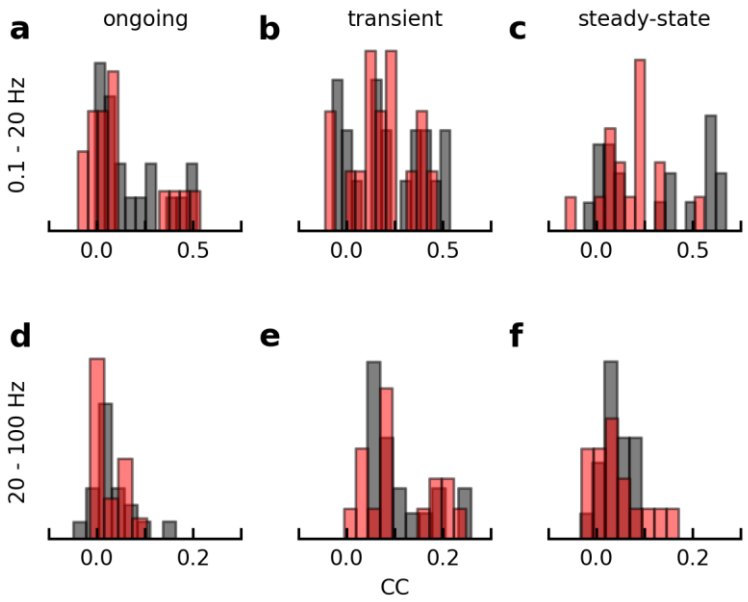

Supplementary Figure 4.5 Correlated variability is similar for responses to brief flashes and continuous visual stimuli. (a-f) Distributions of CC values for continuous stimuli (black) and brief flashes (red), for the ongoing (a, d), transient (b, e), and steady-state (c, f) epochs, for 0.1 – 20 Hz (top row) and 20 – 100 Hz (bottom row) activity. $P > 0.05$ for all pairs of distributions (Wilcoxon rank-sum test).

4.5.5 Supplementary Information 5: additional model results

In order to better understand our model results, we implemented three versions of the small-world network: the model described in Results, in which adaptation was tuned to closely reproduce the experimental results (hereafter referred to as the "synchronous" model, **Fig. 4.6**); a model identical to the synchronous model, but with synaptic adaptation removed ("synchronous, no adaptation"); and a model that was identical to the synchronous model, but with excitatory and inhibitory time constants tuned to result in an asynchronous post-stimulus state ("asynchronous" model, see Methods).

Residual membrane potential relative power spectrum peaks reflect network spike rate oscillations

In the experimental data, the relative power spectra of many cells had clear peaks in the gamma (20 – 100 Hz) spectrum (**Fig. 4.2d**, **Supplementary Fig. 4.2a, b**). This was also true of cells in the synchronous model (**Supplementary Fig. 4.6a**, top). Moreover, the location of the peak in the simulated data coincided with the frequency of the network spike-rate oscillation (**Supplementary Fig. 4.6a**, bottom). In the asynchronous network, the network spike rate power spectrum did not contain prominent peaks (**Supplementary Fig. 4.6c**, bottom), and peaks in the membrane potential spectra were smaller than those in the synchronous network (**Supplementary Fig. 4.6c**, top). In both networks, total gamma power in residual membrane potential traces followed trajectories similar to that observed in experiment (**Supplementary Fig. 4.6b, d**, compare to **Fig. 4.2e**), and generally reflected the average network spike rate in the two evoked epochs (**Supplementary Fig. 4.9a**).

Together, these results suggest the across-epoch changes in gamma power observed in experimental membrane potential residuals reflect changes in the level of network spiking activity, and that peaks in the gamma spectrum reflected oscillations in the network spike rate.

Network spike rate oscillations increase correlated variability, and synaptic adaptation reduces correlated variability by abolishing these oscillations

We used the synchronous, no adaptation and asynchronous models to further test the relationship between network oscillations and membrane potential correlated variability. In the synchronous, no adaptation model, the population-averaged correlated variability (<CC>) increased from ongoing to transient (as with the synchronous model), and continued to increase from transient to steady-state (<CC> = 0.163 transient, 0.314 steady-state, $P = 3.57 \times 10^{-8}$ for transient – steady-state comparison, Wilcoxon signed-rank test, **Supplementary Fig. 4.7a**), as network oscillations became increasingly coherent. In the asynchronous model, <CC> significantly increased from ongoing to transient (<CC> = 0.002 ongoing, 0.033 transient, $P = 1.5 \times 10^{-4}$ ongoing-transient comparison, Wilcoxon signed-rank test, **Supplementary Fig. 4.7b**), although the change was much smaller than in the synchronous model (**Fig. 4.5d**). And in sharp contrast to the synchronous model, synaptic adaptation did not have a significant impact on <CC> (<CC> = 0.028 steady-state, P = 0.48, Wilcoxon signed-rank test). Thus, gamma-band membrane potential correlated variability in the model network is inextricably linked to network spike rate oscillations.

Network oscillations determine synaptic input correlations

As described in the Results and Discussion sections, membrane potential correlations are strongly influenced by correlations in synaptic inputs. As such, we investigated correlated variability between excitatory (g_e-g_e CC), and inhibitory (g_i-g_i CC) synaptic conductances for pairs of excitatory neurons in the model network, as well as correlations between excitatory and inhibitory conductances (g_e-g_i CC). Because CC can be shaped by the lag between excitation and inhibition, we calculated g-g CC as a function of lag. To better understand how these are shaped by network oscillations, we did this for the synchronous and asynchronous models (described above), using 40 pairs generated from 20 neurons randomly-selected from the entire network. For the synchronous model, we used the same neurons and trials as in the Results section.

For both models, g_e-g_e <CC> was relatively small during both the transient and steady-state epochs (and larger for the synchronous than asynchronous model, **Supplementary Fig. 4.8a**). In contrast, g_i-g_i CC was large for both models (and larger for the synchronous model), and only decreased slightly from transient to steady-state (**Supplementary Fig. 4.8b**). The disparity between correlations for these two conductance types likely reflects the stronger, more densely interconnected, and spatially-independent inhibitory synapses (see Methods), and is consistent with earlier experimental recordings of excitatory and inhibitory conductances during gamma oscillations(Hasenstaub et al., 2005; Oren, Mann, Paulsen, Ha, & Hájos, 2006).

Strong g_i-g_i (and/or g_e-g_e) correlations alone are not sufficient to guarantee large membrane potential correlations; if excitation and inhibition are perfectly phase-locked, they will cancel at the level of the membrane potential, resulting in small membrane potential correlations. In the synchronous model, g_e-g_i CC was large, and peaked at -6 ms (**Supplementary Fig. 4.8c, d**, left), indicating a lag between the two conductances. In the asynchronous model, g_e-g_i CC was smaller, and peaked instead at -2 ms (**Supplementary Fig. 4.8c, d**, right).

The dynamics of correlated variability in the synchronous model can thus be understood in the context of synaptic inputs. During the transient epoch, excitatory inputs to pairs of neurons are weakly, but significantly correlated. Inhibitory inputs are much more strongly correlated with one another, and also with the excitatory inputs. Crucially, the lag between excitation and inhibition allows for a "window of opportunity" during each cycle of the oscillation in which g_e-g_e and g_i-g_i correlations are independently manifested in pairs of membrane potentials. During the steady-state, correlations between inhibitory inputs and between inhibitory and excitatory inputs are only moderately reduced. However, correlations between excitatory inputs have decreased to near zero for many pairs, and thus V-V correlations across the population decrease significantly.

The distance-dependence of correlated variability reflects the spatiotemporal dynamics of network spiking

The results in the main text were calculated for forty pairs generated from 20 neurons randomly-selected from the entire network of 800 excitatory neurons. We tested the dependence of CC dynamics on average distance between neurons by repeating the analysis for 20 neurons randomly-selected from a group of 100 neighboring neurons (**Supplementary Fig. 4.9b**, top), and also for 20 neighboring neurons (**Supplementary Fig. 4.9c**, top).

For pairs from the group of 100 neurons, evoked <CC> was larger than when neurons were selected from the entire excitatory network (<CC> = 0.192 transient, 0.144 steady-state, **Supplementary Fig. 4.9b**, bottom). Values were larger still for pairs generated from 20 neighboring neurons (<CC> = 0.294 transient, 0.237 steady-state, **Supplementary Fig. 4.9c**, bottom). In addition, across-population CC variability for a given evoked epoch decreased with pool size. Interestingly, the modulation of <CC> by adaptation (that is, the proportional decrease

in <CC> from transient to steady-state) also decreased: <CC> decreased by 31.5% for neurons selected from the entire excitatory network, by 25% for those selected from the group of 100, and by 19% for the group of 20. This reflected the spatiotemporal dynamics of network spiking activity. During the transient epoch, spiking activity tended to be correlated across the network (thus increasing CC even for pairs of neurons separated by large distances). While adaptation reduced network spiking levels and correlated spiking generally, brief episodes of coherent spiking activity often appeared during the steady-state, during which spiking was far more correlated among nearby neurons than across the population (**Supplementary Fig. 4.9a**). Thus, correlated variability decreased from transient to steady-state for most pairs, but was more strongly diminished for distant pairs.

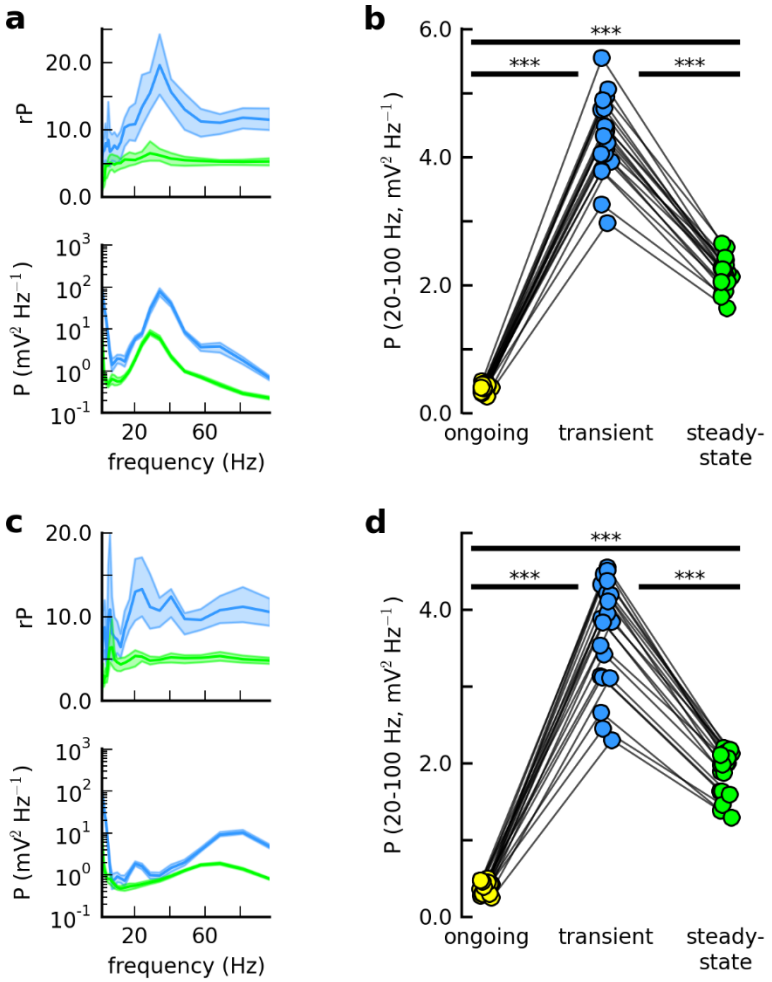

Supplementary Figure 4.6 Residual membrane potential relative power spectrum peaks reflect network spike rate oscillations. (a – b) Synchronous model. (c-d) Asynchronous model. (a) Top: relative power (evoked divided by ongoing) in residual membrane potential traces for one randomly-selected model neuron for the transient (blue) and steady-state (green) epochs. Bottom: power in network spike rate for the transient (blue) and steady-state (green) epochs. Dark lines indicate across-trial averages, bands indicate 95% confidence intervals (via bootstrapping, see Methods). (b) Same as in **Fig. 4.5a**, but for 20 randomly-selected pairs from SWA model. (c - d) Same as (a – b), but for AWA model.

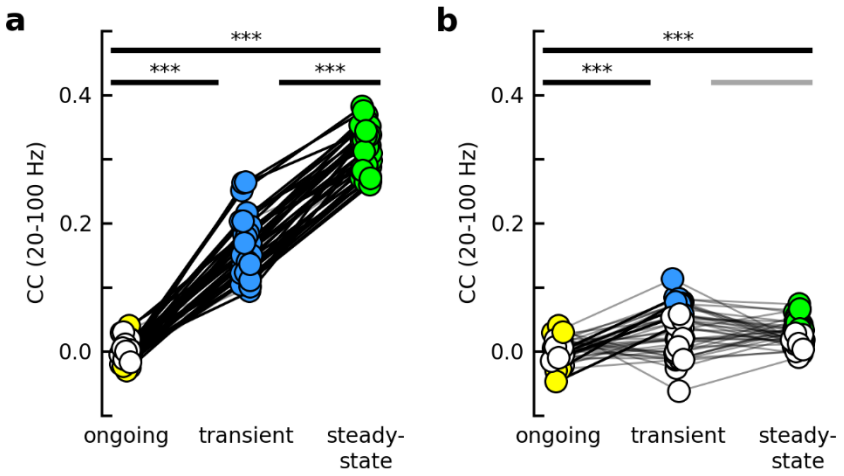

Supplementary Figure 4.7 Network spike rate oscillations increase gamma-band membrane potential correlated variability, and synaptic adaptation reduces correlated variability by abolishing these oscillations. (a) Same as in **Fig. 4.5d**, but for synchronous model without synaptic adaptation. Removing synaptic depression causes oscillations to become increasingly coherent, and correlated variability increases further from transient to steady-state. (b) Same as in (a), but for asynchronous model with synaptic adaptation. In the absence of network oscillations, the initial increase in correlated variability is much smaller, and CC does not decrease significantly from transient to steady-state, despite synaptic depression.

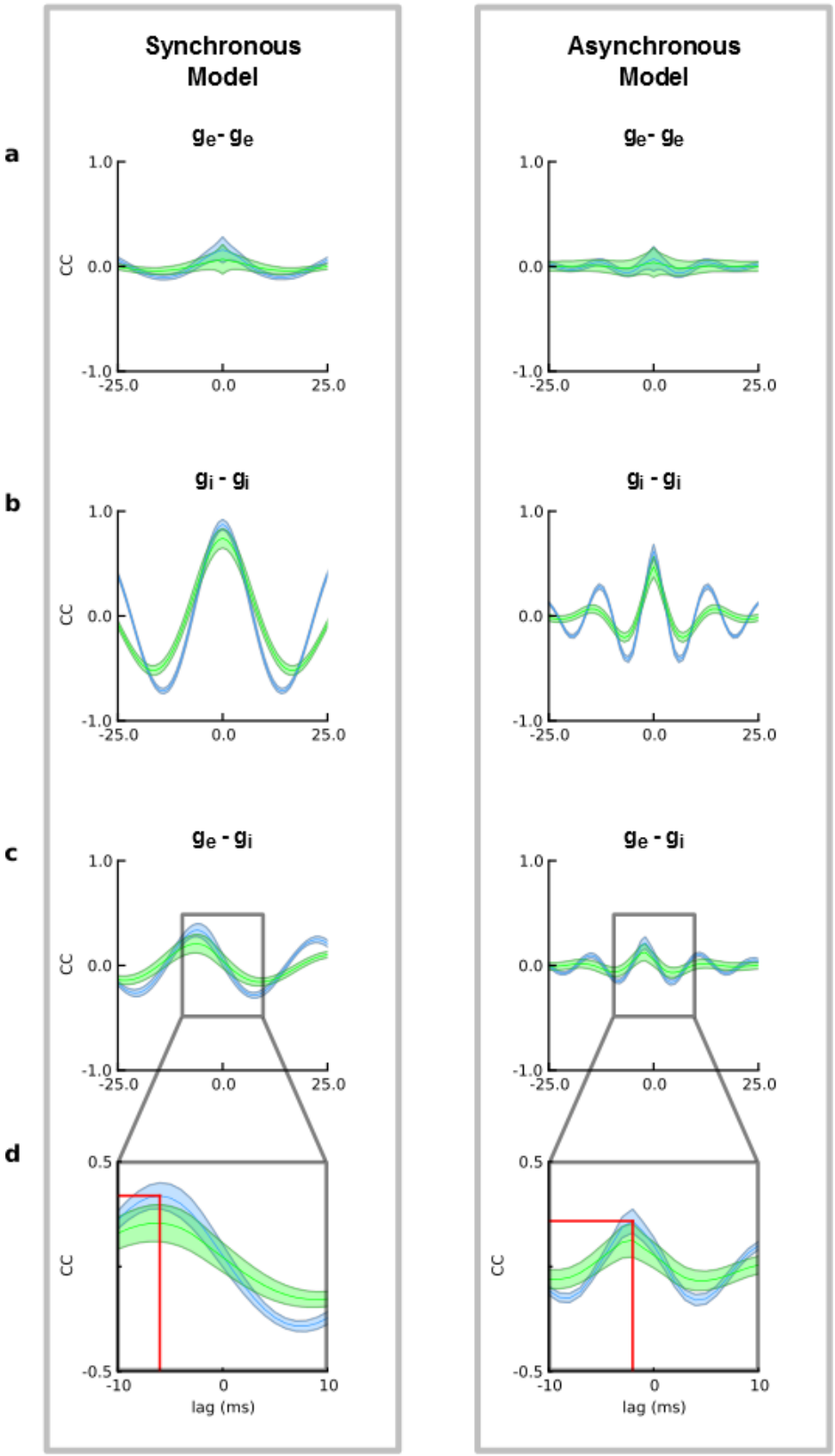
Synchronous Model
Asynchronous Model
a
b
c
d
g_e - g_e
g_i - g_i
g_e - g_i
CC
lag (ms)
1.0
0.0
-1.0
0.5
-0.5
-25.0
25.0
-10
10

Supplementary Figure 4.8 Network oscillations shape synaptic input correlated variability. (a – c) Correlated variability of synaptic conductances as a function of lag for the transient (blue) and steady-state (green) epochs, for the synchronous (left) and asynchronous (right) models (average +/- standard deviation, with average taken over trials and pairs, and standard deviation taken over pairs). Results calculated for inputs to forty pairs generated from twenty neurons randomly-selected from 800 excitatory neurons. Correlated variability is calculated for pairs of excitatory (a) and inhibitory (b) synaptic conductances, and for excitatory-inhibitory synaptic conductance pairs (c). (d) Close-up view of (c). Red lines indicate maximum transient CC values, and lag at which the maxima occur. In general, synaptic conductance correlations are stronger (have larger maximum amplitude) in the synchronous model. Crucial to membrane potential correlations is the larger excitatory lag in the synchronous model (6 ms vs. 2 ms, (d)).

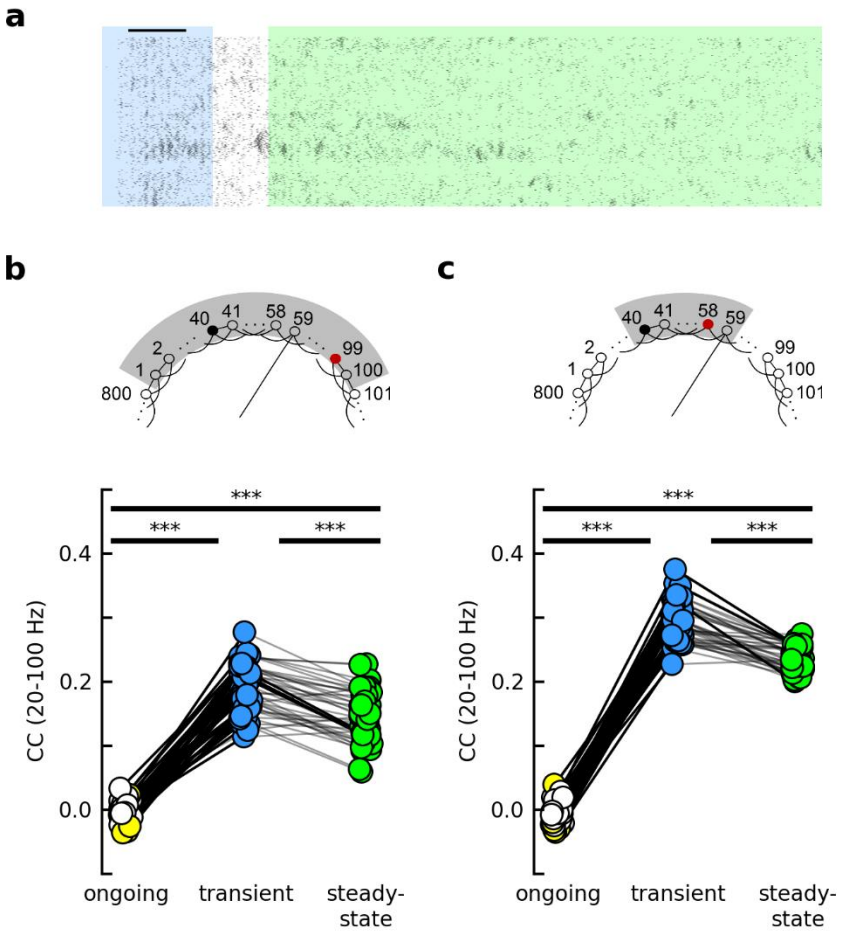

Supplementary Figure 4.9 The distance-dependence of V-V CC reflects the spatiotemporal dynamics of network spiking. (a) Evoked spiking activity for all 800 excitatory neurons (arranged in order of neuron number, or location in network) for one trial. Blue and green regions indicate transient and steady-state epochs, respectively. Scale bar indicates 200 ms. (b) Top: twenty neurons were randomly-selected from 100 neighboring neurons in the network. Bottom: Same as in **Fig. 4.5d**, but for neurons selected from cluster of 100. (c) Top: twenty neighboring neurons were selected from the network. Bottom: Same as in **Fig. 4.5d**, but pairs generated from 20 neighboring neurons.

4.5.6 Supplementary Information 6: Use of "test neurons" to calculate correlated variability in a model network

Individual neurons in our model network had much higher post-stimulus spike rates than those recorded in experiment. Because of the limited network size, this higher spike rate was necessary to generate large avalanches of activity. That is, a large number of synaptic inputs were required to bring a neuron to spike threshold, and in this small network, those inputs necessarily came from a larger percentage of the total network than in a more realistic sparse-spiking network. This is a common issue with small LIF networks(Abbott & Dayan, 2001). Importantly, this higher spike rate has implications for calculating V-V correlated variability: replacing spikes requires interpolation, which tends to mask synaptic inputs.

We sought to avoid this issue while maintaining reasonable simulation times. Therefore, to calculate CC for a pair of neurons in this network, we fed re-scaled versions of the synaptic conductances to "test" LIF pairs. Specifically, all conductances were multiplied by 0.75. In addition, the spike threshold of test neurons was -30 mV (vs. -40 mV in network neurons), thus reducing the probability to spike. Test neurons were identical to network neurons in all other respects. Thus, test neurons subsampled network spiking activity without reaching action potential threshold. All reported CC values for the model were calculated using such test pairs. In this way, each neuron in the model network can be thought to represent the net spiking output of a small cluster of neurons in a large, more sparse-spiking network. This implicitly assumes that individual cortical neurons fire sparsely and variably across trials, but clusters of such neurons are more reliable. We have (unpublished) MEA data that loosely supports this assumption. Specifically, a given stimulus presentation tends to evoke a rhythmic LFP oscillation at a given electrode

(suggesting synchronous activity near the electrode tip), yet spikes recorded from the same electrode (corresponding only to neurons very near the electrode) are sparse when present. In addition, the receptive field defined by spiking activity tends to be correlated with that defined by the LFP, suggesting that each sparse-spiking unit in the cluster follows a similar dynamic when spiking. This is consistent with a picture of a relatively reliable cluster of neurons composed of sparse-spiking and less reliable individual units. This is a common experimental observation, and is captured by LIF network models such as the ones used in this study(Brunel & Wang, 2003).

References for 4.5 Supplementary Information

Abbott, L., & Dayan, P. (2001). *Theoretical Neuroscience*. *Computational and Mathematical Modeling of Neural …* (Vol. 60). Retrieved from http://scholar.google.com/scholar?hl=en&btnG=Search&q=intitle:THEORETICAL+NEUROSCIENCE#3\nhttp://scholar.google.com/scholar?hl=en&btnG=Search&q=intitle:Theoretical+Neuroscience#3

Brunel, N., & Wang, X.-J. (2003). What determines the frequency of fast network oscillations with irregular neural discharges? I. Synaptic dynamics and excitation-inhibition balance. *Journal of Neurophysiology*, *90*(1), 415–430. http://doi.org/10.1152/jn.01095.2002

Buzsáki, G. (2006). *Rhythms of the Brain*. *Rhythms of the Brain* (Vol. 1). Oxford University Press. http://doi.org/10.1093/acprof:oso/9780195301069.001.0001

Hasenstaub, A., Shu, Y., Haider, B., Kraushaar, U., Duque, A., & McCormick, D. a. (2005). Inhibitory postsynaptic potentials carry synchronized frequency information in active cortical networks. *Neuron*, *47*(3), 423–35. http://doi.org/10.1016/j.neuron.2005.06.016

Larson-Prior, L. J., Ulinski, P. S., & Slater, N. T. (1991). Excitatory amino acid receptor-mediated transmission in geniculocortical and intracortical pathways within visual cortex. *Journal of Neurophysiology*, *66*(1), 293–306. Retrieved from http://www.ncbi.nlm.nih.gov/pubmed/1681038

Marchiafava, P. L. (1983). An ``antagonistic'' surround facilitates central responses by retinal ganglion cells. *Vision Research*, *23*(10), 1097–1099. Retrieved from http://www.ncbi.nlm.nih.gov/pubmed/6649427

Mazzoni, A., Brunel, N., & Panzeri, S. (2008). How gamma-band oscillatory activity participates in encoding of naturalistic stimuli in random networks of excitatory and inhibitory neurons. *BMC Neuroscience*, *9*(Suppl 1), P115. http://doi.org/10.1186/1471-2202-9-S1-P115

Oren, I., Mann, E. O., Paulsen, O., Ha, N., & Hájos, N. (2006). Synaptic currents in anatomically identified CA3 neurons during hippocampal gamma oscillations in vitro. *The Journal of Neuroscience : The Official Journal of the Society for Neuroscience*, *26*(39), 9923–9934. http://doi.org/10.1523/JNEUROSCI.1580-06.2006

Shew, W. L. W. L., Clawson, W. P. W. P., Pobst, J., Karimipanah, Y., Wright, N. C. N. C., & Wessel, R. (2015). Adaptation to sensory input tunes visual cortex to criticality. *Nature Physics*, *11*(8), 659–663. http://doi.org/10.1038/nphys3370

Tan, A. Y. Y., Chen, Y., Scholl, B., Seidemann, E., & Priebe, N. J. (2014). Sensory stimulation shifts visual cortex from synchronous to asynchronous states. *Nature*, *509*(7499), 226–229. http://doi.org/10.1038/nature13159

Wang, X.-J. J. (2010). Neurophysiological and computational principles of cortical rhythms in cognition. *Physiological Reviews*, *90*(3), 1195–1268.

http://doi.org/10.1152/physrev.00035.2008

Yang, H., Shew, W. L., Roy, R., & Plenz, D. (2012). Maximal Variability of Phase Synchrony in Cortical Networks with Neuronal Avalanches. *Journal of Neuroscience, 32*(3), 1061–1072. http://doi.org/10.1523/JNEUROSCI.2771-11.2012

Chapter 5

The coupling of synaptic inputs to local cortical activity differs among pyramidal neurons and adapts following stimulus onset

Cortical activity contributes significantly to the high variability of sensory responses of interconnected pyramidal neurons, which has crucial implications for sensory coding. Yet, largely because of technical limitations of in vivo intracellular recordings, the coupling of a pyramidal neuron's synaptic inputs to the local cortical activity has evaded full understanding. Here, we obtained excitatory synaptic conductance (g) measurements from pyramidal neurons and local field potential (LFP) recordings from adjacent cortical circuits during visual processing. We found a range of g-LFP coupling across pyramidal neurons. Importantly, for a given neuron, g-LFP coupling increased at stimulus onset, and then relaxed towards intermediate values during continued visual stimulation with naturalistic movies. A model network with connectivity structure and synaptic depression reproduced both the diversity and the dynamics of g-LFP coupling. In conclusion, these results establish a rich dependence of single-neuron responses on anatomical, synaptic, and emergent network properties.

5.1 Introduction

Cortical neuron sensory responses are remarkably variable across trials(Britten, Shadlen, Newsome, & Movshon, 1993; Carandini, 2004; Scholvinck, Saleem, Benucci, Harris, & Carandini, 2015). Because this variability tends to be correlated between pairs of nearby neurons (see Kohen, Cohn 2011 and Doiron, et al. 2016 for reviews), it likely influences population coding of sensory information(Abbott & Dayan, 1999; Averbeck, Latham, & Pouget, 2006; Shadlen & Newsome, 1998). With advances in recording techniques, it has become increasingly obvious that single-neuron variability reflects fluctuations that are shared across large regions of cortex(Lin, Okun, Carandini, & Harris, 2015; Okun et al., 2015; Scholvinck et al., 2015). That is, sensory input interacts with intrinsic cortical activity, with global cortical fluctuations influencing single-neuron responses. Appropriately, a recent study has introduced the term "population coupling" to describe this relationship(Okun et al., 2015). This and other studies have shown that the coupling of spiking activity is remarkably diverse across neurons (likely reflecting connectivity(Okun et al., 2015; Pernice, Staude, Cardanobile, & Rotter, 2011)), yet can also change with sensory stimulation(Haider, Schulz, & Carandini, 2016; Tan, Chen, Scholl, Seidemann, & Priebe, 2014) and network state(Haider, Schulz, & Carandini, 2016; Okun et al., 2015; Scholvinck et al., 2015). Moreover, the effects of this globally-derived input (i.e., additive vs. multiplicative response gain) may reflect specific mechanisms by which feedback exerts its influence on the response(Larkum, 2013; Reynolds & Heeger, 2009). This rich dependence of single-neuron responses on anatomical and emergent network properties appears to represent a fundamental principle of cortical function, and is only beginning to be explored. Here, we investigate three questions vital to a better understanding of cortical variability and its effects on sensory coding. (1) What is the nature of response variability in cortical microcircuits? (2) How strongly are single-neuron synaptic input fluctuations coupled with those of the local population? (3) To what degree are the dynamics of

response variability and population coupling determined by the cortical network, and what are the relevant network parameters?

While spike-based studies have yielded many important insights, this approach has two inherent shortcomings. First, it excludes the vast majority neurons, which are sparse-spiking(Henze et al., 2015; O'Connor, Peron, Huber, & Svoboda, 2010; Shoham, O'Connor, & Segev, 2006; Thompson & Best, 1989) and therefore yield unreliable statistics for the analysis of correlated variability(Cohen & Kohn, 2011) (**Figure 5.1a, b**). Second, it involves sampling populations of neurons that are visible to the experimentalist, but which may not represent relevant or complete cortical microcircuits. Patch clamp recordings of synaptic inputs represent one solution to these two problems(Shoham et al., 2006). First, when the recorded neuron is viewed as a component member of the network, the subthreshold inputs provide a measure of activity that is agnostic to output spike rate. A second perspective, motivated by anatomical connectivity, recognizes the neuron as a "device" that samples an enormous and extremely relevant pool of presynaptic neurons. Thus, subthreshold recordings allow the experimenter to "tap into" the cortical circuitry itself, and infer response properties (e.g., variability) of these large populations(Ikegaya, Aaron, Cossart, Aronov, & Lampl, 2004; MacLean, Watson, Aaron, & Yuste, 2005; Mokeichev et al., 2007) (**Figure 5.1a, b**). Despite the potential of this technique, it is rarely implemented *in vivo*; it is difficult to obtain stable patch clamp recordings of cortical sensory responses, and spatially-extended cortical pyramidal neurons confound the interpretation of voltage clamp data(Armstrong & Gilly, 1992; Koch, 2004; Spruston, Jaffe, Williams, & Johnston, 1993). Here, we overcome these challenges to address the first two questions above. First, we recorded subthreshold membrane potential visual responses from cortical pyramidal

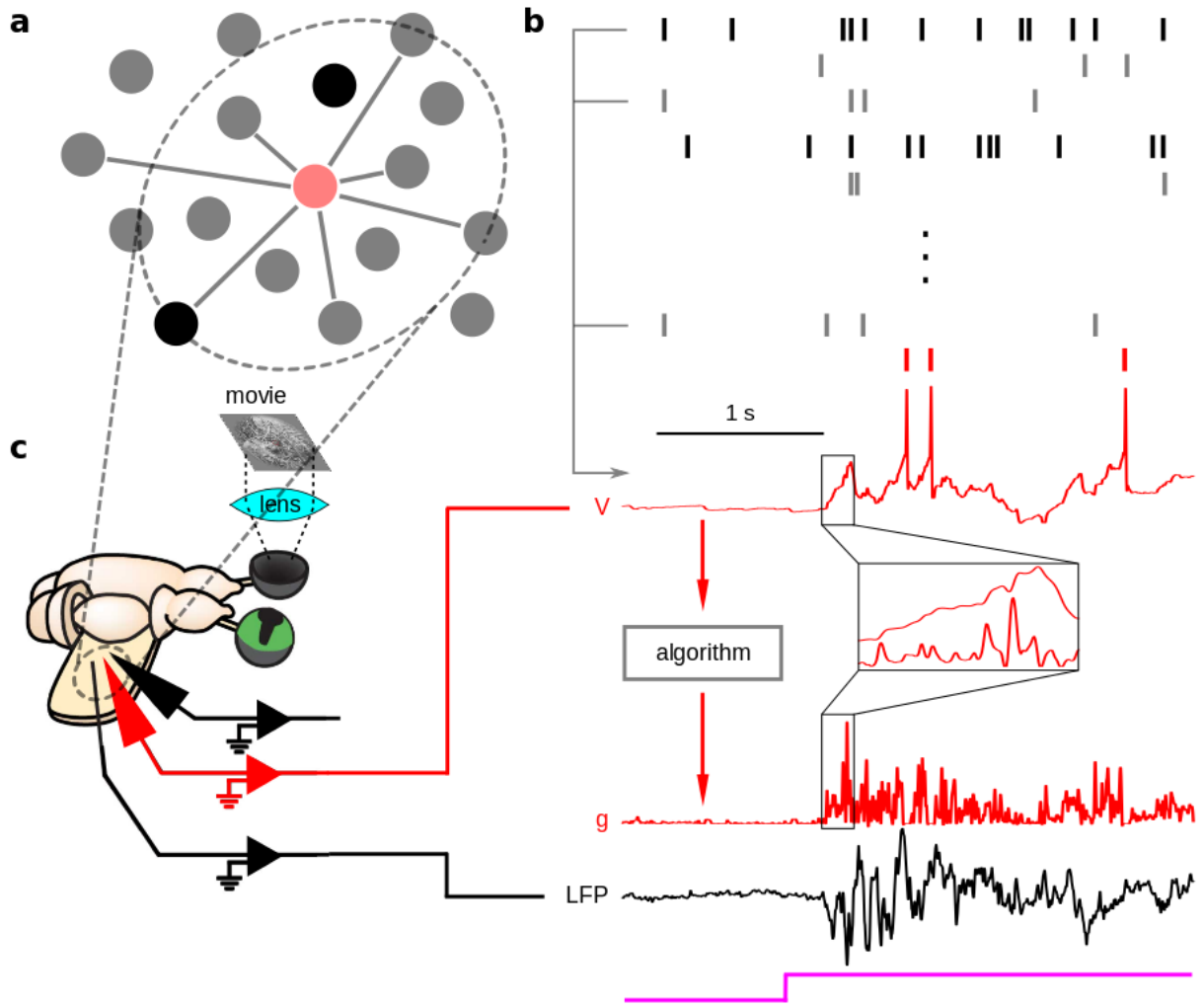

Figure 5.1. Individual neurons subsample the cortex, and provide a spike-rate-independent measure of cortical sensory responses. (a) Cortical neurons are primarily sparse-spiking units (low opacity circles), and each neuron subsamples the cortex by receiving synaptic inputs from a large, biologically relevant subpopulation. (b) While high-spike-rate neurons (high opacity rasters) alone provide reliable statistics for analysis of spiking responses, the subthreshold activity of a randomly-selected neuron (e.g., red voltage trace corresponding to red rasters) communicates information about the time course of presynaptic spiking activity. (c) Left: We recorded the subthreshold membrane potentials of cortical pyramidal neurons, as well as the nearby local field potential (LFP) while presenting movies to the retina in the turtle eye-attached wholebrain *ex vivo* preparation. Right: We used an algorithm (see Methods) to infer the excitatory synaptic conductance (g) from V, which gave a more detailed view of synaptic activity (inset). We investigated the nature of the variability in g, and its coupling with that of the simultaneously-recorded LFP.

neurons in the turtle eye-attached wholebrain *ex vivo* preparation (**Figure 5.1c**). We then applied a recently-developed algorithm(Yaşar et al., 2016) to infer the excitatory synaptic conductance (g) from V (**Figure 5.1c**), and analyzed the response variability in g. Finally, we calculated the correlated variability for g and the nearby local field potential (LFP). We found that visual stimulation evoked significant increases in g and LFP variability. The variability was typically large relative to the average response, and was a mix of multiplicative and additive noise. Across the population of cells, g-LFP correlated variability (CC) was highly variable, and transiently increased with visual stimulation.

We addressed the third question by implementing a small-world network of leaky integrate-and-fire neurons, subject to Poisson process external inputs and synaptic depression with recovery. This model reproduces three experimentally-observed aspects of evoked activity: large across-trial response variability, diverse g-LFP coupling across populations of nearby neurons, and the evoked coupling dynamic. These response properties are largely determined by the distribution of synaptic weights and the network state, which is highly sensitive to such network parameters as spatial clustering, synaptic time constants, and adaptation.

Together, our results provide a clearer picture of the subthreshold coordination dynamics corresponding to suprathreshold response variability and population coupling in cortex. Moreover, they implicate specific anatomical and emergent network properties that shape cortical variability and coordination during sensory processing.

5.2 Results

5.2.1 Visual stimulation increases synaptic and local population activity

To quantify the response variability of synaptic inputs and its coupling with that of the local population, we recorded the membrane potential (V) from 39 pyramidal neurons in visual cortex of the turtle *ex vivo* eye-attached whole-brain preparation during visual stimulation of the retina (**Figure 5.1c**). For 21 of these neurons, we also recorded the nearby LFP, which has been shown to be a reliable estimator of local synaptic activity(Haider, Schulz, Häusser, & Carandini, 2016). We then used a recently-developed algorithm(Yaşar et al., 2016) to estimate the excitatory synaptic conductance (g) from V (**Figure 5.1d**, and see Methods).

Ongoing activity in turtle visual cortex was relatively quiescent, typically with infrequent postsynaptic potentials at the level of the membrane potential, and little to no baseline LFP activity (**Figure 5.1d, 2a**). On a minority of trials, this quiescent activity was interrupted by spontaneous "bursts" of activity lasting up to hundreds of milliseconds that were qualitatively similar to visual responses (**Figure 5.2a, d**). Visual stimulation evoked barrages of postsynaptic potentials, and large fluctuations in the nearby LFP (**Figure 5.1d, 2a**), with orders-of-magnitude increases in average power for both g and LFP (population-averaged relative power $\langle rP \rangle = 3632.7 \pm 3538.0$, mean $\pm$ s.e.m., **Figure 5.2b, c**, $\langle rP_{LFP} \rangle = 1902.9 \pm 1350.7$, data not shown, transient). Response amplitudes (**Figure 5.2a**) and power (**Figure 5.2b, c**) decreased from transient to steady-state, despite persistent visual stimulation ($\langle rP \rangle = 1251.9 \pm 962.5$, steady-state; $P = 6.06 \times 10^{-8}$ for transient – steady-state comparison, Wilcoxon signed-rank test; $\langle rP_{LFP} \rangle = 557.9 \pm 449.1$, steady-state; $P = 1.2 \times 10^{-3}$ for transient – steady-state comparison, Wilcoxon signed-rank test).

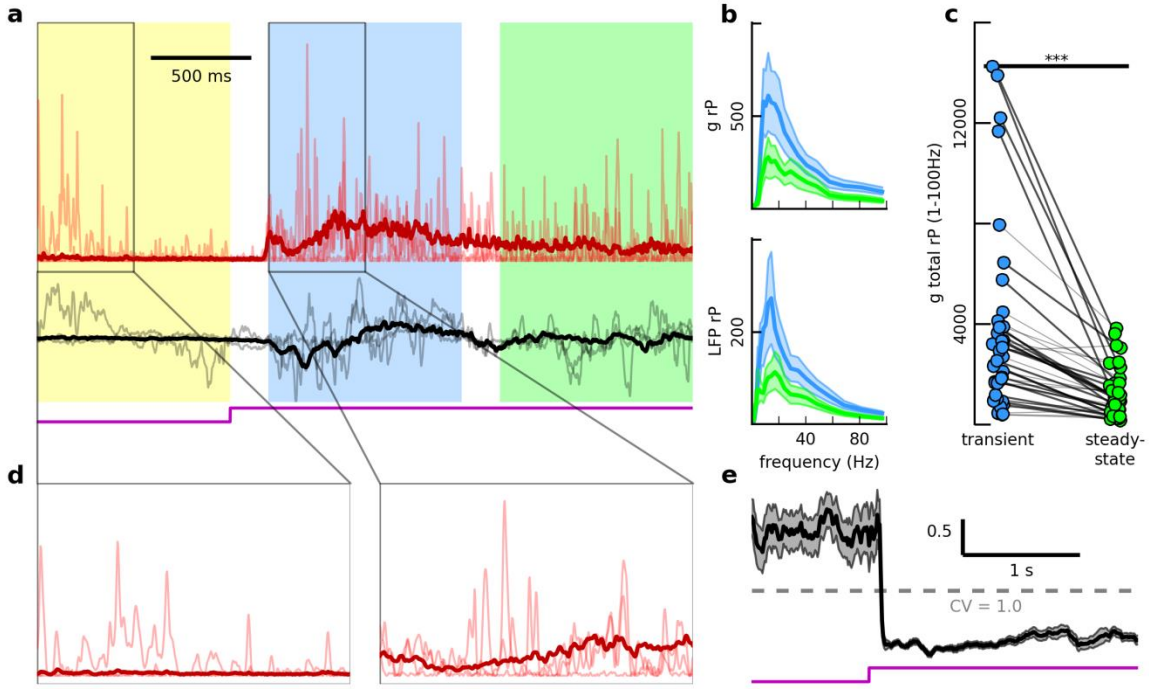

Figure 5.2. Visual stimulation evokes increases in synaptic activity, and responses are highly variable across trials. (a) Inferred excitatory synaptic conductance (g, red) and measured LFP (black) for three trials (low opacity), and average across 32 trials (high opacity). Colors indicate ongoing (yellow), transient (blue), and steady-state (green) epochs (see Results and Methods). (b) Relative power spectra (mean $\pm$ bootstrap intervals, see Methods) for g (top) and LFP (bottom) for transient (blue) and steady-state (green) epochs, for example pair in (a). (c) Total relative power (1 – 100 Hz) for 39 cells. Each blue (green) dot represents the across-trial mean relative power for one cell during the transient (steady-state) epoch. High opacity lines connecting dots indicate significant change across epochs ($P < 0.05$, bootstrap comparison test, see Methods). Asterisks above line connecting epochs indicate $P < 1 \times 10^{-3}$ (Wilcoxon signed-rank test). (d) Close-up view of ongoing (left) and evoked (right) synaptic activity. (e) Coefficient of variation (CV) as a function of time for 39 cells (mean $\pm$ s.e.m.). Dashed line indicates CV = 1.0.

5.2.2 Visual responses are highly variable across trials

For a given cell and nearby LFP, the across-trial average responses to a given stimulus displayed clear temporal structure (**Figure 5.2a**). Still, responses were highly variable across stimulus presentations; single-trial fluctuations were large relative to the mean response, with the across-trial variability increasing along with the across-trial average activity (**Figure 5.2a, d**). To determine the relationship between the variability and the average response, we calculated the scaled variability, or coefficient of variation (CV), as a function of time, for the population of all cells (see Methods). While variability of evoked activity was larger than that of ongoing activity (**Figure 5.2d**), the population-averaged CV (<CV>) decreased after stimulus onset, and slowly recovered (**Figure 5.2e**). Using the windows of activity defined above, we found that this initial decrease was significant (<CV> = 1.83 $\pm$ 0.13 ongoing, 0.22 $\pm$ 0.04 transient, P = 1.74 x 10^{-16} for ongoing – transient comparison, Wilcoxon signed-rank test), and that <CV> increased significantly from transient to steady-state (<CV> =, 0.36 $\pm$ 0.06 steady-state, P = 1.74 x 10^{-16} for transient – steady-state comparison, Wilcoxon signed-rank test), but remained significantly smaller than during ongoing activity (P = 1.74 x 10^{-16} for ongoing – steady-state comparison, Wilcoxon signed-rank test).

5.2.3 Additive and multiplicative noise contribute to response variability

We next investigated the nature of this single-trial variability. Even when a single-trial response deviates significantly from the mean response, it may follow a very similar (or in the extreme case, an identical) time course. This would indicate a high degree of "multiplicative noise": a uniform modulation of the presynaptic population's sensory response. Alternatively, in

the case of purely "additive noise", the single-trial time series fluctuates randomly about the average, consistent with noise amplitudes that vary across members of the presynaptic population.

To address this question, we first binned each single-trial inferred conductance (summing over 100 ms bins, resulting in $\tilde{g}$), and then calculated the across-trial average binned conductance ($\langle \tilde{g} \rangle_{trials}$, **Figure 5.3a**, and see Methods). By visual inspection, it was evident that individual responses contained both additive and multiplicative noise (**Figure 5.3a**). For example, a typical response that was somewhat "enveloped" by the average time course (indicating multiplicative noise) also tended to possess small, random fluctuations about the mean, or in some instances larger deviations away from the mean (**Figure 5.3a**, trial 3, steady-state epoch), examples of additive noise. To quantify the contributions of each component, we regressed $\tilde{g}$ onto $\langle \tilde{g} \rangle_{trials}$ for each trial, and took the across-trial median R^2 value for each cell and epoch. For a given cell, the across-trial average was a relatively poor predictor of the single-trial response (see example cell in **Fig 3b**); across the population, the average response explained only 28.1 $\pm$ 13.9% of the variance in individual trials for the transient epoch (across-cell average explained variance $<R^2>$ = 0.28 $\pm$ 0.14, **Figure 5.3c**). The explained variance was even lower during the steady-state ($<R^2>$ = 0.17 $\pm$ 0.15, **Figure 5.3c**), decreasing significantly from that of the transient epoch (P = 1.5 x 10^{-3} for transient – steady-state comparison, Wilcoxon signed-rank test). Evidently, single-trial responses contained substantial amounts of both multiplicative and additive noise, with additive noise dominating. In addition, the reliability of a single-trial response (as measured by its relationship to the across-trial average) diminished over the duration of the response.

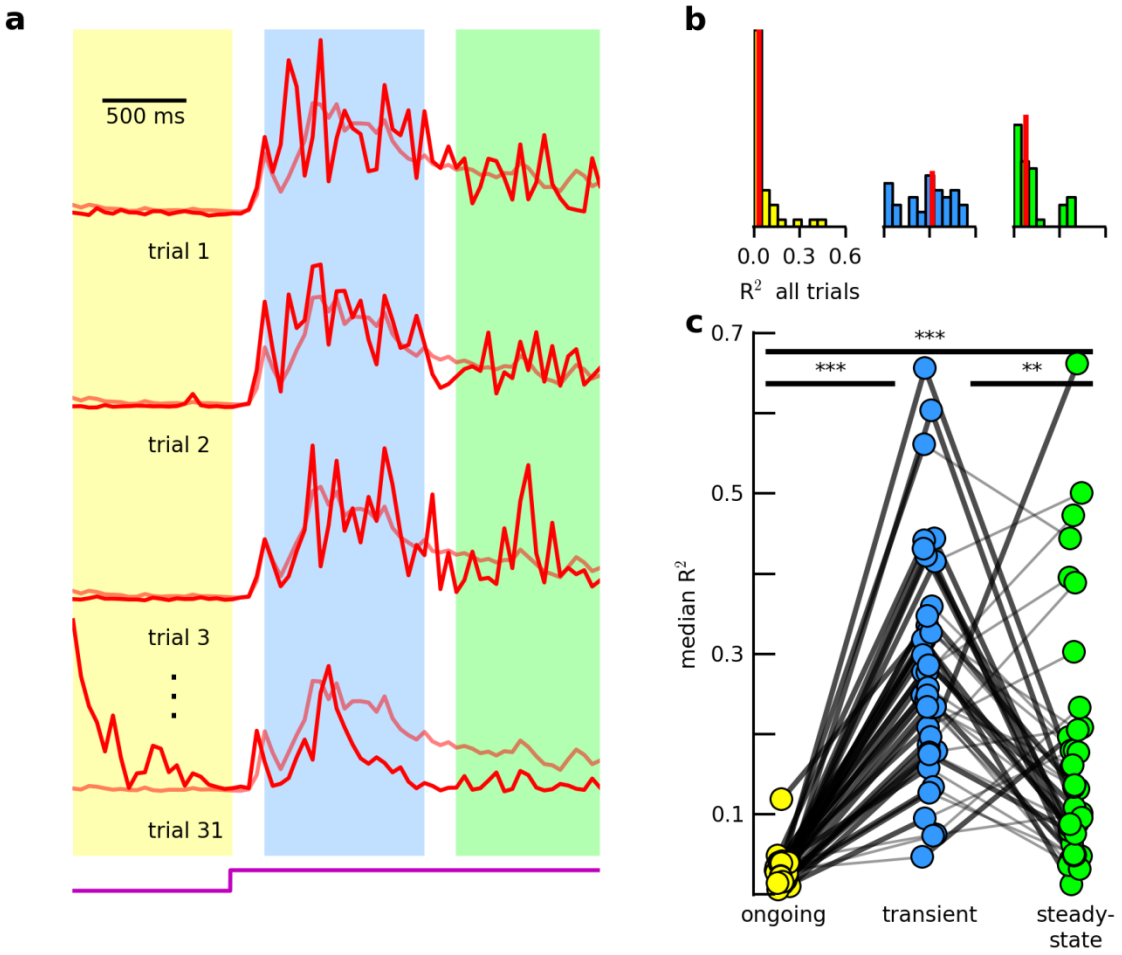

Figure 5.3. Single-trial variability is a mix of additive and multiplicative noise. (a) Inferred excitatory synaptic conductance, integrated over a 50 ms sliding window (with no overlap) for individual trials (high opacity), and across-trial average (low opacity, see Methods). (b) Across-trial distribution of R^2 values resulting from linear regression of single-trial response onto average response for ongoing (left), transient (center), and steady-state (right) epochs. Red vertical lines indicate medians. (c) Across-trial median R^2 values for 39 cells, for each epoch. Dot colors, connecting line opacities, and asterisks as in 2(b), with ** indicating $0.001 \leq P < 0.01$, Wilcoxon signed-rank test.

5.2.4 Correlated variability amplitude transiently increases following visual stimulation

Single-neuron response variability of this magnitude has the potential to profoundly influence sensory coding, provided it is significantly coupled across a population of neurons(Abbott & Dayan, 1999; Averbeck et al., 2006; Shadlen & Newsome, 1998). We quantified this "population coupling" for 21 cells by calculating the single-trial residual responses for the estimated conductance (g_r, the single-trial time series with the across-trial average time series subtracted) and the nearby LFP (**Figure 5.4a**) and calculating the Pearson correlation coefficient for residual pairs for each trial and epoch (see Methods).

For a given stimulus condition, the trial-averaged correlation coefficient (CC) was broadly distributed across the population (**Figure 5.4b**). During ongoing activity, CC was significantly nonzero for seven of 21 pairs ($P < 0.05$, comparison to shuffled data using Wilcoxon signed-rank test, see Methods). With visual stimulation, the population of pairs became more anti-correlated (**Figure 5.4b**); CC amplitudes increased significantly for 10 pairs ($P < 0.05$, across-epoch bootstrap comparison) and the population average decreased significantly (such that the amplitude increased; $\langle CC \rangle = 0.009 \pm 0.04$ ongoing, $P = 0.50$ for comparison to shuffled data; $\langle CC \rangle = -0.07 \pm 0.04$ transient, $P = 1.1 \times 10^{-4}$ for comparison to shuffled data; $P = 1.9 \times 10^{-4}$ for ongoing – transient comparison, Wilcoxon signed-rank test, **Figure 5.4b, 4c, top**). During this transient epoch, CC was significantly nonzero for 14 pairs ($P < 0.05$, comparison to shuffled data). This elevated level of coordination soon relaxed: from transient to steady-state, CC amplitudes significantly decreased for 5 pairs ($P < 0.05$, across-epoch bootstrap comparison), such that CC was significantly nonzero for 7 pairs ($P < 0.05$, comparison to shuffled data), and the population average increased significantly toward zero ($\langle CC \rangle = -0.02 \pm 0.05$ steady-state, $P = 0.005$ for

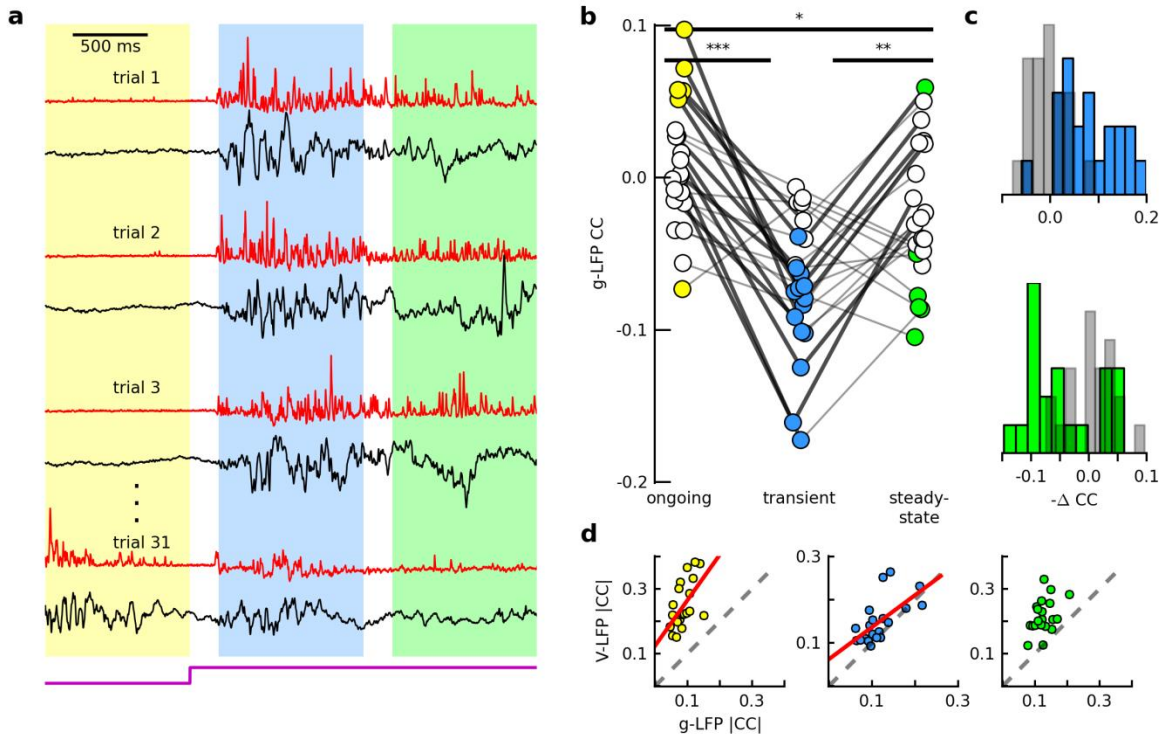

Figure 5.4. Synaptic input correlated variability transiently increases with visual stimulation. (a) Residual traces for g (red) and LFP (black) for multiple trials. (b) Across-trial average Pearson correlation coefficient for g and LFP residual traces, for 21 g-LFP pairs. Each dot indicates the across-trial average CC value for a given g-LFP pair. Filled dots indicate significant average values ($P < 0.05$, bootstrap comparison to shuffled data, see Methods). Connecting lines and asterisks as in 3(c), with * indicating $0.01 \leq P < 0.05$, Wilcoxon signed-rank test. (c) Top: Distribution of change in across-trial average CC values (multipled by -1) from ongoing to transient, for 21 g-LFP pairs (with results for shuffled data shown in gray). Bottom: same, but for transient to steady-state. (d) Absolute value of across-trial average CC for V and LFP vs. that for g and LFP for 21 cell-LFP pairs, for the ongoing (left), transient (center), and steady-state (right) epochs. Dashed line is unity line, and red line indicates significant linear regression fit. V-LFP |CC| values were significantly larger than g-LFP |CC| values for all epochs ($P = 8.86 \times 10^{-5}$ ongoing, $P = 2.2 \times 10^{-3}$ transient, $P = 8.9 \times 10^{-5}$ steady-state, Wilcoxon signed-rank test). Values were significantly related for the ongoing ($r^2 = 0.31$, $P = 0.01$ linear regression) and transient ($r^2 = 0.40$, $P = 0.0029$) epochs, but not the steady-state ($r^2 = 0.18$, $P = 0.06$).

transient – steady-state comparison, Wilcoxon signed-rank test) to values that were not significant across the population (P = 0.11 for comparison to shuffled data, **Figure 5.4b, 4c, bottom**).

These results suggest that the across-trial variability in evoked synaptic inputs to an individual neuron is, on average, coupled to that of other neurons in a nearby population in the early response phase. Moreover, the strength of this coupling is highly variable across cells. Coupling is not static, however; while response reliability decreases from the early to the late phase of the visual response (**Figure 5.3**), the coupling strength does as well (**Figure 5.4b, c**), suggesting that large single-trial fluctuations in the late response are more effectively "averaged out" across a large population.

5.2.5 The dynamics of g-LFP correlated variability are consistent with known excitation-inhibition dynamics

When combined with what is known of the recorded signals and excitatory-inhibitory dynamics, these g-LFP CC results provide a means for testing the validity of the inferred excitatory synaptic conductance. First, V and LFP are both a mix of excitation and inhibition (while our inferred conductance excludes inhibition), so for a given cell, V-LFP CC should be larger than g-LFP CC in a given window of activity. Second, because excitatory currents make a large contribution to V and LFP, and because inhibitory currents generally tend to track excitatory currents(Atallah & Scanziani, 2009; Isaacson & Scanziani, 2011; Wehr & Zador, 2003), g-LFP CC and V-LFP CC should be related.

Our results largely satisfied these predictions. First, for each epoch of activity, across the population of cells, CC amplitudes were larger for V-LFP than for g-LFP (**Figure 5.4d**). This was also true when V and LFP were filtered in the gamma band (thus removing the shared, slow

fluctuation to isolate the fast activity resulting from high-frequency synaptic inputs(Hasenstaub et al., 2005; Nowak, Sanchez-Vives, & McCormick, 1997; Poulet & Petersen, 2008), data not shown). Second, g-LFP and V-LFP CC amplitudes were significantly related for the ongoing and transient epochs for both 100 Hz low-pass (**Figure 5.4d**) and gamma band (data not shown) activity. There was also a positive relationship in the steady-state, but the trend was not significant ($P = 0.059$, **Figure 5.4d, right**). As such, these results provide further evidence for the reliability of the estimation algorithm.

5.2.6 Network properties shape response variability and g-LFP correlated variability

We next sought to infer the relative contributions to the observed response properties from the stimulus and the thalamocortical network. Specifically, we asked which aspects of the experimentally-observed phenomena could be reproduced by a model network subject to random external inputs (mimicking the stimulus), and what network parameters were relevant to these results.

We implemented a model network similar to that described previously (N. C. Wright, M. Hoseini, R. Wessel, unpublished observations, **Figure 5.5a**). The network consisted of 800 excitatory and 200 inhibitory leaky integrate-and-fire neurons. Excitatory – to – excitatory connections had small-world connectivity (3%), and all other connections were random (3% excitatory – to – inhibitory, 20% inhibitory – to – excitatory and inhibitory – to – inhibitory). Nonzero synaptic weights were drawn from a beta distribution with mean value 1.0, which approximated the "constellation-like" connectivity in cortex(Cossell et al., 2015). All neurons received Poisson process external inputs, and the stimulus was modeled as an increase in

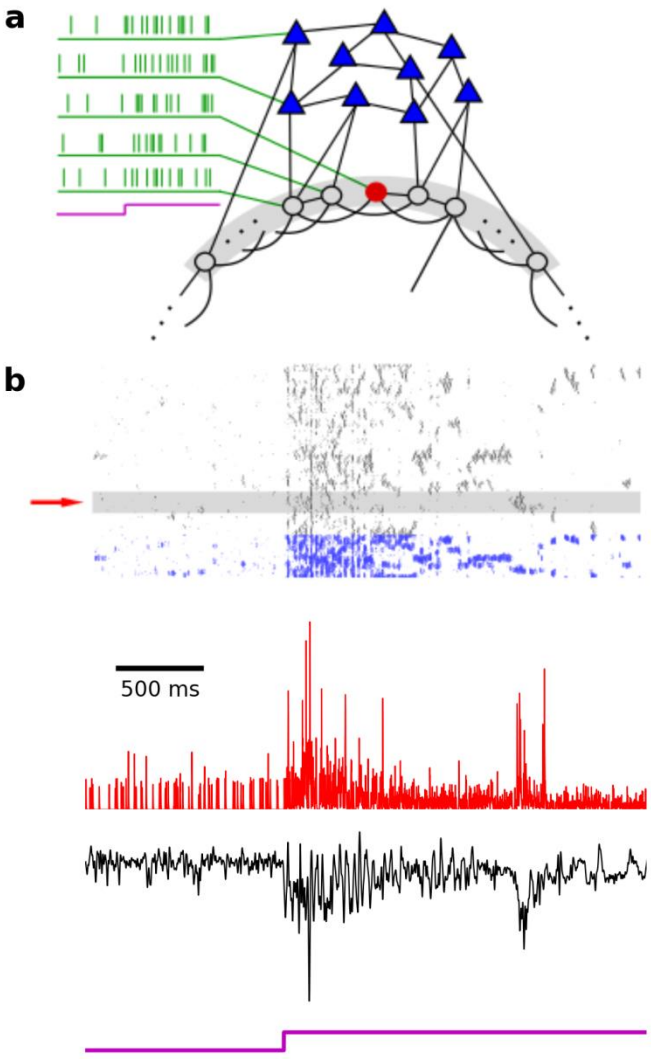

Figure 5.5. Model overview. (a) We implemented a model network of 800 excitatory and 200 inhibitory leaky integrate-and-fire neurons, all subject to Poisson process external inputs. Excitatory-excitatory connections had small-world connectivity, and all other connections were random. (b) Network parameters were tuned to give spike rate oscillations in the inhibitory (blue) and excitatory (black) populations in response to strong external drive. The LFP was modeled as the sum of synaptic currents to a subset of 100 neighboring neurons (gray region, and single trial in black below). The excitatory synaptic conductance was selected for neurons near the geometric center of this subset (single trial in red below, corresponding to neuron indicated by red arrow).

external input rate. The external drive was unique across neurons and trials during the ongoing epoch. After stimulus onset, the external drive was a mix of two components: one that was unique across neurons, but identical across trials (with proportionality constant 0.75) and one that was unique across both neurons and trials (with proportionality constant 0.25). Because visual stimulation reliably evoked strong LFP oscillations (**Figure 5.2a**, and see Shew, et al. 2015), we selected a set of synaptic rise and decay times that were consistent with network spike rate oscillations in response to strong external drive (**Figure 5.5b**). Each synapse depressed and slowly recovered in response to a presynaptic spike. We modeled the LFP as the sum of all synaptic currents(Atallah & Scanziani, 2009; Destexhe, 1998) to a subpopulation of 100 neighboring excitatory neurons. We selected 40 neurons from the geometric center of this population for analysis of excitatory conductances (**Figure 5.5b**, and see Methods).

As in experiment, g and LFP varied considerably across trials (**Figure 5.6a**), despite the stimulus being primarily the same across trials (see Methods). As with our experimental data, we quantified the dynamics of this variability by calculating the scaled variability (CV) over time. The CV dynamics were determined by both the statistics of the external drive and by network properties. When external drive during the ongoing epoch was sufficiently strong to cause sparse network spiking, CV for the total excitatory synaptic conductance to network neurons hovered near 1.0 ($\langle CV \rangle = 0.95 \pm 0.25$, **Figure 5.6b**). This value greatly exceeded that of the external inputs alone ($\langle CV \rangle = 0.15 \pm 0.09$, **Figure 5.6b**), which was due to the highly variable distribution of nonzero synaptic weights (**Figure 5.6c, top**). With stimulus onset, CV for external inputs decreased by design (to $\langle CV \rangle = 0.004 \pm 0.01$), and CV for total excitatory conductance initially did as well ($\langle CV \rangle = 0.40 \pm 0.16$ for transient epoch, $P = 4.27 \times 10^{-18}$ for ongoing – transient comparison, Wilcoxon signed-rank test). This decrease in CV was due inpart to the concerted

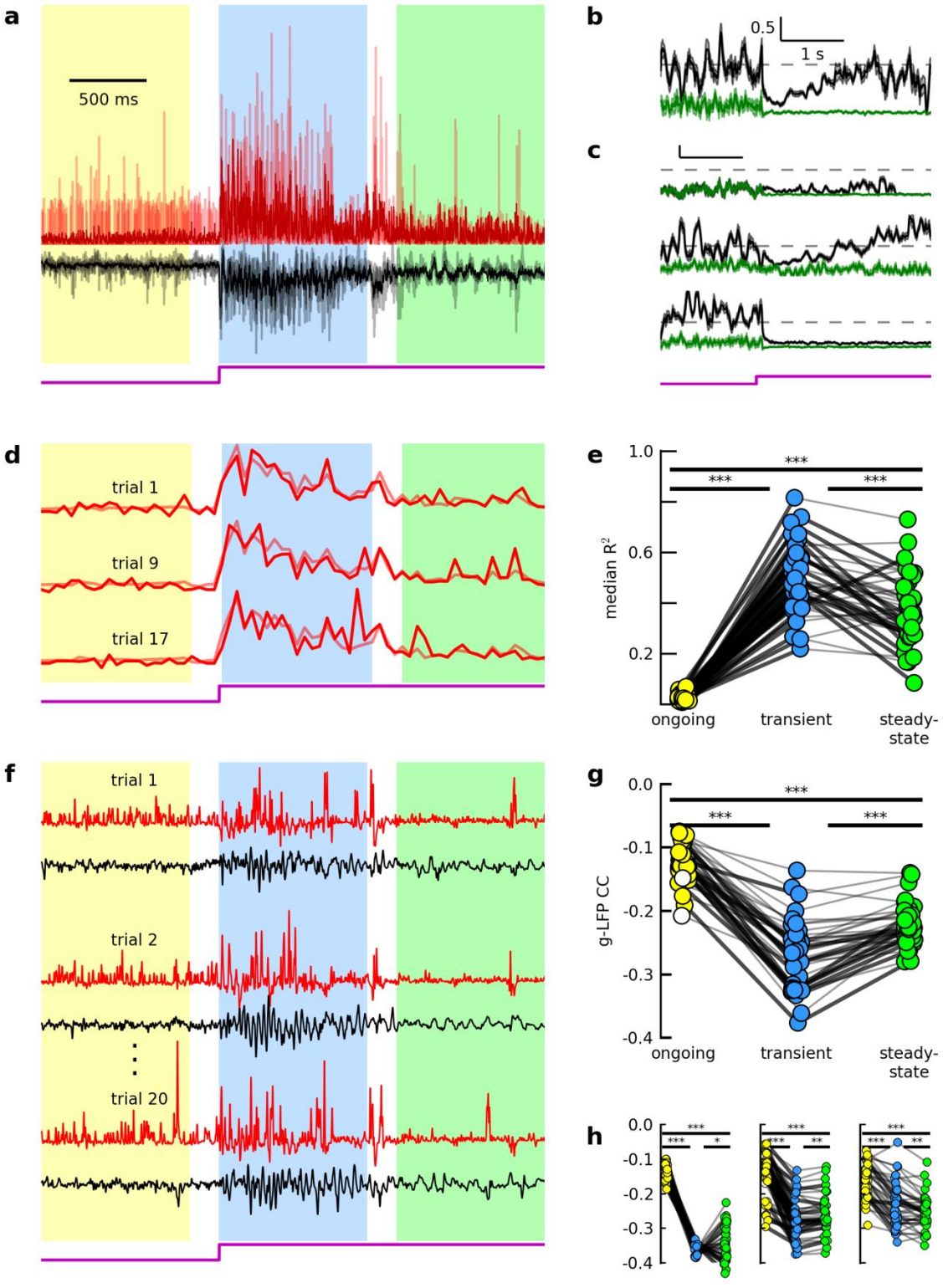
a
500 ms
b
0.5
1 s
c
d
trial 1
trial 9
trial 17
e
1.0
0.6
0.2
median R²
***
***
***
ongoing
transient
steady-state
f
trial 1
trial 2
trial 20
g
0.0
-0.1
-0.2
-0.3
-0.4
g-LFP CC
***
***
***
ongoing
transient
steady-state
h
0.0
-0.1
-0.2
-0.3
-0.4
***
***
*
***
***
**
***
***
**

Figure 5.6. A model network qualitatively reproduces the experimental results. (a) excitatory synaptic conductance for one model neuron (g, red) and nearby LFP (black) for three trials (low opacity), and average across 20 trials (high opacity). Colors indicate ongoing (yellow), transient (blue), and steady-state (green) epochs. Example cell is located at the geometric center of the pool defining the LFP (see Results and Methods). (b-c) A qualitative reproduction of experimental CV(t) depended on the synaptic weight distribution, the nature of the stimulus, and synaptic depression. (b) Coefficient of variation (CV) as a function of time (mean $\pm$ s.e.m.) for 40 cells randomly-selected from the network, for total excitatory synaptic conductance (black), and for external excitatory conductance (green). Dashed line indicates CV = 1.0. (c) CV for alternate model versions. Top: network with binary synaptic weights. Middle: network subject to unique stimulus on each trial. Bottom: network without synaptic adaptation. Scale bar and dashed line same as in (b). (d) Excitatory synaptic conductance for one model neuron, integrated over a 50 ms sliding window (with no overlap) for individual trials (high opacity), and across-trial average (low opacity, see Methods). (e) Across-trial median R^2 values for 40 cells randomly-selected from network, for each epoch. Dot colors, connecting line opacities, and asterisks as in 3(c). (f) Residual traces for g (red) for one model neuron and nearby LFP (black) for multiple trials. (g-h) A qualitative reproduction of the experimental g-LFP dynamic depended on the synaptic weight distribution, synaptic depression, and network oscillations. (g) Across-trial average Pearson correlation coefficient for g and LFP residual traces, for 40 g-LFP pairs (where 40 cells are selected from geometric center of pool defining LFP). Each dot indicates the across-trial average CC value for a given g-LFP pair. Filled dots indicate significant average values ($P \leq 0.05$, bootstrap comparison to shuffled data, see Methods). Connecting lines and asterisks as in 5(f). (h) Same as in (g), for alternate model versions. Left: network with binary synapses (i.e., synaptic weights either 1 or 0). Middle: network without synaptic depression. Right: Asynchronous network.

increase in external drive, and in part to the stimulus possessing a component that was identical across trials (**Figure 5.6c, middle**). Over the course of hundreds of milliseconds, CV for total excitatory conductance recovered to nearly that of the ongoing epoch (<CV> = 0.81 $\pm$ 0.17 for steady-state epoch, P = 1.80 x 10^{-16} for transient – steady-state comparison, P = 1.1 x 10^{-4} for ongoing – steady-state comparison, Wilcoxon signed-rank test), which was an exaggeration of the experimental scaled variability dynamic observed here (**Figure 5.2e**) and elsewhere(Churchland et al., 2010). Synaptic depression mediated this recovery (**Figure 5.6c, bottom**). Thus, CV values and dynamics depended on the distribution of synaptic weights, the across-trial reliability of external inputs, and synaptic adaptation.

The model qualitatively reproduced the contribution of additive and multiplicative noise to the total response variability. As in experiment, single-trial variability was a mix of both noise types (**Figure 5.6d**, compare to **Figure 5.3a**), and the relative contribution from additive noise increased from transient to steady-state (<R^2> = 0.50 $\pm$ 0.13 ongoing, <R^2> = 0.37$\pm$ 0.13 steady-state, P = 7.6 x 10^{-6} for transient – steady-state comparison, Wilcoxon signed-rank test, **Figure 5.6e**, compare to **Figure 5.3c**). This decrease in response reliability was not related to synaptic depression (data not shown), suggesting single trial "errors" compounded over the duration of the response. Notably, the percent of single-trial variance explained by the average response in either epoch was smaller than the 75% predicted by the stimulus. This surplus variability is therefore due to the only other source of randomness in the model: the state of the intracortical synapses at stimulus onset (due to the variable external drive and intracortical synaptic depression during the ongoing epoch, see Methods).

As in experiment, we calculated correlated variability (CC) for g-LFP pairs (**Figure 5.6f**). The synaptic weight distribution strongly influenced g-LFP CC distributions. For each epoch, CC

was broadly distributed across the population (**Figure 5.6g**). While some variability is to be expected from such a sparsely-connected network, CC distributions were far less variable in a network with binary synapses (but the same average synaptic weight, **Figure 5.6h, left**).

The dynamics of g-LFP CC depended on a variety of network parameters. We recently used a similar network to demonstrate the effects of coordinated spiking on gamma band membrane potential correlated variability (N. C. Wright, M. Hoseini, R. Wessel, unpublished observations). Briefly, when the external drive triggers network spike rate oscillations, excitatory synaptic inputs to a given neuron become strongly correlated with both excitatory and inhibitory inputs to other neurons (with a small lag between excitation and inhibition). This leads to strong membrane potential oscillations that are correlated across neurons, an effect that is not observed in an asynchronous driven network. This coordination dynamic is also manifested as an increase in g-LFP correlated variability from the ongoing to transient epoch ($\langle CC \rangle = -0.12 \pm 0.03$ ongoing; $\langle CC \rangle = -0.27 \pm 0.05$ transient; $P = 3.57 \times 10^{-8}$ for ongoing – transient comparison, Wilcoxon signed-rank test **Figure 5.6f**). Synaptic depression with slow recovery (see Methods) diminished network activity levels, and crucially, abolished large-scale coordinated spiking (**Figure 5.5b**). This had the effect of drastically reducing g-LFP CC amplitudes from transient to steady-state ($\langle CC \rangle = -0.22 \pm 0.03$ steady-state; $P = 1.1 \times 10^{-7}$ for transient – steady-state comparison, Wilcoxon signed-rank test, **Figure 5.6g**), despite persistent network activity (**Figure 5.5b, 6f**). When either synaptic depression was removed (**Figure 5.6h, middle**) or the network was tuned to remain asynchronous (**Figure 5.6h, right**, see Methods), changes in <CC> were much smaller across epochs, and did not qualitatively match the experimental results. As such, these results implicate emergent network oscillations – and the corresponding relevant anatomical network

properties (i.e., synaptic time constants and synaptic depression) – in the determination of g-LFP CC dynamics.

Taken together, the model investigation points to the cortical network as the primary determiner of the experimentally-observed response variability and population coupling dynamics of synaptic inputs. Specifically, the model identifies synaptic clustering, time constants, and depression as extremely relevant anatomical properties.

5.3 Discussion

To obtain a spike-rate-independent measure of single-neuron variability, and to measure its coupling with local population activity, we simultaneously recorded the membrane potential from pyramidal neurons and the nearby LFP in the turtle visual cortex during ongoing and visually-evoked activity (**Figure 5.1**). We estimated the excitatory synaptic conductance (g) from the membrane potential, and quantified the across-trial variability in g and correlated variability with the LFP. To identify relevant cortical network mechanisms, we implemented a small-world network of leaky integrate-and-fire neurons subject to external drive (**Figure 5.5**).

Studies spanning several decades have described the remarkable degree of variability in the sensory-evoked spiking responses of cortical neurons(Britten et al., 1993; Carandini, 2004; Scholvinck et al., 2015). Certain aspects of this variability suggest it is shaped by the cortex itself. First, cortical variability surpasses that of the inputs from LGN(Scholvinck et al., 2015). Second, evoked variability, when scaled by the overall activity level, tends to be smaller than that of spontaneous activity across a variety of cortical areas and behavioral states, suggesting it is a property of large, recurrent networks(Churchland et al., 2010). Third, single-neuron spiking

variability can be modeled as a mix of multiplicative and additive noise due to global cortical activity(Goris, Movshon, & Simoncelli, 2014; Lin et al., 2015). Our experimental results agree with this "cortico-centric" view of response variability. We observed that individual neurons subsampling the cortex receive excitatory synaptic inputs that are extremely variable across stimulus presentations (**Figure 5.2a, d, Figure 5.3**), with scaled variability (CV) decreasing soon after stimulus onset (**Figure 5.2e**). The time course of the visual response revealed the presence of both additive and multiplicative noise in the spatiotemporal sequence of presynaptic firing (**Figure 5.3**). Finally, across a variety of stimuli, scaled variability (**Figure 5.2e**) and the contribution from additive noise (**Figure 5.3**) increased from transient to steady-state. That is, response reliability and the nature of the variability changed in a stimulus-independent manner. Each of these results was qualitatively reproduced by a model network subject to an extremely simple external drive (**Figure 5.5, 6**).

Partitioning synaptic input variability into additive and multiplicative noise essentially assigns a measure of influence to two types of network fluctuations: a uniform scaling of the entire presynaptic pool (i.e., multiplicative noise), and scaling that is independent across subpopulations within the presynaptic pool (i.e., additive noise). Our experimental results suggest both types of modulation are present in visual responses, with the latter dominating at the time scale considered (**Figure 5.3**). Moreover, the variability in the early response contains almost twice as much multiplicative noise as that in the late response (**Figure 5.3c**). While it is possible that this dynamic is due to hidden, temporally variable, extracortical influences, our simple model network gave a similar result (**Figure 5.6d, e**), and points to an alternative explanation: a sensitivity to conditions at stimulus onset, with small deviations leading to increasingly random fluctuations about the mean over the duration of the response. Such chaotic dynamics are a hallmark of balanced

networks(Shadlen & Newsome, 1998; Vreeswijk & Sompolinsky, 1996). While at first glance this seems extremely disadvantageous to sensory coding, the balanced regime has other advantages, including fast responses to changes in external stimuli(Vreeswijk & Sompolinsky, 1996), effective signal propagation(Vogels & Abbott, 2005), and maximized information capacity(W. L. Shew, Yang, Yu, Roy, & Plenz, 2011).

Previous work has shown that population coupling based on spiking activity is broadly-distributed across cells, which may reflect the degree to which a given neuron samples the local population(Okun et al., 2015), and the structure of that connectivity(Pernice et al., 2011). In agreement with this, we found that g-LFP correlated variability was broadly-distributed across cells for a given stimulus condition (**Figure 5.4b**). Our model results further reinforce the hypothesis that connectivity underlies this variability: CC distributions were broadly-distributed for relatively realistic, "constellation-like" synaptic weight distributions (**Figure 5.6g**), but narrowly-distributed for binary synapses (**Figure 5.6h, left**). These distributions also shaped the dynamics of scaled variability (**Figure 5.6b, c, top**). Evidently, cortical connectivity patterns are manifested in the response variability and coordinated variability of synaptic activity, which likely reflect the response properties of population spiking observed elsewhere.

Despite this apparent dependence on anatomical connectivity, previous work has shown that g-LFP coupling can increase with visual stimulation(Haider, Duque, Hasenstaub, & McCormick, 2006). In agreement with this, we found that g-LFP correlated variability amplitudes significantly increased when we presented movies to the retina (**Figure 5.4b, 4c, top**). This effect was short-lived, however; g-LFP CC amplitudes decreased significantly after the early response phase (**Figure 5.4b, 4c, bottom**), despite persistent synaptic and local population activity (**Figure 5.2a-c, 4a**). Was this a case of external stimuli imposing a particular coordination dynamic on the

cortical circuitry, or was the thalamocortical system itself capable of exhibiting multiple coordination "states"? Our model results support the latter hypothesis: sufficiently strong external drive that is uncorrelated across neurons can trigger intrinsic network oscillations, which are characterized by elevated coupling of synaptic inputs, and the elevated coupling is abolished along with the oscillation (**Figure 5.5, 6**). These results are consistent with the observation that spontaneous fluctuations in cortical state can influence g-LFP(Haider, Schulz, Häusser, et al., 2016) and spike-spike(Okun et al., 2015; Scholvinck et al., 2015) population coupling. In addition, this decrease in g-LFP coupling is consistent with the observed decrease in multiplicative noise (**Figure 5.3**); single-trial fluctuations become increasingly independent across neuronal subpopulations, which should be reflected in the nearby LFP(Deweese & Zador, 2004). Moreover, our results build on this previous work by identifying specific anatomical features of cortex (e.g., synaptic time constants and synaptic adaptation) capable of influencing population coupling dynamics via emergent network phenomena.

According to one view of population coding, the decrease in g-LFP coupling in the late response may benefit cortical function: while steady-state activity is less reliable than that in the early response (**Figure 5.2e, 3**), these later fluctuations are more private, and therefore tend to average out across a neural ensemble(Zohary, 1994). Our model results suggest this does not simply reflect a decrease in overall activity level, but rather the abolition of large-scale spike rate oscillations by synaptic depression (**Figure 5.5b, 6**). This is consistent with the emerging view that adaptation (in cortex and elsewhere) serves as much more than a modulator of activity levels, but is in addition a "knob" for fine-tuning a variety of functionalities(Gutnisky & Dragoi, 2008; Ollerenshaw, Zheng, Millard, Wang, & Stanley, 2014; Woodrow L Shew, Clawson, Pobst, Karimipanah, & Wright, 2015; Zheng, Wang, & Stanley, 2015).

One major limitation of our experimental work is the lack of direct measurements of inhibitory synaptic conductances, which are a key component of single-neuron and network-wide response properties. Inhibition represents a significant proportion of the total synaptic input to a given neuron(Haider, Häusser, & Carandini, 2012), tends to be correlated across pairs of neurons(Hasenstaub et al., 2005), and the relative timing of excitatory and inhibitory currents may determine precise spike timing(Haider & McCormick, 2009; Hasenstaub et al., 2005; Nowak et al., 1997) and feature selectivity(Wilent & Contreras, 2005). Furthermore, the inhibitory population is known to play a vital role in such emergent network phenomena as spike rate oscillations(Brunel & Wang, 2003), and the excitation-inhibition balance may represent a fundamental aspect of the cortical code(Denève & Machens, 2016). Our experimental approach can be modified to investigate inhibition. For example, excitatory conductances can be pharmacologically blocked, and/or the resting membrane potential of a patched neuron can be shifted to the excitatory reversal potential. In this case, the algorithm would provide a temporally-precise view of the inhibitory conductances responsible for the observed (relatively slow and convoluted) membrane potential deflections. More importantly, this approach can be combined with multi-whole-cell recording to simultaneously infer excitatory conductances in one cell, and inhibitory in another, similar to studies of evoked activity in rat somatosensory cortex(Okun & Lampl, 2008), and spontaneous activity in rat hippocampus(Atallah & Scanziani, 2009) and mouse thalamocortical slice(Graupner & Reyes, 2013). This would be particularly useful in areas such as visual cortex, where responses can be complex and highly variable (thus limiting the utility of recording excitation and inhibition from one cell on alternating trials).

Here, we have treated each recorded neuron as a network sub-sampler, viewing the synaptic inputs as a record of presynaptic spiking activity. Of course, each neuron is also a contributing

member of the network. And although the relationship is complex(Carandini, 2004), the nature of the synaptic inputs is likely extremely relevant to that of output spiking activity(Doiron, Litwin-Kumar, Rosenbaum, Ocker, & Josić, 2016; Litwin-Kumar, Oswald, Urban, & Doiron, 2011; Lyamzin et al., 2015). We therefore hypothesize that the broad g-LFP coupling distribution observed here corresponds to the diverse spike-spike population coupling observed elsewhere. A carefully-designed experiment can directly test this hypothesis. For instance, the resting membrane potential of a recorded neuron can be systematically manipulated to support spiking in some trials (which can be compared to local or global spiking activity), and limit it in others (which would be used to calculate g-LFP coupling). It is this ability to study both suprathreshold and subthreshold activity that makes whole-cell recordings so valuable in our quest to understand coordinated network activity(Doiron et al., 2016).

Taken together, our results demonstrate the highly variable nature of visually-evoked spatiotemporal spike patterns in cortical microcircuits. Further, they suggest that several properties of this variability are largely determined intracortically, and identify specific, highly relevant cortical parameters. Importantly, these cortical properties together lead to an adapted network state that is in many ways ideal for sensory processing. As such, these results contribute to a clearer picture of the effects of anatomical and emergent network properties on single-neuron sensory responses and network-wide function.

5.4 Methods

5.4.1 Surgery

All procedures were approved by Washington University's Institutional Animal Care and Use Committees and conform to the guidelines of the National Institutes of Health on the Care and Use of Laboratory Animals. Fourteen adult red-eared sliders (*Trachemys scripta elegans*, 150-1000 g) were used for this study. Turtles were anesthetized with Propofol (2mg Propofol/kg), then decapitated. Dissection proceeded as described previously(Crockett, Wright, Thornquist, Ariel, & Wessel, 2015; Saha, Morton, Ariel, & Wessel, 2011; W. L. W. L. Shew et al., 2015). In brief, immediately after decapitation, the brain was excised from the skull, with right eye intact, and bathed in cold extracellular saline (in mM, 85 NaCl, 2 KCl, 2 $MgCl_2$*$6H_2O$, 20 Dextrose, 3 $CaCl_2$-$2H_2O$, 45 $NaHCO_3$). The dura was removed from the left cortex and right optic nerve, and the right eye hemisected to expose the retina. The rostral tip of the olfactory bulb was removed, exposing the ventricle that spans the olfactory bulb and cortex. A cut was made along the midline from the rostral end of the remaining olfactory bulb to the caudal end of the cortex. The preparation was then transferred to a perfusing chamber (Warner RC-27LD recording chamber mounted to PM-7D platform), and placed directly on a glass coverslip surrounded by Sylgard. A final cut was made to the cortex (orthogonal to the previous and stopping short of the border between medial and lateral cortex) allowing the cortex to be pinned flat, with ventricular surface exposed. Multiple perfusion lines delivered extracellular saline, adjusted to pH 7.4 at room temperature, to the brain and retina in the recording chamber.

5.4.2 Intracellular Recordings

We performed whole-cell current clamp recordings from 39 cells in 14 preparations. Patch pipettes (4-8 MΩ) were pulled from borosilicate glass and filled with a standard electrode solution (in mM; 124 $KMeSO_4$, 2.3 $CaCl_2$-$2H_2O$, 1.2 $MgCl_2$, 10 HEPES, 5 EGTA) adjusted to pH 7.4 at room temperature. Cells were targeted for patching using a dual interference contrast microscope

(Olympus). All cells were located within 300 microns of an extracellular recording electrode. Intracellular activity was collected using an Axoclamp 900A amplifier, digitized by a data acquisition panel (National Instruments PCIe-6321), and recorded using a custom Labview program (National Instruments), sampling at 10 kHz. The visual cortex was targeted as described previously(W. L. W. L. Shew et al., 2015)].

5.4.3 Extracellular Recordings

We performed extracellular recordings at 12 recording sites in seven preparations. We used tungsten microelectrodes (MicroProbes heat treated tapered tip), with approximately 0.5 MΩ impedance. Electrodes were slowly advanced through tissue under visual guidance using a manipulator (Narishige), while monitoring for spiking activity using custom acquisition software (National Instruments). Extracellular activity was collected using an A-M Systems Model 1800 amplifier, band-pass filtered between 1 Hz and 20,000 Hz, digitized (NI PCIe-6231), and recorded using custom software (National Instruments), sampling at 10 kHz.

5.4.4 Visual Stimulation

The visual stimulation protocol has been described previously (N. C. Wright, M. Hoseini, R. Wessel, unpublished observations). Briefly, visual stimuli were presented using a projector (Aaxa Technologies, P4X Pico Projector), combined with a system of lenses (Edmund Optics) to project images generated by a custom software package directly onto the retina. The stimulus was either a sustained gray screen, a naturalistic movie ("catcam"), a motion-enhanced movie (courtesy Jack Gallant), or a phase-shuffled version of the same movie (courtesy Jack Gallant and Woodrow Shew). In all cases, the stimulus was triggered using a custom Labview program (National Instruments).

For each cell and extracellular recording site, we selected one of the four stimuli listed above to present across all trials. The preparation was in complete darkness before and after each stimulus presentation. Stimuli lasted either 10 s or 20 s, and were shown at least 12 times, with at least 30 s between the end of one presentation and the beginning of the next.

5.4.5 Processing of intracellular and extracellular voltage recordings

Raw data traces were down-sampled to 1000 Hz. We used an algorithm to detect spikes in the membrane potential, and the values in a 20 ms window centered on the maximum of each spike were replaced via interpolation. Finally, we applied a 100 Hz lowpass Butterworth filter. For extracellular recordings, we used a sine-wave removal algorithm to minimize 60 Hz line noise.

5.4.6 Data included in analysis

For each extracellular recording site, we used visual inspection to determine the quality of the recordings. In general, we excluded recording sites from consideration if voltage traces displayed excessive 60 Hz line noise, low-frequency noise (likely reflecting a damaged electrode), or on average small response amplitudes relative to baseline.

For intracellular recordings, we also excluded some trials and cells. To include a given trial, we required the membrane potential to remain at or above the calculated inhibitory reversal potential from the beginning of the ongoing epoch to the end of the steady-state epoch. The inhibitory reversal potential was calculated using the Chloride concentrations in the intracellular and extracellular solutions, but because of partial transfer of intracellular solution to the cell interior, it was possible for the recorded membrane potential to drop below this value. This causes the conductance estimation algorithm to return a singularity. Rather than reset the inhibitory

reversal potential to the minimum membrane potential value for such a trial, we took the more conservative approach of excluding the trial from consideration. We also excluded trials with excessive low-frequency artifacts or membrane potential drift. Finally, we considered only cells with twelve or more retained trials for analysis.

In some cases, an extracellular electrode remained at a single recording site while we performed whole-cell recordings either simultaneously or sequentially from multiple nearby cells. To calculate CC for a given g-LFP pair, we included only the trials in which both the intracellular and extracellular voltage were recorded and retained.

5.4.7 Inferred excitatory conductance

The algorithm for obtaining an estimated excitatory synaptic conductance (g) from V for single trials has been described previously(Yaşar et al., 2016). Briefly, our algorithm approximates a solution to the underdetermined equation

$$0 = C\frac{dV(t)}{dt} + g_l(V(t) - E_l) + g_e(t)(V(t) - E_e) + g_i(t)(V(t) - E_i)$$

where C is the known membrane capacitance, $V(t)$ is the measured membrane potential as a function of time, E_e (E_i) is the known excitatory (inhibitory) reversal potential, E_l is the known leak reversal potential, g_l is the known leak conductance, and $g_e(t)$ ($g_i(t)$) is the unknown excitatory (inhibitory) synaptic conductance. To estimate $g_e(t)$, we first introduce a mathematical construct $\eta(t)$, which is defined according to

$$0 = C\frac{dV(t)}{dt} + g_l(V(t) - E_l) + \eta(t)(V(t) - E_i).$$

For each recording, we solve this equation for $\eta(t)$. This attributes all membrane potential fluctuations to a single (unrealistic) inhibitory conductance. As such, $\eta(t)$ contains negative values and rapid downward fluctuations that are due to the influence of excitatory currents on the membrane potential. Because conductance cannot have negative values, we then set the negative values in $\eta(t)$ equal to zero, resulting in $\tilde{\eta}(t)$ (previously called "non-negative $\eta(t)$)". Next, we use linear interpolation to smooth out the rapid fluctuations in $\tilde{\eta}(t)$. The output of this smoothing process is $\xi(t)$, a smoother and therefore more realistic estimation of the inhibitory synaptic conductance. Finally, we substitute $\xi(t)$ into the equation

$$0 = C\frac{dV(t)}{dt} + g_l(V(t) - E_l) + g(t)(V(t) - E_e) + \xi(t)(V(t) - E_i)$$

to obtain an estimation of the excitatory synaptic conductance (g). In general, this algorithm sacrifices knowledge about the inhibitory conductance to gain a better estimation of the excitatory conductance. Further, it capitalizes on the fact that excitatory currents are faster than – and therefore tend to interrupt – inhibitory currents.

We have made several improvements to the algorithm since introducing it. The original algorithm worked remarkably well on simulated membrane potentials. A recorded membrane potential, however, will contain high-frequency noise, which is removed by filtering (with, e.g., a 100 Hz Butterworth low-pass filter). This filtering process also leads to a smoother $\tilde{\eta}(t)$. As mentioned above, detecting fast fluctuations in this signal is a critical step in the estimation process, and the algorithm's performance was thus compromised by the filter (as evidenced by its application to filtered, noisy simulated membrane potentials). We therefore revised the criteria for detecting and replacing rapid fluctuations in $\tilde{\eta}(t)$ (see Yasar, et al. 2016 for previous criteria). First, after calculating $\tilde{\eta}(t)$, we obtained the time series $d(\tilde{\eta}(t))/dt$. We then determined each

time *t'* at which $d(\tilde{\eta}(t))/dt$ crossed a threshold of one negative standard deviation. This threshold optimized the algorithm's performance when applied to noisy simulated data. Finally, we linearly connected the local maxima of $\tilde{\eta}(t)$ immediately prior and posterior to *t'*.

When applying the algorithm to a membrane potential recording, the experimenter must estimate the resting membrane potential for that trial. An unrealistic choice will lead to spurious waveforms in the estimated conductance. We estimated the resting membrane potential for each trial by calculating the median membrane potential value during the quiescent activity in that trial. To isolate this quiescent activity, we first removed a window of activity starting at stimulus onset, and ending 6 s after stimulus offset. This resulted in either a 14 s or 24 s trace of "spontaneous" activity that was on average quiescent relative to that in the removed window. We then used an algorithm to detect spontaneous "bursts" of activity lasting at least 1 s in duration within the remaining trace, and removed these bursts. Finally, we took the median value (which is more robust to outliers than the mean) of the resulting trace to be the resting membrane potential for the corresponding visual stimulation trial.

5.4.8 Coefficient of variation

The coefficient of variation (CV) is a scaled measure of variability: the standard deviation divided by the mean. For the set of all cells (N = 39), we calculated CV as a function of time (CV(t), **Fig 2e**) for the inferred excitatory conductance. First, we applied a 100 ms "box filter" to each g trace: for each time step, we replaced the value of the trace with the average value in a 100 ms window starting at that time step. We then advanced the window ten milliseconds, and repeated the process for the full length of the trace. Then, for each cell, we calculated the across-trial standard deviation and mean of the filtered traces as a function of time. This was done for the

entire population, resulting in 39 (mean, standard deviation) ordered pairs for each time step. For each time step, we fit the set of means to the set of standard deviations using linear regression. The slope (standard error) of this fit was the coefficient of variation (s.e.m.) for the time step. To determine the significance of a change in CV across epochs, we compared the set of all CV values for one epoch with that from the other (e.g., the 100 values from the ongoing epoch and the 100 values from the transient) using the Wilcoxon signed-rank test.

5.4.9 Correlated variability

For each single-trial time series X, the residual (X_r or deviation from the average activity) was found by subtracting the across-trial average time series from the single-trial time series:

$$X_r = X - \langle X \rangle_{trials}$$

Residuals were then separated into three epochs: the ongoing epoch (defined to be the one second prior to the onset of visual stimulation), the transient epoch (200 to 1200 ms after stimulus onset), and the steady-state epoch (1400 to 2400 ms after stimulus onset; **Figure 5.4a**). For each g-LFP pair, the Pearson correlation between residuals was then calculated for each epoch and trial. The results were averaged across all trials, resulting in the trial-averaged correlated variability (CC) for each pair and epoch:

$$CC^{epoch} = \langle cov(g_r^{epoch}, LFP_r^{epoch}) / [var(g_r^{epoch}) var(LFP_r^{epoch})]^{1/2} \rangle_{trials}$$

Significance tests for each pair and the population of pairs were applied as described below in "statistical analysis".

5.4.10 Power

For each trial and signal, we extracted a 4.4 s window of activity (with epoch windows and gaps between epochs as described above, plus 500 ms windows on each end to avoid filtering artifacts in the ongoing and steady-state epochs), and calculated the residual time series as described above. For each residual trace, we performed wavelet analysis in Matlab using software provided by C. Torrence and G. Compo(Torrence & Compo, 1998) (available at URL: http://paos.colorado.edu/research/wavelets/). This resulted in a power time series for each cell, for multiple frequencies. For each frequency below 100 Hz, we averaged the time series across each epoch to obtain the average power at each frequency for each epoch. We then averaged across trials to obtain P^{epoch}. For each cell, we also obtained the relative power spectrum (rP^{epoch}) for the transient and steady-state epochs, defined to be the trial-averaged evoked spectrum divided by the trial-averaged ongoing spectrum (**Figure 5.3b**):

$$rP^{epoch} = P^{epoch}/P^{ongoing}$$

For each frequency, we calculated the bootstrap interval for the relative power as described below in "statistical analysis".

5.4.11 Network Models

To investigate the roles of network properties in our experimental results, we implemented a model network of 800 excitatory and 200 inhibitory leaky-integrate-and-fire neurons (**Figure 5.5a**). Excitatory-excitatory connections had small-world connectivity(Watts & Strogatz, 1998) (with 3% connection probability), and all other connections were random (with 3% excitatory-inhibitory, and 20% inhibitory-excitatory and inhibitory-inhibitory connection probability). To generate each nonzero entry in the connection weight matrix (W_{ij}^0) we drew a

value from a beta distribution (over the interval [0.0, 1.0), with average value 0.1), and multiplied by 10.

The dynamics of the membrane potential (V) of each neuron evolved according to

$$\tau_m \frac{dV}{dt} = -g_L[V(t) - E_L] + I_{syn}(t)$$

where the membrane time constant τ_M = 50 ms (excitatory neurons), 25 ms (inhibitory), and the leak conductance g_L = 10 nS (excitatory), 5 (inhibitory). The leak reversal potential E_L for each neuron was a random value between -70 and -60 mV, drawn from a Gaussian distribution (to model the variability in resting membrane potentials observed across neurons in the experimental data). The reversal potentials for the synaptic current $I_{syn}(t)$ were E_{GABA} = -68 mV, and E_{AMPA} = 50 mV.

The synaptic current for each synapse type (between presynaptic neurons of type X and postsynaptic neurons of type Y) had three relevant time course parameters: delay (τ_{LX}, that is, the lag between presynaptic spike time and beginning of conductance waveform), rise time (τ_{RYX}), and decay time (τ_{DYX}). Synaptic conductances were modeled as products of time-varying gating variables (S_{YX}) and maximum conductances (g_{YX}). Following a presynaptic spike at time 0, the gating variable dynamics were described by

$$S_{YX}(t) = \frac{\tau_m}{\tau_{DYX} - \tau_{RYX}} \left[exp\left(-\frac{t - \tau_{LX}}{\tau_{DYX}}\right) - exp\left(-\frac{t - \tau_{LX}}{\tau_{RYX}}\right) \right]$$

with time constants (in ms) τ_{LE} = 1.5, τ_{REE} = 0.2, τ_{DEE} = 1.0, τ_{RIE} = 0.2, τ_{DIE} = 1.0, τ_{LI} = 1.5, τ_{RII} = 1.5, τ_{DII} = 6.0, τ_{REI} = 1.5, τ_{DEI} = 6.0. Maximum conductance values (in nS) were g_{EE} = 3.0, g_{IE} =

6.0, g_{EI} = 30.0, g_{II} = 30.0. In response to a presynaptic spike in neuron *j* at time t_j^{spk}, the weight (W_{ij}) of a synapse connecting neurons *j* and *i* depressed and recovered according to

$$\frac{dW_{ij}}{dt} = -\frac{W_{ij}(t)}{\tau_{depress}}\delta(t - t_j^{spk}) + \frac{W_{ij}^0 - W_{ij}(t)}{\tau_{recover}}$$

with depression time constant $\tau_{depress}$ = 300 ms and recovery time constant $\tau_{recover}$ = 2500 ms. Intracortical synapses were subject to depression for the entire simulation.

The spike threshold for each neuron was -40 mV. A neuron reset to -59 mV after spiking, and was refractory for 10 ms (excitatory) and 5 ms (inhibitory).

All excitatory and inhibitory neurons received Poisson external inputs. During "ongoing" activity, the external input rate to each neuron was 65 Hz, which was sufficiently high to cause intracortical spiking (**Figure 5.5b**). The ongoing external input was unique across cells and trials. The stimulus was modeled as a gradual increase to 375 Hz; the input rate was increased by 77.5 Hz at stimulus onset, and by an additional 77.5 Hz every 50 ms for 200 ms. This gradual increase provided more realistic excitatory conductances than did a single step function stimulus, but did not qualitatively impact the results. The post-stimulus external drive was composed of two components: one that was unique across cells and trials, and one that was unique across cells, but identical across trials, multiplied by proportionality constants 0.25 and 0.75, respectively. Thus, for the post-stimulus external drive to each neuron, 25% of the variance was explained by an input that was unique to each trial, and 75% was explained by an input that was identical across trials. The gating variables for external inputs had the same parameters as for excitatory-excitatory connections, and maximum conductances were g_E = 6.0 nS. There was no

thalamocortical synaptic depression during the ongoing epoch; the external drive during this window was simply used to generate stimulus-independent intracortical spiking, and thus treated as the "hidden" source triggering intrinsic events, as observed in experiment (**Figure 5.2a, d**).

Each trial was 4.4 s in duration, with stimulus onset at 1.7 s, and the time step was 0.05 ms. The ongoing epoch was defined to be 1200 ms to 200 ms before stimulus onset, the transient epoch 0 ms to 1000 ms after stimulus onset, and the steady-state epoch 1200 ms to 2400 ms after stimulus onset. The additional 500 ms at the beginning and end of each trial ensured there were no wavelet filtering artifacts in the ongoing and steady-state epochs.

We modeled the LFP as the sum of all synaptic currents(Atallah & Scanziani, 2009; Destexhe, 1998) to 100 neighboring neurons (**Figure 5.5b, d**), multiplied by a factor of -1 (to mimic the change in polarity between voltages measured intracellularly and extracellularly). The contribution of each neuron to the LFP was not distance-dependent. We then randomly selected 40 neurons from this subpopulation of 100 neurons, and used the excitatory synaptic conductances (**Figure 5.5c**) to generate 40 g-LFP pairs for g-LFP CC analysis (**Figure 5.6f-h**). For CV and R^2 analysis (**Figure 5.6b-e**), we used 40 neurons randomly selected from the full population of 800 excitatory neurons.

5.4.12 Statistical analysis

All statistical tests were performed using Python 2.7.

Before applying any significance test that assumed normality, we performed an omnibus test for normality on the associated dataset(s). This test compares the skew and kurtosis of the population from which the dataset was drawn to that of a normal distribution, returning a p-value

for a two-sided chi-squared test of the null hypothesis that the data is drawn from a normal distribution. This test is valid for sample sizes of 20 or larger, and was implemented using scipy.stats.mstats.normaltest (documentation and references available at http://docs.scipy.org/doc/scipy-0.14.0/reference/generated/scipy.stats.mstats.normaltest.html). We report these p-values as the result of a "two-sided omnibus chi-shared test for normality".

When asking whether a parameter of interest changed significantly across epochs for a population (e.g., whether the population-averaged CC for 21 g-LFP pairs changed significantly from the ongoing to transient epoch, see **Fig 4b**), we applied the Wilcoxon signed-rank test, which returns a p-value for the two-sided test that the two related paired samples (representing, e.g., the 21 ($CC^{ongoing}$, $CC^{transient}$) paired values) are drawn from the same distribution. This test assumes normality, and was implemented using scipy.stats.wilcoxon (documentation and references available at http://docs.scipy.org/doc/scipy/reference/generated/scipy.stats.wilcoxon.html).

To test whether a trial-averaged parameter of interest for one cell or electrode (e.g., CC, averaged over 15 trials for one cell) changed significantly from one epoch to another, we used a bootstrap comparison test. For each epoch of interest, we calculated the +/- 97.5% confidence intervals for the average value by bootstrapping (that is, resampling with replacement). If the bootstrap intervals for the two epochs did not overlap, we reported that the two sets of values were significantly different ($p < 0.05$).

When calculating correlations between a pair of signals in which at least one is slowly-varying, it is possible for broad autocorrelations to introduce spurious cross-correlations. This should be dealt with by either removing the broad autocorrelations (e.g., by "pre-whitening" the

signals), or by accounting for their contribution to the cross-correlation. To avoid changing the temporal structure of the visual responses, we chose the latter approach. First, for each epoch and g-LFP pair, we randomly shuffled the trial order for one of the channels. We then calculated CC_{shuff} and the bootstrap interval for this shuffled data. The CC value for each pair and epoch was determined to be significant (with $p < 0.05$) if the bootstrap intervals for CC and CC_{shuff} data did not overlap. We indicate a significant CC value with a filled dot in the CC trajectory (**Figure 5.4b, 6g, h**). Finally, for a given epoch, we compared the sets of CC and CC_{shuff} values for the population of g-LFP pairs using the Wilcoxon signed-rank test (as described above for across-epoch comparisons of CC). The population average for unshuffled data was determined to be significant for $p < 0.05$. We repeated this second test using bootstraps intervals rather than the signed-rank test, with similar results (data not shown).

Abbott, L. F., & Dayan, P. (1999). The Effect of Correlated Variability on the Accuracy of a Population Code. *Neural Computation*, *11*(1), 91–101. http://doi.org/10.1162/089976699300016827

Armstrong, C. M., & Gilly, W. F. (1992). Access resistance and space clamp problems associated with whole-cell patch clamping. *Methods in Enzymology*, *207*(1960), 100–122. http://doi.org/10.1016/0076-6879(92)07007-B

Atallah, B. V., & Scanziani, M. (2009). Instantaneous Modulation of Gamma Oscillation Frequency by Balancing Excitation with Inhibition. *Neuron*, *62*(4), 566–577. http://doi.org/10.1016/j.neuron.2009.04.027

Averbeck, B. B., Latham, P. E., & Pouget, A. (2006). Neural correlations, population coding and computation. *Nature Reviews. Neuroscience*, *7*(5), 358–66. http://doi.org/10.1038/nrn1888

Britten, K. H., Shadlen, M. N., Newsome, W. T., & Movshon, J. A. (1993). Responses of neurons in macaque MT to stochastic motion signals. *Visual Neuroscience*, *10*(06), 1157–1169. http://doi.org/10.1017/S0952523800010269

Brunel, N., & Wang, X.-J. (2003). What determines the frequency of fast network oscillations with irregular neural discharges? I. Synaptic dynamics and excitation-inhibition balance. *Journal of Neurophysiology*, *90*(1), 415–430. http://doi.org/10.1152/jn.01095.2002

Carandini, M. (2004). Amplification of trial-to-trial response variability by neurons in visual cortex. *PLoS Biology*, *2*(9), E264. http://doi.org/10.1371/journal.pbio.0020264

Churchland, M. M., Yu, B. M., Cunningham, J. P., Sugrue, L. P., Cohen, M. R., Corrado, G. S., … Shenoy, K. V. (2010). Stimulus onset quenches neural variability: a widespread cortical phenomenon. *Nature Neuroscience*, *13*(3), 369–378. http://doi.org/10.1038/nn.2501

Cohen, M. R., & Kohn, A. (2011). Measuring and interpreting neuronal correlations. *Nature Neuroscience*, *14*(7), 811–819. http://doi.org/10.1038/nn.2842

Cossell, L., Iacaruso, M. F., Muir, D. R., Houlton, R., Sader, E. N., Ko, H., … Mrsic-flogel, T. D. (2015). Functional organization of excitatory synaptic strength in primary visual cortex. *Nature*, *000*(00), 1–5. http://doi.org/10.1038/nature14182

Crockett, T., Wright, N., Thornquist, S., Ariel, M., & Wessel, R. (2015). Turtle dorsal cortex pyramidal neurons comprise two distinct cell types with indistinguishable visual responses. *PLoS ONE*, *10*(12), 1–22. http://doi.org/10.1371/journal.pone.0144012

Denève, S., & Machens, C. K. (2016). review Efficient codes and balanced networks, *19*(March), 375–382. http://doi.org/10.1038/nn.4243

Destexhe, a. (1998). Spike-and-wave oscillations based on the properties of GABAB receptors. *The Journal of Neuroscience : The Official Journal of the Society for Neuroscience*, *18*(21), 9099–9111.

Deweese, M. R., & Zador, A. M. (2004). Shared and private variability in the auditory cortex. *Journal of Neurophysiology*, *92*(3), 1840–55. http://doi.org/10.1152/jn.00197.2004

Doiron, B., Litwin-Kumar, A., Rosenbaum, R., Ocker, G. K., & Josić, K. (2016). The mechanics of state-dependent neural correlations. *Nature Neuroscience*, *19*(3), 383–393. http://doi.org/10.1038/nn.4242

Goris, R. L. T., Movshon, J. A., & Simoncelli, E. P. (2014). Partitioning neuronal variability. *Nature Neuroscience*, *17*(6), 858–65. http://doi.org/10.1038/nn.3711

Graupner, M., & Reyes, A. D. (2013). Synaptic Input Correlations Leading to Membrane Potential Decorrelation of Spontaneous Activity in Cortex. *Journal of Neuroscience*, *33*(38), 15075–15085. http://doi.org/10.1523/JNEUROSCI.0347-13.2013

Gutnisky, D. a, & Dragoi, V. (2008). Adaptive coding of visual information in neural populations. *Nature*, *452*(7184), 220–4. http://doi.org/10.1038/nature06563

Haider, B., Duque, A., Hasenstaub, A. R., & McCormick, D. A. (2006). Neocortical Network Activity In Vivo Is Generated through a Dynamic Balance of Excitation and Inhibition, *26*(17), 4535–4545. http://doi.org/10.1523/JNEUROSCI.5297-05.2006

Haider, B., Häusser, M., & Carandini, M. (2012). Inhibition dominates sensory responses in the awake cortex. *Nature*, *493*(7430), 97–100. http://doi.org/10.1038/nature11665

Haider, B., & McCormick, D. A. (2009). Rapid Neocortical Dynamics: Cellular and Network Mechanisms. *Neuron*, *62*(2), 171–189. http://doi.org/10.1016/j.neuron.2009.04.008

Haider, B., Schulz, D. P. A., & Carandini, M. (2016). Millisecond Coupling of Local Field Potentials to Synaptic Currents in the Awake Visual Cortex Report Millisecond Coupling of Local Field Potentials to Synaptic Currents in the Awake Visual Cortex, *90*, 35–42. http://doi.org/10.1016/j.neuron.2016.02.034

Haider, B., Schulz, D. P. A., Häusser, M., & Carandini, M. (2016). Millisecond Coupling of Local Field Potentials to Synaptic Currents in the Awake Visual Cortex. *Neuron*, *90*(1), 35–42. http://doi.org/10.1016/j.neuron.2016.02.034

Hasenstaub, A., Shu, Y., Haider, B., Kraushaar, U., Duque, A., & McCormick, D. a. (2005). Inhibitory postsynaptic potentials carry synchronized frequency information in active cortical networks. *Neuron*, *47*(3), 423–35. http://doi.org/10.1016/j.neuron.2005.06.016

Henze, D. A., Borhegyi, Z., Csicsvari, J., Mamiya, A., Kenneth, D., Buzsáki, G., … Harris, K. D. (2015). Intracellular Features Predicted by Extracellular Recordings in the Hippocampus In Vivo Intracellular Features Predicted by Extracellular Recordings in the Hippocampus In Vivo, 390–400.

Ikegaya, Y., Aaron, G., Cossart, R., Aronov, D., & Lampl, I. (2004). Synfire Chains and Cortical Songs: Temporal Modules of Cortical Activity. *Science (New York, NY)*, *559*(2004). http://doi.org/10.1126/science.1093173

Isaacson, J. S., & Scanziani, M. (2011). How inhibition shapes cortical activity. *Neuron*, *72*(2), 231–243. http://doi.org/10.1016/j.neuron.2011.09.027

Koch, C. (2004). *Biophysics of Computation*. Oxford, UK: Oxford University Press.

Larkum, M. (2013). A cellular mechanism for cortical associations: An organizing principle for the cerebral cortex. *Trends in Neurosciences*, *36*(3), 141–151. http://doi.org/10.1016/j.tins.2012.11.006

Lin, I. C., Okun, M., Carandini, M., & Harris, K. D. (2015). The Nature of Shared Cortical Variability. *Neuron*, *87*(3), 645–657. http://doi.org/10.1016/j.neuron.2015.06.035

Litwin-Kumar, A., Oswald, A.-M. M., Urban, N. N., & Doiron, B. (2011). Balanced synaptic input shapes the correlation between neural spike trains. *PLoS Computational Biology*, *7*(12), e1002305. http://doi.org/10.1371/journal.pcbi.1002305

Lyamzin, D. R., Barnes, S. J., Donato, R., Garcia-Lazaro, J. A., Keck, T., & Lesica, N. A. (2015). Nonlinear Transfer of Signal and Noise Correlations in Cortical Networks. *Journal of Neuroscience*, *35*(21), 8065–8080. http://doi.org/10.1523/JNEUROSCI.4738-14.2015

MacLean, J. N., Watson, B. O., Aaron, G. B., & Yuste, R. (2005). Internal dynamics determine the cortical response to thalamic stimulation. *Neuron*, *48*(5), 811–823. http://doi.org/10.1016/j.neuron.2005.09.035

Mokeichev, A., Okun, M., Barak, O., Katz, Y., Ben-Shahar, O., & Lampl, I. (2007). Stochastic Emergence of Repeating Cortical Motifs in Spontaneous Membrane Potential Fluctuations In Vivo. *Neuron*, *53*(3), 413–425. http://doi.org/10.1016/j.neuron.2007.01.017

Nowak, L. G., Sanchez-Vives, M. V., & McCormick, D. A. (1997). Influence of low and high frequency inputs on spike timing in visual cortical neurons. *Cerebral Cortex*, *7*(6), 487–501. http://doi.org/10.1093/cercor/7.6.487

O'Connor, D. H., Peron, S. P., Huber, D., & Svoboda, K. (2010). Neural activity in barrel cortex underlying vibrissa-based object localization in mice. *Neuron*, *67*(6), 1048–1061. http://doi.org/10.1016/j.neuron.2010.08.026

Okun, M., & Lampl, I. (2008). Instantaneous correlation of excitation and inhibition during ongoing and sensory-evoked activities. *Nature Neuroscience*, *11*(5), 535–7. http://doi.org/10.1038/nn.2105

Okun, M., Steinmetz, N. a., Cossell, L., Iacaruso, M. F., Ko, H., Barthó, P., … Harris, K. D. (2015). Diverse coupling of neurons to populations in sensory cortex. *Nature*, *521*(7553), 511–515. http://doi.org/10.1038/nature14273

Ollerenshaw, D. R. R., Zheng, H. J. V. J. V, Millard, D. C. C., Wang, Q., & Stanley, G. B. B. (2014). The adaptive trade-off between detection and discrimination in cortical representations and behavior. *Neuron*, *81*(5), 1152–1164. http://doi.org/10.1016/j.neuron.2014.01.025

Pernice, V., Staude, B., Cardanobile, S., & Rotter, S. (2011). How structure determines correlations in neuronal networks. *PLoS Computational Biology*, *7*(5), e1002059. http://doi.org/10.1371/journal.pcbi.1002059

Poulet, J. F. a, & Petersen, C. C. H. (2008). Internal brain state regulates membrane potential synchrony in barrel cortex of behaving mice. *Nature*, *454*(7206), 881–5. http://doi.org/10.1038/nature07150

Reynolds, J. H., & Heeger, D. J. (2009). The Normalization Model of Attention. *Neuron*, *61*(2), 168–185. http://doi.org/10.1016/j.neuron.2009.01.002

Saha, D., Morton, D., Ariel, M., & Wessel, R. (2011). Response properties of visual neurons in the turtle nucleus isthmi. *Journal of Comparative Physiology A*, *197*(2), 153–165. http://doi.org/10.1007/s00359-010-0596-3

Scholvinck, M. L., Saleem, A. B., Benucci, a., Harris, K. D., & Carandini, M. (2015). Cortical State Determines Global Variability and Correlations in Visual Cortex. *Journal of Neuroscience*, *35*(1), 170–178. http://doi.org/10.1523/JNEUROSCI.4994-13.2015

Shadlen, M. N., & Newsome, W. T. (1998). The Variable Discharge of Cortical Neurons : Implications for Connectivity , Computation , and Information Coding, *18*(10), 3870–3896.

Shew, W. L., Clawson, W. P., Pobst, J., Karimipanah, Y., & Wright, N. C. (2015). Adaptation to to sensory sensory input cortex to criticality, 1–48. http://doi.org/10.1038/NPHYS3370

Shew, W. L. W. L., Clawson, W. P. W. P., Pobst, J., Karimipanah, Y., Wright, N. C. N. C., & Wessel, R. (2015). Adaptation to sensory input tunes visual cortex to criticality. *Nature Physics*, *11*(8), 659–663. http://doi.org/10.1038/nphys3370

Shew, W. L., Yang, H., Yu, S., Roy, R., & Plenz, D. (2011). Information Capacity and Transmission Are Maximized in Balanced Cortical Networks with Neuronal Avalanches. *Journal of Neuroscience*, *31*(1), 55–63. http://doi.org/10.1523/JNEUROSCI.4637-10.2011

Shoham, S., O'Connor, D. H., & Segev, R. (2006). How silent is the brain: Is there a "dark matter" problem in neuroscience? *Journal of Comparative Physiology A: Neuroethology, Sensory, Neural, and Behavioral Physiology*, *192*(8), 777–784. http://doi.org/10.1007/s00359-006-0117-6

Spruston, N., Jaffe, D. B., Williams, S. H., & Johnston, D. (1993). Voltage- and space-clamp

errors associated with the measurement of electrotonically remote synaptic events. *Journal of Neurophysiology*, *70*(2), 781–802.

Tan, A. Y. Y., Chen, Y., Scholl, B., Seidemann, E., & Priebe, N. J. (2014). Sensory stimulation shifts visual cortex from synchronous to asynchronous states. *Nature*, *509*(7499), 226–229. http://doi.org/10.1038/nature13159

Thompson, L. T., & Best, P. J. (1989). Place cells and silent cells in the hippocampus of freely-behaving rats. *The Journal of Neuroscience : The Official Journal of the Society for Neuroscience*, *9*(7), 2382–90. Retrieved from http://www.ncbi.nlm.nih.gov/pubmed/2746333

Torrence, C., & Compo, G. C. (1998). A Practical Guide to Wavelet Analysis.

Vogels, T. P., & Abbott, L. F. (2005). Signal Propagation and Logic Gating in Networks of Integrate-and-Fire Neurons. *The Journal of Neuroscience*, *25*(46), 10786–10795. http://doi.org/10.1523/JNEUROSCI.3508-05.2005

Vreeswijk, C. Van, & Sompolinsky, H. (1996). Chaos in Neuronal Networks with Balanced Excitatory and Inhibitory Activity Author (s): C . van Vreeswijk and H . Sompolinsky Published by : American Association for the Advancement of Science Stable URL : http://www.jstor.org/stable/2890956, *274*(5293), 1724–1726.

Watts, D. J., & Strogatz, S. H. (1998). Collective dynamics of "small-world" networks. *Nature*, *393*(6684), 440–2. http://doi.org/10.1038/30918

Wehr, M. S., & Zador, A. M. (2003). Balanced inhibition underlies tuning and sharpens spike timing in auditory cortex. *Nature*, *426*(6965), 442–6. http://doi.org/10.1038/nature02116

Wilent, W. B., & Contreras, D. (2005). Dynamics of excitation and inhibition underlying stimulus selectivity in rat somatosensory cortex. *Nature Neuroscience*, *8*(10), 1364–70. http://doi.org/10.1038/nn1545

Yaşar, T. B., Wright, N. C. N. C., Wessel, R., Ya?ar, T. B., Wright, N. C. N. C., & Wessel, R. (2016). Inferring presynaptic population spiking from single-trial membrane potential recordings. *Journal of Neuroscience Methods*, *259*, 13–21. http://doi.org/10.1016/j.jneumeth.2015.11.019

Zheng, H. J. V., Wang, Q., & Stanley, G. B. (2015). Adaptive shaping of cortical response selectivity in the vibrissa pathway. *Journal of Neurophysiology*, *113*(10), 3850–3865. http://doi.org/10.1152/jn.00978.2014

Zohary, E. (1994). correlated neuronal discharge rate and its implications for psychophysical performance.

Chapter 6

Adaptation to sensory input tunes visual cortex to criticality

A long-standing hypothesis at the interface of physics and neuroscience is that neural networks self-organize to the critical point of a phase transition, thereby optimizing aspects of sensory information processing[1–3]. This idea is partially supported by strong evidence for critical dynamics observed in the cerebral cortex[4–10], but the impact of sensory input on these dynamics is largely unknown. Thus, the foundations of this hypothesis – the self-organization process and how it manifests during strong sensory input – remain unstudied experimentally. Here we show in visual cortex and in a computational model that strong sensory input initially elicits cortical network dynamics that are not critical, but adaptive changes in the network rapidly tune the system to criticality. This conclusion is based on observations of multifaceted scaling laws predicted to occur at criticality[4,11]. Our findings establish sensory adaptation as a self-organizing mechanism which maintains criticality in visual cortex during sensory information processing.

6.1 Introduction

Sensory nervous systems adapt, dynamically tuning interactions among large networks of neurons, to cope with a changing environment[12,13]. The principles governing such adaptation at the macroscopic level of neuronal network dynamics are not well understood. Computational models and theory suggest that such adaptation can maintain critical network dynamics[14–16], but these previous studies did not consider the strongly driven regime that is expected during intense sensory input. Indeed, sufficiently strong input may increase the overall excitability of a network by bringing neurons closer to their firing thresholds and potentially tipping the network into a high firing rate regime that is inconsistent with critical dynamics (Supplementary Information 1). Thus, the question remains: does strong sensory input drive cortical network dynamics away from criticality or can adaptation counteract this tendency and maintain the critical regime?

6.2 Results

Here we addressed this question in turtle visual cortex and in a companion computational model. In our experiments, we obtained long-duration recordings of population neural activity (local field potential, LFP) using a microelectrode array inserted into the geniculo-recipient dorsal cortex (visual cortex) of the turtle eye-attached whole-brain *ex vivo* preparation[17] (Fig. 1a and Supplementary Information 2). We measured multi-scale spatiotemporal patterns of neural activity while visually stimulating the retina. Similarly, in our model we studied changes in neural network activity in response to changes in external input. Experimentally and in the model, we assessed whether the measured dynamics were near or far from criticality. For this, we examined statistics and spatiotemporal scaling laws of "neuronal avalanches", which are bouts of elevated population activity with correlations in space and time[5] (Fig. 1b). In brief, a neuronal avalanche

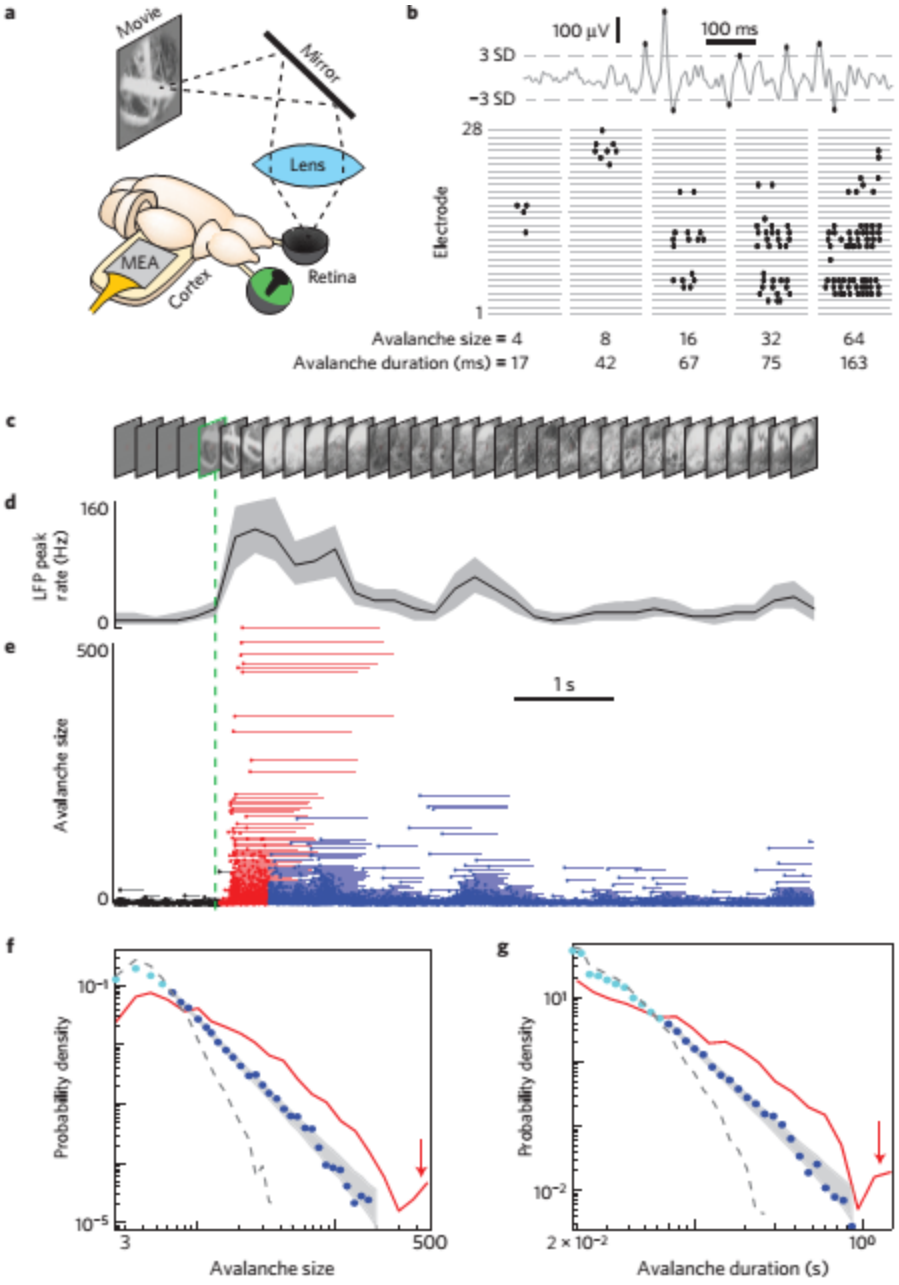

Figure 6.1. Visually driven network dynamics are power law distributed after non-power law transient. **(a)** *Ex vivo* whole brain with eyes attached. Visual stimuli are projected onto the intact retina while activity is recorded with a 96-channel microelectrode array (MEA) inserted into the unfolded visual cortex. **(b)** Avalanches are defined as spatiotemporal clusters of large amplitude LFP peaks (black dots). Five example avalanches are displayed with one dot per LFP peak. Avalanche size = number of LFP peaks; duration = time between the first and last peaks. **(c)** Natural movie visual stimulus (subset of 1 frame per 200 ms shown). **(d)** At movie start (green dashed line), there is a transient increase in stimulus-triggered average LFP peak rate. Average is over 315 movie presentations. Gray region delineates quartiles. **(e)** Stimulus-triggered avalanche

size time series reveals tendency for very large avalanches during the transient response (red). Later, during the visually-driven steady state, less extreme avalanches occur (blue). Each point represents one avalanche. The line following each point indicates avalanche duration. Responses to 315 repeats of movie stimulation are overlaid. **(f,g)** Probability density functions for sizes and durations of avalanches during the transient response (red line) and during the visually-driven steady-state (blue dots). Large avalanches (arrow) occur during the transient response, yielding bimodal distributions of avalanche sizes and durations. Avalanches during the visually-driven steady state are power law distributed over the range indicated with dark blue dots. Gray shading indicates the range (0.05-0.95) of expected probabilities for a perfect power law with the same number of samples as the experiment. Jittering the times of LFP peaks destroys the power-law (dashed line) by abolishing large sized avalanches. Panels d-g are from one experiment with one turtle.

is defined as a group of LFP peaks, occurring on any electrode, irrespective of location, and separated by inter-peak intervals less than a specified time (Methods). For experiments in which spikes (i.e. multiunit activity) were also measureable, we confirmed that the rate of LFP peaks increases with the rate of spikes (Supplementary Information 3). Thus, a period of time with many LFP peaks, e.g. a neuronal avalanche, reflects an increase in population spike rate in the cortex.

At the onset of stimulation, we observed that LFP amplitude, LFP peak rate, and avalanches were typically large scale – not consistent with critical dynamics – during a transient period (Figs. 1c-e and Supplementary Information 4). More specifically, avalanche sizes *S* and durations *D* were often bimodally distributed during the transient (Fig. 1f,g and Supplementary Information 5). Following this large-scale transient response, LFP amplitude decreased and avalanches became more diverse in spatiotemporal scale (Fig. 1e), resulting in power-law distributions, $P(S) \sim S^{-\tau}$ (Fig. 1f) and $P(D) \sim D^{-\alpha}$ (Fig. 1g) over a wide range of sizes and durations. This fact is supported by rigorous maximum likelihood fitting methods[10,18] and strict statistical criteria for fit quality ($q > 0.1$, Methods).

These conclusions held for nine turtles and four types of visual stimuli (n = 13 data sets; complex movies, static gray screen, diffuse flashes, moving dots) with power law quality values $q = 0.31 \pm 0.13$ (mean ± SD). Importantly, the different visual stimuli had very different spatiotemporal structure, yet all resulted in power law avalanche distributions. This indicates that the power laws were due to inherent neuronal network dynamics rather than externally imposed statistics of the stimulus. Notably, randomizing the recorded LFP peak times abolished the power law distributions of avalanche size and duration, thus demonstrating the importance of correlations, (Fig. 1f,g). Moreover, activity recorded outside visual cortex was not power law distributed (Supplementary Information 6).

What biophysical mechanisms could mediate self-organization towards scale-free population activity during visual processing? To address this question, we investigated a parsimonious model network of probabilistic integrate-and-fire neurons with all-to-all connectivity (Fig. 2a)[6,19,20]. A subset of neurons (20%) was inhibitory. Motivated by previous experiments[21] and models[14], we modeled adaptation as short-term synaptic depression with recovery (Methods). However, our model differed from previously studied models as detailed in Supplementary Information 7. We studied how the model dynamics and avalanche statistics change due to increasing the input rate. During a transient period after increasing the input rate, the population spike rate increased and synapses depressed (Fig. 2b,c). During the transient, avalanches also increased dramatically in size and duration (Fig. 2d), qualitatively similar to the experimental observations (Fig. 1e). Avalanche size and duration distributions during the transient period displayed a distinct bimodal character consisting of small and large avalanches (Fig. 2e,f), qualitatively similar to what we found experimentally (Fig. 1f,g) and inconsistent with a power law. Following the transient jump in population activity, the network dynamically reached a new

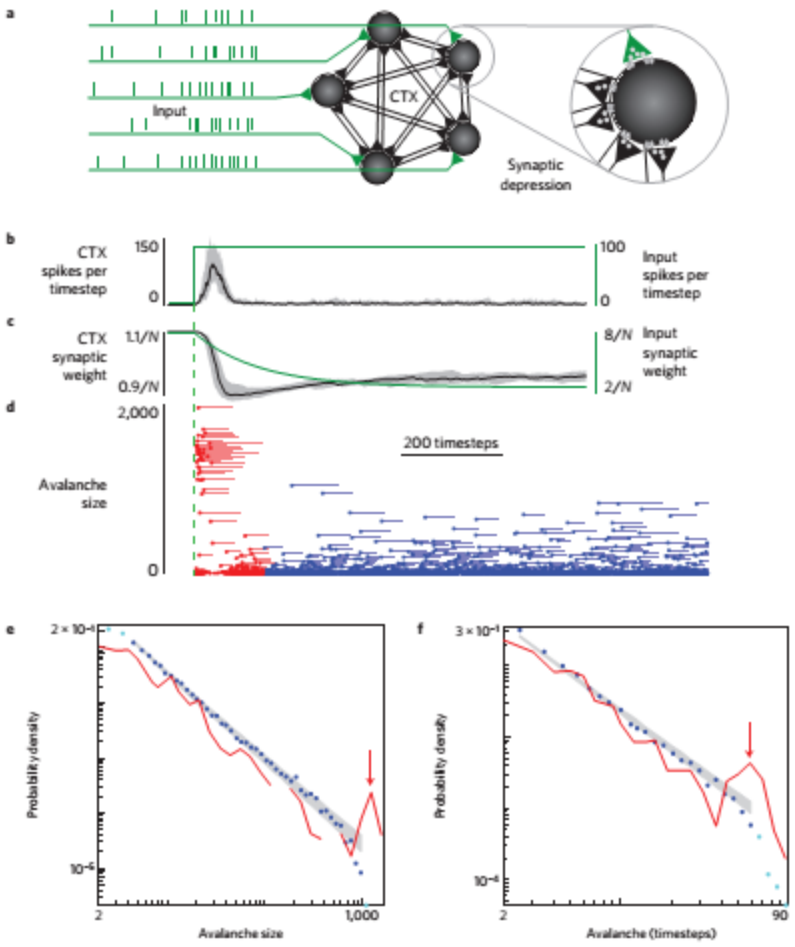

Figure 6.2. Depressing synapses tune model dynamics to critical regime after noncritical transient**. (a)** Conceptual cartoon illustrating model features, including recurrent synapses (black) and input synapses (green) which change strength according short-term depression. **(b)** A step increase in input (green, input spikes per timestep for whole network) causes a transient increase in the population spike rate of the network (black, median). Time series is averaged over 40 trials. Gray region delineates quartiles. **(c)** Following the input rate increase, there is a relatively slow decrease in median synaptic strength for both recurrent (black) and input (green) synapses (average over 40 trials). Gray region delineates quartiles. Dashed line marks stimulus onset. **(d)** Stimulus-triggered avalanche time series. During a transient period after increase in input rate, avalanches of very large size occur (red). **(e)** Distributions of avalanche size during the transient period (red) reveal a 'bump' in the avalanche size distribution at large size (arrow). Avalanche sizes are power law distributed after synapses have adapted (blue). Gray shading indicates the range (0.05-0.95) of expected probabilities for a perfect power law with the same number of samples. **(f)** Avalanche durations follow a similar trend. Model parameters: low input R=0.05, high input R=100, default synapses Λ_0=1.1, 30% subsampling, 5000 timesteps computed after increase in R.

steady-state of population activity and average synaptic strength (Fig. 2b,c). In this driven steady state, during continued high external input rate, the simulated neuronal avalanche size and duration distributions were power laws ($q > 0.1$) (Fig. 2e,f, Supplementary Information 7).

In the model, a sufficiently strong increase in input rate transiently tips the system into a regime without critical dynamics (Supplementary Information 1). Adaptation then tunes the system to a critical regime. Given the similarity between our model results and our experiment, it is tempting to conclude that the experimentally observed power law avalanche distributions occurred because adaptation tunes the visual cortex to criticality. However, caution is called for, because power laws provide necessary, but insufficient evidence for the critical regime[22–24]. Therefore, additional tests are needed to determine whether criticality underlies the experimentally observed power laws.

Two such tests arise from a particular relationship between the size and duration of avalanches, which is predicted to occur at criticality[4,11] and confirmed by our model (Fig. 3d-f, Supplementary Information 1 and 7). First, the average avalanche size increases with duration according to a specific function $S \sim D^{\beta}$. Second, the exponent β is predicted to depend on the exponents τ and α as $\beta = (\alpha - 1)/(\tau - 1)$. (A third additional test is confirmed in Supplementary Information 8.)

Our experiments confirmed both these predictions (Fig. 3a-c). First, we showed that avalanche size scales with duration according to a power law (Fig. 3a). Second, we determined the "best-fit β" from the size versus duration data for each experiment (Fig. 3a). Next we computed the "predicted β" using the observed exponents τ and α. For different turtles and different visual stimuli, we obtained a range of exponents; $1.7 < \tau < 2.6$ and $1.8 < \alpha < 2.8$ (Fig. 3b). Importantly,

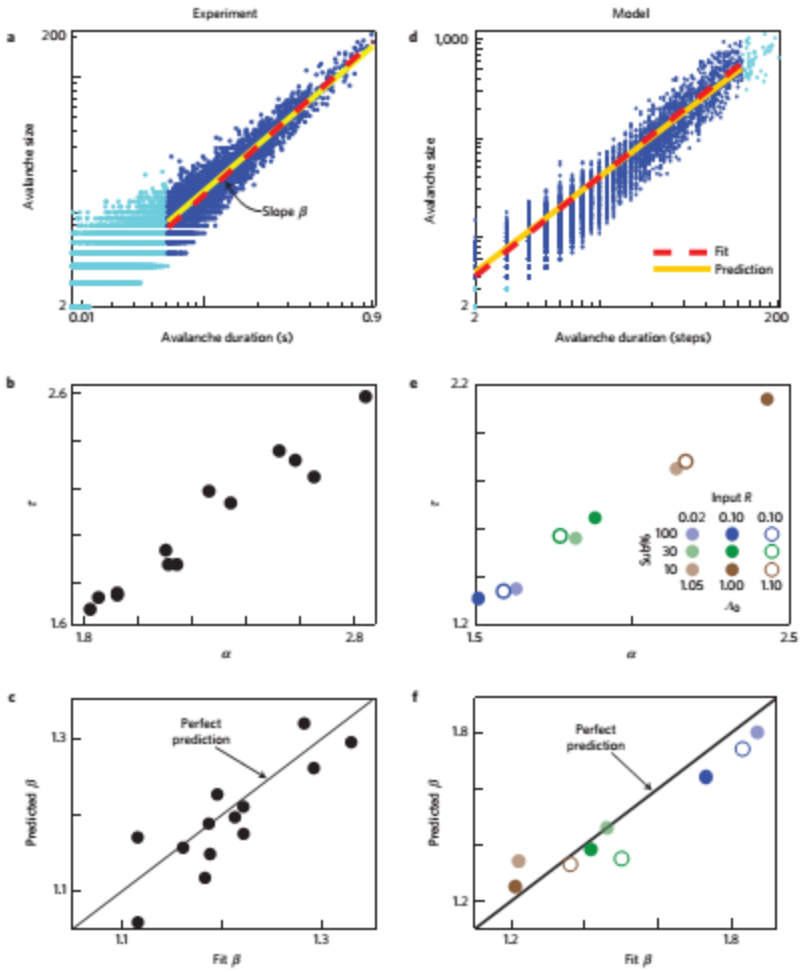

Figure 6.3. Steady state visually-driven avalanches follow predictions for critical regime**. (a)** Each point displays the size and duration of one avalanche (from one experiment, one turtle, same as Fig. 1). Avalanches from the visually-driven steady state are shown. The linear relationship on logarithmic axes reveals a power law relationship between avalanche size and duration as predicted by criticality theory: $S \sim D^{\beta}$. The slope of the best-fit line (red) matches with the predicted $\beta = (\alpha - 1)/(\tau - 1)$ (yellow). **(b)** In different experiments, different values were found for duration exponents α and size exponents τ. **(c)** Different best-fit β were found for different turtles. Predicted β matched the best-fit β in the visually-driven steady state. Line indicates identical match. **(d-f)** Computational model displays the same relationship among power law exponents as found experimentally. Different size and duration exponents (e) were obtained by varying the input rate *R*, the degree of subsampling, and default synapse strengths Λ_0 (see inset legend).

the observed values of τ and α provided a good prediction, $\beta = (\alpha - 1)/(\tau - 1)$, of the best-fit β for all experiments (Fig. 3c, Supplementary Information 5).

The experimentally observed range of the values for the exponents τ and α (Fig. 3b) raises an important question as to the origin of this variability. In the model, we demonstrated that τ and α depended on three factors (Fig. 3e): 1) the subsample fraction, 2) the external input rate, and 3) the default synaptic strength (parameterized by the largest eigenvalue Λ_0 of the default synaptic weight matrix[25], see Supplementary Information 7). Subsampling, i.e. creating avalanche distributions based on spikes from a subset of all model neurons, tended to increase τ and α, consistent with previous studies[26,27]. The effects of input rate and default synapse strengths depended on the level of subsampling. Importantly, the various combinations of τ and α observed in the model preserve the size versus duration scaling relationship (Fig. 3f), similar to what we found experimentally (Fig. 3c). We note that the near linear relationship between τ and α (Fig. 3b,e) has not, to our knowledge, been predicted theoretically.

6.3 Discussion

The close match between our experimental observations and our model results, suggest that adaptation plays a crucial role in tuning cortical circuits towards the critical regime during vision. Why should adaptation in sensory cortex tune the network to operate near a critical regime? Previous computational studies and cortex slice experiments suggest that the critical regime optimizes several aspects of information processing (reviewed in ref. 3) including dynamic range[20,25,28] and information transmission[5,6]. Our observation that transient response to stimulus onset is not critical suggests that sensory cortex dynamically adapts to gain the functional benefits of critical dynamics during strong sensory input.

The critical regime has long been hypothesized to be a target of homeostatic processes in neural networks. This could be achieved by some 'top-down' mechanism (e.g. neuromodulators like dopamine[29]) that tunes the network or as the result of local self-organization[14,16,30,31]. In either case, one concern with this hypothesis has been that, theoretically, the critical regime occupies an infinitesimal volume in state space (the boundary between two different regimes), which may be too small a target to hit for a real biological tuning process contending with noise and imperfections. Recent theoretical findings mitigate this concern, showing that in networks with complex structure, the critical regime expands, occupying a substantial region (Griffiths phase) in state space[32]. Thus, our experiments, together with previous theory, establish the critical regime as a viable target for adaptive self-tuning during cortical sensory information processing.

6.4 Methods

6.4.1 Ex vivo eye-attached whole-brain preparation.

All procedures were approved by Washington University's and University of Arkansas' Institutional Animal Care and Use Committees and conform to the guidelines of the National Institutes of Health on the Care and Use of Laboratory Animals. Adult red-eared turtles (n=9, Trachemys scripta elegans, 150 – 200 g weight, 12-15 cm carapace length) were studied. Following anesthesia (Propofol 10 mg/kg) and decapitation, we surgically removed the brain, optic nerves, and eyes, from the cranium (Supplementary Information 9). One eye was hemisected and drained, thus exposing the retina for visual stimulation; the other eye was removed. Two cuts allowed the cortex to be unfolded, exposing the ventricular surface, thus facilitating the subsequent insertion of the microelectrode array. The eye and the brain were continuously perfused with

artificial cerebrospinal fluid (in mM; 85 NaCl, 2 KCl, 2 MgCl2, 45 Na HCO3, 20 D glucose, and 3 CaCl2 bubbled with 95% O2 and 5% CO2), adjusted to pH 7.4 at room temperature. Recordings began 2-3 hrs after induction of anesthesia.

6.4.2 Microelectrode array measurements.

We recorded wideband (0.7 Hz – 15 kHz) extracellular voltages relative to a silver chloride pellet electrode in the bath at 30 kHz sample rate (Blackrock Microsystems, Cerebus). With post-processing filtering (band-pass 5-100 Hz) we extracted local field potential (LFP). We used two different electrode arrays. The first was a 96-channel microelectrode array (10x10 square grid, 400 µm inter-electrode spacing, 500 µm electrode length, no corner electrodes, Blackrock Microsystems). Using a micromanipulator (Sutter, MP-285), we inserted this array to a depth of 250-500 µm with the plane of electrodes parallel to the dorsal surface of cortex. The second array was comprised of a three dimensional grid of electrodes (4x4x8 grid, 16 shanks, 8 electrodes per shank, 300 µm inter shank spacing, 100 µm interelectrode spacing on each shank, Neuronexus). This second array was inserted to a depth such that electrodes spanned the cortex from the ventricular to the dorsal surface. We analyzed data from electrodes that were located with the visually responsive region of cortex (Supplementary Information 2). This included between 13 and 28 electrodes (19 on average) for 10x10 electrodes and approximately 48 electrodes for the 3D grid electrodes.

6.4.3 Visual stimuli

Visual stimuli (two types of grayscale movie, black dots moving on a white background, uniform black to gray transition) were created by a computer and delivered with either a miniature video projector (Aaxa Technologies, P4X Pico Projector) or an LCD monitor (Samsung 19”,

1440x900 pixels, contrast ratio = 20000:1, response time = 2 ms). The projector/monitor image was focused onto the retina with additional lenses (Fig. 1a). The mean light intensity (irradiance) at the retina was 20 mW/m^2.for the monitor and 1 W/m^2 for the projector. In two experiments, we also used brief flash from a light emitting diode (LED, 60 W/m^2 at retina) placed near the retina to stimulate with a 1 s flash. Additional details about the stimuli including timing are in Supplementary Information 10.

6.4.4 Avalanche analysis

The first step of avalanche detection was to compute the standard deviation of every LFP trace. Next we defined an *'LFP peak'* as a period of time during which an LFP trace fluctuates beyond 3 to 4 standard deviations, due to either a positive or negative deflection (Fig. 1b). For each LFP peak, we determined the time of its extreme value and the identity of the channel on which it was recorded. The channel information was used to exclude from analysis LFP peaks which were not within visual cortex. An avalanche was defined as a spatiotemporal cluster of consecutive LFP peaks with inter-peak intervals not exceeding a temporal threshold ΔT (channel information does not play a role in avalanche definition). ΔT was chosen to be the average inter-peak interval (<IPI>, inverse of population LFP peak rate), resulting in $\Delta T = 24 \pm 18$ ms (mean ± SD). Avalanche duration was defined as the difference between the first and last LFP peak time within the avalanche. The size of an avalanche was defined as the number of LFP peaks comprising the avalanche. Avalanches analyzed separately depending on whether they occurred during the transient period or visually-driven steady state period. Robustness of results to changes in ΔT and definitions of time periods are in Supplementary Information 11.

6.4.5 Power law fitting and fit quality, q

Using maximum likelihood methods[18,10], we fit a truncated power law (truncated at both the head and tail) to the avalanche distributions during visually-driven steady state (Supplementary Information 12). The fitting function for the avalanche size distribution was $f(S) = S^{-\tau}(\sum_{x=x_0}^{x_M} x^{-\tau})^{-1}$, where the maximum size x_M was assumed to be the largest observed size. The minimum size x_0 and the exponent τ were fitting parameters. Since avalanche duration is a non-integer variable, the fitting function for the duration distribution was $g(D) = (1-\alpha)(y_M^{1-\alpha} - y_0^{1-\alpha})^{-1} D^{-\alpha}$, where the maximum y_M was taken as the largest observed duration, and y_0 and α were fitting parameters. Exponents τ and α between -1 and -4 in increments of 0.01 were tried. Minimum values x_0 and y_0 were tried increasing from 0, but only up to the point when the fitted power law matches the data well enough to have a Kolmogorov-Smirnov statistic $KS < 1/\sqrt{N_{samp}}$, where N_{samp} is the number of avalanches comprising the dataset (Supplementary Information 12). For fitting model data size and duration distributions, we used the fitting function *f*(*S*) above, because both size and duration are discrete variables for the model.

After finding the best-fit power law, the next step was to assess goodness-of-fit q[10,18]. We compared the experimental data to 1000 surrogate data sets drawn from the best-fit power law distribution with the same number of samples as the experimental data set. The deviation between the surrogate data sets and a perfect power law was quantified with the KS statistic. The quality q of the power law fit was defined as the fraction of these surrogate KS statistics which were greater than the KS statistic for the experimental data. We use a very conservative criterion, q>0.1, for judging the data to be power law distributed. This is demonstrated visually in Fig 1f,g

and Fig 2e,f by plotting the experimental distribution over a gray band which delineates the 5-95 percentiles of the surrogate data sets.

6.4.6 Computational model

$N = 1000$ all-to-all connected binary neurons received input from outside the network. The 'strength' of the synapse from neuron *j* onto neuron *i* at time *t* is determined by the corresponding element of the synaptic weight matrix $W_{ij}(t)$. 20% of neurons are inhibitory, i.e. with negative entries in the weight matrix. $\Omega_i(t)$ is the strength of the input synapse onto neuron *i* (all excitatory). The binary state $s_i(t+1)$ of neuron *i* ($s = 0$ inactive, $s = 1$ spiking) is determined probabilistically based on the sum $p(t+1)$ of its inputs $p(t+1) = \Omega_i(t)\sigma_i(t) + \sum_{j=1}^{N} W_{ij}(t)s_j(t)$. If $0 < p < 1$, then the neuron fires with probability p. If $p \geq 1$, then the neuron fires with probability 1. If $p \leq 0$, then the neuron does not fire. Time is discrete and state updates are synchronous. The input $\sigma_i(t)$ from the *i*th input synapse is binary (1 with probability *r*). The onset of stimulation is modelled as a step increase from r=5x10^{-5} to either r=0.02 or r=0.1. In Figs. 2 and 3, we report the population input rate of $R = Nr$. The update rules for synaptic dynamics are

$$W_{ij}(t+1) = W_{ij}(t) + \tau_r^{-1}\left(W_{ij}^o - W_{ij}(t)\right) - \tau_d^{-1} W_{ij}(t)s_j(t)$$

$$\text{and } \Omega_i(t+1) = \Omega_i(t) + \tau_r^{-1}\left(\Omega_i^o - \Omega_i(t)\right) - \tau_d^{-1}\Omega_i(t)\sigma_i(t).$$

The default weight matrix was constructed such that its largest eigenvalue Λ_0 has absolute value equal to either 1.0, 1.05, or 1.1 (Supplementary Information 7). A largest eigenvalue of 1.0 corresponds approximately to an average synaptic weight of 1/N and is known to result in critical

dynamics for models with static synapses[25]. Synapses depress with a time constant of $\tau_d = 20$ timesteps following a presynaptic spike and recover exponentially with a time constant of $\tau_r = 400$ timesteps.

Each avalanche is initiated by external input. Upon reaching a timestep with no active cortical neurons, the avalanche is considered to be ended. We simulated 30 trials of step increase in input. In each trial, we ran the model for 5000 timesteps following the onset of increased input. Subsampling (Fig. 3) entailed analyzing the spikes from a randomly chosen 30% or 10% of the network.

6.5 Supplementary Information

6.5.1 Weakly-driven versus strongly-driven model network dynamics

Our modelling efforts highlight an important distinction between weakly and strongly driven systems. For simplicity, we first consider a model with static synapses (Supplementary Figs. 1,2). In contrast with our dynamic model, here we fixed synaptic weight matrices W and Ω and did not implement the dynamic rules for changing synapse strengths. Otherwise, the model was identical to the dynamic model. In the weakly driven case, the timescales of driving and avalanches are well separated. In this case, interactions among neurons (e.g. synapse strengths, number of connections per neuron, relative strength of excitatory versus inhibitory synapses) determine whether or not a system produces critical dynamics (i.e. power law avalanche distributions and size vs duration scaling). More succinctly, in the weakly driven case, a synaptic weight matrix with largest eigenvalue Λ=1 defines criticality[1]. In contrast, in the strongly driven case, non-critical dynamics may occur, even with 'structurally critical' synapses,

i.e. Λ=1. In the case of strong drive and depressing synapses (Fig 2), both the intensity of external input and Λ are dynamic variables. If synaptic depression sufficiently decreases effective input to the cortex and Λ is near unity after such depression, only then will critical dynamics result. In conclusion, to maintain critical dynamics and associated functional advantages, a system must account for both Λ and the level of external drive it receives.

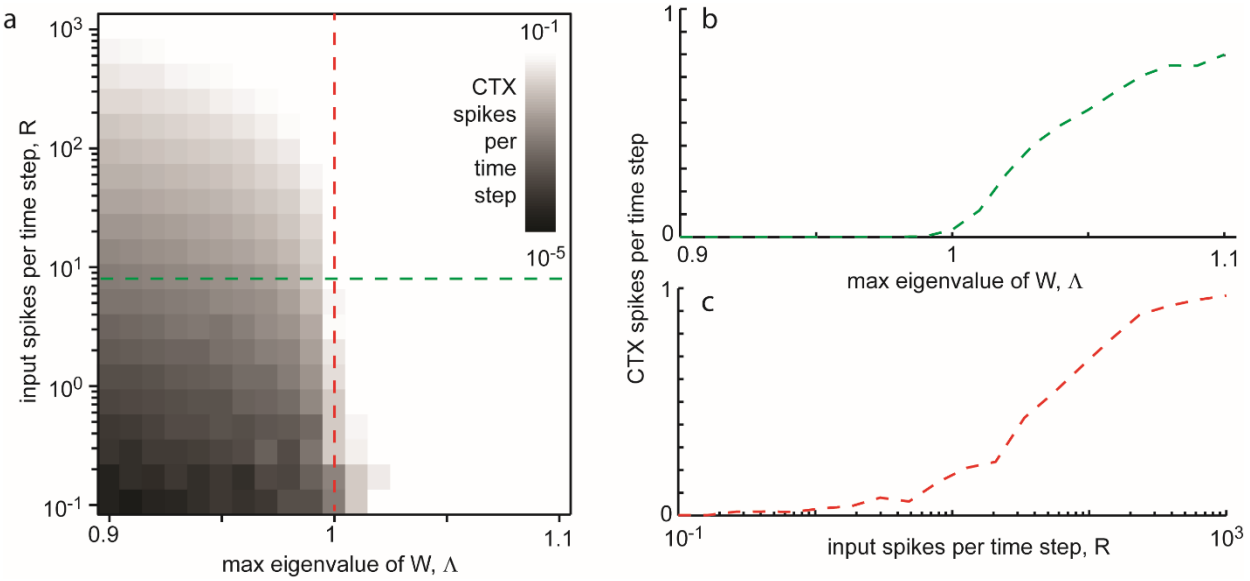

Supplementary Figure 6.1. Sufficiently strong input results in a noncritical dynamics**.** These results are from our model with static synapses. The synaptic weight matrix is fixed. Otherwise the model is identical to the model presented in the main text. **(a)** Population spike rate (gray scale) varies with both the strength of synapses (parameterized by Λ, the absolute value of the largest eigenvalue of the synaptic weight matrix) and the input rate (total spikes per time step for the whole network). The color scale is logarithmic. **(b)** Phase transition from subcritical to supercritical dynamics as synapse strength is increased. Critical dynamics occur at Λ≈1. Input rate is fixed just below R=10 spikes per time step. Corresponds to the green dashed line in panel a. **(c)** Increasing from low to high input rates causes a transition from critical dynamics (R < ~10 spikes per time step) to non-critical dynamics for high input rates. Synapses are fixed at Λ=1. Corresponds to the red dashed line in panel a.

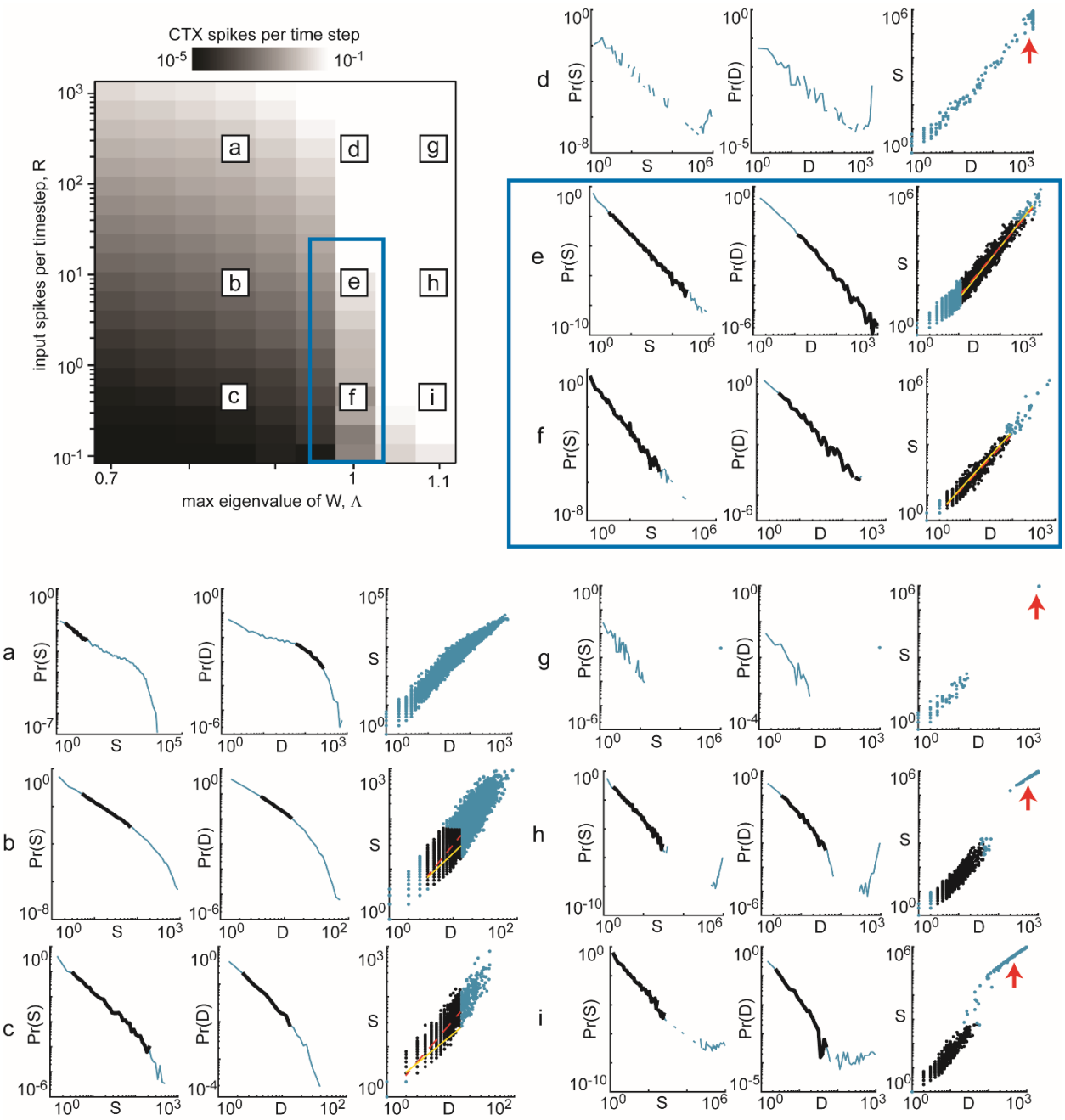

Supplementary Figure 6.2. Strong drive and Λ far from 1 preclude critical dynamics. (upper left) A phase diagram like that shown in Supplementary Fig. 1a. The letters a-i indicate the parameters corresponding to the example avalanche distributions and scaling laws shown in panels a-i. The blue box encloses the two examples that match best with our experimental observations. **(panels a-i)** *LEFT*: Avalanches size S probability density function. Heavy black line: range of power law scaling. Blue: full range. *MIDDLE*: Avalanche duration D probability density function. *RIGHT*: Avalanche size versus duration. Red dashed lines: best fit S vs D scaling relationship. Yellow lines: predicted S vs D scaling. Red arrows: Indicate the large avalanches (bimodally distributed) that occur for Λ>1(g,h,i) or for intense input with Λ=1 (d). Note that critical dynamics

(large range of power law scaling and well-predicted S vs D scaling) are not found if either Λ is far from 1 or if the input rate is too high.

6.5.2 Visual cortex in turtles

Turtle visual cortex is defined by the geniculo-recipient area of the dorsal cortex[2,3]. We accepted a recording channel as part of visual cortex when its average LFP response to visual stimulation exceeded a given threshold. For the 10x10 grid electrodes, we identified visually responsive channels based on stimulus-triggered average maps of the absolute value of LFP (for an example see Supplementary Fig. 3b). For the 3D grid electrodes, we placed the entire array in visual cortex, but used data from every other electrode along each shank (total of about 48 electrodes). Based on this approach, visual cortex included between 13 and 28 electrodes (19 on average) for 10x10 electrodes and approximately 48 electrodes for the 3D grid electrodes. Importantly, the visually responsive region defined by our approach was always centered on rostral dorsal cortex (Supplementary Fig. 3c), which is where previous anatomy studies have identified LGN projections to cortex[2,4].

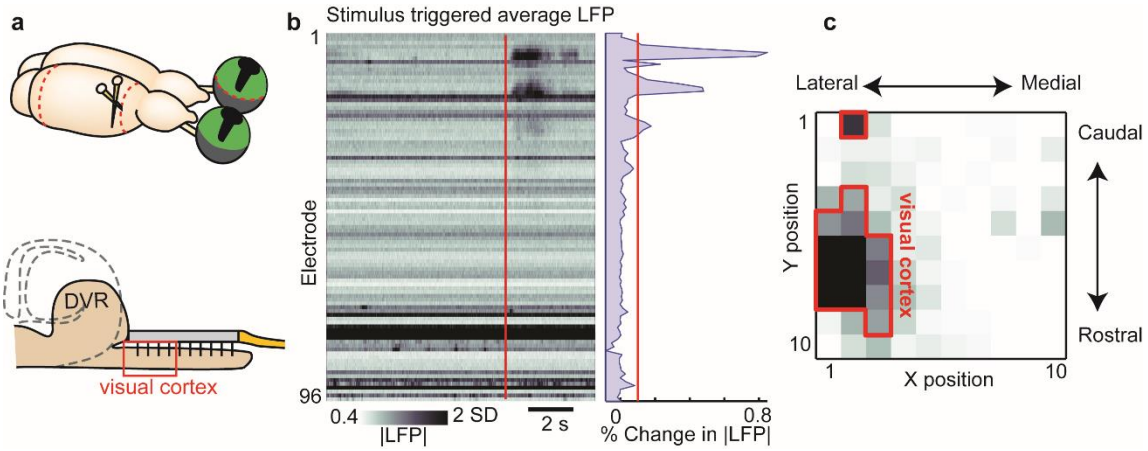

Supplementary Figure 6.3. Delineating visual cortex based on visually responsive channels**. a)** The whole brain is removed from the turtle with eyes attached. The ventricle beneath the cortex allows the unfolding of the cortex without severing afferent/efferent fibers. A 96-channel microelectrode array (MEA) is inserted into the unfolded visual cortex and surrounding cortical regions. DVR = Dorsal Ventricular Ridge. **(b, left)** Stimulus triggered average |LFP| is shown for

every electrode in the 96 channel array. Each row of the image represents one electrode. Time advances from left to right. The red line is the time the stimulus was turned on. Grayscale indicate magnitude of |LFP| normalized by SD averaged over 45 trials. Note that some channels have significant LFP amplitude, but little response to stimulus. These channels are located in the medial cortex, outside visual cortex (compare to Supplementary Fig. 8 data). **(b, right)** Percent change in |LFP| relative to the pre-stimulus baseline is plotted for every electrode. The post-stimulus time window is 4 s. We define a channel as visually responsive if the % change in |LFP| exceeds a threshold (10% in this example). **(c)** Each pixel in this image represents the % change in |LFP| for one electrode (same data as Middle panel). The pixels are spatially arranged according to actual electrode positions. The visually-responsive (above-threshold) channels are shown outlined in red. In all turtles, the visually-responsive channels were primarily in the rostral-lateral corner of the array. Note that this figure is relevant for experiments with the 10x10 microelectrode arrays. In contrast, the three dimensional grid array covered less area was positioned such that all electrodes were in the visually responsive area.

6.5.3 LFP-spike relationship

Our two primary reasons for analyzing LFP peaks rather than spikes were that 1) spikes were not always clearly measurable in our experiments and 2) that LFP may better represent a large population of neurons. Here we show that the rate of LFP peaks rises with the rate of multi-unit spikes for one turtle that did have clearly measurable spikes. This relationship suggests that although we specify avalanche size in terms of number of LFP peaks, the avalanche may be interpreted as comprised of a roughly proportional number of spikes.

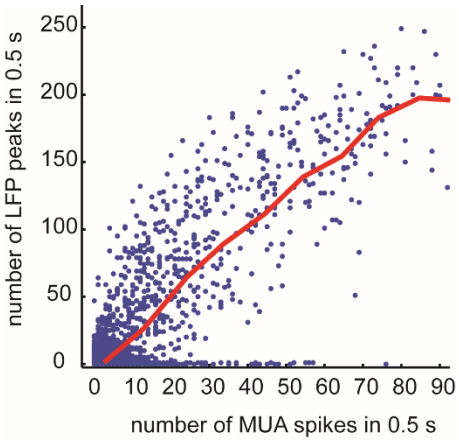

Supplementary Figure 6.4. LFP peak rate increases with multi-unit spike rate**.** Each point represents the numbers of peaks and spikes counted in one 0.5 s period. This was done in consecutive 0.5 s windows over the entire recording. The red line is the average of the points. Multi-unit activity was detected with a 5 SD threshold after band-pass filtering 300 - 3000 Hz.

6.5.4 Spatiotemporal dynamics of visually-driven population activity (beyond LFP peaks)

The data we present in our main results are based on LFP peaks and their statistics. Here we present some alternative perspectives showing the spatiotemporal dynamics of continuous LFP signals.

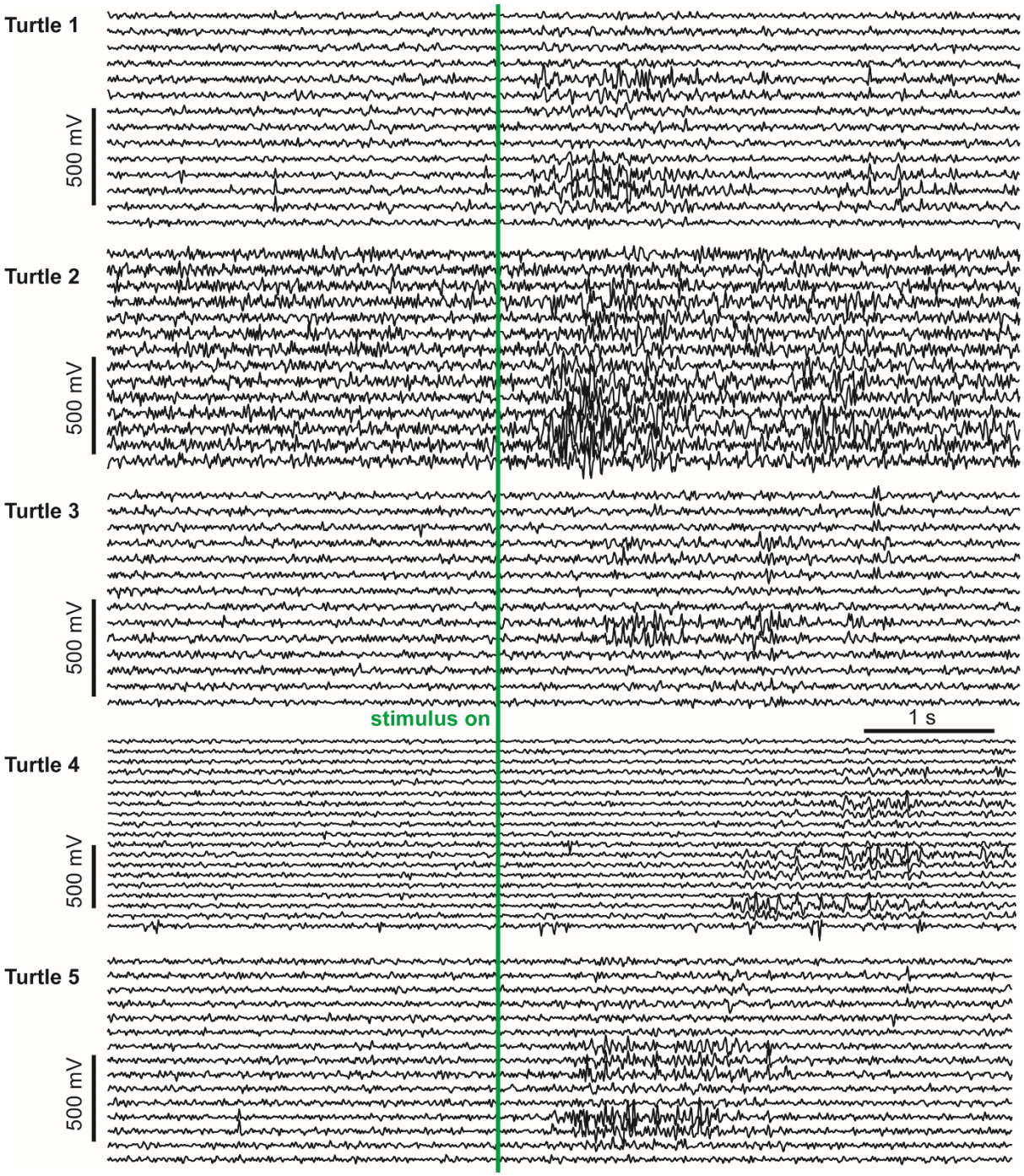

Supplementary Figure 6.5. Examples of raw data**.** Shown are examples of raw LFP traces (from all visually responsive electrodes) for the first five turtles. For turtles 1 and 2, the stimulus (onset at green line) was a complex movie. For turtles 3-5, the stimulus was black dot scanning across a white background.

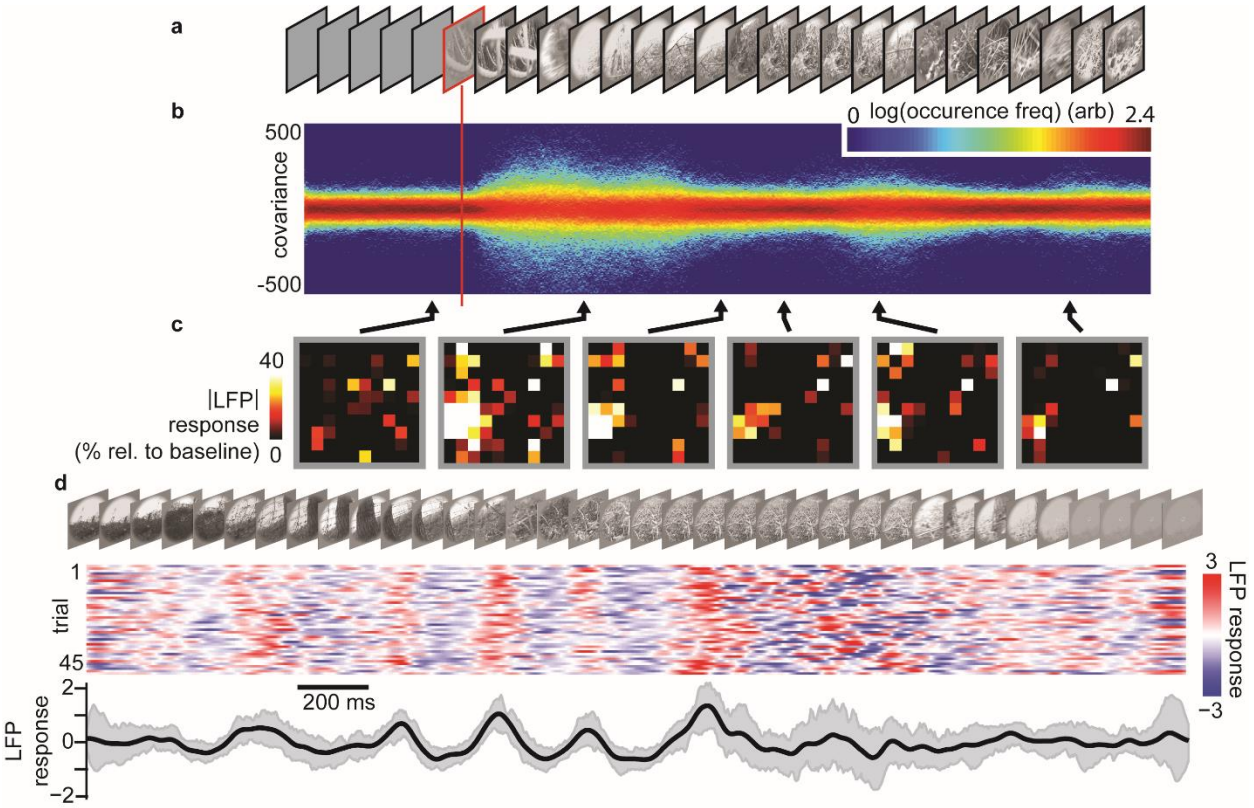

Supplementary Figure 6.6. Spatiotemporal dynamics of visually driven population activity**.** (**a**) Natural movie visual stimulus (for clarity, a subset of frames is shown). (**b**) At movie start, there is a transient increase in pairwise covariance of LFP. Each vertical strip of this plot displays one distribution of pairwise covariance computed during a 300 ms sliding time window (10 ms slide step). Data is from 45 repeated movie presentations. Color indicates how often a given covariance was observed. (**c**) Spatial patterns of stimulus-triggered average |LFP|. Each image represents the average LFP (% change relative to pre-stimulus baseline) at all 96 channels on the array at the time indicated by each arrow. (**d**) Low frequency LFP (1-5 Hz) recorded at one channel during repeated presentation (n = 45 trials) of the natural movie. For each trial (row), LFP amplitude is represented (color coded) in terms of z-score (difference from mean, normalized by SD). Small variability (gray) about the cross-trial average (black) demonstrates reliability of response to repeated stimuli. Frame-specific changes in LFP indicate stimulus specificity of response. The gray shaded region delineates quartiles.

6.5.5 Avalanche distributions and scaling relations for all experiments

The following 13 plots (Supplementary Fig. 7) shows avalanche size and duration distributions for all experiments. Each plot includes probability density functions (PDF) with logarithmic bins **(top left, top middle)** as well as cumulative distribution functions **(bottom left, bottom middle)**

for three data sets: 1) avalanches that occurred during the visually-driven steady state (blue), 2) avalanches during the transient (red), and 3) avalanches based on temporally jittered LFP peaks (T_j=10 s) from the visually-driven steady state (gray). In addition, we show the size versus duration scaling plot **(top right)** comparing the predicted scaling (yellow line) with the best fit scaling (red dashed line). In all plots, dark blue points represent the range of avalanches that best fits a truncated power law. The light blue points indicate the range that is outside the fitted range. In the PDF plots, the gray band delineates the range of expected probabilities for N avalanches drawn from a perfect power law distribution with the same exponent as the best fit power law for the data. Here, N is the number of experimentally observed avalanches within the fitting range. Finally each plot specifies what values were found for power law exponents τ and α, the parameter ΔT used in the avalanche analysis, the deviations δ between the best fit power law and the other distributions, the power law quality *q*, predicted β, best fit β, the total number of avalanches N_a, and the number of avalanches included in the fitted range for sizes (N_{fS}) and durations (N_{fD}).

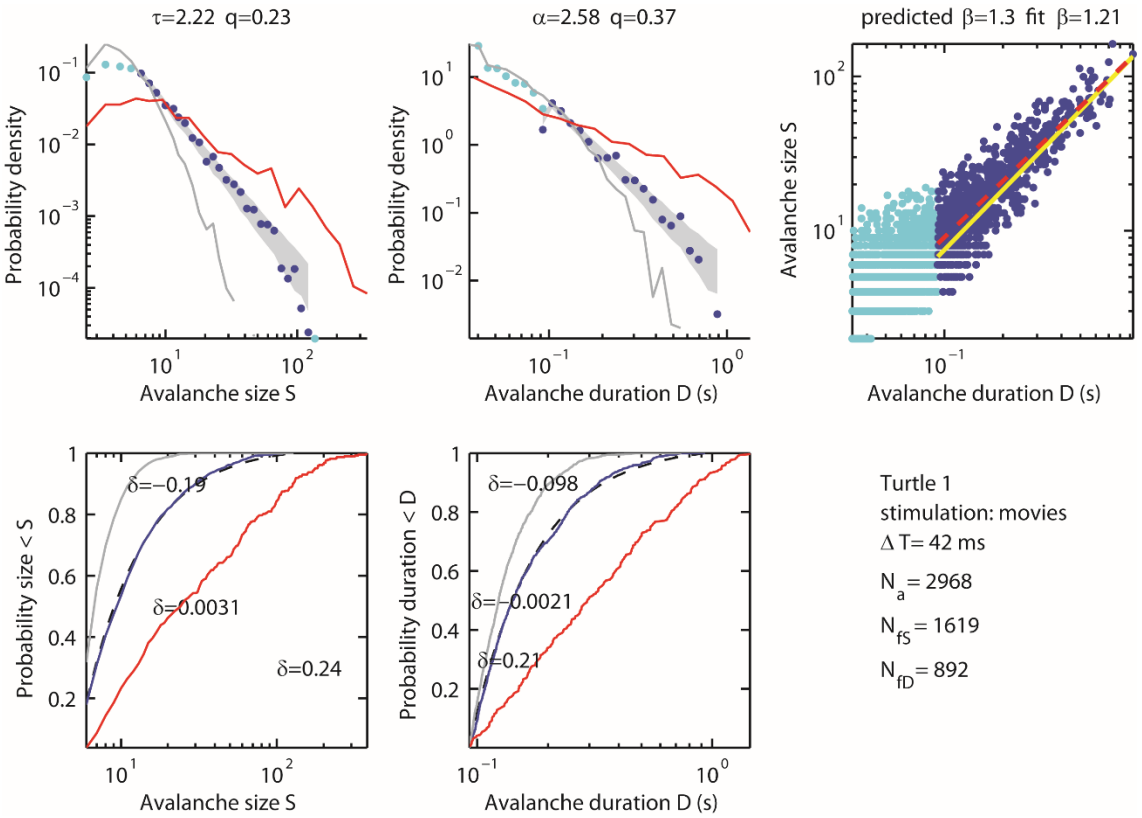

Supplementary Figure 6.7. Avalanche distributions and scaling laws for all experiments**.** A general caption for this figure and the following 12 figures is given above in Supplementary Information 5.

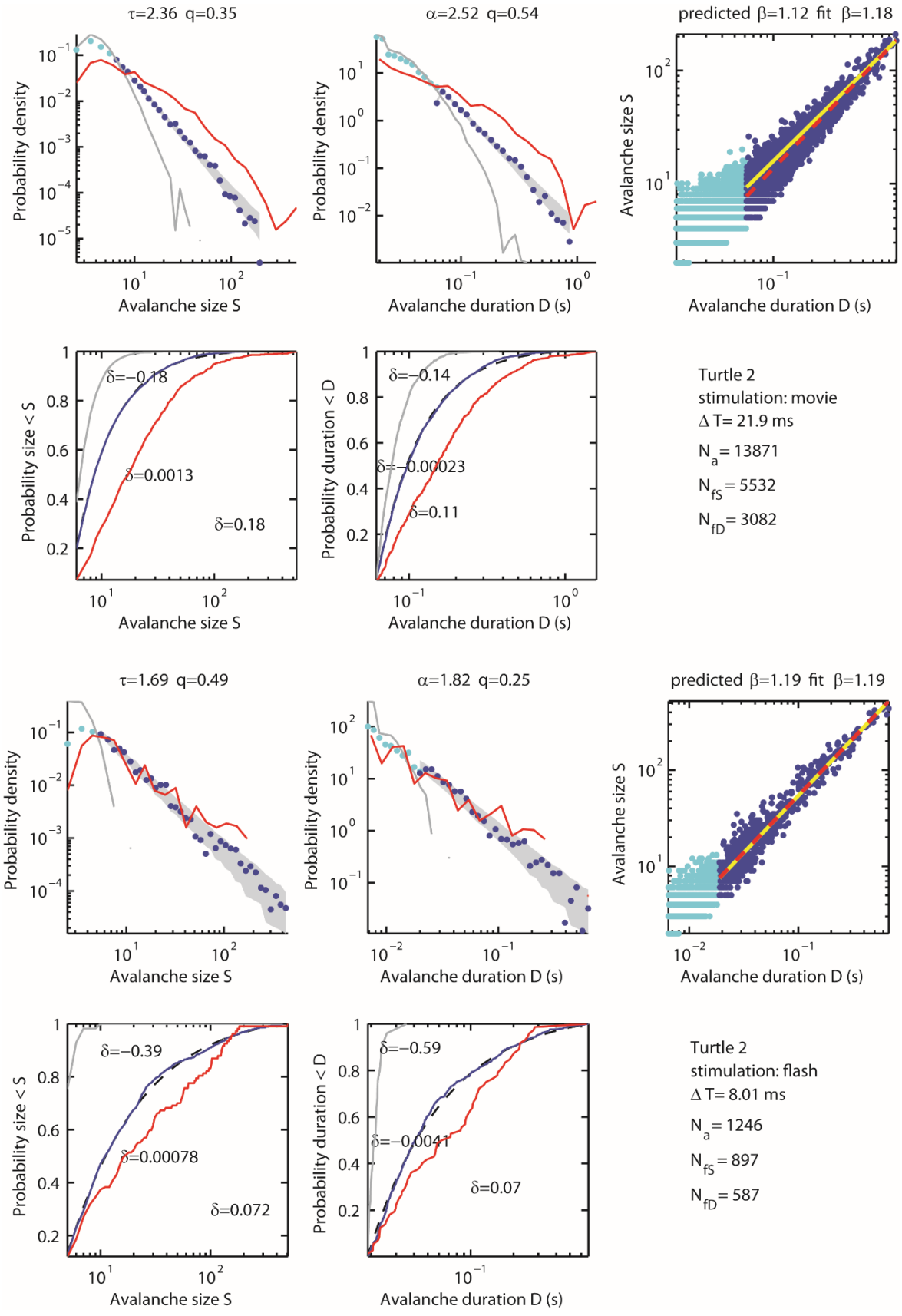
τ=2.36 q=0.35
α=2.52 q=0.54
predicted β=1.12 fit β=1.18
Probability density
Avalanche size S
Avalanche duration D (s)
Avalanche size S
Probability size < S
δ=−0.18
δ=0.0013
δ=0.18
Probability duration < D
δ=−0.14
δ=−0.00023
δ=0.11
Turtle 2
stimulation: movie
Δ T= 21.9 ms
N_a = 13871
N_fS = 5532
N_fD = 3082
τ=1.69 q=0.49
α=1.82 q=0.25
predicted β=1.19 fit β=1.19
δ=−0.39
δ=0.00078
δ=0.072
δ=−0.59
δ=−0.0041
δ=0.07
Turtle 2
stimulation: flash
Δ T= 8.01 ms
N_a = 1246
N_fS = 897
N_fD = 587

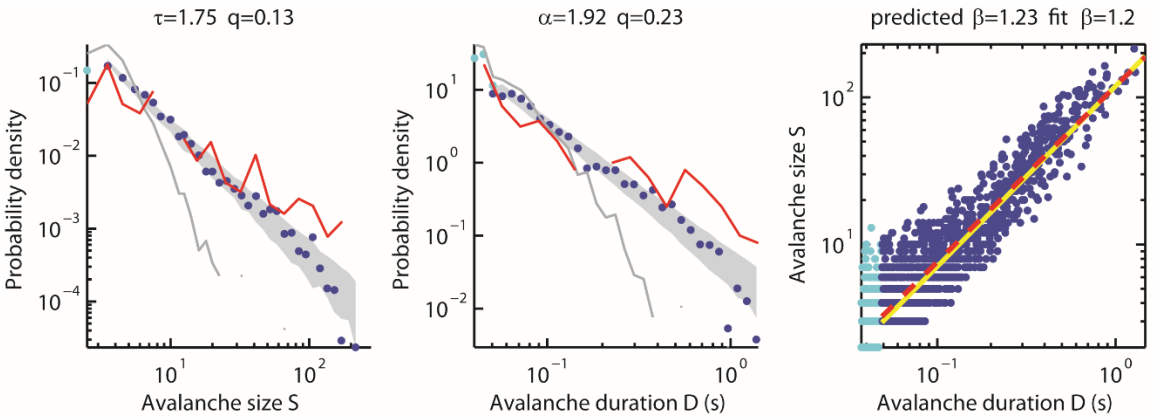

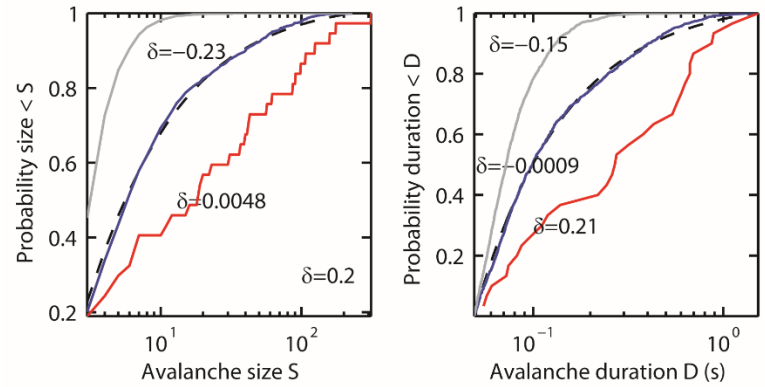

Turtle 3
stimulation: dots
$\Delta T = 47$ ms
$N_a = 1638$
$N_{fS} = 1393$
$N_{fD} = 1134$

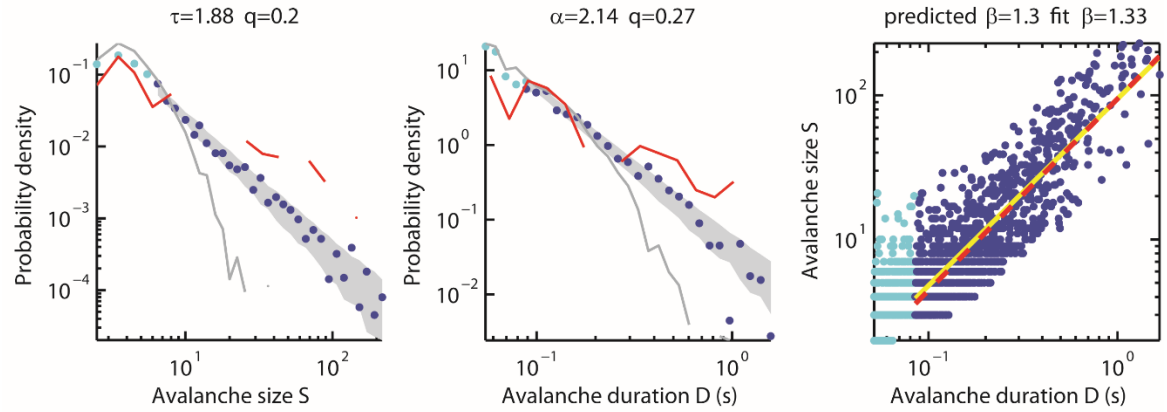

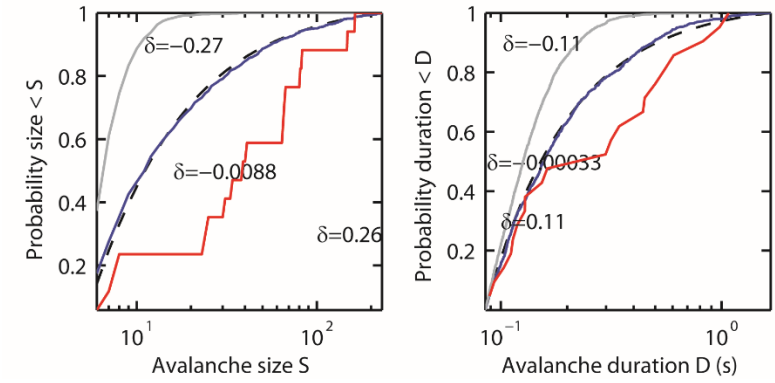

Turtle 4
stimulation: dots
$\Delta T = 64.3$ ms
$N_a = 1920$
$N_{fS} = 824$
$N_{fD} = 1129$

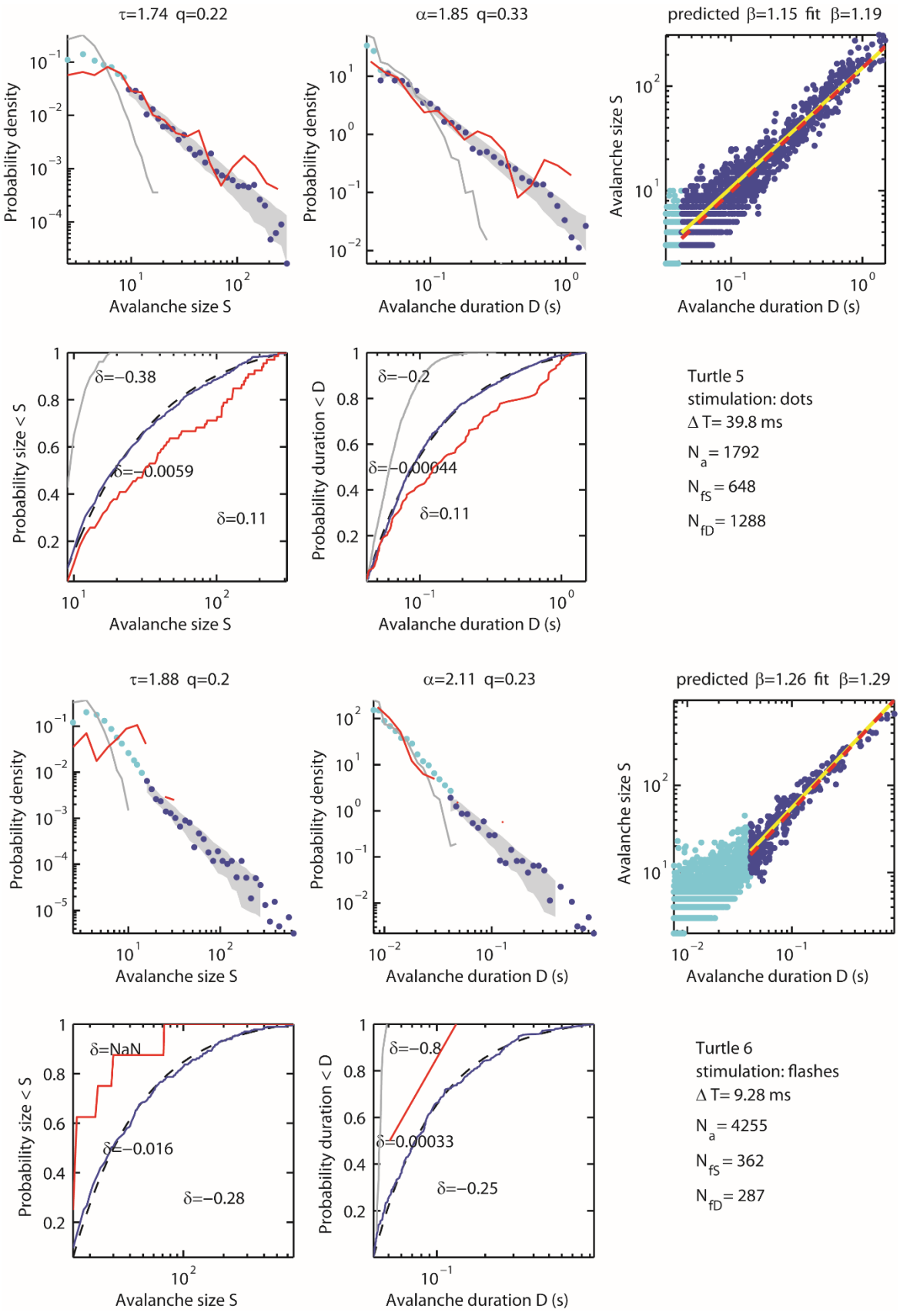
τ=1.74 q=0.22
α=1.85 q=0.33
predicted β=1.15 fit β=1.19
Probability density
Avalanche size S
Avalanche duration D (s)
Avalanche size S
Probability size < S
δ=−0.38
δ=−0.0059
δ=0.11
Avalanche duration D (s)
Probability duration < D
δ=−0.2
δ=−0.00044
δ=0.11
Turtle 5
stimulation: dots
Δ T= 39.8 ms
N a = 1792
N fS = 648
N fD = 1288
τ=1.88 q=0.2
α=2.11 q=0.23
predicted β=1.26 fit β=1.29
δ=NaN
δ=−0.016
δ=−0.28
δ=−0.8
δ=0.00033
δ=−0.25
Turtle 6
stimulation: flashes
Δ T= 9.28 ms
N a = 4255
N fS = 362
N fD = 287

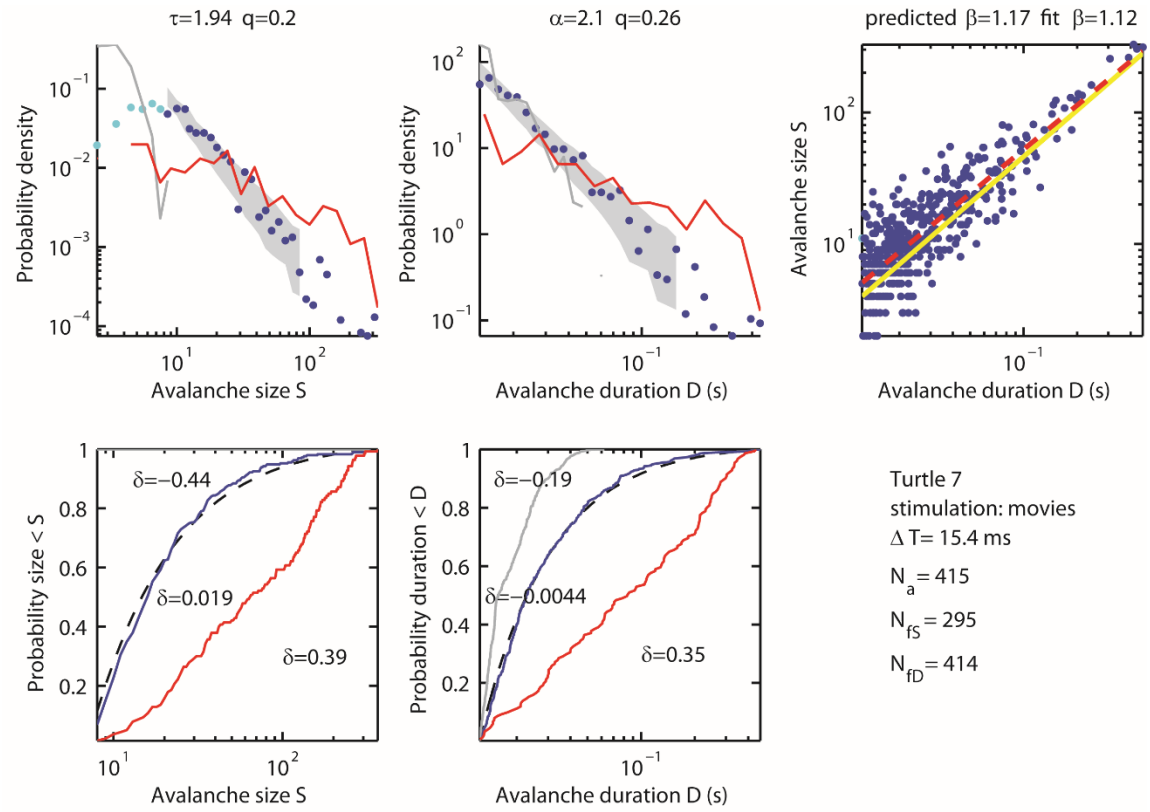
τ=1.94 q=0.2
α=2.1 q=0.26
predicted β=1.17 fit β=1.12
Probability density
Avalanche size S
Avalanche duration D (s)
Avalanche size S
Probability size < S
Probability duration < D
δ=−0.44
δ=0.019
δ=0.39
δ=−0.19
δ=−0.0044
δ=0.35
Turtle 7
stimulation: movies
Δ T= 15.4 ms
N a = 415
N fS = 295
N fD = 414

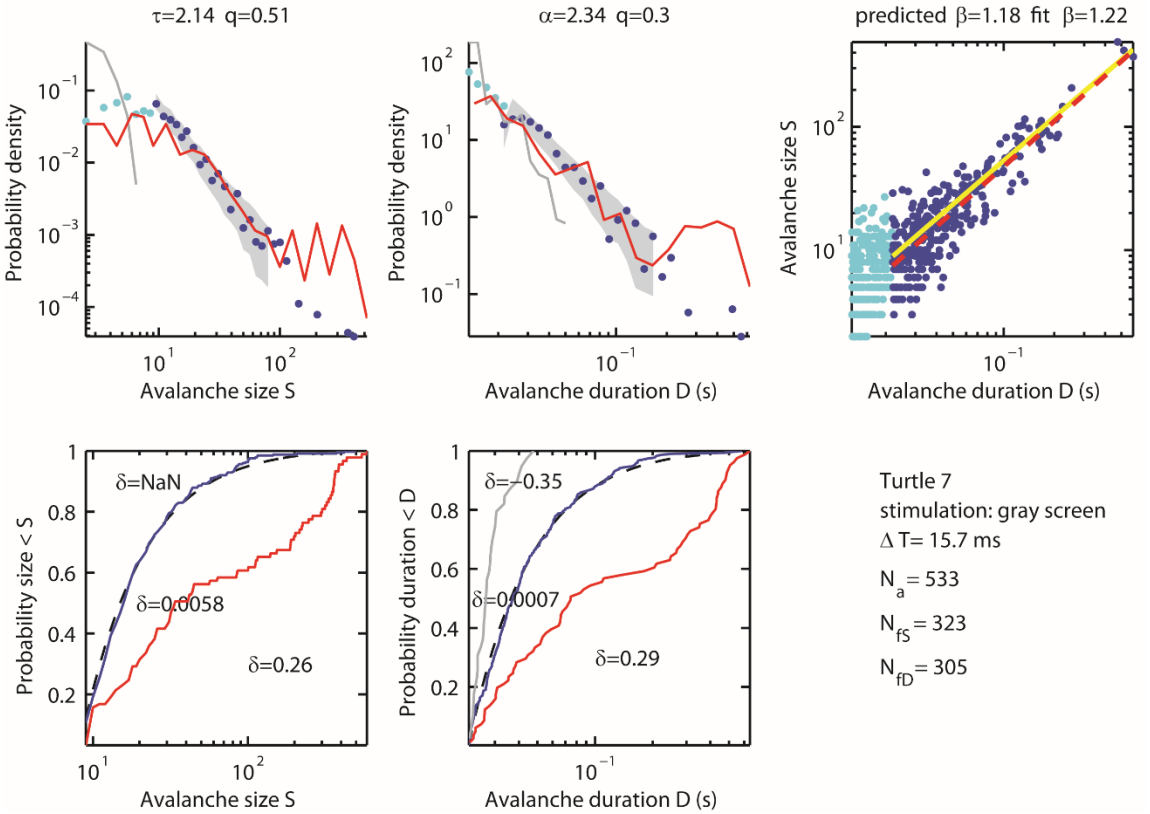
τ=2.14 q=0.51
α=2.34 q=0.3
predicted β=1.18 fit β=1.22
Probability density
Avalanche size S
Avalanche duration D (s)
Avalanche size S
Probability size < S
Probability duration < D
δ=NaN
δ=0.0058
δ=0.26
δ=−0.35
δ=0.0007
δ=0.29
Turtle 7
stimulation: gray screen
Δ T= 15.7 ms
N a = 533
N fS = 323
N fD = 305

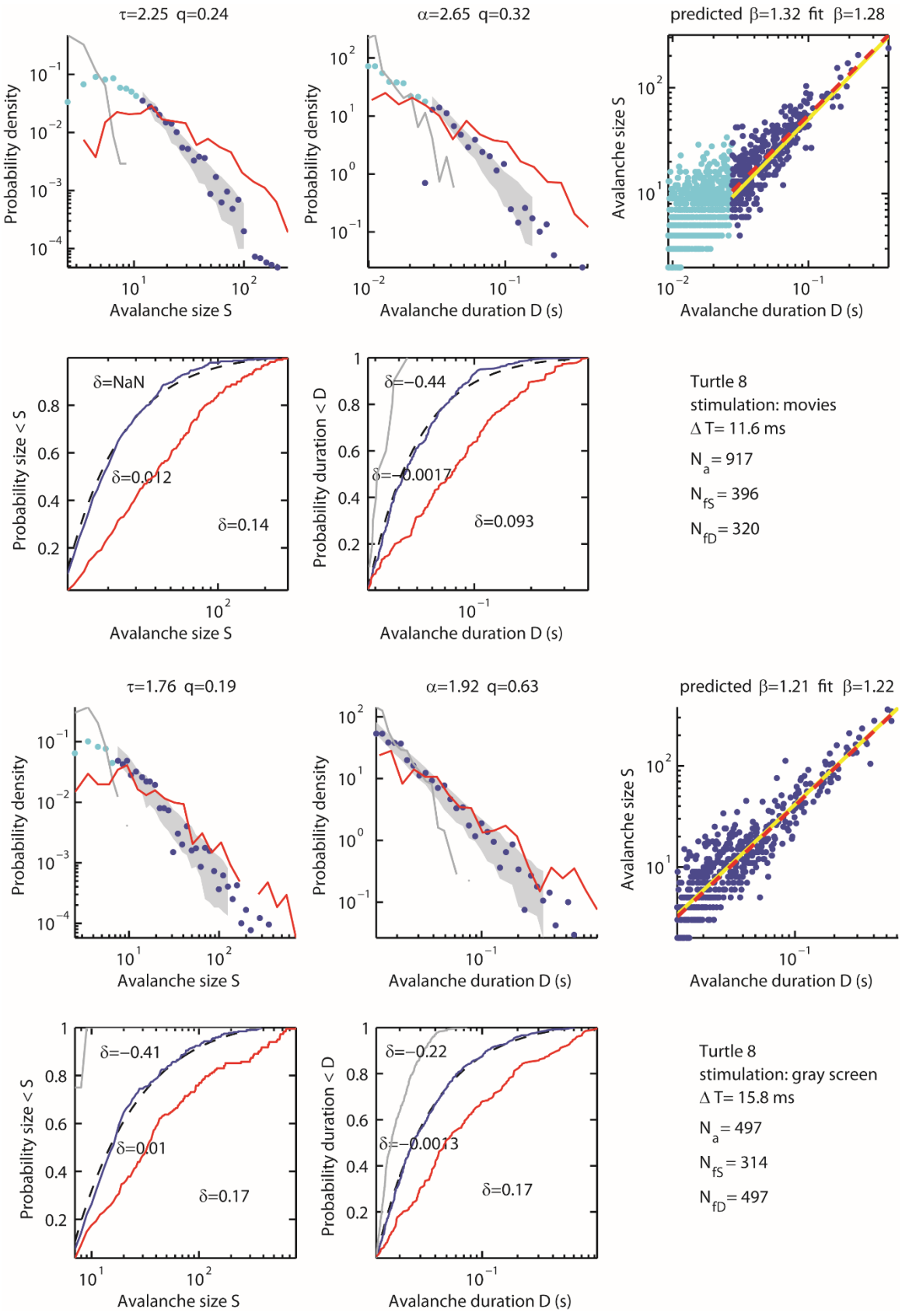
τ=2.25 q=0.24
α=2.65 q=0.32
predicted β=1.32 fit β=1.28
Probability density
Avalanche size S
Avalanche duration D (s)
Avalanche size S
δ=NaN
δ=0.012
δ=0.14
Probability size < S
Probability duration < D
δ=−0.44
δ=−0.0017
δ=0.093
Turtle 8
stimulation: movies
Δ T= 11.6 ms
N a = 917
N fS = 396
N fD = 320
τ=1.76 q=0.19
α=1.92 q=0.63
predicted β=1.21 fit β=1.22
δ=−0.41
δ=−0.01
δ=0.17
δ=−0.22
δ=−0.0013
δ=0.17
Turtle 8
stimulation: gray screen
Δ T= 15.8 ms
N a = 497
N fS = 314
N fD = 497

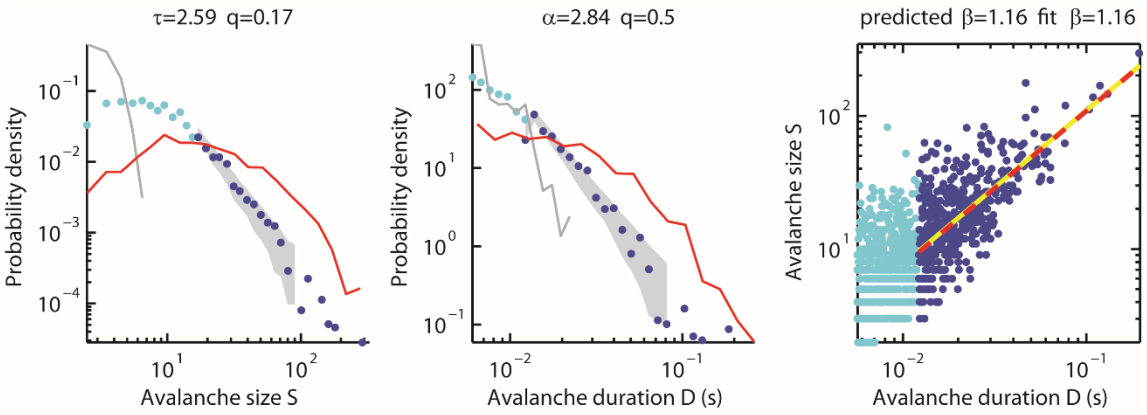

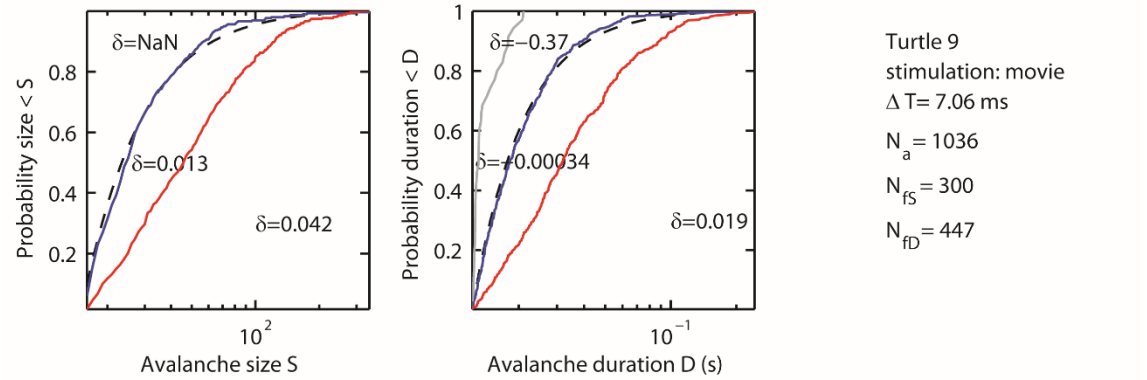

Turtle 9
stimulation: movie
Δ T= 7.06 ms
N_a = 1036
N_{fS} = 300
N_{fD} = 447

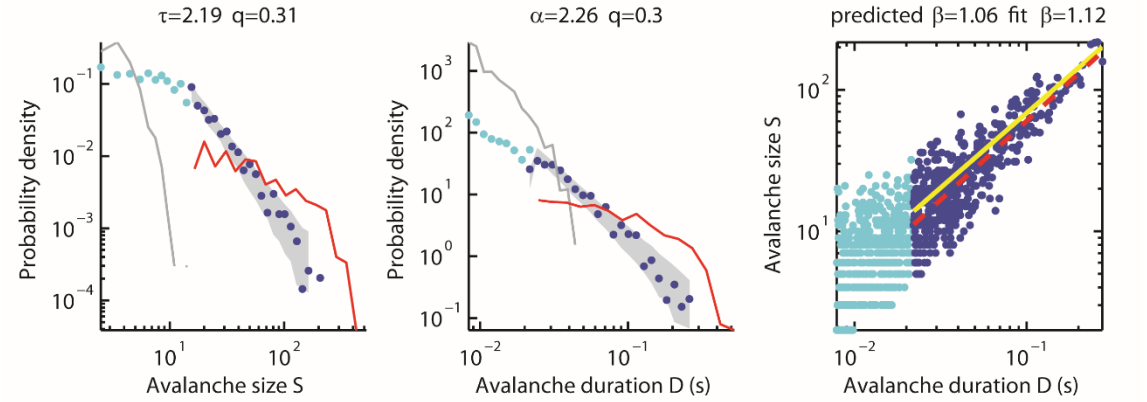

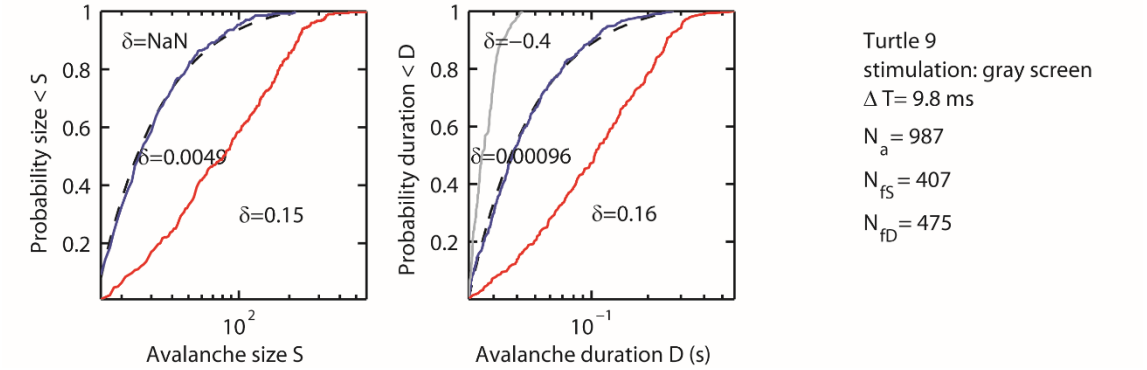

Turtle 9
stimulation: gray screen
Δ T= 9.8 ms
N_a = 987
N_{fS} = 407
N_{fD} = 475

6.5.6 Avalanche statistics outside visual cortex

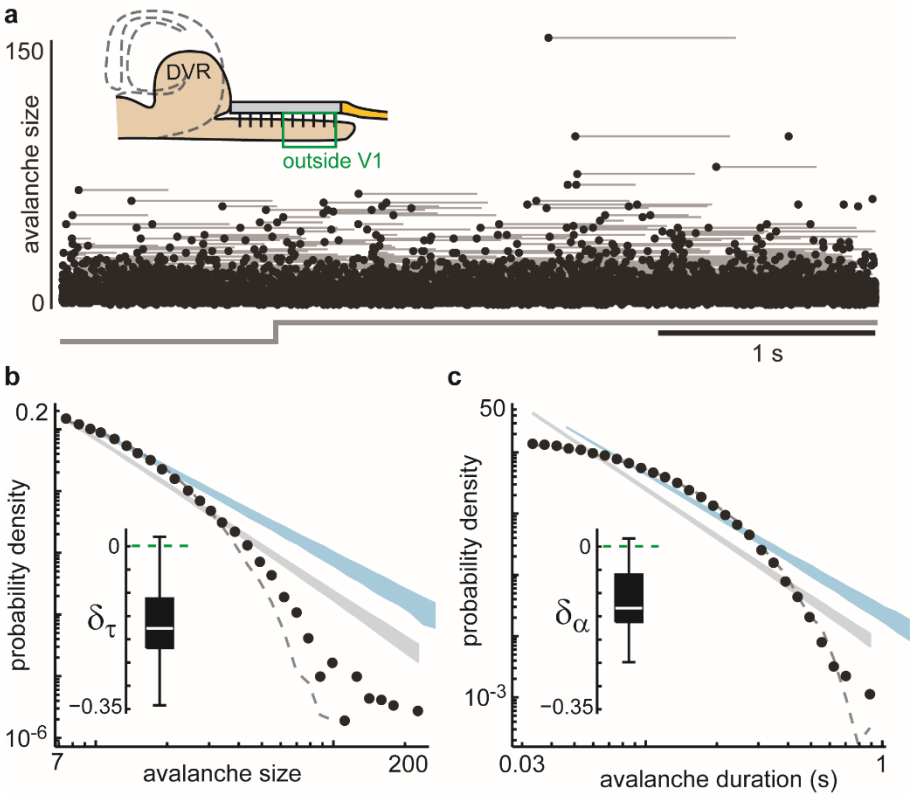

Supplementary Figure 6.8: Critical dynamics are not a universal feature of cortical circuits: no power laws outside visual cortex**.** Here we present recordings from outside visual cortex (Supplementary Fig. 3) in the cortical region adjacent to visual cortex, known as medial cortex, the putative homolog of mammalian hippocampus[4]. (**a**) Stimulus-triggered avalanche size time series confirms that, among electrodes outside visual cortex, the cortex is active, but activity is independent of visual response. Each point represents one avalanche. Avalanche durations are represented by the gray line to the right of each point. The avalanches recorded during 45 repeats of movie stimulation are overlaid. (**b,c**) Outside visual cortex, avalanche size (b) and duration (c) distributions are not power laws. For comparison, the best fit power law is represented by the gray shaded region and the power law for avalanches within visual cortex is shown in blue (data from same turtle as Fig 1). Jittering LFP peak times (dashed) leaves avalanche size statistics largely unchanged, indicating that cross-channel correlations are weak outside visual cortex. Inset summarizes the deviation from the visual cortex power law for all experiments. While fitting power laws to activity outside of visual cortex (Supplementary Fig. 8), we did not fit the y_0 parameter, because such fitting resulted in y_0 very close to y_M excluding the vast majority of the

dataset. This fact is further demonstration that the data are not power law outside visual cortex. Likewise χ_0 was not a fitting parameter for activity outside visual cortex.

6.5.7 Details and example data from model with adapting synapses.

Our model with adapting synapses was designed to test the idea that short-term depression may account for our primary experimental observation: power law avalanches after a transient period of depressive adaptation. The model consisted of $N = 1000$ all-to-all connected binary neurons (mimicking cortex). In addition, each neuron receives input from outside the network (mimicking thalamic drive). The 'strength' of the synapse from cortical neuron *j* onto neuron *i* at time *t* is determined by the corresponding element of the synaptic weight matrix $W_{ij}(t)$. 20% of neurons are inhibitory. All the output synapses of inhibitory neurons are modeled with negative entries in the weight matrix. Similarly, $\Omega_i(t)$ is the strength of the thalamocortical synapse onto neuron *i* (all excitatory). The binary state $s_i(t+1)$ of neuron *i* ($s = 0$ inactive, $s = 1$ spiking) is determined probabilistically based on the sum $p(t+1)$ of its inputs

$$p(t+1) = \Omega_i(t)\sigma_i(t) + \sum_{j=1}^{N} W_{ij}(t)s_j(t)$$

If $0 < p < 1$, then the neuron fires with probability p. If $p \geq 1$, then the neuron fires with probability 1 (p is very rarely >1). If $p \leq 0$, then the neuron does not fire (p is very rarely <0). Time is discrete and state updates are synchronous. The input $\sigma_i(t)$ from the *i*th thalamocortical synapse is 1 with probability *r* and zero with probability 1- *r*, for all *i*. To simulate the onset of visual stimulation, we implement a step increase from r=5x10^{-5} to either r=0.02 or r=0.1. In the

main text and in figures (Figs. 2, 3, Supplementary Figs. 1,2,9) we report the population input rate of $R = Nr$,which specifies the total number of input spikes per timestep for the whole network. Data from both of these situations is summarized in Fig. 3 and Supplementary Fig. 9.

At time $t = 0$ the corticocortical synapse matrix is equal to the default matrix W_{ij}^0 . The default matrix is constructed as follows. Initially all entries are drawn from a uniform distribution on $[0,1]$. Then a randomly chosen subset of 20% of columns are multiplied by -1 (these are the inhibitory output synapses.) Then, the weight matrix is normalized so that its largest eigenvalue Λ_0 has absolute value equal to either 1.0, 1.05, or 1.1. Data generated with these different model parameters is summarized in Fig. 3 and Supplementary Fig. 9. A largest eigenvalue of 1.0 corresponds approximately to an average synaptic weight of 1/N and is known to result in critical dynamics for models with static synapses and weak input[1] (Supplementary Figs 1, 2). The initial thalamocortical synapses Ω_i^0 are all equal to $8/N$. Both the corticocortical and thalamocortical synapses are dynamic in an activity-dependent manner, similar to previous models[5,6]. They depress with a time constant of $\tau_d = 20$ timesteps following a presynaptic spike. They also recover exponentially with a time constant of $\tau_r = 400$ timesteps. These timescales for depression and recovery were chosen so that the synapses reach a steady state in less than about 500 timesteps, which is consistent the timescales of adaptation we observed experimentally, if we interpret one timestep as approximately 1 ms. The discrete time update rules for synaptic dynamics are

$$W_{ij}(t+1) = W_{ij}(t) + \frac{1}{\tau_r}\left(W_{ij}^o - W_{ij}(t)\right) - \frac{1}{\tau_d} W_{ij}(t) s_j(t)$$

$$\Omega_i(t+1) = \Omega_i(t) + \frac{1}{\tau_r}\left(\Omega_i^o - \Omega_i(t)\right) - \frac{1}{\tau_d}\Omega_i(t)\sigma_i(t)$$

In this model, avalanches are initiated by thalamocortical input and sustained by a combination of corticocortical interactions plus thalamocortical input. Upon reaching a timestep with no active cortical neurons, the avalanche is considered to be ended. Model avalanche size and duration distributions were treated with the same statistical tests as the experimental data. One exception to this was that, for the model data, the upper cutoff x_M was a fitting parameter, but in experiments it was fixed. This was done because in the model there was a clear cutoff at large size avalanches that needed to be accounted for.

We used this model to simulate 30 repetitions of step increase in thalamocortical drive. The transient period in the model was defined in the same way as the experiments and was typically 200-300 timesteps. We ran the model for 5000 timesteps following the onset of increased drive. This allowed us to obtain distributions based on thousands of avalanches; a similar number of avalanches was found in experiments (Supplementary Table 1). We also used the model to investigate how greater or lesser degrees of subsampling might impact the statistics of avalanche distributions during the visually-driven steady state (Fig. 3, Supplementary Fig. 9). Our findings are consistent with previous studies of subsampling, which found that increasing subsampling in densely connected networks steepens the avalanche distributions[7,8].

Comparison to related models. Although the synaptic dynamics in our model was motivated by the model studied by Levina et al. (2007), our model differs in important ways from Levina et al's model. Our neurons are leaky, as in numerous recent studies of criticality in neural systems[1,9–11]; they do not integrate inputs over indefinite time intervals. We set the timescale of depression to

be somewhat slower 20 timesteps than the ~5 timesteps for Levina et al. We chose this timescale to approximately match the observed duration of the transient response in our experiments. Another difference is that we include inhibitory neurons, similar to other recent studies[11–13]. Finally, we consider the strongly driven case, whereas Levina et al. maintained a separation of timescales that is typical in models of self-organized criticality. In contrast, Hartley et al. (2014) considered a range of different driving including similar rates of external input to what we studied here. Interestingly, Hartley et al. concluded that strong drive does not preclude critical dynamics. We suspect that this apparent discrepancy with our results is due their defining avalanches using a very short ΔT for segmenting avalanches and implementing continuous time modeling, but this possibility remains to be verified in further studies.

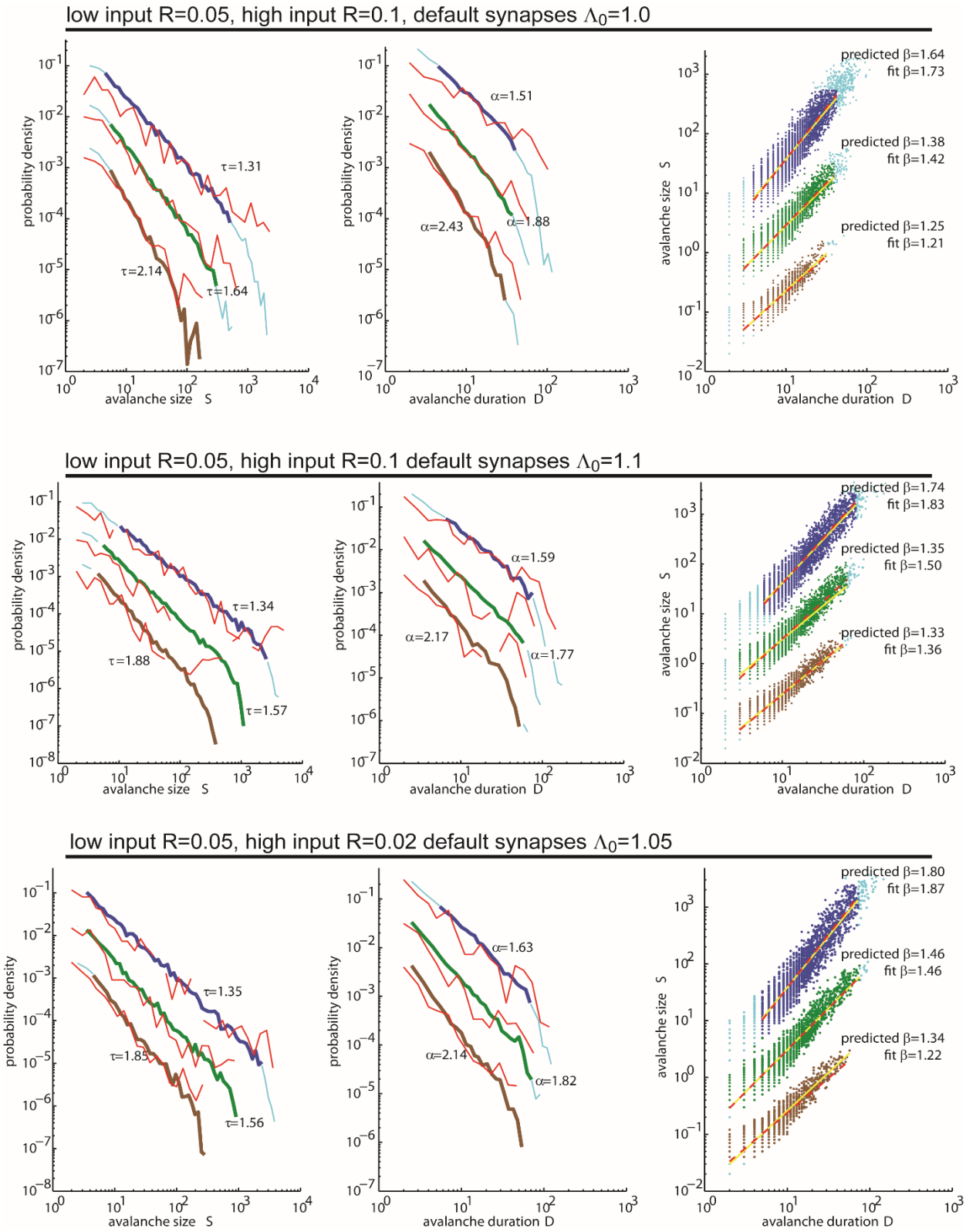

Supplementary Figure 6.9. Detailed examples from model with dynamic synapses**.** In Fig 3 of the main manuscript, we summarize the exponents and scaling relations for nine different sets of

model parameters. Here we show the corresponding avalanche distributions and scaling laws for each of these different model data sets. Each row is for a different level of input R and default synapses Λ_0. For a given R and Λ_0, we show the effects of subsampling (green – fully sampled, blue-30% subsampled, brown-10% subsampled). Red distributions represent avalanches during the transient following the increase in drive. The best fit power law exponents α and τ as well as the scaling exponents β are displayed for each condition. In the probability distributions the light blue portions of each line are outside the range of power law scaling.

6.5.8 Empirical branching parameter versus ΔT

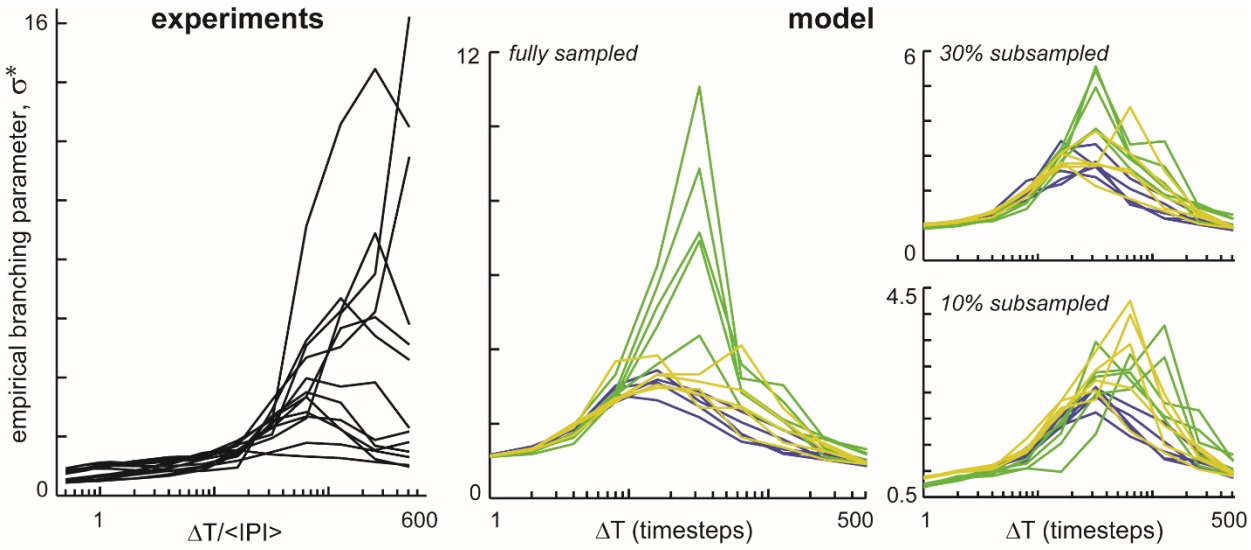

Supplementary Figure 6.10. Empirical branching parameter versus ΔT curves support the hypothesis that visually-driven steady state activity and our model operate in critical regime**.** Here we study the empirical branching parameter σ* following previously developed methods[7]. In brief, for the experiments **(LEFT)**, we computed the ratio of the number of LFP peaks observed in a time bin of duration ΔT to the number observed in the previous time bin. This ratio was averaged over all consecutive pairs of time bins to obtain σ*. This was then repeated for a different sized time bin to determine how σ* depends on ΔT. As shown in previous work[7], if this curve reaches a peak significantly above σ*=2 then this may be considered as evidence for critical dynamics. **(MIDDLE)** Results from the model with adapting synapses. Different colors represent different model parameters (green: Λ_0=1.1, R=0.1; purple Λ_0=1.0, R=0.1; yellow Λ_0=1.05, R=0.02). **(RIGHT)** Results from the model with two different levels of subsampling (top 30%; bottom 10%).

6.5.9 Ex vivo eye-attached whole-brain preparation

Following anesthesia (Propofol 10 mg/kg) and rapid decapitation with a guillotine, we surgically removed the brain, optic nerves, and eyes, from the cranium as described earlier[14–16]. In brief, during surgery we cut the conjunctiva and extraocular muscles to free the eyes from their orbits. After removing the brain from the skull, we made a cut rostro-caudally along the medial cortex, starting at the ventricle of the olfactory bulb. This cut preserves the normal afferent input of the visual cortical area, because the geniculocortical pathway traverses the lateral cortical wall within

the lateral forebrain bundle[2]. Subsequently, two medio-lateral cuts to the telencephalon at its anterior and posterior ends prepared for unfolding of the hemisphere and exposing the ventricular surface (Supplementary Fig. 3a). The contralateral eye was hemisected and drained of its vitreous, thus exposing the retina; the ipsilateral eye was removed. The preparation was transferred to the perfusion chamber positioned on an air table with the eye-cup beneath a focusing lens (Fig. 1a). The unfolded cortex was pinned with short pieces of tungsten wires (25 µm diameter) to an agar block in the recording chamber with the ventricular side up, thus facilitating the subsequent insertion of the microelectrode array.

6.5.10 Details and timing of visual stimuli

Visual stimuli were created by a computer and delivered with either of two methods. In the first method, an LCD monitor (Samsung 19", 1440x900 pixels, contrast ratio = 20000:1, response time = 2 ms). The image on the monitor was projected onto the retinal surface of the hemisected eye-cup with a converging lens system (Fig. 1a). The mean light intensity (irradiance) at the retina was 20 mW/m^2. A monitor pixel corresponded to 7 µm on the retina or ~0.08^o of visual angle[17,18]. This first method was used in turtles 1-5. In the second method, visual stimuli were projected directly onto the retina with a miniature video projector (Aaxa Technologies, P4X Pico Projector) with additional lenses. Resolution was similar to method 1, but the mean light intensity was higher, 1 W/m^2. This method was used for turtles 7-9. For turtle 6 and one additional experiment with turtle 2, we used brief flash from a light emitting diode (LED) placed near the retina to stimulate as described further below. For the LED, the light intensity was 60 W/m^2 (flash duration 1 s). Stimuli were created using *psychopy*, an open-source psychophysics module written for the Python programming language[19]. Software tools were written to allow the experimenter to characterize the projection of the computer screen onto the retina[20]. A computer game controller was used to

position stimulus image and the eye-cup interactively. The eye-cup parameters, including the position and orientation of the visual streak, and the size and position of the optic disk were documented. An image based on these parameters overlaid on the eye cup preparation (in the recording chamber) when projected through the focusing system. The image was not corrected for curvature of the retina. Two of the turtles were presented with gray-scale naturalistic movies ("CatCam"[21]) as used in studies of the mammalian geniculo-cortical system[22]. The movie clip was 10 s in duration and presented in blocks of 45 repetitions at 20 s intervals. 15 min of gray screen was presented between blocks. Three turtles were presented with a previously studied, 5 s duration "motion enhanced" movie[23]. The screen was black before movie presentation. These three turtles were also presented with a 5 s uniform gray screen, preceded by black screen. The movies were alternated with the gray screen stimuli, presented 80 times at 35 s intervals. Three turtles were presented with black dots (6 deg) moving (6 deg/s) linearly across a white background. 8 directions of motion were used, each repeated 8 times in pseudorandom order. For each direction, a dot traversed the visual field on 8 to 15 paths during an 86 - 182 s period followed by 5 minutes of darkness before starting the next direction. Two turtles were presented with diffuse red LED flashes (1 s in duration, 2 min intervals, 200 repetitions). The movies and dots were generated on the projection systems described above. For diffuse flashes, the LED was positioned 2 cm above the retina, diffusely illuminating the entire retina. As specified in Supplementary Table 1, some turtle were tested with two different types of visual stimuli.

6.5.11 Robustness to changes in ΔT and defining transient, visually-driven steady state, and ongoing time periods

An avalanche was defined as a spatiotemporal cluster of consecutive LFP peaks with inter-peak intervals not exceeding a temporal threshold ΔT (Methods). Consistent with previous studies[24], ΔT was chosen to be the average inter-peak interval (<IPI>, inverse of population LFP peak rate). This resulted in ΔT in the range 7 to 64 ms (24 ± 18 ms, mean ± SD). We note that avalanche statistics and scaling laws were robust to deviations in ΔT within about ±30% from <IPI> (Supplementary Figs. 11, 12).

The transient time periods T were determined based on the overlaid avalanche time series of all trial of visual stimuli (e.g. Figs. 1e, 2d). T was computed automatically by first calculating an envelope curve of the avalanche time series defined as the 90 percentile of the avalanche time series in consecutive time bins. Then T was defined as the full width at half max of this envelope curve. This resulted in T ranging from 108 to 784 ms (423 ± 202 ms, mean ± SD, see also Supplementary Table 1). The visually-driven steady state time periods were defined as any period of visual stimulation, excluding the transient period. Thus, the visually-driven steady state period ended when the visual stimulus ended. One exception was for the two experiments with LED flash stimuli, for which a sustained neural response continued long after the flash ended. For these, we included the sustained response (10 s) as part of the visually-driven period. Ongoing time periods were defined as all periods when no visual stimulus was presented.

Avalanches that started within a period were assigned to that period, irrespective of whether the avalanche extended into the next period. One exception was that avalanches in the ongoing period that ended during the transient period were excluded from analysis. We also note that we excluded avalanches within periods of time when the LFP peak rate was nonstationary over long time scales (Supplementary Fig. 13). Data from outside visual cortex was not analyzed except for the data shown in Supplementary Fig 8.

Most previous studies of neuronal avalanches which have focused on ongoing activity recorded in mammalian cortex. Although ongoing activity was not the focus of our work, we note that, in some experiments, ongoing avalanches were power law distributed similar to the visually-driven avalanches steady state (Supplementary Fig. 14 top). However, in several experiments the rate of ongoing LFP peaks was too low to obtain enough avalanches to draw sound statistical conclusions about how ongoing avalanches were distributed (Supplementary Fig. 14 bottom). Rates of LFP peaks, durations of recording periods, and numbers of avalanches for each of the three different periods (transient, steady-state visually-driven, ongoing) are shown in Supplementary Table 1.

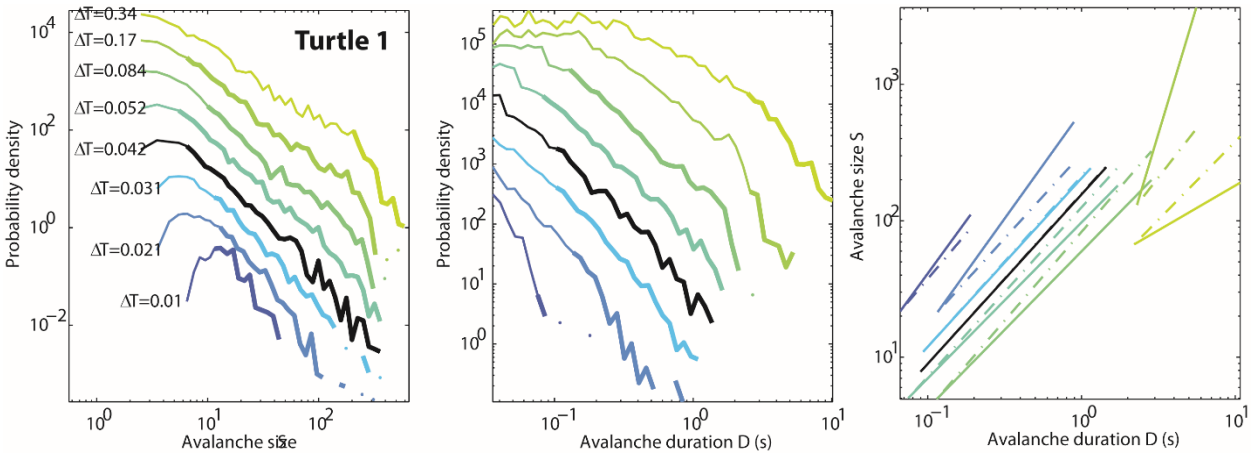

Supplementary Figure 6.11: Dependence of experimental results on choice of ΔT**.** The figure together with the following 12 plots shows how the form of avalanche size and duration distributions as well as scaling between size and duration depends on ΔT. ΔT values are specified in seconds. In all figures, the black curve represents the actual ΔT=<IPI> used in the manuscript. **(LEFT, MIDDLE)** In each distribution the range that was determined to be well-fit by a truncated power law is shown with a heavier line. (When the range is very small, the distribution is not well fit by a power law.) **(RIGHT)** The right panel compares the predicted size versus duration scaling (dash dot line) and the best fit scaling (solid line) for each ΔT. Points are omitted for clarity. Notice that values of ΔT within about ±30% from the <IPI> still give a reasonable scaling relation, but more severe changes in ΔT result in non-power law size and duration distributions and/or poor prediction of the scaling relation.

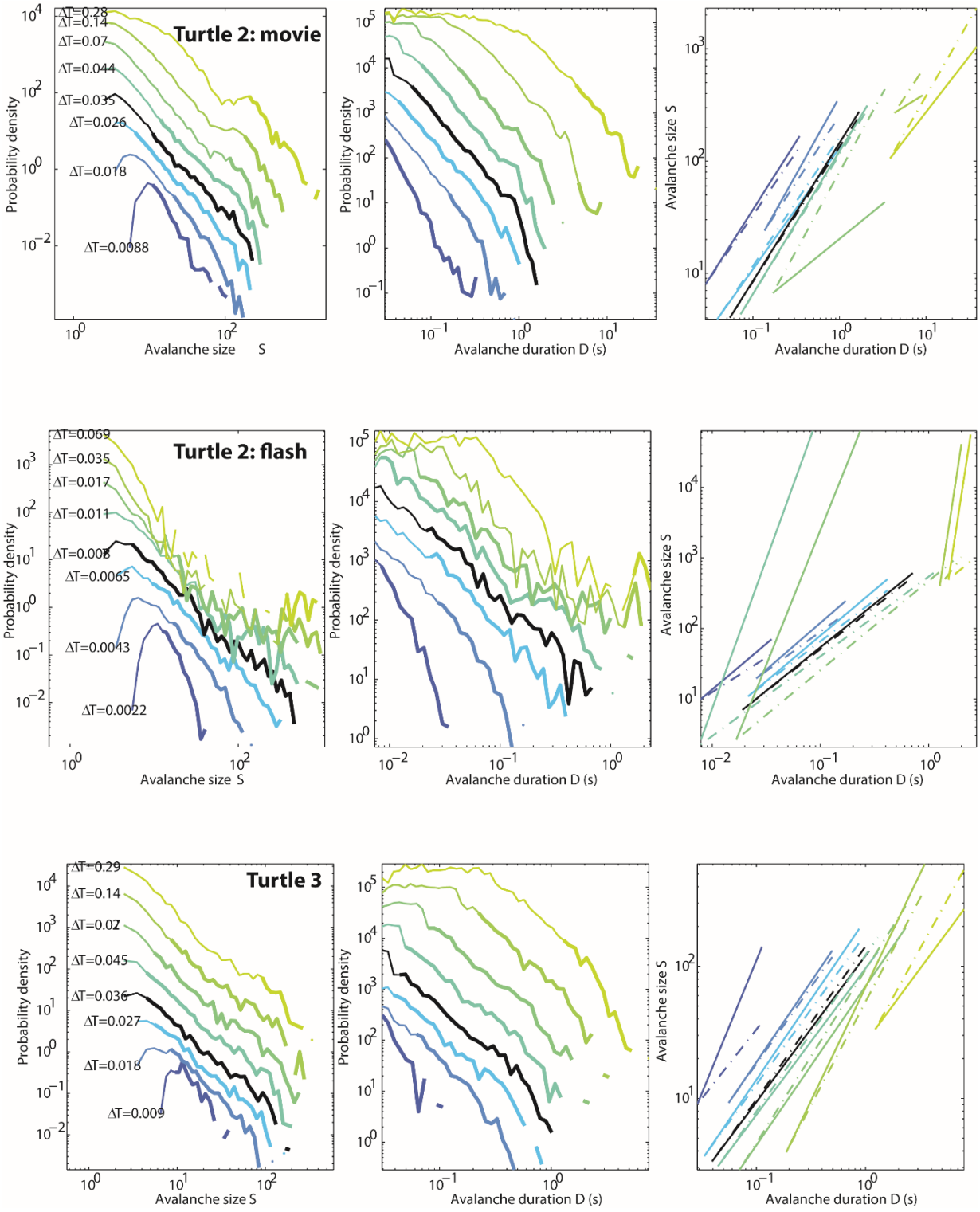
Turtle 2: movie
ΔT=0.28
ΔT=0.14
ΔT=0.07
ΔT=0.044
ΔT=0.035
ΔT=0.026
ΔT=0.018
ΔT=0.0088
Probability density
Avalanche size S
Avalanche duration D (s)
Avalanche size S
Avalanche duration D (s)
Turtle 2: flash
ΔT=0.069
ΔT=0.035
ΔT=0.017
ΔT=0.011
ΔT=0.0065
ΔT=0.0043
ΔT=0.0022
Probability density
Avalanche size S
Avalanche duration D (s)
Avalanche size S
Avalanche duration D (s)
Turtle 3
ΔT=0.29
ΔT=0.14
ΔT=0.07
ΔT=0.045
ΔT=0.036
ΔT=0.027
ΔT=0.018
ΔT=0.009
Probability density
Avalanche size S
Avalanche duration D (s)
Avalanche size S
Avalanche duration D (s)

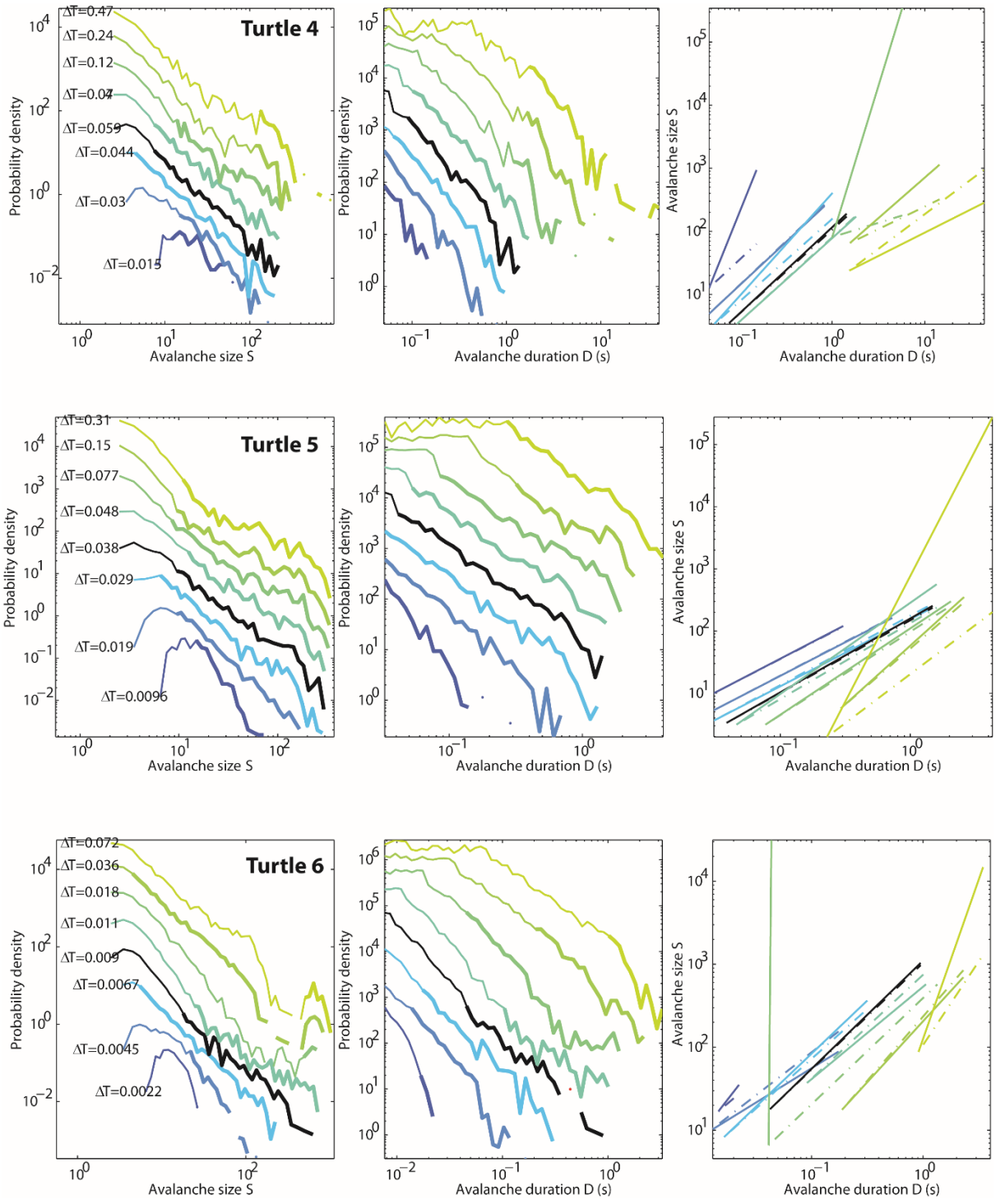
Turtle 4
ΔT=0.47
ΔT=0.24
ΔT=0.12
ΔT=0.07
ΔT=0.059
ΔT=0.044
ΔT=0.03
ΔT=0.015
Probability density
Avalanche size S
Avalanche duration D (s)
Avalanche size S
Avalanche duration D (s)
Turtle 5
ΔT=0.31
ΔT=0.15
ΔT=0.077
ΔT=0.048
ΔT=0.038
ΔT=0.029
ΔT=0.019
ΔT=0.0096
Probability density
Avalanche size S
Avalanche duration D (s)
Avalanche size S
Avalanche duration D (s)
Turtle 6
ΔT=0.072
ΔT=0.036
ΔT=0.018
ΔT=0.011
ΔT=0.009
ΔT=0.0067
ΔT=0.0045
ΔT=0.0022
Probability density
Avalanche size S
Avalanche duration D (s)
Avalanche size S
Avalanche duration D (s)

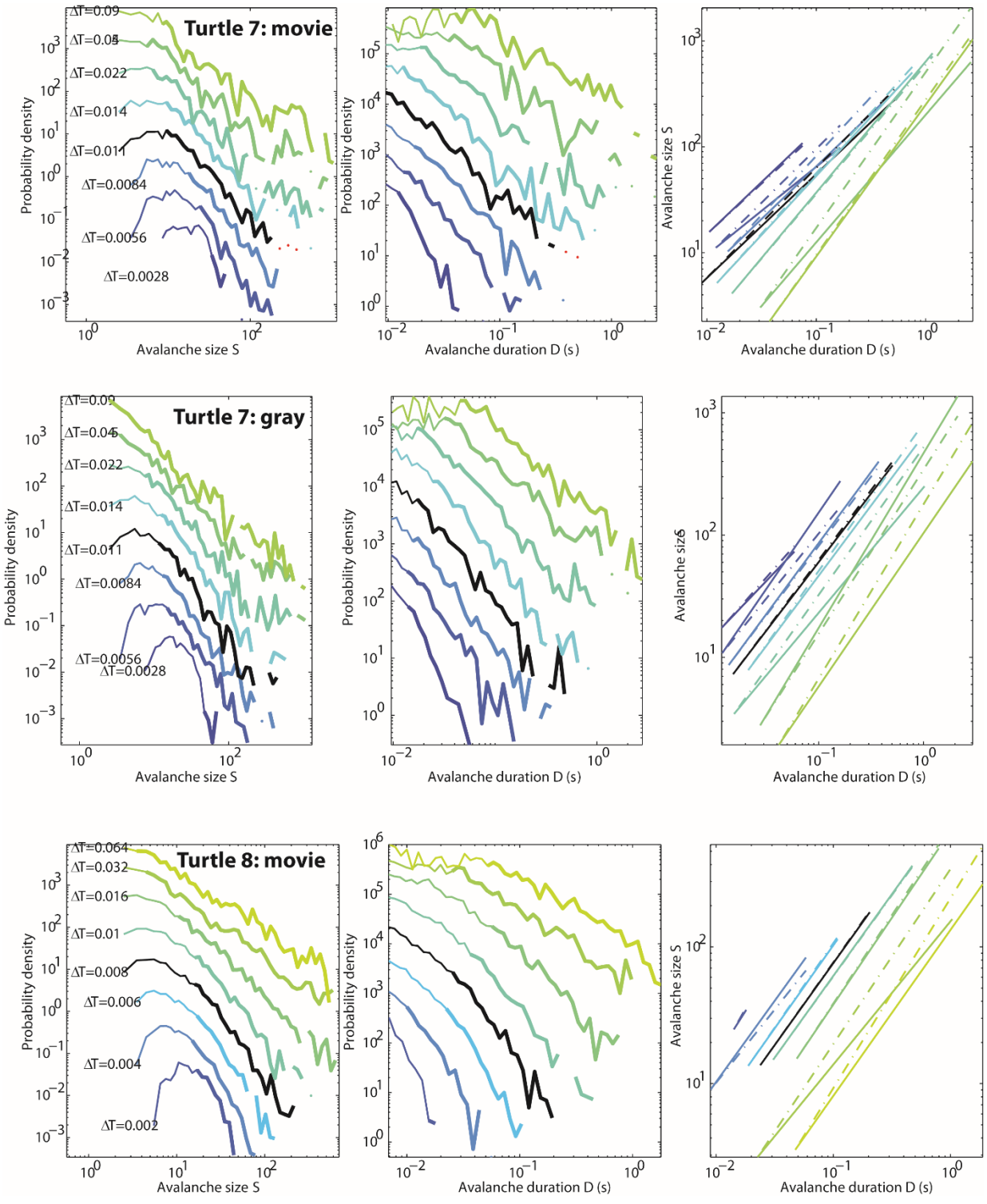
Turtle 7: movie
ΔT=0.09
ΔT=0.05
ΔT=0.022
ΔT=0.014
ΔT=0.011
ΔT=0.0084
ΔT=0.0056
ΔT=0.0028
Probability density
Avalanche size S
Avalanche duration D (s)
Avalanche size S
Avalanche duration D (s)
Turtle 7: gray
ΔT=0.09
ΔT=0.045
ΔT=0.022
ΔT=0.014
ΔT=0.011
ΔT=0.0084
ΔT=0.0056
ΔT=0.0028
Probability density
Avalanche size S
Avalanche duration D (s)
Avalanche size S
Avalanche duration D (s)
Turtle 8: movie
ΔT=0.064
ΔT=0.032
ΔT=0.016
ΔT=0.01
ΔT=0.008
ΔT=0.006
ΔT=0.004
ΔT=0.002
Probability density
Avalanche size S
Avalanche duration D (s)
Avalanche size S
Avalanche duration D (s)

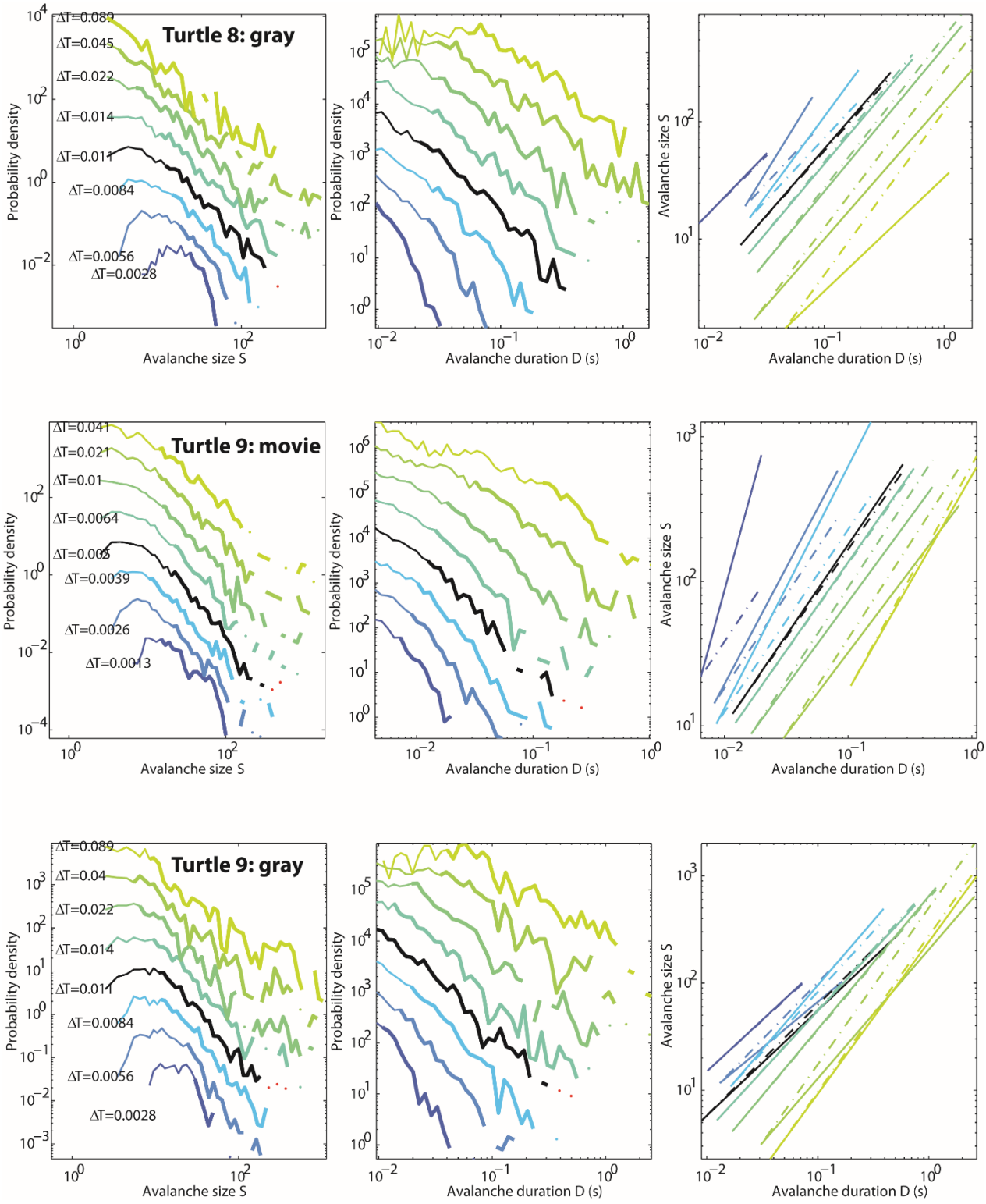
Turtle 8: gray
ΔT=0.089
ΔT=0.045
ΔT=0.022
ΔT=0.014
ΔT=0.011
ΔT=0.0084
ΔT=0.0056
ΔT=0.0028
Probability density
Avalanche size S
Avalanche duration D (s)
Avalanche size S
Avalanche duration D (s)
Turtle 9: movie
ΔT=0.041
ΔT=0.021
ΔT=0.01
ΔT=0.0064
ΔT=0.0039
ΔT=0.0026
ΔT=0.0013
Probability density
Avalanche size S
Avalanche duration D (s)
Avalanche size S
Avalanche duration D (s)
Turtle 9: gray
ΔT=0.089
ΔT=0.04
ΔT=0.022
ΔT=0.014
ΔT=0.011
ΔT=0.0084
ΔT=0.0056
ΔT=0.0028
Probability density
Avalanche size S
Avalanche duration D (s)
Avalanche size S
Avalanche duration D (s)

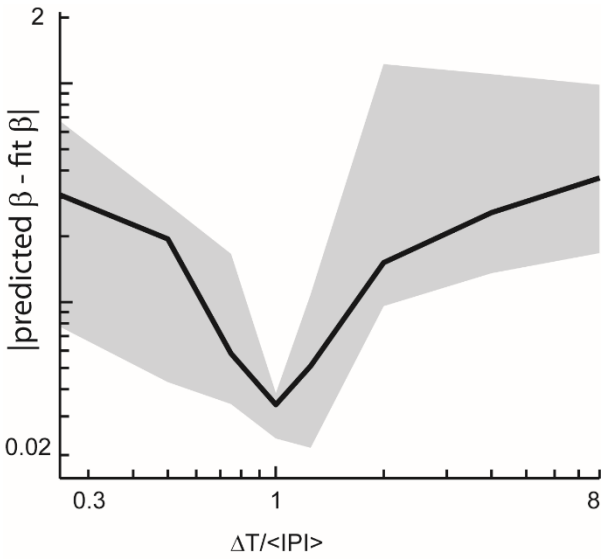

Supplementary Figure 6.12. Good prediction of scaling relation occurs if ΔT is chosen nearby <IPI>. This plot summarizes one feature of the series of plots in Supplementary Fig 11. It summarizes how well the predicted scaling relation matches the best fit scaling relation and how this depends on ΔT. Here it is clear that a small difference (good prediction) occurs in a range of approximately ±30% around ΔT=<IPI>.

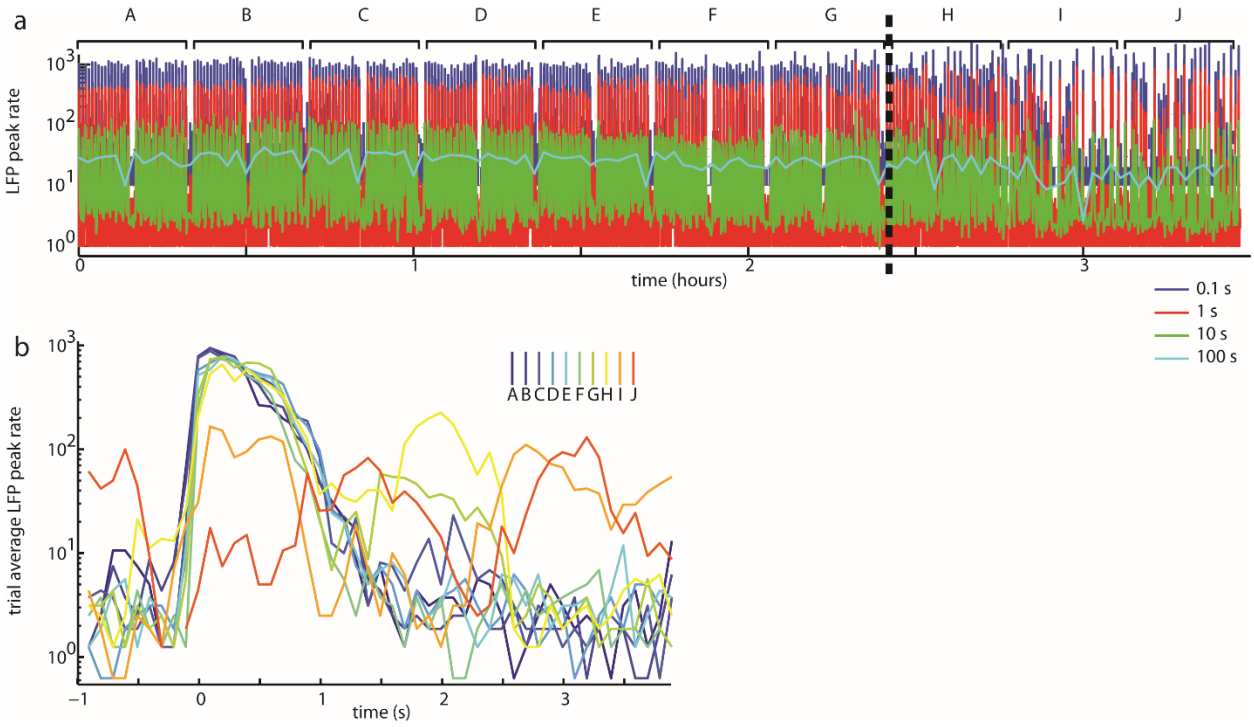

Supplementary Figure 6.13: Stationarity of experimental system**. (a)** The rate of LFP peaks recorded over the course of multiple hours is steady (one representative example experiment

shown). Each rate timeseries was computed by counting LFP peaks in consecutive time windows of duration dt and normalizing by dt. Durations dt=0.1, 1, 10, and 100 s were used (colors indicated in legend). The apparent 10 min cyclic pattern is due the timing of repeated visual stimulus presentation. Note that after about 2.5 hours (epochs labeled H, I and J), non-stationarity sets in. In all experiments, we include data in our analysis only during stationary periods. **(b)** The stimulus-triggered average response to repeated visual stimulation is also steady (except for epoch H, I, and J). The color code corresponds to the periods labeled alphabetically in panel a.

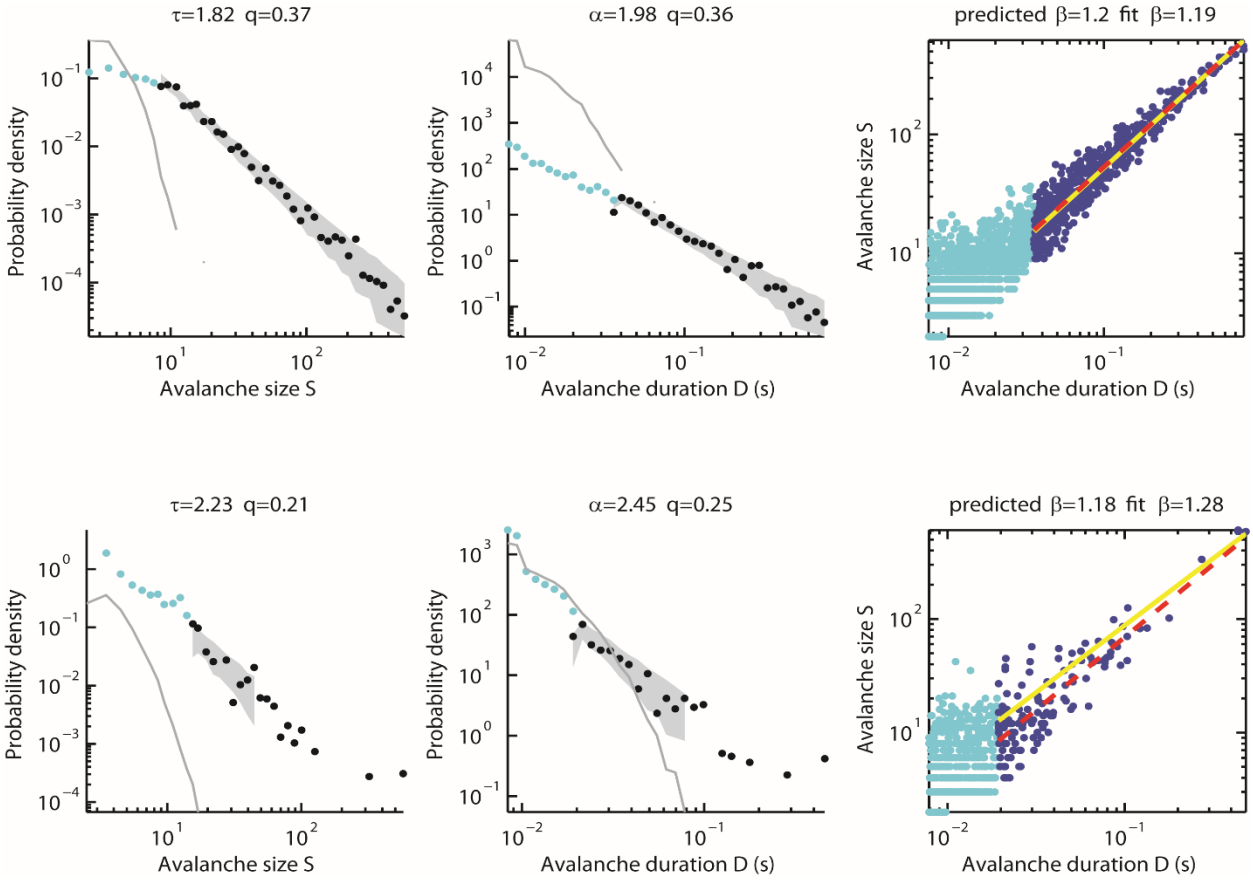

Supplementary Figure 6.14: Ongoing activity exhibited critical dynamics in a subset of experiments**. (top)** In some of our experiments, ongoing activity also exhibited strong evidence for critical dynamics, similar to the visually-driven steady state avalanches. These cases are consistent with previous studies of neuronal avalanches in mammals, which have primarily been based on ongoing activity. **(bottom)** In other experiments, we observed that ongoing activity occurred at such low rate that statistically sound conclusions were not possible.

		Turtle	1	2	2	3	4	5	6	7	7	8	8	9	9
		Stimulation type	movie	movie	flash	dots	dots	dots	flash	movie	gray	movie	gray	movie	gray
total recording time (s)		ongoing	3263.8	6818.3	7010.3	6260.9	11963.4	9061.5	11950.8	2673.3	2287.0	589.8	1996.8	3800.4	4836.0
		transient	134.3	172.4	6.7	107.7	62.7	275.2	30.7	21.6	22.6	25.4	22.3	49.4	41.8
		visually-driven steady state	3474.8	6127.6	199.6	5035.6	4059.6	6980.0	2227.6	196.4	170.8	71.8	151.9	227.6	317.1
		all	6872.9	13118.3	7216.7	11404.3	16085.8	16316.7	14209.2	2891.3	2480.5	687.1	2171.0	4077.5	5194.9
rate of recorded LFP peaks (Hz)		ongoing	5.8	10.8	7.6	3.8	3.8	2.9	5.5	12.9	25.6	59.4	53.4	42.5	45.2
		transient	92.4	100.6	357.2	5.7	5.7	9.6	52.7	391.6	303.6	530.8	411.5	604.7	828.0
		visually-driven steady state	16.9	31.3	196.6	7.4	8.8	7.6	38.8	101.0	115.1	275.9	165.2	91.8	92.4
number of avalanches	ongoing	total	900	667	1096	1090	2679	721	1692	88	218	416	583	255	1115
		in ongoing size distribution fitting range	*304*	*268*	*404*	*554*	*259*	*544*	*1016*	*67*	*145*	*204*	*444*	*167*	*97*
		in ongoing duration distribution fitting range	*272*	*208*	*489*	*588*	*1437*	*313*	*507*	*52*	*172*	*227*	*471*	*254*	*132*
	transient	total	447	915	126	39	28	123	57	152	116	267	203	555	318
	visually-driven steady state	total	2968	13871	1246	1638	1920	1792	4255	415	533	917	497	1036	987
		in size distribution fitting range	*964*	*5532*	*897*	*1393*	*824*	*648*	*362*	*295*	*323*	*396*	*314*	*300*	*407*
		in duration distribution fitting range	*892*	*3082*	*587*	*1134*	*1129*	*1288*	*287*	*414*	*305*	*320*	*497*	*447*	*475*
		jitter time Tj (s)	1.4	1.4	1.2	0.9	2	1.1	1.1	1.1	2	1.5	1.8	1.9	1.2
		transient time (s)	0.746	0.547	0.108	0.436	0.302	0.784	0.256	0.260	0.293	0.462	0.306	0.618	0.380

Supplementary Table 6.1. Basic statistics for each experiment.

6.5.12 Power law fitting and the measure δ

To test whether evoked and ongoing avalanches were distributed according to a power law, we carried out a two-step analysis. First, we identified the best-fit power law using established maximum likelihood methods[25–27]. As in previous studies, we assumed that there is a lower size limit, below which power law statistics are not expected[25,26]. The rationale for this assumption was that some measurement noise is unavoidable and likely to be uncorrelated across channels, thus resulting in some small size 'noise-corrupted' avalanches. In line with this idea, we found that avalanches that were shorter than approximately ΔT in duration were distributed quite differently than larger duration avalanches (Supplementary Fig 15). For this reason, in all of our figures (except Supplementary Fig 15) we plot avalanches with durations exceeding 0.8ΔT. An important difference between our method and the typical approach[25] is that we assumed that avalanches are also limited in how large they can be. Such avalanche size and duration limits have been recognized in other work as well[26,27]. Thus, we identified the maximum likelihood truncated power law fit to our data. This approach obviates the need for comparing to similar distributions (e.g. power law with exponential cutoff[25,27]), because the truncation cuts off such end effects already. Since our definition of avalanche size is a discrete, integer variable, the fitting function for the avalanche size distribution was

$$f(S) = \frac{S^{-\tau}}{\sum_{x=x_0}^{x_M} x^{-\tau}}$$

The maximum size x_M was assumed to be the largest size actually observed in the experimental data. We note that, in our experiments, unlike many previous experiments in mammals, we did not observe a clear size cutoff at the number of channels used to record. This reflects the tendency

for a single channel to have many LFP peaks during a single avalanche. The minimum size x_0 and the power law exponent τ were fitting parameters. Since avalanche duration is a non-integer variable, the fitting function for the avalanche duration distribution was

$$g(D) = \frac{D^{-\alpha}}{\int_{y_0}^{y_M} y^{-\alpha} dy} = \frac{1-\alpha}{y_M^{1-\alpha} - y_0^{1-\alpha}} D^{-\alpha}$$

Again, the maximum duration y_M was taken as the largest observed duration, while y_0 and α were fitting parameters. The fitting process involved trying all exponents in the range from -1 to -4 with increments of 0.01, similar to previous work[25]. However, another important difference between our approach and previous work[25] is that our fitting algorithm tried values of y_0 values increasing from 0, but only up to the point when the fitted power law matches the data well enough to have a Kolmogorov-Smirnov statistic $KS < 1/\sqrt{N_{samp}}$, where N_{samp} is the number of avalanches comprising the dataset. This prevents the algorithm from increasing the minimum size until most of the data are excluded from fitting. The threshold of $1/\sqrt{N_{samp}}$ is justified based on how KS variability is expected to vary with N_{samp} for surrogate datasets drawn from a true power law[28] (Supplementary Fig. 16).

For fitting model data size and duration distributions, we used the fitting function *f*(*S*) above, because both size and duration are discrete variables for the model. Also, for the model data, x_M was used as a fitting parameter because there typically was a clear exponential cutoff in the model avalanche distributions.

After finding the best-fit power law, the next step was to assess goodness-of-fit *q*. For this, we again follow established methods[25,28]. We compared the experimental data to 1000 surrogate data sets drawn from the best-fit power law distribution. The surrogate data sets had the same number of samples as the experimental data set. In this way, the surrogate data sets are as close as possible to a power law, for a given finite sample size. The deviation between the surrogate data sets and a perfect power law was quantified with the KS statistic. The quality *q* of the power law fit was defined as the fraction of these surrogate KS statistics which were greater than the KS statistic for the experimental data. Thus, if the experimental data had a smaller KS statistic than at least 100 of the surrogate values, then $q>0.1$. We use a very conservative criterion, $q>0.1$, for judging the data to be power law distributed. This is demonstrated visually in Fig 1f,g and Fig 2e,f by plotting the experimental distribution over a gray band which delineates the 5-95 percentiles of the surrogate data sets. It should be noted that for a large number of samples, this goodness-of-fit test is very strict (i.e. more than about 200 avalanches[25]). In our experiments, the number of avalanches during visual stimulation was 2467, on average (ranging from 415 to 13871).

Deviation between two distributions, δ. Avalanches occurring during the transient period following stimulus onset were not power law distributed. Large avalanches occurred with high probability, often resulting in bimodally distributed sizes and durations. To quantitatively measure how avalanche distributions from the transient periods deviate from the power laws observed during the visually-driven steady state periods, we used a measure δ, which is similar to measures developed in previous studies[29,30]. To compute δ, we first constructed a cumulative distribution function (CDFs) for the test distribution (transient) and the reference distribution (visually-driven steady state). Then δ is the sum of 10 differences between the reference CDF and the test CDF

(Supplementary Fig 17). The points, at which the 10 differences were taken, were equally spaced on a logarithmic scale between the minimum and maximum avalanche size. When $\delta > 0$, which typically was the case for avalanche distributions from the transient periods, this indicates that large events occurred more frequently than would be expected if they came from the same distribution as the visually-driven steady state periods (Supplementary Fig. 17).

We also used δ to examine control distributions, in which avalanches were reanalyzed after randomly jittering the occurrence times of LFP peaks. For this, we added to each LFP peak time a random number drawn from a uniform distribution on $[-T_j,+T_j]$. Such jittering decreases spatiotemporal correlations and reduces the probability of large avalanches. In terms of δ, this results in $\delta < 0$. To quantify the effects of jittering, we determined how large the jitter time T_j must be to reach $\delta<-0.1$, a significant deviation. We found $T_j=1.4\pm0.4$ (mean±SD) across all experiments (Supplementary Table 1).

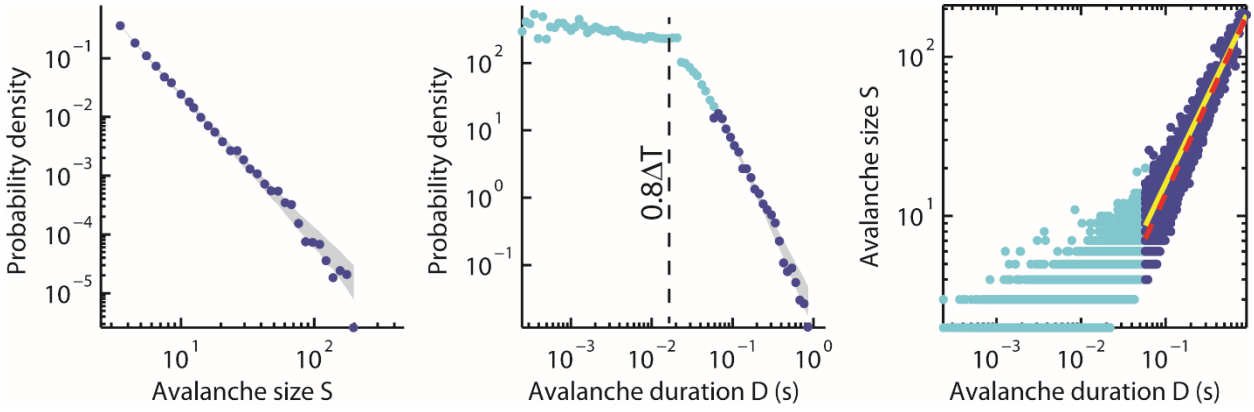

Supplementary Figure 6.15. Very short duration avalanches are distributed differently**.** The analysis of experimental data presented in the manuscript is based on analyzing only those avalanches with durations longer than 0.8ΔT. The reason for this approach was that for very

short duration avalanches, with D less than about ΔT, a different regime of avalanches is clear in the duration distribution (the flat region in the middle panel). The low D regime tends to have a nearly flat distribution of durations and scales differently with avalanche size (light blue points in right panel) This different regime may be due to influence of noise for small, short duration avalanches.

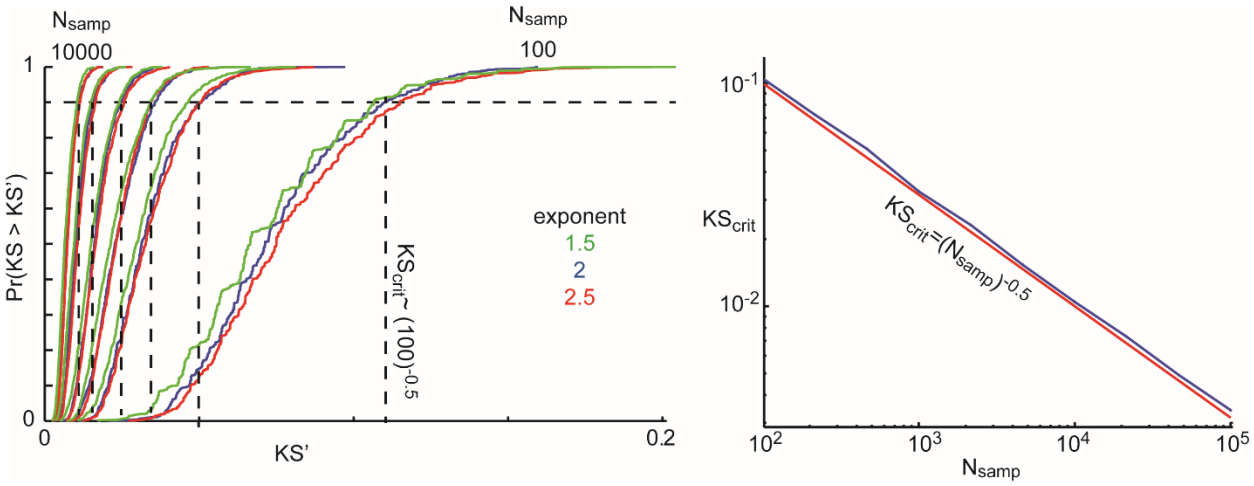

Supplementary Figure 6.16. Fitting the lower bound cutoff of power law regime depending on sample size**.** As discussed in methods, we used the KS statistic for fitting the lower cut off point x_0 in the power-law fitting process. We increased x_0 until a criterion level of KS was reached. The sensible choice for a criterion KS depends on the number of samples N. In this figure we describe numerical simulations used to determine the criterion KS. First, we computed the KS statistic for a perfect power-law reference CDF with exponent ε, compared to a surrogate data set with N samples drawn randomly from a power-law with exponent ε. We repeated this 1000 times. CDFs of these 1000 KS values are shown in the left panel above. Colors represent different exponents ε. Then we defined the criterion KS_{crit} to be the KS value below which 90% of the values lie (dashed line). We carried out this process for six different sample sizes N= 100, 500, 1000, 2000, 5000, and 10000. We found that KS_{crit} was very close to $1/\sqrt{N_{samp}}$ as shown in the right panel above (blue – data from left panel plot; red – exact $1/\sqrt{N_{samp}}$ function). This approach generalizes existing tabulated values for such fitting criteria[28].

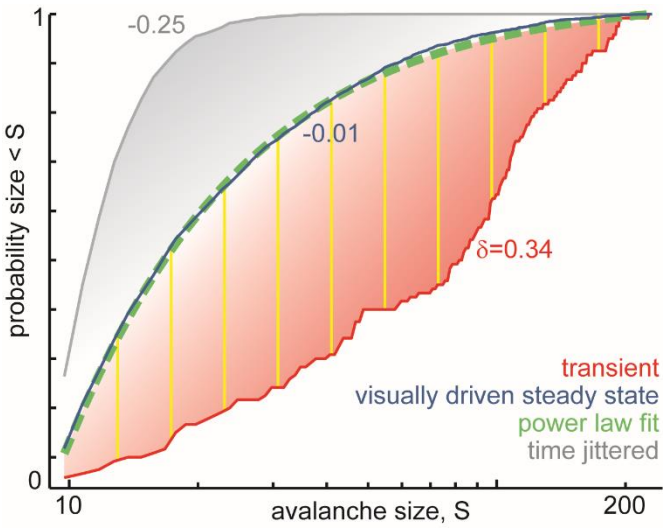

Supplementary Figure 6.17: Quantifying how avalanche distributions differ between transient periods, visually-driven steady state periods**.** The deviation δ is computed as the sum of 10 differences (e.g. yellow lines for transient avalanches) between a reference CDF (green) and the measured CDF (red). Here, the reference CDF is the best-fit power law for the visually-driven steady state (blue). If large avalanches are more or less prevalent in the measured CDF than in the reference CDF, then $\delta > 0$ or $\delta < 0$, respectively. Near zero deviation occurs when the measured CDF matches the reference CDF (e.g. blue). See Supplementary Fig 7 for similar CDF plots and δ values for avalanche size and duration distributions for all experiments.

1. Plenz, D., Niebur, E. & Schuster, H. G. *Criticality in Neural Systems*. (Wiley, 2014).

2. Beggs, J. M. The criticality hypothesis: how local cortical networks might optimize information processing. *Philos. Trans. A. Math. Phys. Eng. Sci.* **366,** 329–43 (2008).

3. Shew, W. L. & Plenz, D. The functional benefits of criticality in the cortex. *Neuroscientist* **19,** 88–100 (2013).

4. Friedman, N. *et al.* Universal Critical Dynamics in High Resolution Neuronal Avalanche Data. *Phys. Rev. Lett.* **108,** 1–5 (2012).

5. Beggs, J. M. & Plenz, D. Neuronal avalanches in neocortical circuits. *J. Neurosci.* **23,** 11167–77 (2003).

6. Shew, W. L., Yang, H., Yu, S., Roy, R. & Plenz, D. Information Capacity and Transmission Are Maximized in Balanced Cortical Networks with Neuronal Avalanches. *J. Neurosci.* **31,** 55–63 (2011).

7. Petermann, T. *et al.* Spontaneous cortical activity in awake monkeys composed of neuronal avalanches. *Proc. Natl. Acad. Sci. U. S. A.* **106,** 15921–6 (2009).

8. Haimovici, A., Tagliazucchi, E., Balenzuela, P. & Chialvo, D. R. Brain Organization into Resting State Networks Emerges at Criticality on a Model of the Human Connectome. *Phys. Rev. Lett.* **110,** 178101 (2013).

9. Priesemann, V., Valderrama, M., Wibral, M. & Le Van Quyen, M. Neuronal Avalanches Differ from Wakefulness to Deep Sleep – Evidence from Intracranial Depth Recordings in Humans. *PLoS Comput. Biol.* **9,** e1002985 (2013).

10. Klaus, A., Yu, S. & Plenz, D. Statistical analyses support power law distributions found in neuronal avalanches. *PLoS One* **6,** e19779 (2011).

11. Sethna, J. P., Dahmen, K. a & Myers, C. R. Crackling noise. *Nature* **410,** 242–50 (2001).

12. Kohn, A. Visual adaptation: physiology, mechanisms, and functional benefits. *J. Neurophysiol.* **97,** 3155–64 (2007).

13. Bialek, W. *Biophysics: Searching for Principles*. (Princeton University Press, 2012).

14. Levina, A., Herrmann, J. M. & Geisel, T. Dynamical synapses causing self-organized criticality in neural networks. *Nat. Phys.* **3,** 857–860 (2007).

15. Levina, A., Herrmann, J. & Geisel, T. Phase Transitions towards Criticality in a Neural System with Adaptive Interactions. *Phys. Rev. Lett.* **102,** 118110 (2009).

16. Meisel, C. & Gross, T. Adaptive self-organization in a realistic neural network model. *Phys. Rev. E* **80,** 1–6 (2009).

17. Saha, D., Morton, D., Ariel, M. & Wessel, R. Response properties of visual neurons in the turtle nucleus isthmi. *J. Comp. Physiol. A. Neuroethol. Sens. Neural. Behav. Physiol.* **197,** 153–65 (2011).

18. Clauset, A., Shalizi, C. R. & Newman, M. E. J. Power-Law Distributions in Empirical Data. *SIAM Rev.* **51,** 661–703 (2009).

19. Haldeman, C. & Beggs, J. M. Critical Branching Captures Activity in Living Neural Networks and Maximizes the Number of Metastable States. *Phys. Rev. Lett.* **94,** (2005).

20. Kinouchi, O. & Copelli, M. Optimal dynamical range of excitable networks at criticality. *Nat. Phys.* **2,** 348–351 (2006).

21. Chung, S., Li, X. & Nelson, S. B. Short-term depression at thalamocortical synapses contributes to rapid adaptation of cortical sensory responses in vivo. *Neuron* **34,** 437–46 (2002).

22. Sornette, D. *Critical Phenomena in Natural Sciences: Chaos, Fractals, Selforganization and Disorder: Concepts and Tools*. (Springer-Verlag, 2006).

23. Stumpf, M. P. H. & Porter, M. A. Mathematics. Critical truths about power laws. *Science* **335,** 665–6 (2012).

24. Beggs, J. M. & Timme, N. Being critical of criticality in the brain. *Front. Physiol.* **3,** 163 (2012).

25. Larremore, D. B., Shew, W. L. & Restrepo, J. G. Predicting Criticality and Dynamic Range in Complex Networks: Effects of Topology. *Phys. Rev. Lett.* **106,** 1–4 (2011).

26. Priesemann, V. *et al.* Spike avalanches in vivo suggest a driven, slightly subcritical brain state. *Front. Syst. Neurosci.* **8,** 108 (2014).

27. Ribeiro, T. L., Ribeiro, S., Belchior, H., Caixeta, F. & Copelli, M. Undersampled critical branching processes on small-world and random networks fail to reproduce the statistics of spike avalanches. *PLoS One* **9,** e94992 (2014).

28. Shew, W. L., Yang, H., Petermann, T., Roy, R. & Plenz, D. Neuronal Avalanches Imply Maximum Dynamic Range in Cortical Networks at Criticality. *J. Neurosci.* **29,** 15595–15600 (2009).

29. Gireesh, E. & Plenz, D. Neuronal avalanches organize as nested theta- and beta/gamma-oscillations during development of cortical layer 2/3. *Proc. Natl. Acad. Sci. U. S. A.* **105,** 7576–81 (2008).

30. Bak, P., Tang, C. & Wiesenfeld, K. Self-organized criticality: An explanation of the 1/f noise. *Phys. Rev. Lett.* **59,** 381–384 (1987).

31. Bornholdt, S. & Röhl, T. Self-organized critical neural networks. *Phys. Rev. E* **67,** 1–5 (2003).

32. Moretti, P. & Muñoz, M. a. Griffiths phases and the stretching of criticality in brain networks. *Nat. Commun.* **4,** 2521 (2013).

References for Supplementary Information

1. Larremore, D. B., Shew, W. L. & Restrepo, J. G. Predicting Criticality and Dynamic Range in Complex Networks: Effects of Topology. *Phys. Rev. Lett.* **106,** 1–4 (2011).

2. Mulligan, K. A. & Ulinski, P. S. Organization of geniculocortical projections in turtles: isoazimuth lamellae in the visual cortex. *J. Comp. Neurol.* **296,** 531–47 (1990).

3. Cosans, C. E. & Ulinski, P. S. Spatial organization of axons in turtle visual cortex: intralamellar and interlamellar projections. *J. Comp. Neurol.* **296,** 548–58 (1990).

4. Ulinski, P. *Evolution of Nervous Systems*. *Evol. Nerv. Syst.* 195–203 (Elsevier, 2007). doi:10.1016/B0-12-370878-8/00133-6

5. Levina, A., Herrmann, J. M. & Geisel, T. Dynamical synapses causing self-organized criticality in neural networks. *Nat. Phys.* **3,** 857–860 (2007).

6. Levina, A., Herrmann, J. & Geisel, T. Phase Transitions towards Criticality in a Neural System with Adaptive Interactions. *Phys. Rev. Lett.* **102,** 118110 (2009).

7. Priesemann, V. *et al.* Spike avalanches in vivo suggest a driven, slightly subcritical brain state. *Front. Syst. Neurosci.* **8,** 108 (2014).

8. Ribeiro, T. L., Ribeiro, S., Belchior, H., Caixeta, F. & Copelli, M. Undersampled critical branching processes on small-world and random networks fail to reproduce the statistics of spike avalanches. *PLoS One* **9,** e94992 (2014).

9. Shew, W. L., Yang, H., Petermann, T., Roy, R. & Plenz, D. Neuronal avalanches imply maximum dynamic range in cortical networks at criticality. *J. Neurosci.* **29,** 15595–600 (2009).

10. Kinouchi, O. & Copelli, M. Optimal dynamical range of excitable networks at criticality. *Nat. Phys.* **2,** 348–351 (2006).

11. Wang, S.-J., Hilgetag, C. C. & Zhou, C. Sustained activity in hierarchical modular neural networks: self-organized criticality and oscillations. *Front. Comput. Neurosci.* **5,** 30 (2011).

12. Yang, H., Shew, W. L., Roy, R. & Plenz, D. in *Crit. Neural Syst.* (Plenz, D. & Niebur, E.) 335–346 (Wiley, 2014).

13. Larremore, D. B., Shew, W. L., Ott, E., Sorrentino, F. & Restrepo, J. G. Inhibition Causes Ceaseless Dynamics in Networks of Excitable Nodes. *Phys. Rev. Lett.* **112,** 138103 (2014).

14. Kriegstein, A. R. Synaptic responses of cortical pyramidal neurons to light stimulation in the isolated turtle visual system. *J. Neurosci.* **7,** 2488–92 (1987).

15. Mancilla, J. G., Fowler, M. & Ulinski, P. S. Responses of regular spiking and fast spiking cells in turtle visual cortex to light flashes. *Vis. Neurosci.* **15,** 979–93 (1998).

16. Senseman, D. M. Correspondence between visually evoked voltage-sensitive dye signals and synaptic activity recorded in cortical pyramidal cells with intracellular microelectrodes. *Vis. Neurosci.* **13,** 963–77 (1996).

17. Northmore, D. P. & Granda, A. M. Ocular dimensions and schematic eyes of freshwater and sea turtles. *Vis. Neurosci.* **7,** 627–35 (1991).

18. Ariel, M. & Kogo, N. Direction tuning of inhibitory inputs to the turtle accessory optic system. *J. Neurophysiol.* **86,** 2919–30 (2001).

19. Peirce, J. W. Generating Stimuli for Neuroscience Using PsychoPy. *Front. Neuroinform.* **2,** 10 (2008).

20. Saha, D., Morton, D., Ariel, M. & Wessel, R. Response properties of visual neurons in the turtle nucleus isthmi. *J. Comp. Physiol. A. Neuroethol. Sens. Neural. Behav. Physiol.* **197,** 153–65 (2011).

21. Betsch, B. Y., Einhäuser, W., Körding, K. P. & König, P. The world from a cat's perspective--statistics of natural videos. *Biol. Cybern.* **90,** 41–50 (2004).

22. Mante, V., Bonin, V. & Carandini, M. Functional mechanisms shaping lateral geniculate responses to artificial and natural stimuli. *Neuron* **58,** 625–38 (2008).

23. Nishimoto, S. & Gallant, J. L. A three-dimensional spatiotemporal receptive field model explains responses of area MT neurons to naturalistic movies. *J. Neurosci.* **31,** 14551–64 (2011).

24. Beggs, J. M. & Plenz, D. Neuronal avalanches in neocortical circuits. *J. Neurosci.* **23,** 11167–77 (2003).

25. Clauset, A., Shalizi, C. R. & Newman, M. E. J. Power-Law Distributions in Empirical Data. *SIAM Rev.* **51,** 661–703 (2009).

26. Langlois, D., Cousineau, D. & Thivierge, J. P. Maximum likelihood estimators for truncated and censored power-law distributions show how neuronal avalanches may be misevaluated. *Phys. Rev. E* **89,** 012709 (2014).

27. Klaus, A., Yu, S. & Plenz, D. Statistical analyses support power law distributions found in neuronal avalanches. *PLoS One* **6,** e19779 (2011).

28. Goldstein, M. L., Morris, S. a. & Yen, G. G. Problems with fitting to the power-law distribution. *Eur. Phys. J. B* **41,** 255–258 (2004).

29. Shew, W. L., Yang, H., Petermann, T., Roy, R. & Plenz, D. Neuronal Avalanches Imply Maximum Dynamic Range in Cortical Networks at Criticality. *J. Neurosci.* **29,** 15595–15600 (2009).

30. Tetzlaff, C., Okujeni, S., Egert, U., Wörgötter, F. & Butz, M. Self-Organized Criticality in Developing Neuronal Networks. *PLoS Comput. Biol.* **6,** e1001013 (2010).

Chapter 7

Future work in the *ex vivo* turtle eye-attached whole-brain preparation

The *ex vivo* turtle eye-attached whole-brain preparation is a unique and extremely useful experimental tool; with it, the experimentalist can achieve stable multi-whole-cell recordings of ongoing and evoked activity in a largely intact visual system. This experimental approach is somewhat rare in experimental systems neuroscience, and will likely remain so for several years. Here, we list a few open questions that are of broad interest, explain how this preparation is suited to address those questions, and propose initial study designs for doing so. Where applicable, we present preliminary experimental results that suggest certain hypotheses.

7.1 Introduction

As detailed elsewhere in this thesis, the *ex vivo* turtle eye-attached whole-brain preparation is a powerful experimental tool. This preparation has three primary advantages, making it uniquely well-suited to address several important open questions in systems neuroscience.

First, the experimenter can achieve stable whole-cell recordings. Such mechanical stability is a key ingredient in certain analyses. For example, tracking cortical "state" using subthreshold fluctuations (see Chapter 3) requires minutes-long recordings. Some analyses are even more demanding; calculating correlated variability, for instance, requires many repetitions of the same stimulus (with appropriate inter-trial-intervals) to achieve reliable across-trial average responses. This can mean an hour or more of recording from a given cell or pair of cells (see Chapters 4 and 5), which is not a realistic expectation for *in vivo* preparations.

Second, it's possible to perform simultaneous whole-cell recordings from groups of nearby neurons. While single-whole-cell recordings are becoming increasingly common *in vivo* (even in awake mammals(Crochet & Petersen, 2006; Mcginley et al., 2015; Sachidhanandam, Sreenivasan, Kyriakatos, Kremer, & Petersen, 2013; Andrew Y Y Tan, Chen, Scholl, Seidemann, & Priebe, 2014)), multi-whole-cell recordings remain elusive. This is because *in vivo* patching is usually (but not always(Margrie et al., 2003)) done without visual guidance. The higher failure rates of "blind patching" make it nearly impossible to record from more than one cell at a time. In contrast, this whole-brain preparation (with unflapped cortex) is, for the purposes of patching, essentially a thick slice preparation. It is therefore relatively easy to achieve multi-whole-cell recordings, which may be put to good use studying subthreshold correlated variability (see Chapter 4), as well as describing cortical activity in novel and likely relevant ways (discussed later in this chapter).

Third, this can all be done in a largely intact visual system. Stable whole-cell (and even multi-whole-cell) recordings are readily performed in cortical slice or thin cell cultures, but this approach at best preserves short-range connectivity, and can't be used to study responses to sensory stimulation. So while these *in vitro* preparations are ideal for addressing certain questions, the whole-brain prep offers the distinct advantage of a subthreshold view of visual responses in a minimally-disrupted cortex.

Here, we list several open questions that are of broad interest in systems neuroscience. We discuss ways in which whole-cell (and/or extracellular) recordings in the turtle whole-brain preparation can provide unique insights in these areas. Finally, we propose very general experimental approaches, intended to be starting points for these future studies. In places, we identify specific technical challenges the future experimentalist will need to overcome.

As experimental techniques advance, the particular advantages of the turtle whole-brain preparation will expire. Until then, this chapter is intended to be a resource for future students in search of a project to make their own.

7.2 The excitation-inhibition balance

Mounting experimental evidence suggests that cortical excitation and inhibition are balanced. Specifically, the ratio of excitatory and inhibitory inputs to a given neuron or population of neurons may remain approximately constant over time (possibly even across stimulus conditions), made possible by the sparse nature of cortical connectivity, and relatively strong inhibitory synapses. This has profound consequences for cortical function. In particular, it promotes a chaotic network dynamic, which is associated with the fast tracking of input

signals(Vreeswijk & Sompolinsky, 1996), effective signal propagation(Vogels & Abbott, 2005), and maximized information capacity(Shew, Yang, Yu, Roy, & Plenz, 2011) (see Deneve, Machens 2016 for a review). This balance may also be a key variable in the dynamics and coherence of cortical oscillations(Brunel & Wang, 2003; Yang, Shew, Roy, & Plenz, 2012) and "propagating waves"(Keane & Gong, 2015), linking it to the vast literature on these ubiquitous cortical phenomena.

Still, several questions about this phenomenon have yet to be fully addressed. The first deals with the inherent lag between excitation and inhibition. Is the balance "tight" (with a very short lag between E and I) or "loose" (with I tracking E at longer lags)? Does this lag change across stimulus conditions? Second, does inhibition balance excitation only generally, or does this relationship hold on a single-trial basis? Finally, what are the implications for cortical function when the balance is disrupted?

Patch clamp recordings in the *ex vivo* preparation are particularly well-suited to address these questions. First, the E-I balance is typically discussed in terms of synaptic currents, which are not easily inferred from spike data. Second, with pairwise recordings, it's possible to estimate the lag between E and I (with certain important caveats, as discussed below). Finally, measuring the balance across stimulus conditions, and inferring the ramifications for sensory coding, require a responsive sensory system; a reduced preparation just won't do.

From our initial experimental results, we make three key observations regarding the E-I balance during visually-evoked activity: (1) populations of excitatory and inhibitory neurons may alternate spiking on a relatively long time scale (hundreds of milliseconds) after stimulus onset; (2) the nature of fast subthreshold fluctuations suggests very brief (tens of milliseconds) E-I

imbalances, or in other words, small lags between E and I; (3) evoked spikes are preceded by brief imbalances that heavily favor excitation. The second and third observations are discussed at length in chapters four and three, respectively. The first we detail below.

In response to visual stimulation, most neurons are initially depolarized by several millivolts, and this initial depolarization is followed by a mix of excitatory and inhibitory postsynaptic potentials (**Figures 3.3, 4.2c**). Is this initial depolarization evidence for strong excitatory conductances that are not balanced by inhibitory conductances? Not necessarily; because the resting neuron is near the inhibitory reversal potential, any initial increase in inhibitory conductance will have little effect on the membrane potential. In fact, some inhibitory neurons in turtle visual cortex can receive strong inputs from LGN (**Fig. 7.1**)(Fournier, Müller, & Laurent, 2015; MANCILLA, FOWLER, & ULINSKI, 1998; Mancilla & Ulinski, 2001). Thus, pyramidal cells do receive short-latency disynaptic feedforward inhibition(Kriegstein, 1987; Mancilla & Ulinski, 2001), which appears to be a general principle of cortical function(A. Y Y Tan & Wehr, 2009; Wehr & Zador, 2003; Wilent & Contreras, 2005). But because of the discrepancy in driving force for the two types of input, the early response phase favors excitatory currents, while the later response is a more even mix of (feedforward and feedback) excitation and inhibition. We have one set of recordings for a putative pyramidal-inhibitory pair that supports this hypothesis (**Fig. 7.2**). This slow back-and-forth between excitatory and inhibitory populations (which is initiated by favorable conditions for excitatory currents in the quiescent state) persists for the first few hundred milliseconds of the response, before giving way to a more even mix of excitation and inhibition. The early dynamic is fairly consistent across trials

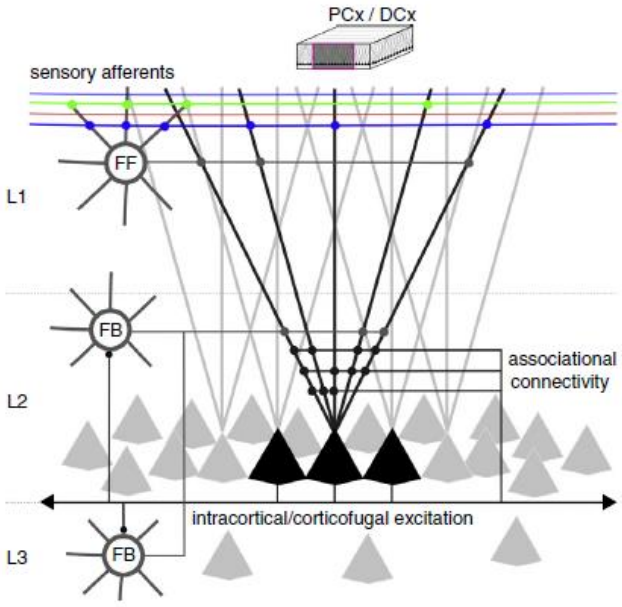

Figure 7.1 Schematic of the three-layer turtle dorsal (visual) cortex (DCx) and mammalian piriform cortex (PCx). Sensory inputs from LGN project to the apical dendrites of L2 pyramidal neurons and L1 inhibitory neurons. These inhibitory neurons (FF) provide feedforward disynaptic inhibition to pyramidals. Other inhibitory neurons (FB) in L2 and the "subcellular" L3 likely do not receive direct LGN inputs, but provide feedback inhibition to pyramidals. In experiment, electrodes pierce the ependymal surface (corresponding to the bottom of this figure), and are advanced through L3 toward L2. Thus, it is possible to target (L3) inhibitory – (L2) pyramidal pairs for simultaneous whole-cell recordings. Reproduced from Fournier, Muller, Laurent 2014 with permission from publisher (license # 4012651023358).

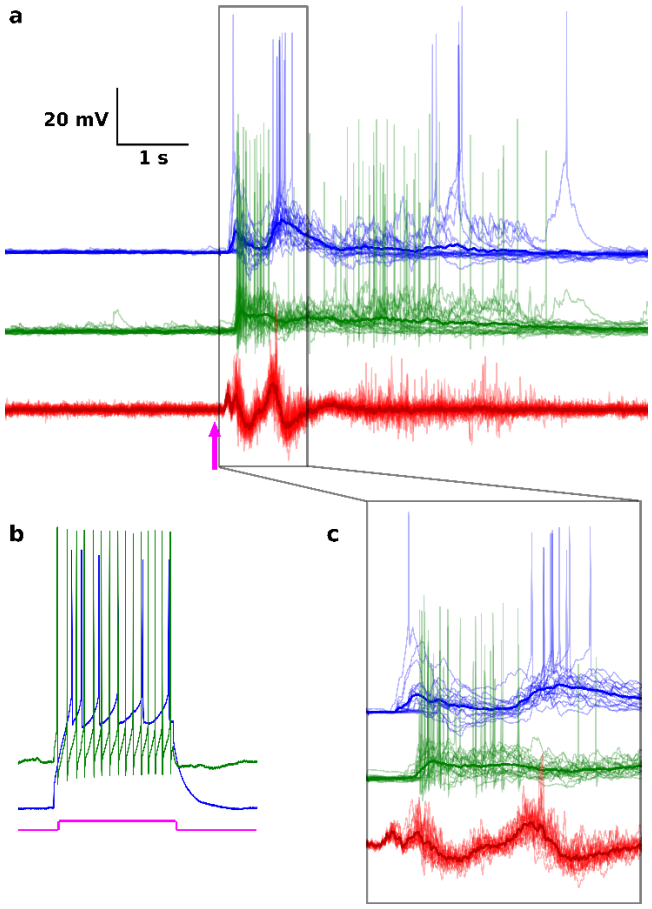

Figure 7.2 Visual stimulation evokes a slow "back-and-forth" excitation-inhibition dynamic in the early response. (a) Responses to multiple presentations of a 10 ms whole-field red flash, and across-trial averages (high opacity) for two simultaneously-recorded neurons (blue and green traces) and the nearby LFP (red traces). Stimulus onset at magenta arrow. Subthreshold activity, spike times, and LFP deflections are more consistent across trials in the early response than in the late response. (b) The spiking responses to tonic current injection suggest this is a pyramidal – inhibitory pair. Current injection amplitude is 100 pA. (c) Zoomed view of 1200 ms post-stimulus window. Note the alternating periods of spiking in the putative pyramidal (blue) and inhibitory (green) neurons, and the slow oscillation in the nearby LFP. The putative inhibitory neuron was located in the subcellular layer (i.e., L3, see Fig. 7.1), and the lack of feedforward LGN input to these interneurons is consistent with the delay in depolarization relative to the putative pyramidal neuron.

(compared with the more variable late response), and this synchronous activity likely contributes to the observed strong, early, low-frequency LFP oscillations.

This last result highlights one of the two ways pairwise whole-cell recordings can be used to study the E-I balance (but likely only at longer times scales, due to the averaging process, as described below). This approach involves targeting pyramidal-inhibitory pairs, and treating the membrane potentials as the "outputs" of the two neurons, or proxies for probability to spike. With a large population of pairs, the relative dynamics of the membrane potentials will provide an estimate of the dynamics of the E-I balance. Alternatively, both cells can be maintained at high resting membrane potentials (via holding current), to promote spiking. They will then represent "loud" members of the pyramidal and inhibitory populations, indicating when each population is prone to spike. Two things should be noted. First, this definition of the E-I balance is different from that described above; it tracks the activities of the two populations, not the excitatory and inhibitory currents. Second, while inhibitory neurons are relatively sparse in the cell layer, they are the dominant neuron in the sparsely-populated subcellular layer (**Figure 7.1**), making them easy to identify and target. Thus, a large population of pyramidal-inhibitory pairs is a realistic experimental goal.

The second approach involves measuring (or inferring) a neuron's synaptic inputs. Ideally, the experimenter would record excitatory and inhibitory synaptic inputs to the same neuron. This is impossible in cortical pyramidal neurons (although there are ways to do this in more spatially confined neurons(Cafaro & Rieke, 2010)). Instead, the experimenter can record excitatory inputs to one cell, and inhibitory inputs to a neighbor. Previous work has shown than in some areas, the inputs to one cell are good approximations of those to the neighboring neuron(Graupner & Reyes, 2013; Okun & Lampl, 2008). In this case, a pairwise recording approximates the simultaneous

recording of excitation and inhibition in one cell. In contrast, we observe relatively low correlations in membrane potentials of neighboring neurons (see Chapter 4). Therefore, it is not safe to make this same approximation, and the interpretation of the E-I ratio and lag for a given stimulus condition is unclear. However, we can still track changes in the balance across stimulus conditions with a sufficiently large population of pairs (as we have done for V-V and g-LFP correlated variability in Chapters 4 and 5).

First, the experimenter can record the membrane potentials from pairs of nearby cells, using holding current to set one near the reversal potential for inhibition, and the other near that of excitation (which will require blocking the spiking mechanisms of recorded neurons). It will be important to switch the holding potentials on alternating trials (for reasons discussed below). Up to this point, this approach follows earlier studies. Next, the conductance estimation algorithm (see Chapter 5) can be used to infer the excitatory and inhibitory currents, which have higher temporal resolution than the corresponding membrane potential recordings (**Fig. 5.1**). While we have only used the algorithm to estimate excitatory conductances, the algorithm should provide a reliable estimate of inhibition when excitatory inputs are negligible.

With this dataset, there are two ways to estimate the dynamics of the E-I ratio, and one to estimate the lag. First, because the holding potential of a given neuron has been switched across trials (resulting in "high" and "low" subsets of trials for each cell), it's possible to calculate the total excitatory (by, e.g., integrating the current in "low" trials) and inhibitory (using "high" trials) input to a given cell, for a given window of activity. Repeating this for multiple windows yields the dynamics of the E-I ratio (at the temporal resolution defined by the window used to integrate the current). Importantly, this is the ratio of the trial-averaged excitation to the trial-averaged inhibition. The second approach utilizes simultaneous recordings; the approach is the same, but

using excitatory inputs to one cell and inhibitory inputs to the other allows the experimenter to calculate the dynamics of the E-I ratio for each trial. This approach has three distinct advantages. First, it can be used to test the hypothesis that the E-I balance is maintained on a *single-trial* basis. Second, the E-I lag (corresponding to the peak in the E-I cross-correlogram) can be calculated for several windows of activity. Note that alternating "high" and "low" holding potentials across trials results in "high-low" and "low-high" pairwise recordings, and allows the experimenter to distinguish the E-I lag from any inherent lag in all synaptic inputs to the two cells (as in Okun, Lampl 2008). Finally, it is more straightforward to test the statistical significance of the resulting values (e.g., by bootstrapping).

7.3 Comparison of spontaneous and evoked cortical activity

Previous experimental and computational work has suggested that the mature sensory cortex possesses an intrinsic set or "manifold" of activity patterns. Spontaneous and sensory-evoked events both sample the same manifold (with evoked activity triggered by sensory inputs, and spontaneous activity by events hidden from the experimenter)(Luczak, Barthó, & Harris, 2009). This hypothesis relating spontaneous and evoked activity predicts that the two activity types should be similar in measurable ways. Furthermore, because circuits can be influenced by repetitive stimulation(Carrillo-Reid, Yang, Bando, Peterka, & Yuste, 2016), it's possible that spontaneous and sensory-evoked activity may become more similar through "training", or repetitions of a given visual stimulus.

Because the subthreshold membrane potential of a cortical neuron gives a measure of cortical spatiotemporal spiking patterns, it is a useful signal for testing these predictions. Indeed,

previous work in thalamocortical slice has revealed repeating temporal "motifs" in membrane potential recordings of spontaneous activity(Ikegaya, Aaron, Cossart, Aronov, & Lampl, 2004; Mokeichev et al., 2007), which resemble those evoked by electrical stimulation of the thalamus(MacLean, Watson, Aaron, & Yuste, 2005). This work, then, generally supports the above hypothesis.

Still, several open questions remain. First, it's impossible to study the influences of long-range connectivity and naturalistic sensory stimulation in slice. Do the above results hold when these variables are included? Furthermore, the experimenter can't "train" the cortical slice by providing repetitions of a relevant and complex stimulus (that is, sensory input that engages specific populations of cortical neurons in a particular temporal order, similar to what might be evoked in the organism's natural environment). Can such training influence spontaneous activity patterns? Finally, can we learn anything new by simultaneously recording the membrane potentials of multiple neurons?

The wholebrain preparation is ideal for addressing these questions, and the appropriate experimental protocol is a relatively straightforward extension of our existing approach. After patching onto one or more neurons, the experimenter should first collect a set of "baseline" recordings in complete darkness, to provide a measure of spontaneous activity before training. Second, sets of stimulus trials (incorporating a complex, naturalistic stimulus) should be interleaved with sets of spontaneous recordings. With this data set, it will be possible to both compare spontaneous and evoked events, and inspect for training effects. Finally, multi-whole-cell recordings can provide a higher-dimensional description of cortical activity. For example, the (z-scored) membrane potentials of simultaneously-recorded neurons can be plotted against one

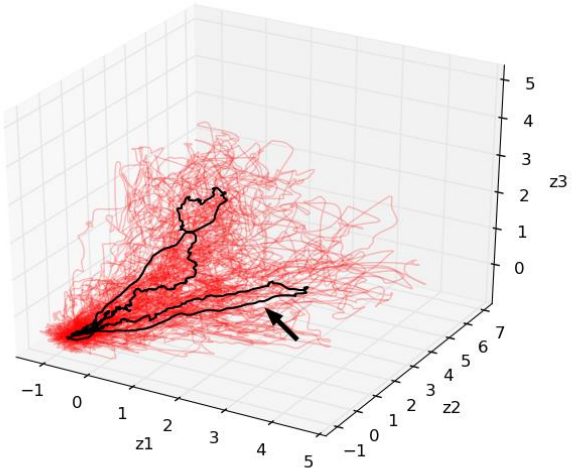

Figure 7.3 A "trajectory" view of multi-whole-cell recordings reveals distinguishable cortical responses to movie onset and embedded red dot. Membrane potentials from three simultaneously-recorded neurons are z-scored and plotted vs. one another for each repetition of a stimulus, to give a multi-whole-cell "trajectory" view of evoked activity (red traces). Across-trial average trajectory in black. Stimulus is motion-enhanced movie, with "embedded" red dot presented 4 s after movie onset (courtesy Jack Gallant and Woodrow Shew). The red dot is centered in and fills approximately half of the visual field. The "upper" trajectory above describes the first 4 s of the movie response, and the "lower" trajectory (indicated by black arrow) is the response to the embedded red dot. Thus, while single-trial variability is large (as indicated by the highly-variable nature of the red traces), the movie onset and dot onset evoked average cortical responses that are easily distinguishable using the membrane potentials from just three simultaneously-recorded neurons.

another, forming "response trajectories" (**Figure 7.3**) that may reveal patterns not readily apparent in individual whole-cell recordings.

7.4 Thalamic and Cortical Contributions to Visually-evoked Activity

As discussed in earlier chapters, a relatively simple view of cortex segregates sensory-evoked cortical inputs into two sources: thalamic and cortical. What does each of these sources contribute to the total cortical response? Previous work in mouse visual(Y. Li, Ibrahim, Liu, Zhang, & Tao, 2013; Lien & Scanziani, 2013) and auditory(L. Li, Li, Zhou, Tao, & Zhang, 2013) cortex conclude that thalamic input to cortical neurons is tuned to particular stimulus features (either because the thalamic neurons themselves are tuned, or as a result of patterns of convergence in thalamic inputs), and that intracortical inputs amplify this tuned signal. Yet the cortex is distinguishable from earlier sensory areas by its complex interconnectivity (including both short- and long-range connections) and spatiotemporal activity patterns. Further, although cortical neurons do display subthreshold orientation selectivity in response to scanning bars, they tend to respond to a wide variety of stimuli; scanning bars may not be the best stimulus for defining cortical neurons. In short, the cortex likely serves as more than an amplifying relay between thalamus and higher-order areas. Addressing this possibility requires presenting more complex stimuli and obtaining measures of evoked activity beyond response amplitude (see below) under two conditions: one in which the cortex is active, and one in which the cortex is relatively inactive.

Our initial results suggest that we may be able to distinguish between thalamic and cortical inputs. It has been shown that electrical stimulation of the lateral forebrain bundle (LFB, which projects from thalamus to cortex) evokes short-latency, unitary EPSPs in cortical neurons, followed by more complex mixtures of EPSPs and IPSPs (provided the stimulus is strong enough to evoke cortical spiking, **Figure 7.4a - d**). In contrast, cortical stimulation evokes only the late

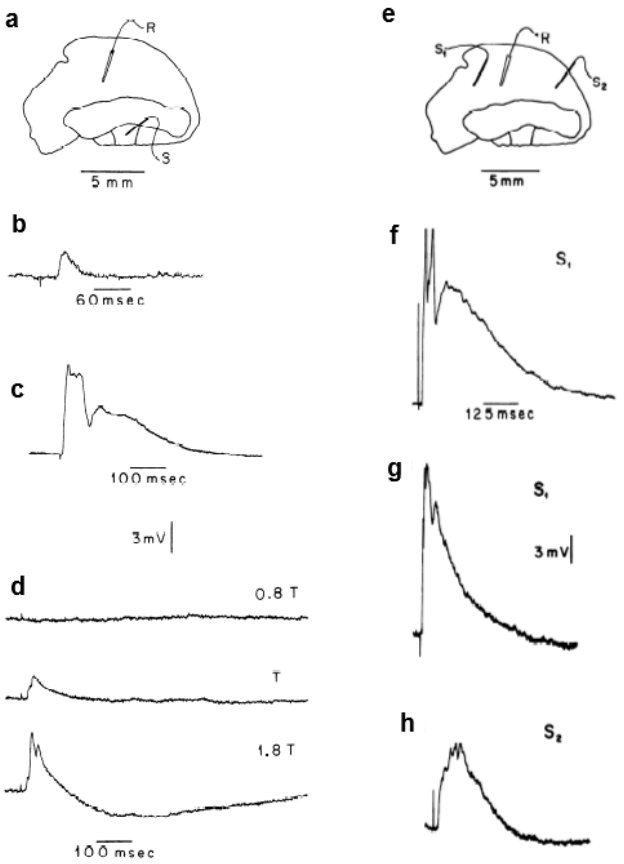

Figure 7.4 Lateral forebrain bundle (LFB) stimulation evokes short-latency cortical EPSPs, which are absent in response to cortical stimulation. (a) One experimental setup, in which one electrode (S) is used to electrically stimulate the LFB, and another (R) is used to record the membrane potential of individual pyramidal neurons. This reduced preparation consists of the cortex, LFB, and dorsal ventricular ridge. (b, c) Intracellular cortical responses to low-amplitude (c) and high-amplitude (d) stimulation of the LFB. Artifacts indicate stimulus onset. (d) Intracellular recordings of responses to various levels of LFB stimulation. Stimulus amplitudes are listed in multiples of the threshold value (T) that evokes cortical PSPs. (e) Alternate experimental setup, in which the cortex is electrically stimulated by an electrode that is either near to (S_1) or far from (S_2) the recording electrode. (f, g) Intracellular recordings of responses of two different neurons to near-electrode stimulation. (h) Same as in (g), but for far-electrode stimulation. From Larson-Prior, Ulinksi, Slater 1991.

inputs(Larson-Prior, Ulinski, & Slater, 1991) (**Figure 7.4e - h**). This suggests that it should be possible to segregate thalamocortical and corticocortical inputs by latency and waveform. For some cells and stimuli, we observe distinct short- and long-latency inputs in response to visual stimulation (**Figure 7.6**), and two observations suggest they are indeed thalamic and cortical in origin, respectively. First, the short-latency inputs have a more reliable time course across trials than the later inputs (**Figure 7.6**), consistent with a more spontaneously-active cortex (which leads to a variable cortical state at stimulus onset, as discussed in Chapter 3). Second, the amplitude and duration of the barrages of late inputs are highly variable across preparations, in contrast to the early inputs (**Figure 7.5**). This is consistent with the hypothesis that cortical excitability (and therefore the size of the cortical response that can be evoked by a given thalamic input) is variable across preparations (as indicated by the variable degree of spontaneous "synchrony", as described in Chapter 3).

Our results also suggest there is indeed more to the picture than amplification of thalamic inputs. First, thalamic inputs to cortical pyramidal neurons in turtle are thought to correspond to narrow "isoazimuths" in the visual field(Mulligan & Ulinski, 1990). Yet we observe that individual neurons receive substantial subthreshold inputs in response to visual stimulation nearly anywhere in the visual field (**Figure 7.6**), which is likely due to extensive lateral intracortical connections(Cosans & Ulinski, 1990). Second, there is no clear relationship between the amplitude (or presence) of short-latency inputs and the total response amplitude. For instance, the region of the visual field corresponding to the largest total subthreshold response in a given neuron may not elicit a short-latency response (**Figure 7.6**). Thus, the late (likely intracortical) inputs to a neuron define receptive fields that are complex compared to those predicted by thalamocortical architecture, and do not appear to be simple amplifications of thalamic inputs.

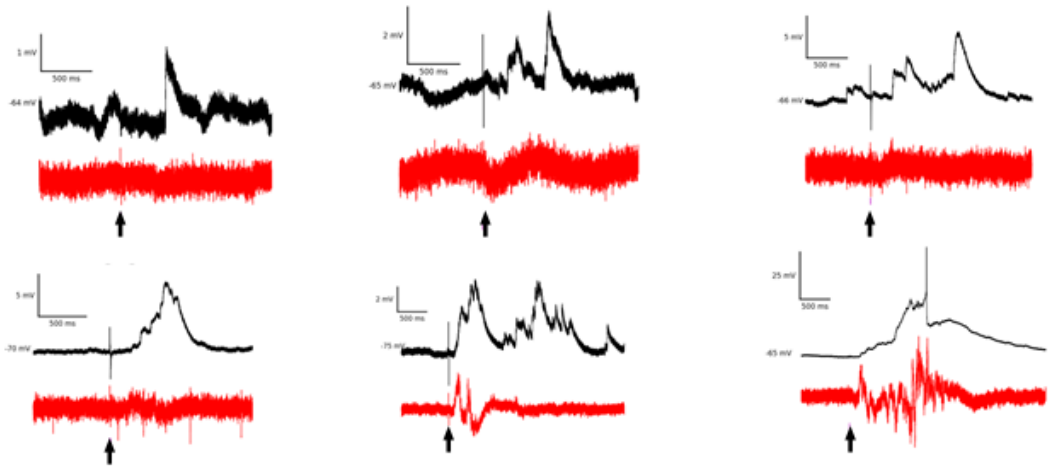

Figure 7.5 Visually-evoked response amplitude and duration varied continuously across experiments. Subthreshold membrane potential (black traces) and nearby LFP (red traces) recordings of responses to brief whole-field flashes (with stimulus onset indicated by black arrow). Each paired recording from a different preparation. Responses varied from small, short-latency EPSPs (top left), to long-duration barrages of EPSPs and IPSPs, which often evoked spikes (bottom right). Nearby LFP activity increased along with late intracellular activity.

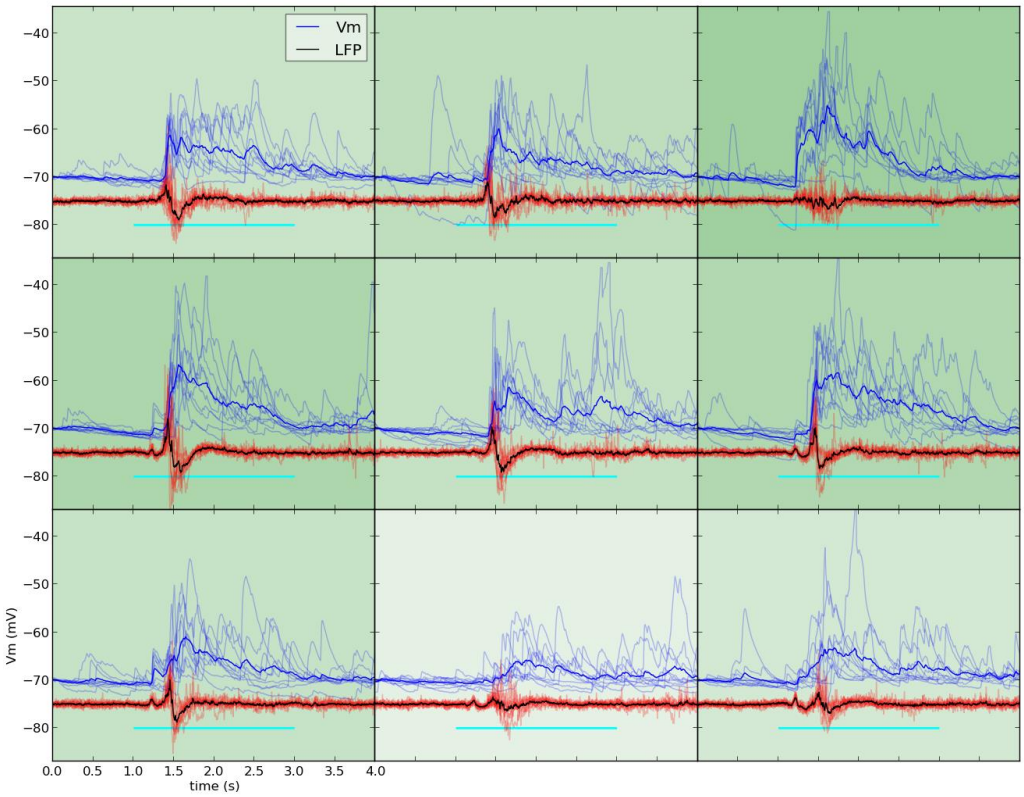

Figure 7.6 Individual cortical neurons have extremely large and complex receptive fields. Subthreshold membrane potential (blue traces) and nearby LFP (red traces) responses to multiple presentations of 2s white sub-field flash. Individual responses are in low opacity, and across-trial averages in high opacity. Cyan line below traces indicates stimulus duration. Stimulus is white square (randomly-selected from a 3x3 grid) presented on a black background. Opacity of green background on each subplot corresponds to average subthreshold response amplitude. Location of each subplot corresponds to the location of the flashed square in the visual field. Note that stimulation in some regions resulted in short-latency "bumps" in the LFP and unitary EPSPs in the membrane potential, suggesting this and nearby neurons received direct LGN inputs in response to flashes in those sub-fields. These features were absent in response to flashes in other regions, but responses could still be quite large. Indeed, the largest subthreshold responses (upper right) did not include short-latency inputs.

In this preparation, then, there appears to be a nontrivial contribution by cortical inputs to the sensory response, and these inputs may be distinguishable from thalamic inputs. How can an experiment be designed to disentangle the two types of inputs? With modern optogenetic tools, it is possible to reversibly silence the cortex by exciting cortical inhibitory neurons, or by depressing pyramidal neurons. These tools are not available in the turtle cortex. Instead, the experimenter can either reversibly influence cortical activity via pharmacology, or irreversibly disrupt cortical connectivity. In the first case, a GABA receptor agonist (e.g., muscimol) can be focally applied to cortex for a subset of trials. The enhanced inhibition should silence cortical activity, and ideally have no influence on thalamic inputs (provided a minimal amount is applied). Here, it will be important to protect the retina from exposure to muscimol. With the second approach, the experimenter can first collect a set of visual stimulation recordings with cortical connectivity intact. Next, the experimenter disrupts cortical connectivity by making two cuts: one rostral to and one caudal to the region of interest, from the medial cortex to the DVR. Ideally, this leaves the majority of thalamic inputs to the region intact. There are two technical considerations that motivate using extracellular recordings for this approach. First, it may be difficult to stabilize the "flap" of interest to the degree required for patching. Second, it will be important to resume recording as quickly as possible after making the cuts to minimize the influence of tissue death on the later recordings. With either approach, it will be impossible to completely silence cortical inputs, while leaving thalamic inputs completely unaffected. However, it will be sufficient to show that early and late inputs are differentially influenced by the manipulation.

Finally, what are appropriate stimuli and response measures for probing the roles of the two input types? First, as already mentioned, the two sources may be distinguishable by the latency and waveform of subthreshold PSPs in response to brief visual stimulation. Thus, the method

chosen for disrupting cortical inputs should have a greater impact on the late response than on short-latency inputs. As such, a brief stimulus, combined with one of the approaches described above, should be useful for assigning the early and late inputs to a particular source. Second, it is possible to probe the actual computational roles of the two input types. We propose two approaches. In the first, the experimenter presents a naturalistic movie on some trials, and a motion-enhanced (or phase-shuffled naturalistic) movie on other trials, and then calculates stimulus-response mutual information. The results can be compared for the two cortical conditions (activated/intact vs. silenced/disrupted) to infer the role of cortex in stimulus discrimination. This approach directly compares the "performance" of the two input types, with the hypothesis being that thalamocortical and intracortical inputs together will outperform thalamocortical inputs alone. The strength of this approach is that it quantifies the comparison. Alternatively, the experimenter can show a single complex stimulus across all trials, and calculate the reverse correlation between the response and the stimulus(Ramirez et al., 2014), which identifies the complex receptive field (or pattern of pixels) of the cell/electrode. This approach allows the experimenter to assess how the receptive field of inputs changes when the cortex is silenced, and moves beyond the classical probing of receptive fields with simplistic stimuli.

Brunel, N., & Wang, X.-J. (2003). What determines the frequency of fast network oscillations with irregular neural discharges? I. Synaptic dynamics and excitation-inhibition balance. *Journal of Neurophysiology*, *90*(1), 415–430. http://doi.org/10.1152/jn.01095.2002

Cafaro, J., & Rieke, F. (2010). Noise correlations improve response fidelity and stimulus encoding. *Nature*, *468*(7326), 964–7. http://doi.org/10.1038/nature09570

Carrillo-Reid, L., Yang, W., Bando, Y., Peterka, D. S., & Yuste, R. (2016). Imprinting Cortical Ensembles. *Science*, *353*, 691–694.

Cosans, C. E., & Ulinski, P. S. (1990). Spatial organization of axons in turtle visual cortex: intralamellar and interlamellar projections. *The Journal of Comparative Neurology*, *296*(4), 548–58. http://doi.org/10.1002/cne.902960404

Crochet, S., & Petersen, C. C. H. (2006). Correlating whisker behavior with membrane potential in barrel cortex of awake mice. *Nature Neuroscience*, *9*(5), 608–610. http://doi.org/10.1038/nn1690

Fournier, J., Müller, C. M., & Laurent, G. (2015). Looking for the roots of cortical sensory computation in three-layered cortices. *Current Opinion in Neurobiology*, *31*, 119–126. http://doi.org/10.1016/j.conb.2014.09.006

Graupner, M., & Reyes, A. D. (2013). Synaptic Input Correlations Leading to Membrane Potential Decorrelation of Spontaneous Activity in Cortex. *Journal of Neuroscience*, *33*(38), 15075–15085. http://doi.org/10.1523/JNEUROSCI.0347-13.2013

Ikegaya, Y., Aaron, G., Cossart, R., Aronov, D., & Lampl, I. (2004). Synfire Chains and Cortical Songs: Temporal Modules of Cortical Activity. *Science (New York, NY)*, *559*(2004). http://doi.org/10.1126/science.1093173

Keane, A., & Gong, P. (2015). Propagating waves can explain irregular neural dynamics. *J Neurosci*, *35*(4), 1591–1605. http://doi.org/10.1523/jneurosci.1669-14.2015

Kriegstein, a R. (1987). Synaptic responses of cortical pyramidal neurons to light stimulation in the isolated turtle visual system. *The Journal of Neuroscience : The Official Journal of the Society for Neuroscience*, *7*(8), 2488–92. Retrieved from http://www.ncbi.nlm.nih.gov/pubmed/3612249

Larson-Prior, L. J., Ulinski, P. S., & Slater, N. T. (1991). Excitatory amino acid receptor-mediated transmission in geniculocortical and intracortical pathways within visual cortex. *Journal of Neurophysiology*, *66*(1), 293–306. Retrieved from http://www.ncbi.nlm.nih.gov/pubmed/1681038

Li, L., Li, Y., Zhou, M., Tao, H. W., & Zhang, L. I. (2013). Intracortical multiplication of thalamocortical signals in mouse auditory cortex. *Nature Neuroscience*, *16*(9), 1179–81. http://doi.org/10.1038/nn.3493

Li, Y., Ibrahim, L. a, Liu, B., Zhang, L. I., & Tao, H. W. (2013). Linear transformation of thalamocortical input by intracortical excitation. *Nature Neuroscience*, *16*(9), 1324–30. http://doi.org/10.1038/nn.3494

Lien, A. D., & Scanziani, M. (2013). Tuned thalamic excitation is amplified by visual cortical circuits. *Nature Neuroscience*, *16*(9), 1315–23. http://doi.org/10.1038/nn.3488

Luczak, A., Barthó, P., & Harris, K. D. (2009). Spontaneous Events Outline the Realm of Possible Sensory Responses in Neocortical Populations. *Neuron*, *62*(3), 413–425. http://doi.org/10.1016/j.neuron.2009.03.014

MacLean, J. N., Watson, B. O., Aaron, G. B., & Yuste, R. (2005). Internal dynamics determine the cortical response to thalamic stimulation. *Neuron*, *48*(5), 811–823. http://doi.org/10.1016/j.neuron.2005.09.035

MANCILLA, J. G., FOWLER, M., & ULINSKI, P. S. (1998). Responses of regular spiking and

fast spiking cells in turtle visual cortex to light flashes. *Visual Neuroscience*, *15*(05), 979–93. http://doi.org/10.1017/S0952523898155190

Mancilla, J. G., & Ulinski, P. S. (2001). Role of GABA(A)-mediated inhibition in controlling the responses of regular spiking cells in turtle visual cortex. *Visual Neuroscience*, *18*(1), 9–24. Retrieved from http://www.ncbi.nlm.nih.gov/pubmed/11347819

Margrie, T. W., Meyer, A. H., Caputi, A., Monyer, H., Hasan, M. T., Schaefer, A. T., … Brecht, M. (2003). Targeted whole-cell recordings in the mammalian brain in vivo. *Neuron*, *39*(6), 911–8. Retrieved from http://www.ncbi.nlm.nih.gov/pubmed/12971892

Mcginley, M. J., Stephen, V., Mccormick, D. A., Mcginley, M. J., David, S. V, & Mccormick, D. A. (2015). Cortical Membrane Potential Signature of Optimal States for Sensory Signal Detection Cortical Membrane Potential Signature of Optimal States for Sensory Signal Detection. *Neuron*, *87*(1), 179–192. http://doi.org/10.1016/j.neuron.2015.05.038

Mokeichev, A., Okun, M., Barak, O., Katz, Y., Ben-Shahar, O., & Lampl, I. (2007). Stochastic Emergence of Repeating Cortical Motifs in Spontaneous Membrane Potential Fluctuations In Vivo. *Neuron*, *53*(3), 413–425. http://doi.org/10.1016/j.neuron.2007.01.017

Mulligan, K. a, & Ulinski, P. S. (1990). Organization of geniculocortical projections in turtles: isoazimuth lamellae in the visual cortex. *The Journal of Comparative Neurology*, *296*(4), 531–47. http://doi.org/10.1002/cne.902960403

Okun, M., & Lampl, I. (2008). Instantaneous correlation of excitation and inhibition during ongoing and sensory-evoked activities. *Nature Neuroscience*, *11*(5), 535–7. http://doi.org/10.1038/nn.2105

Ramirez, A., Pnevmatikakis, E. A., Merel, J., Paninski, L., Miller, K. D., & Bruno, R. M. (2014). Spatiotemporal receptive fields of barrel cortex revealed by reverse correlation of synaptic input. *Nat Neurosci*, *17*(6), 866–875. http://doi.org/10.1038/nn.3720

Sachidhanandam, S., Sreenivasan, V., Kyriakatos, A., Kremer, Y., & Petersen, C. C. H. (2013). Membrane potential correlates of sensory perception in mouse barrel cortex. *Nature Neuroscience*, *16*(11), 1671–7. http://doi.org/10.1038/nn.3532

Shew, W. L., Yang, H., Yu, S., Roy, R., & Plenz, D. (2011). Information Capacity and Transmission Are Maximized in Balanced Cortical Networks with Neuronal Avalanches. *Journal of Neuroscience*, *31*(1), 55–63. http://doi.org/10.1523/JNEUROSCI.4637-10.2011

Tan, A. Y. Y., Chen, Y., Scholl, B., Seidemann, E., & Priebe, N. J. (2014). Sensory stimulation shifts visual cortex from synchronous to asynchronous states. *Nature*. http://doi.org/10.1038/nature13159

Tan, A. Y. Y., & Wehr, M. (2009). Balanced tone-evoked synaptic excitation and inhibition in mouse auditory cortex. *Neuroscience*, *163*(4), 1302–1315. http://doi.org/10.1016/j.neuroscience.2009.07.032

Vogels, T. P., & Abbott, L. F. (2005). Signal Propagation and Logic Gating in Networks of

Integrate-and-Fire Neurons. *The Journal of Neuroscience*, *25*(46), 10786–10795. http://doi.org/10.1523/JNEUROSCI.3508-05.2005

Vreeswijk, C. Van, & Sompolinsky, H. (1996). Chaos in Neuronal Networks with Balanced Excitatory and Inhibitory Activity Author (s): C . van Vreeswijk and H . Sompolinsky Published by : American Association for the Advancement of Science Stable URL : http://www.jstor.org/stable/2890956, *274*(5293), 1724–1726.

Wehr, M. S., & Zador, A. M. (2003). Balanced inhibition underlies tuning and sharpens spike timing in auditory cortex. *Nature*, *426*(6965), 442–6. http://doi.org/10.1038/nature02116

Wilent, W. B., & Contreras, D. (2005). Dynamics of excitation and inhibition underlying stimulus selectivity in rat somatosensory cortex. *Nature Neuroscience*, *8*(10), 1364–70. http://doi.org/10.1038/nn1545

Yang, H., Shew, W. L., Roy, R., & Plenz, D. (2012). Maximal Variability of Phase Synchrony in Cortical Networks with Neuronal Avalanches. *Journal of Neuroscience*, *32*(3), 1061–1072. http://doi.org/10.1523/JNEUROSCI.2771-11.2012